Magnetism with two-dimensional MXenes : impacts of structure and composition

Himangshu Sekhar Sarmah

Roll No: 196121107

Under the supervision of

Prof. Subhradip Ghosh

Department of Physics
Indian Institute of Technology Guwahati
Guwahati-781039, Assam, India

Thursday 9th October, 2025

Magnetism with two-dimensional MXenes : impacts of structure and composition

A thesis submitted by
Himangshu Sekhar Sarmah

to

Department of Physics
Indian Institute of Technology Guwahati
in partial fulfillment of the requirements
for the award of the degree of
Doctor of Philosophy in Physics

Department of Physics
Indian Institute of Technology Guwahati
Guwahati-781039, Assam, India


Indian Institute of Technology Guwahati

Statement

The research presented in this thesis, titled **Magnetism with two-dimensional MXenes : impacts of structure and composition** was conducted by me at the Department of Physics, Indian Institute of Technology Guwahati, under the supervision of Prof. Subhradip Ghosh.

I hereby declare that the content of this thesis is the result of my original work and has not been submitted, either in part or in full, for the award of any other degree or diploma. All material that is not my own has been properly cited and acknowledged within the thesis.

Himangshu Sekhar Sarmah
Roll no: 196121107
Department of Physics
Indian Institute of Technology Guwahati
Guwahati - 781039, India

Thursday 9th October, 2025

Disclaimer

The bibliography presented in this thesis is by no means exhaustive, but it includes the sources that were thoroughly consulted during the course of this work. I sincerely apologize for any unintentional omission of relevant research papers, review articles, or other scientific documents that deserve citation.
Some figures have been reproduced from external sources for illustrative purposes and are duly cited.

Certificate

It is certified that the work contained in the thesis entitled **Magnetism with two-dimensional MXenes : impacts of structure and composition** by Himangshu Sekhar Sarmah, a Ph.D. student of the Department of Physics, Indian Institute of Technology Guwahati is carried out under my supervision and has not been submitted elsewhere for the award of any other degree.

(Prof. Subhradip Ghosh)
Department of Physics
Indian Institute of Technology Guwahati
Guwahati-781039, Assam, India

Thursday 9th October, 2025

Dedicated to my parents

Acknowledgement

At the beginning, I would like to extend my heartfelt gratefulness to my thesis supervisor, Prof. Subhradip Ghosh. His continuous support during my PhD time is truly invaluable. The depth of his knowledge, along with his insightful feedback from time to time, has helped me grow both as a person and as a researcher. I particularly appreciate the freedom he allowed me to explore ideas, make mistakes, and grow from those experiences. Being under his supervision has been an enriching and transformative experience, and I am genuinely grateful for it.

I would also like to extend my heartfelt gratitude to my doctoral committee members, Dr. Uday Narayan Maiti, Prof. Saurabh Basu, and Prof. Chandan Mukherjee, for their various constructive insights during the annual progress seminars. I want to especially thank Prof. Indra Das Gupta and Kunal Dutta from the Indian Association of Cultivation of Science for collaborating with me on a work. I also want to acknowledge Prof. Biplab Sanyal from Uppsala University and Dr. Aarti Kashyap from IIT Mandi for the enlightening discussions we had during my PhD period. I'm sincerely thankful to the Heads of the Departments for their various assistance during my Ph.D. journey(Prof. Subhradip Ghosh, Prof. Perumal Alagarsamy, and Prof. Basanta Ranjan Boruah). I acknowledge the technical and other office staff of the Department of Physics, IIT Guwahati, whose help made various aspects of my research more efficient and smooth. I would also like to express my gratitude to Param Ishan and Param Kamrupa, IIT Guwahati, for granting access to high-performance computing resources , which was essential for conducting the computational aspects of this research. Furthermore, I am thankful to the Department of Physics, IIT Guwahati, for providing access to the Newton Cluster. I acknowledge SERB, India, for hosting my conference visit to Poland.

I also want to express my gratitude to my senior colleagues — Dr. Sheuly Ghosh, Dr. Ujjwal Saikia, Dr. Mandira Das, and Dr. Mayuri Bora — for their constant support, guidance, and encouragement throughout my Ph.D. journey. I would also like to thank Madhumita, Himanshu, Swati, and Arvind, my fellow juniors, whose friendship and cooperation made our time in the lab genuinely delightful.

A big thank you to all my batchmates — Mijanur, Sunil, Santanu, Chinmoy, Dev, Bhairab, Anupam, Didwmsha, Seshadri, and Lipika — for being an essential part of my PhD life. Special thanks go out to Sunil and Mijanur, whose friendliness and warmth made this place a true home away from home. I would also like to thank all my labmates for creating a healthy learning environment in the labs. I'm also grateful to all my teachers, from school through university, whose inspiration and encouragement have shaped my academic journey and fueled my passion for research.

Lastly, and most importantly, I extend my deepest gratitude and respect to my parents and brother for their unwavering love, patience, and support. Their faith in me has been my greatest strength throughout this journey.

Abstract

With the advent of quantum information processing, and rising demand of energy-efficient , fast memory devices, spin based technological innovation has become state of art. Magnetism , the fundamental science behind the success of such innovations, has therefore taken the centre stage of current day materials research. As components have shrunk in size and the need for high-speed, low-energy, and non-volatile functionalities has grown, researchers have been looking for materials that demonstrate magnetic properties that can be adjusted at smaller scales. The unique electrical properties and thin atomic layers of two-dimensional (2D) materials make them outstanding in this field. Because of their chemical diversity, structural adaptability, and ease of surface modification, MXenes—a broad family of 2D transition metal carbides, nitrides, and carbonitrides—have drawn attention . Initially recognized for their exceptional capabilities in energy storage and shielding against electromagnetic interference, recent theoretical and experimental studies have revealed their considerable potential in the domain of magnetism research. Their ability to support intrinsic and induced magnetism, excellent electrical conductivity, and mechanical strength make MXenes strong candidates for magnetic applications. However, the research on magnetism with MXenes is still in its infancy. In this thesis, we try to achieve two things: first, to explore the structure-property relationships in intrinsically magnetic MXenes, and second, to investigate how other traits of non-magnetic MXenes can be utilised for magnetism-related applications. Our investigation starts with studying i-MXenes, a class of in-plane chemically ordered MXenes whose MAX phase precursors have already been synthesized. We show these systems possess tunable magnetic behavior strongly influenced by surface terminations and compositional ordering. Subsequently, the magnetic and electronic properties of nitride-based MXenes with unconventional stacking sequences are explored. This study reveals how variations in stacking can substantially alter the magnetic ground state and finite-temperature behavior, introducing a novel route to tailor material properties through structural engineering. Next, we attempt to investigate multiferrocity using MXene/TMDCs heterostructure. We have shown that our heterostructure possesses magneto-electric coupling, where ferroelectric polarization in the MXene layer can control the spin polarization in the adjacent TMDC layer. Such systems hold potential for non-volatile memory technologies and electric-field-controlled spintronic devices. Finally, we investigate the role of spin-orbit coupling (SOC) in non-centrosymmetric, non-magnetic MXenes Ta_2CS_2. We find the emergence of Rashba-like spin splitting and valley-dependent Zeeman effects arising from symmetry and orbital interactions, making these systems highly useful for use in valleytronics and SOC-driven spintronic platforms.

This thesis, in summary, expands our understanding of magnetism with MXene and emphasizes its enormous potential to make a splash in state of the art technologies that rely on the complex interplay between structure, symmetry, and spin degrees of freedom.

Contents

List of Figures

List of Tables

Chapter 1

Introduction

1.1 Two dimensional(2D) materials

Since the 1970s, materials with reduced dimensions have attracted researchers' interest. 2D materials, with their atomic thickness and high surface-to-volume ratio, offer exceptional strength and reactivity, making them ideal for advanced applications. Their tunable properties enable their use for energy, medicine, electronics, and environmental technology applications. Emerging from nanotechnology and green chemistry innovations, they hold promise for next-generation catalysts, sensors, membranes, and innovative therapeutic systems. However, the idea that atomically thin 2D materials could exist was initially met with skepticism within the physics community. According to classical ideas, thermal fluctuations in the lattice would cause such materials to become thermodynamically unstable at any non-zero temperature [1]. The fact that thinner films typically had lower melting points provided evidence in favor of this theory [2]. However, thanks to developments in contemporary spectroscopy, three-dimensional materials with naturally occurring layered structures, such as graphite and molybdenum disulfide, were discovered. Although these materials could be exfoliated into only one atom thick layers, in theory, this was long thought to be implausible experimentally.

However, the first breakthrough came in the year 2004 when the researchers Andre Geim and Konstantin Novoselov of the University of Manchester used a straightforward mechanical exfoliation method called the "scotch tape technique" to successfully separate monolayer graphene from graphite, which is a single-layer carbon atom arranged in a honeycomb lattice [3]. This discovery earned them the Nobel Prize in Physics in 2010 and launched the modern era of 2D materials. Due to its remarkable properties, this graphene has quickly got the title "wonder material." Some of these include greater flexibility, higher conductivity(even higher than copper), and extraordinary strength (even stronger than steel) [4]. This has motivated the researchers to focus on synthesizing other 2D materials. Recent advancements in exfoliation methods—such as micromechanical cleavage, ion intercalation, and surfactant-assisted ultrasonication—have paved the way for producing a wide range of layered bulk materials down to their monolayer forms [5, 6, 7]. Subsequently, a broad family of 2D materials emerged today, which includes transition metal dichalcogenides (TMDs),(Example MoS_2, WS_2, and WSe_2) [8, 9], hexagonal boron nitride (h-BN) [10], known as "white graphene," Black phosphorus [11], Silicene [12], MXene [13] etc to name a few. With a wide range of elements from the periodic table, the universe of 2D materials is incredibly diverse. These materials have electronic structures with bandgaps that span the electromagnetic spectrum, from ultraviolet to

infrared. Some of them are metallic and semi-metallic too. This increases the range of possible uses for 2D materials. Additionally, because of their ultrathin structures, 2D materials show quantum confinement effect, dramatically changing how heat, light, and charge carriers travel and producing unique and improved electrical and optical properties. Researchers have already demonstrated the potential of 2D materials by building integrated circuits that include components like memory units, logic gates, amplifiers, oscillators, mixers, switches, and modulators—all at atomic thicknesses [14, 15].
A significant breakthrough in the study of two-dimensional materials is the observation of inherent long-range magnetic order within single-layer atomic crystals. The following section will discuss 2D magnetic materials and their applications.

1.2 2D magnetic materials and their applications

Initially, it was thought that intrinsic magnetism in 2D materials is impossible as per the Mermin Wagner theorem, that rules out any possibility of long-range ordering in lower dimensions due to thermal fluctuations [16]. Researchers tried various approaches to induce magnetism in non-magnetic elements. These included creating vacancy defects [17], substitutional or adatom doping of magnetic atoms [18]. However, such processes often run into various design challenges. In the year 2017, the first successful discovery of intrinsic magnetism in 2D materials was observed in CrI_3 [19]. In the same year another 2D material $Cr_2Ge_2Te_6$ was also succesfully exfoliated [20] . These newly discovered materials exhibited significant magnetic anisotropy, allowing for robust magnetism even in their monolayer forms.

Since then, the field of 2D magnetism has grown very rapidly. This is due to the following three reasons: (1) Significant experimental advances in the field have been made with the successful synthesis of high-quality 2D magnetic monolayer and multilayer materials employing methods like molecular beam epitaxy (MBE), chemical vapor deposition (CVD), and micromechanical exfoliation [21]. (2)Advanced optical and electronic characterization methods have been developed, with tools like spin-polarized scanning tunneling microscopy (SP-STM) and x-ray magnetic circular dichroism (XMCD) becoming standard for probing the magnetic properties of 2D materials [21]. (3) The continuous growth in computational power has enabled accurate first-principles calculations, allowing researchers to predict magnetic ground states and extract key magnetic parameters for a wide range of 2D systems [21]. As a result, we have many candidates in the 2D magnetic family today. This includes but are not limited to VSe_2 [22], MPS_3 [23, 24](M=Fe,Mn,Ni), VTe_2 [25], α-$RuCl_3$ [26] to name a few. In addition, various substitution approaches and alloying in 2D materials have been made, giving rise to complex magnetic behavior and enhancing the scope of 2D materials [27, 28]. The evolutionary algorithm and particle swarm optimization (PSO) approach is another method that has already demonstrated its validity in discovering potential 2D magnets [21, 29, 30].

These 2D magnetic materials provide many benefits as compared to the 3D ones: (1) The magnetic behavior of the 2D materials can be easily tuned through intercalation and surface functionalization [21]. (2)The strength of the exchange interactions and anisotropy energy can be tuned through applications of strain and pressure. [21] (3) 2D magnets can be as thin as a single atomic layer, enabling the fabrication of ultra-compact devices. This helps in achieving device miniaturization. (4)2D magnets provide a platform to explore low-dimensional magnetism, phase transitions, and spin-lattice interactions at the atomic scale, which are not readily accessible in 3D.

Due to such advantages, they are propelling scientific progress in several industries. They have found applications in various sectors, such as biomedical applications, energy conversion, sensing, data storage, and cutting-edge domains like quantum computing. The search for materials with tailored magnetic properties—such as high Curie temperatures, low losses, and intense spin polarization, motivates interdisciplinary research across physics, chemistry, and materials science. These magnetic materials are combined with other functional materials like superconductors, ferroelectrics and ferrovalleys to create fascinating new hybrid systems that open up new possibilities in fields like twistronics and valleytronics. In the realm of advanced information technologies, spintronics has emerged as a transformative field. Devices such as magnetic tunnel junctions (MTJs) and spin valves utilize spin-dependent transport phenomena like tunneling magnetoresistance (TMR) and giant magnetoresistance (GMR) for data storage and sensing [31, 32]. Spin-transfer torque (STT) and spin-orbit torque (SOT) mechanisms enable the manipulation of magnetic states using spin-polarized currents, forming the basis for magnetic random access memory (MRAM), a promising non-volatile memory technology [33, 34].

One of the 2D materials that has shown lots of promise for magnetism-related applications is the MXenes. The following section will discuss the MXenes and their potential applications.

1.3 MXenes

MXene is a two-dimensional material derived from the three-dimensional MAX phase [35]. MAX phases represent a broad class of layered hexagonal compounds with a $P6_3/mmc$ space group symmetry with general formula $M_{n+1}AX_n$, where $n = 1, 2,$ or 3 [35]. In this structure, M = early transition metal; A = group III-VI elements, and X = carbon, nitrogen, or a combination of both [36]. The compounds contain a layer of X atoms sandwiched between two layers of M-atoms. These $M_{n+1} X_n$ layers are interleaved with layers of A atoms [37]. The crystal structure of a MAX phase with $n = 2$, i.e., M_3AX_2 is shown in Figure 1.1(a) for reference. When the A layers are selectively removed — typically through chemical methods — the resulting 2D structure, known as MXene, is shown in Figure 1.2(a). In the MXene structure, each X atomic layer remains sandwiched between the M atomic layers. These MXenes have chemical formula $M_{n+1}X_n$.

So far, over 150 different MAX phases have been successfully synthesized [38]. One of the key differences between MAX phases and other well-known layered materials like graphite or transition metal dichalcogenides (TMDCs) is the nature of the interlayer bonding. In TMDCs and graphite, weak van der Waals interactions are responsible for holding the layers together, making it feasible for mechanical exfoliation [39]. In contrast, MAX phases are bonded more strongly: the M-A bonds are metallic, while the M-X bonds exhibit covalent, metallic, and ionic characteristics. As a result, MXene cannot be obtained from the MAX phase through the mechanical exfoliation process. Instead, chemical etching routes have to be employed for this purpose of obtaining 2D MXene sheets [40, 41]. Few MAX compounds possess two distinct types of transition metal atoms present in their structures in an ordered fashion. These are broadly classified into o-MAX(out-of-plane ordered MAX) and i-MAX(in-plane ordered MAX) phases.

In o-MAX phases, the two transition metals are layered in an out-of-plane configuration. A typical example is the $M'_2M"AX_2$-type structure, shown in Figure 1.1(b). Upon

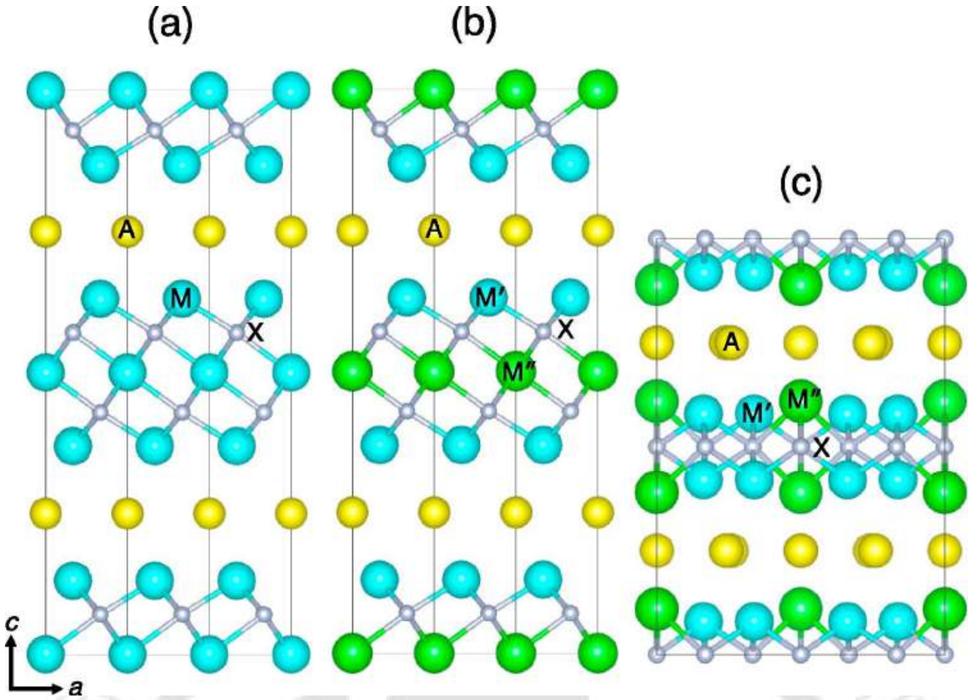

Figure 1.1: Various MAX phases: (a) Normal MAX phase $M_3AX_2$with only one transition metal atom(b) Out-of-plane ordered MAX phase $M'_2M"AX_2$ with two different transition metal with out-of -plane ordering and (c) In-plane ordered MAX phase $(M'_{2/3}M"_{1/3})_2AX$with two differrent transition metal with in-plane ordering (Reused with permission from [37]).

etching out the A-layer, the resulting 2D material — o-MXene — exhibits a distinctive structure, as seen in Figure 1.2(b). In this configuration, the outer transition metal layers consist entirely of one metal (M′), while the inner layers consist of a different transition metal (M"). The space group of this family of compounds is $P6_3/mmc$. Some examples of of o-MAX are Mo_2TiAlC_2, $Mo_2Ti_2AlC_3$, Cr_2TiAlC_2, and Mo_2ScAlC_2. They have been successfully exfoliated into Mo_2TiC_2, $Mo_2Ti_2C_3$, Cr_2TiC_2, and Mo_2ScC_2 MXenes, respectively [42, 43, 44].

The i-MAX phases, on the other hand, have the in-plane ordering of the two transition metals. The chemical formula for these compounds is $(M'_{2/3}M"_{1/3})_2AX$, where M′ and

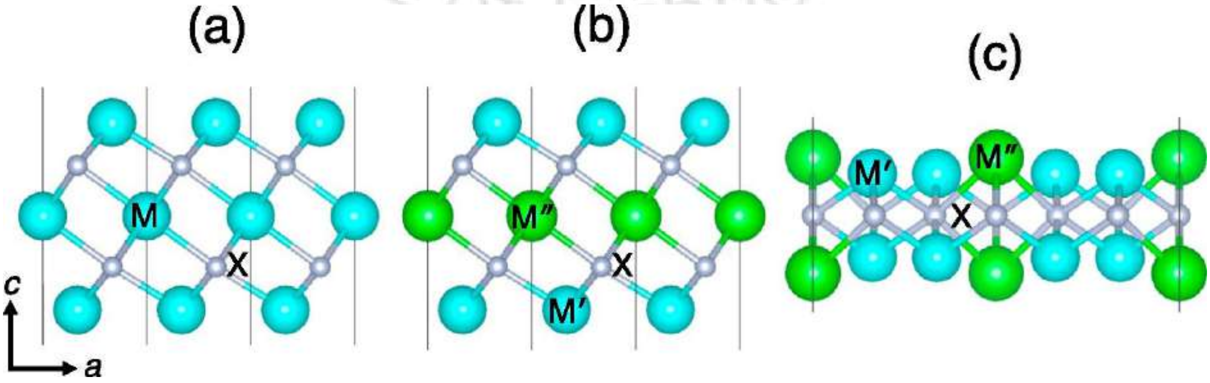

Figure 1.2: Various MXene phases: (a) Normal MXene phase M_3X_2(b) o-MXene phase $M'_2M"X_2$ and (c) i-MXene phase $(M'_{2/3}M"_{1/3})_2X$ (Reused with permission from [37]).

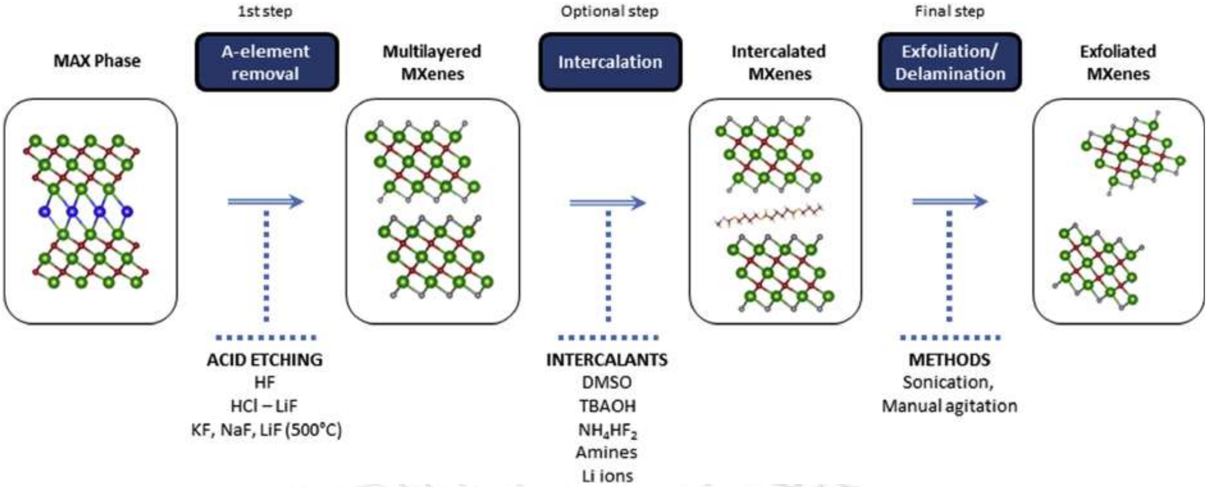

Figure 1.3: The schematics of the synthesis procedure of MXenes(Used with permission from [53]).

M" are transition metals arranged in a fixed stoichiometric ratio of 1:2 within each metal layer. This configuration differs from o-MAX phases in that here, both transition metals coexist within the same atomic layer. i-MAX phases are known to adopt crystal structures with symmetries such as C2/c, C2/m, or Cmcm [45]. The structure of an i-MAX phase is shown in Figure 1.1(c). The corresponding 2D derivative — i-MXene — is shown in Figure 1.2(c). In i-MXenes, similar to the i-MAX phase, each M-layer contains M′ and M" atoms distributed in a well-defined ratio. Experimentally, several i-MAX phases have already been synthesized, such as $(M'_{2/3}M''_{1/3})_2$ AlC (M′ = Cr, Mo, W; M" = Sc, Y) [46, 47, 48, 49], and $(M'_{2/3}Zr_{1/3})_2AlC$ (M′ = V, Cr) [50, 51, 49]. Out of them $(Mo_{2/3}Y_{1/3})_2AlC$ has been succesfully exfoliated to $(Mo_{2/3}Y_{1/3})_2C$ [52].

1.3.1 Synthesis of MXenes

Gogotsi and his group were the first to synthesize MXene from the bulk MAX phase in 2011 successfully [13]. They exfoliated Ti_3C_2 from the bulk Ti_3AlC_2 by removing the layer of aluminium(Al) atoms. They used a top-down chemical etching process, in which the A-layer of a MAX phase is selectively dissolved using specific etchants. In the case of Ti_3C_2, aqueous hydrofluoric acid (HF) solution was used for this purpose [13]. Alternatively, etching solutions, such as a mixture of hydrochloric acid (HCl) and lithium fluoride (LiF), can also be used for this purpose [48]. This synthesis route is popular because it is cost-effective, relatively simple, and provides a high yield of MXene.

As an illustration of the process, let us consider the case of Ti_3AlC_2. When exposed to HF, the acid dissociates into hydrogen (H) and fluorine (F) radicals. Since these radicals are reactive, they quickly attach to the Ti atoms on the surface, weakening the Ti-Al bonds. As a result, the interlayer spacing increases, and the HF penetrates deeper into the structure. As the reaction progresses, AlF_3 (aluminum fluoride) and H_2 gas are formed and removed, resulting in the exfoliation of Ti_3C_2 layers. A fluorine-terminated MXene is the result [41]. The entire chemical process is as follows:

$$Ti_3AlC_2 + 3HF \rightarrow Ti_3C_2 + AlF_3 + 3/2H_2$$
$$Ti_3C_2 + 2H_2 \rightarrow Ti_3C_2(OH)_2 + H_2$$

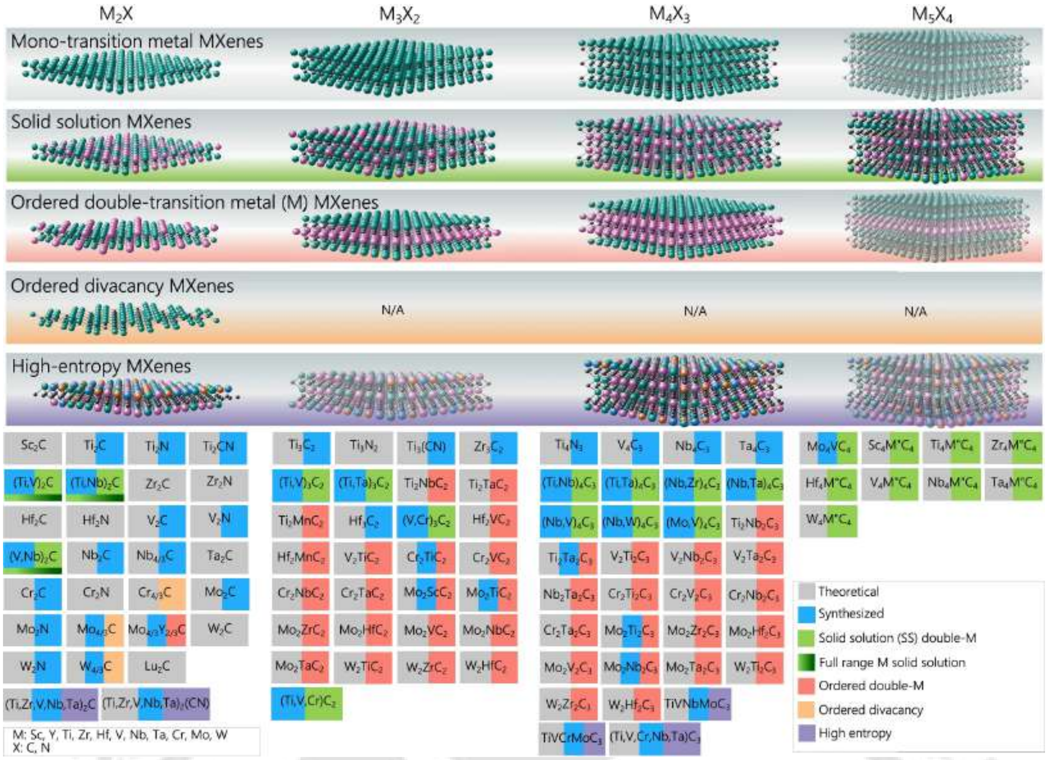

Figure 1.4: Different MXenes compositions and structures reported till date(Reused with permission from [54]) .

$$Ti_3C_2 + 2HF \rightarrow Ti_3C_2F_2 + H_2$$

The MXene formed using the above method is multilayered. Various techniques, such as intercalation and sonication, are used to obtain a single layer of MXene. However, this acid-based process does not yield pristine MXene sheets. Instead, the dangling bonds present on the surface of the newly formed MXene react rapidly with the aqueous environment, forming surface terminations such as –O (oxygen), –OH (hydroxyl), and –F (fluorine) groups [13]. These functional groups play an important role in defining the surface chemistry and properties of MXenes but also make it challenging to isolate completely termination-free structures. The schematic of the exfoliation process of MXenes is given in Figure 1.3.

1.3.2 MXene family of compounds

As stated earlier, over 150 different MAX phases have been experimentally synthesized using various combinations of the three primary components (M, A, and X). However, despite its potential, only about 30 have been successfully exfoliated to MXenes to date. The mono-transition metal-based MXenes that have been exfoliated from their corresponding MAX phase precursors are V_2C [55], Ti_2C [40], Mo_2C [56], Ti_2N [57], Nb_2C [55], Mo_2N [58], Ti_3C_2 [13], Zr_3C_2 [59], Ti_3CN [40], Hf_3C_2 [60], V_4C_3, Ti_4N_3 [61], Ta_4C_3 [40], and Nb_4C_3 [62]. Double transition metal MXenes exhibiting greater structural complexity, can be broadly categorized as either ordered compounds or solid solution types. As discussed previously, the ordered ones can be classified into o-MXenes and i-MXenes. Prominent o-MXenes that are synthesized so far include Mo_2TiC_2, $Mo_2Ti_2C_3$, Cr_2TiC_2,

Mo_2ScC_2 [42, 43, 44]. $Mo_4VC_4T_x$, a novel MXene with a unique structure consisting of five transition metal layers (n = 4), was synthesized in 2019 [63]. This material is one of the thickest known 2D structures, with a total of nine atomic layers. It increases to eleven or more when surface terminations are considered. Its remarkable bending stiffness paves way for exciting possibilities in mechanical and electromechanical applications. Solid-solution MXenes are typically represented by $(M'_{n\text{-}y}M"_y)C_{n\text{-}1}$ (n=2,3,4; M′ and M" denote different transition metals). In these structures, the metals are randomly distributed, forming solid solutions that enable gradual and flexible tuning of material properties. $(Ti_{2\text{-}y}Nb_y)C$ [64, 65], $(V_{2\text{-}y}Nb_y)C$ [64, 65], $(Ti_{2\text{-}y}V_y)C$ [64, 65], and $(Mo,V)_4C_3$ [66] are the solid solution MXenes that are experimentally synthesised. More than 84 different types of solid solution MAX phases have been reported to date [67], indicating the solid solution MXenes is largely unexplored. The count on i-MXene is extremely poor on the other hand. The sole i-MXene synthesized so far is $(Mo_{2/3}Y_{1/3})_2C$ [52], which is derived through exfoliation from its parent MAX phase $(Mo_{2/3}Y_{1/3})_2AlC$.
In addition to these traditional MXenes, a new class of MXenes featuring ordered metal vacancies were also synthesized from i-MAX phases. During exfoliation stage of the i-MAX phases, some M′ atoms get dissolved, forming MXenes with ordered vacancies. For example $Mo_{1.33}C$ [52] , $W_{1.33}C$ [48] are synthesised .In 2021, the discovery of high-entropy MXenes containing multiple transition metals marked a significant breakthrough in the field of MXenes [68, 69, 70]. In addition to these experimentally synthesized MXenes, several MXenes have been explored theoretically for a multitude of applications. Figure 1.4 shows different MXenes that have been explored both theoretically and experimentally to date.The following subsection explores how variations in composition and structure lead to the emergence of unique and unconventional properties in MXenes.

1.3.3 Properties of MXenes

MXenes offer exceptional tunability through the different combinations of the transition metal composition (M), the number of atomic layers (n), and the type of surface terminations (T). Because of such structural flexibility, precise control over their properties, including electrical conductivity, magnetism, electronic transport behavior, chemical stability, and electrochemical performances, can be achieved [71, 72, 73, 74, 75]. Due to these attributes, MXenes have shown positive potential across a range of applications, such as energy storage [76], electromagnetic interference shielding [77], and water splitting for hydrogen production [78]. Here, we select to discuss only the electronic and magnetic properties of MXenes.

1.3.3.1 Electronic properties

The electronic properties of MXenes are largely determined by their elemental composition and surface termination group [79].MXenes exhibit a broad spectrum of electronic phenomena, ranging from semiconductor- metallic transitions [80], extremely low work functions [81], topological insulating phases citekhazaei2016topological, and anisotropic conduction [83], to Dirac cones and giant spin-orbit splitting [84]. Most of these phenomena have been studied through Density Functional Theory (DFT) based simulations since experimental verification is still relatively scarce. The electronic band structure determines how MXenes respond to electronic and optical stimuli. In their pristine form, without any surface terminations, most MXenes display metallic properties [85]. However, when functional groups like –O, –F, or –OH are bonded to their surfaces, they significantly change the electronic structures, frequently leading to semiconducting properties [85].

In pristine MXenes, near the Fermi level the states are mainly due to the transition metal d-orbitals , with a slight separation from the p-orbitals of the surrounding elements [85]. Upon surface termination, these d-states and the p-orbitals of functional groups hybridize. This creates new filled states below the Fermi energy thereby causing the Fermi level to shift downward, resulting in a semiconducting nature. For example, DFT-based studies have reported semiconducting gaps in Sc_2CT_2 (T = OH, F, O), Ti_2CO_2, Zr_2CO_2, and Hf_2CO_2, ranging approximately from 0.24 to 1.8 eV [86]. Although the band structures of OH- and F-terminated Sc_2C are similar because of their almost equal electron affinities, oxygen provides a stronger electron-accepting tendency, which causes a more noticeable shift.

In the case of o-MXenes, such as those having chemical formula $M'_2M"C_2T_2$ and $M'_2M"_2C_2T_2$, the outer transition metal layer (M') is crucial in governing the surface chemistry and electronic properties. This indicates how the metal elements can be carefully chosen and arranged to tune the properties of MXene. Few MXenes, $M_2C(OH)_2$ (where M=Ti, Zr, Hf, Nb, Ta) and $M_2N(OH)_2$ (M= Zr, Hf) can also develop nearly free electron (NFE) states at the Fermi level, due to certain surface functional groups [85, 87]. These NFE states are particularly intriguing because they could improve the electronic transport efficiency of next-generation devices by acting as low-scattering channels for charge carriers.

Furthermore, it has been determined that some MXenes, especially those that contain heavy transition metals like Mo, W, Zr, and Hf, have the potential to be two-dimensional topological insulators(TI) in which the band topology is reorganized primarily by spin-orbit coupling (SOC) [88, 82, 89]. W_2CO_2, for instance, has been suggested as a 2D TI with a large gap, potentially providing room-temperature TI capabilities [82]. It has also been projected that other oxygen-functionalized double transition metal MXenes (such as $Mo_2TiC_2O_2$, $W_2HfC_2O_2$, etc.) [82, 90]may exhibit either topological insulating or semimetallic properties, broadening the potential applications of MXenes in upcoming spintronic and quantum electronics technologies.

1.3.3.2 Magnetic properties

Most of the members of the MXene family exhibit a non-magnetic ground state in both pristine and functionalized form. This is largely due to the robust covalent interactions between the transition metal atoms and the carbon or nitrogen atoms, which favor electronic arrangements that do not support magnetism [91]. However, with the use of external stimuli, surface functionalization, and compositional tailoring, magnetic behaviors have been anticipated and demonstrated in specific MXenes.

According to DFT calculations, a number of MXenes may display magnetic ordering. Cr_2C, Cr_3C_2, and Fe_2C [93] are among the MXenes exhibiting ferromagnetic behavior [94, 95]. On the other hand, antiferromagnetic behavior is reported to be shown by Zr_2N[96] and Cr_2N. Meanwhile, both Ti_2C and Ti_2N are ferromagnetic half-metals [97].

DFT simulations have predicted Mn_2C monolayers to be an antiferromagnet with Néel temperature of 720 K [98], significantly above room temperature. Interestingly, a ferromagnetic state with a Curie temperature of about 520 K can be induced by surface functionalization with groups like F, Cl, and OH [99]. The nominal oxidation states of

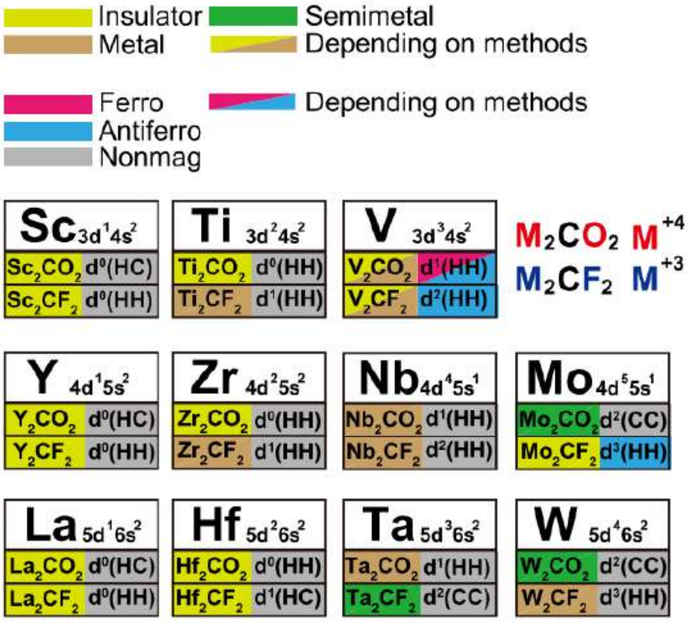

Figure 1.5: A comprehensive overview of the structure, electronic, and magnetic characteristics of carbide MXenes is presented. For each MXene, details are provided on its electronic nature (insulating, metallic, or semimetallic), magnetic behavior (non-magnetic, ferromagnetic, or antiferromagnetic), ground-state structure, and formal d^n electron configuration of transition metal [92].

the transition metals, accounting for the anions (such as C^{4-}, N^{3-}, F^{-}, OH^{-}, and O^{2-}), the coordination environment, and the number of d-electrons, provide a general understanding of the magnetic moments in these systems. The nonbonding d-orbitals close to the Fermi level are crucial in determining the magnetism, just like in transition metal dichalcogenides. Extensive investigations of Cr-based MXenes have revealed promising results among the double transition metal-based MXenes. For example, $Cr_2Ti_2C_3O_2$ and $Cr_2V_2C_3O_2$ MXenes are reported to be ferromagnetic with magnetic transition temperatures calculated to be 720.6 K and 246.8 K [100], respectively. Some of these MXenes show strain-induced magnetic phase transitions, such as switching from ferromagnetic (FM) to antiferromagnetic (AFM) phases, providing a potential route to externally control their magnetic states [100]. A recent study demonstrated that $Ti_2MnC_2T_2$ (T = O, OH, F) monolayers exhibit robust ferromagnetism with high Curie temperatures ranging from 495 K to 1133 K, surpassing those of many existing 2D ferromagnetic materials [101, 102]. Similarly, $Hf_2MnC_2O_2$ and $Hf_2VC_2O_2$ have been predicted to show ferromagnetic nature [101]. $Hf_2VC_2F_2$ is reported to exhibit in-plane non-collinear 120° Y-type antiferromagnetic ordering, leading to ferroelectric polarization, establishing it as a type-II multiferroic with strong intrinsic magnetoelectric coupling [103, 102]. Magnetic behaviour has also been studied in Janus MXenes $M_{2-x}XT_xT'_{2-x}$ (X = C/N; T/T′ = O, F) using DFT. For example, Mn_2C shows stable ferromagnetism for all mixed termination cases. On the other hand, Cr_2C, Ti_2C, and V_2C shows robust antiferromagnetic ordering [104].Furthermore, magnetic ordering was found in 62 out of 319 compounds in a high-throughput DFT investigation on i-MXenes [105]. This implies that the MXene family offers possibilities for the synthesis of several magnetic materials.

MXenes have also shown considerable promise for spintronic applications in recent investigations, such as in the construction of magnetic tunnel junctions (MTJs). For example, insulating Ti_2CO_2 MXene as the spacer layer and half-metallic Mn_2CF_2 MXene as magnetic electrodes have been used to build MTJs [106]. A separate study reported that an MTJ constructed using Cr-based MXenes demonstrated a maximum (minimum) TMR value of $6.58 \times 10^{10}(3.86 \times 10^{6})$ [107]. Even the lowest value found here is comparable to that of the traditional FETs [107]. The observation of room-temperature magnetic skyrmions with tunable properties enabled by the Rashba-type Dzyaloshinskii–Moriya interaction (DMI) in MXenes [108] has offered further functionality for magnetoelectric multiferroic devices.

Experimentally, research on magnetism in MXenes is still in its infancy. The magnetic transition in $Cr_2TiC_2T_x$ at 30 K was first observed experimentally by Gogotsi et al., though it was not present in its MAX phase precursor [109]. Allen-Perry showed that paramagnetic-to-AFM transitions are caused by etching conditions influencing phase transitions in $Ti_3C_2T_x$ [110]. Similarly, $Ti_3C_2T_x$ synthesized by LiF/HCl etching and annealed in H_2 demonstrated enhanced ferromagnetism [111], highlighting the significant changes in magnetic behavior that can occur during synthesis and post-treatment.

The promising magnetic properties observed in MXenes open up several exciting avenues for further research: (1) a thorough investigation into the role of atomic layer stacking and its influence on the magnetic behavior of MXenes (2) i-MXenes, a new subclass with fractional stoichiometry, offer an uncharted territory where the interaction between atomic composition and magnetic ordering is still mostly unclear (3) The incorporation of MXenes into device heterostructures for possible spintronic applications (4) The investigation of spintronics and valleytronics in non-centrosymmetric MXenes presents exciting opportunities. There is a chance for advancements in the design of next-generation multifunctional 2D materials based on MXenes because these directions are yet understudied physically and conceptually.

1.4 Importance of first principles based modelling and simulation for exploring magnetism in MXenes

The above discussion clearly establishes that since the experimental investigation into magnetism in MXene-based systems is still in its infancy, robust and accurate modelling and simulation is the only possible way to understand the magnetic interactions in various different MXene-based structures and compositions. Moreover, experimental investigation into effects such as stacking patterns, substitutions, and surface engineering can be challenging. Thus, theory and simulation-based techniques are the only way to get insights regarding the relation between structure, composition, and magnetism in MXene single phases or MXene-based heterostructures. In this regard, first-principles simulation techniques, especially those based on Density Functional Theory (DFT), are the most desirable ones. Without the need for empirical factors, they accurately address the attributes of electronic, magnetic, mechanical, and surface ground states. The difficult many-body Schrödinger Equation is simplified to a single-particle affair by DFT. These approaches have been widely used to predict magnetic ground states, exchange interactions, and magnetic anisotropy in a vast swath of materials. In the existing literature, as discussed above, DFT-based calculations have revealed the induction of ferromagnetism, antiferromagnetism, and multiferroicity in specific MXenes by compositional tunings and surface terminations. In my Ph.D. work, therefore, DFT-based calculations have been the backbone for probing the cause and controllability of magnetic response in MXenes, significantly advancing our basic understanding of the engineering of materials for innovative magnetic and spintronic applications.

1.5 Outline of the thesis

In this thesis, using Density Functional Theory (DFT) based first-principles calculations, a systematic investigation of a number of MXenes, emphasizing their potential for magnetic applications, is done. The investigation starts with an exploration of the tunable magnetic properties of a few i-MXenes, whose MAX precursors are synthesized, implying that exfoliation to these i-MXenes is only a matter of time. This implies that the findings can work as a guide to the experimentalists. In the next chapter, comparative magnetic behavior of nitride-based MXenes with an unconventional layer stacking, which is different from the one commonly observed in traditional MXenes is explored. Subsequently, focus is put on designing and analyzing an MXene/TMDC heterostructure that exhibits multiferroic behavior and offers promising applications in multifunctional devices. Finally, the role of spin-orbit coupling (SOC) in non-centrosymmetric, non-magnetic MXenes, with a particular emphasis on their potential in the emerging fields of valleytronics and spintronics, is investigated. The chapters in this thesis are organized as follows:

Chapter 1 explores the fascinating world of 2D materials, highlighting their crucial role in numerous technical fields. It explores 2D magnetic materials in further detail and highlights their exciting potential in spintronics and related domains. The chapter also examines MXenes' structural characteristics and their potential for use in a variety of magnetic applications.

In **Chapter 2**, the computational approaches applied throughout this thesis are discussed. The chapter starts with a brief introduction to Density Functional Theory (DFT) and the electronic structure computation methods used in this work. Magnetic exchange parameters are evaluated using the Full-Potential Linear Muffin-Tin Orbital (FP-LMTO) approach. A discussion of this method is also provided in this chapter. The Magnetic Force Theorem is used to determine exchange parameters, and a brief discussion of this approach is given. A synopsis of the procedure for calculating the Curie temperature, specifically using the Metropolis algorithm, is also included in this chapter.

In **Chapter 3**,how the magnetic properties of Cr-based iMXenes can be tuned through alloying with non-magnetic transition metals and through surface functionalisation is investigated. By employing Density Functional Theory (DFT) calculations, the impact of compositional variations on the electronic and magnetic behavior of these in-plane ordered 2D materials is investigated. Their magnetic and electronic ground states are found to be strongly influenced by both structural arrangement and elemental composition. Because of its intrinsic tunability, i-MXenes are attractive options for real-world magnetic applications. Additionally, the magnetic anisotropy energies and calculated magnetic transition temperatures are shown to be comparable to those of well-known 2D magnets, highlighting the potential of i-MXenes in spintronics and multifunctional applications.

In **Chapter 4**, the investigation is focused on how various stacking configurations affect the electronic and magnetic properties of several nitride-based MXenes. Although carbide MXenes have been extensively researched, their nitride equivalents are still relatively unexplored. Furthermore, the variability in structure and its ability to modify material properties has only recently gained interest. This study connects these two less-explored areas—structural stacking and nitride chemistry—to examine their joint impact on magnetism. The research demonstrates that within the M_2NT_2 family (where M = Sc, Ti, V, Cr, Mn and T = O, F), variations in transition metal layer stacking significantly influence both the magnetic ground state and finite-temperature magnetic behavior. Moreover, the stacking arrangement affecting the electronic ground state is shown in this work, highlighting its role in enabling material design for spintronic and magnetic applications. A thorough indepth analysis reveals that this stacking-induced tunability in magnetic and electronic properties is strongly related to the local crystal field symmetry variations, structural homogeneity, and electronic structure characteristics.

Two-dimensional van der Waals heterostructures are poised to revolutionize our understanding of fundamental physics while also paving the way for innovative devices that utilize nanoscale magnetism. Among these, multiferroic systems made up of 2D ferroelectric and ferromagnetic layers stand out for their ability to allow electric-field control over magnetic properties, a crucial aspect of developing non-volatile memory technologies. These heterostructures are best made from materials known for their structural and compositional flexibility, such as MXenes and transition metal dichalcogenides (TMDs). In **Chapter 5**, the magneto-electric coupling in VSe_2-Sc_2CO_2 in bi-layer and tri-layer systems are investigated. The results demonstrate that changing the ferroelectric polarization state in the MXene layer can affect the spin-polarized electronic structure of the neighboring VSe_2, leading to a semiconducting to a half-metallic transition. These findings show that these heterostructures have the ability to improve field-effect transistor designs and open the door to dependable, non-volatile memory solutions at the nanoscale.

Spin-orbit coupling (SOC) allows us to control spin degrees of freedom without the need for external magnetic fields, which opens up exciting possibilities for new spintronic technologies. In **Chapter 6** the impacts of SOC in Ta_2CS_2 MXene is explored. The findings demonstrate how local symmetries and orbital arrangements play a crucial role in band splitting and the development of different spin textures at the Brillouin zone's high-symmetry points. Using first-principles calculations and a $\mathbf{k}\cdot\mathbf{p}$ model, this work shows the presence of both linear and higher-order Rashba-type spin splittings at the center of the Brillouin zone, in perfect agreement with the system's C_{3v} point group symmetry. Furthermore, this work also shows unique Zeeman-like, valley-dependent spin splittings occurring at the K and K′ points, which are non-time-reversal-invariant momenta (non-TRIM). These splittings arise from a complex orbital structure that results in an inherent orbital magnetic moment, showcasing a sign difference between K and K′. The study's findings demonstrate how symmetry and orbital characteristics interact to influence spin behavior, which makes Ta_2CS_2 a viable option for spintronics and valleytronics developments, much like transition metal dichalcogenides.

Chapter 7 discusses the possible extension of the present work.

Chapter 2

Methodology

This chapter describes the theoretical foundations employed in this thesis for the simulation of material properties. The work presented in this thesis is carried out by Density Functional Theory (DFT) based calculations. After the introduction of DFT and its framework used for ab initio calculations, we provide two different implementations of DFT: the plane wave pseudopotential based Projector Augmented Wave (PAW) method used for calculations of ground state properties and electronic structures and the Full Potential Linearized Muffin Tin Orbital (FP-LMTO) method which is used for calculation of magnetic exchange interactions. A brief discussion on the Monte Carlo simulation method, which is used for the calculation of magnetic transition temperature, follows. The chapter ends with a brief description of the ways to calculate magnetocrystalline anisotropy energy (MAE).

2.1 Density Functional Theory

Density Functional Theory (DFT) is a powerful quantum mechanical approach used to study the electronic structure of atoms, molecules, and solids. Unlike traditional methods that rely on solving the complex many-body Schrödinger equation to obtain the wavefunction of a system, DFT simplifies the problem by expressing the system's energy as a functional of the electron density, which is much easier to calculate. Solving the Schrödinger equation and obtaining the wavefunction directly is possible for simple systems like the hydrogen atom. However, as the system becomes larger and more complex, solving the Schrödinger equation for all interacting electrons becomes impractical due to the computational demands. DFT provides a more feasible way to study such larger systems by focusing on the electron density, allowing researchers to obtain valuable information about chemical properties and material behaviour without the computational burden of wavefunction-based methods. In the following sections we shall discuss this method in details.

2.1.1 The Many Body Schrödinger equation

The time-independent nonrelativistic Schrödinger equation for a multiparticle systems like solids containing atoms and nuclei is given as:

$$H\Psi(\mathbf{r}_1, \mathbf{r}_2, ..., \mathbf{r}_N, \mathbf{R}_1, \mathbf{R}_2, ..\mathbf{R}_{N_s}) = E\Psi(\mathbf{r}_1, \mathbf{r}_2, ..., \mathbf{r}_N, \mathbf{R}_1, \mathbf{R}_2, ..\mathbf{R}_{N_s}) \tag{2.1}$$

Here, H corresponds to the Hamiltonian operator, and E is the total energy associated with the system.The system consist of N electrons and N_s nuclei. The variables $\mathbf{r}_1, \mathbf{r}_2, ..., \mathbf{r}_N$ corresponds to the the electronic coordinates while $\mathbf{R}_1, \mathbf{R}_2, ..\mathbf{R}_{N_s}$ represents nuclear coordinates .The form of the Hamiltonian is given as:

$$H = \frac{-\hbar^2}{2m_e} \sum_e \Delta_i^2 + \frac{1}{2} \sum_{i \neq j} \frac{e^2}{\mid \mathbf{r}_i - \mathbf{r}_j \mid} - \frac{\hbar^2}{2M_n} \sum_I \Delta_I^2 - \sum_{i,I} \frac{Z_I e^2}{\mid \mathbf{r}_i - \mathbf{R}_I \mid} + \frac{1}{2} \sum_{i \neq j} \frac{Z_I Z_J e^2}{\mid \mathbf{R}_I - \mathbf{R}_J \mid} \tag{2.2}$$

There are a total of five terms in the above expression of the Hamiltonian. The first and the third terms represent the kinetic energy of the electrons and nuclei, respectively. Here, m_e and M_n represent the electrons and the nuclear mass, respectively. The second (fifth) term represents the columb interactions between the electrons(nuclei). And lastly, the fourth term is the interaction between the electrons and nuclei. The goal of electronic structure calculations is to solve this many-body Hamiltonian as accurately as possible. However, solving it directly is a daunting task and requires a number of approximations. These approximations will be discussed in the following sections.

2.1.2 The Born-Oppenheimer approximation

The Born-Oppenheimer approximation, proposed by Max Born and Robert Oppenheimer in 1927, was introduced to simplify the complex many-body Hamiltonian governing systems with both electrons and nuclei [112]. The core idea behind the approximation lies in the large mass difference between the nuclei and electrons in a system. Since the nuclei are significantly more massive than the electrons, they move much more slowly. This means that, from the perspective of the rapidly moving electrons, the nuclei appear almost stationary. Consequently, the kinetic energy of the nuclei can be neglected, and the Coulomb interactions between the nuclei (which are independent of the electronic motion) become constant. As a result, the problem is reduced to one where the electrons are treated as moving in a fixed potential created by the stationary nuclei. Using this approximation, the Hamiltonian takes the form:

$$H = \frac{-\hbar^2}{2m_e} \sum_e \Delta_i^2 + \frac{1}{2} \sum_{i \neq j} \frac{e^2}{\mid \mathbf{r}_i - \mathbf{r}_j \mid} - \sum_{i,I} \frac{Z_I e^2}{\mid \mathbf{r}_i - \mathbf{R}_I \mid} \tag{2.3}$$

The first term is the Kinetic energy of the electron (T_e), the second term is the Coulomb interaction between the electrons (V_{ee}), and the last term is the potential energy due to electron-nucleus interaction($V_{external}$).

2.1.3 Hartree and Hartee Fork methods

The Hartree method, developed by Douglas Hartree in 1928, is a first approximation used to describe the behavior of many-electron systems [113]. In this method, each electron is treated as moving independently in an average electrostatic field created by the other electrons rather than solving for the full many-body wave function directly. The method assumes that the electrons are not correlated, and their wavefunctions are approximated as a product of single-particle wavefunctions. The interactions between electrons are replaced by an average potential, which leads to a set of self-consistent equations describing the motion of each electron in this effective field. For a system of N interacting electrons, the Hartree method leads to a set of N single-particle Schrödinger equations, which are given by:

$$\frac{-\hbar^2}{2m_e}\Delta_i^2 + V_H(\mathbf{r}_i)\Psi(\mathbf{r}_i) = \epsilon_i\Psi(\mathbf{r}_i) \tag{2.4}$$

Where V_H is the effective potential, which includes both the Coulomb attraction to the nucleus and the average electrostatic repulsion from the other electrons.

The wavefunction of the system in this approximation is represented as a product of single-particle wavefunctions for each electron:

$$\Psi(\mathbf{r}) = \Psi_1(\mathbf{r}_1).\Psi_2(\mathbf{r}_2)......\Psi_n(\mathbf{r}_n) \tag{2.5}$$

The Hartree-Fock method was developed as a natural extension of the Hartree method because the latter, while providing a useful approximation for many-electron systems, ignored important physical effects [114]. Specifically, the Hartree method treats electrons as independent particles moving in an average field created by the other electrons, neglecting the exchange interactions that arise due to the Pauli exclusion principle. This means that the Hartree method does not account for the antisymmetry of the many-electron wavefunction, which is crucial for describing fermions like electrons. The Hartree-Fock method was introduced to address this limitation by enforcing the antisymmetry of the wavefunction through a Slater determinant and by including exchange effects, where the interaction between electrons is not merely a mean field but also reflects the Pauli exclusion principle. Under this approximation, the wave function for a N-electron system can be written as:

$$\Psi(\mathbf{r}) = \frac{1}{\sqrt{N!}}\begin{vmatrix} \Psi_1(\mathbf{r}_1) & \Psi_2(\mathbf{r}_1) & \cdots & \Psi_N(\mathbf{r}_1) \\ \Psi_1(\mathbf{r}_2) & \Psi_2(\mathbf{r}_2) & \cdots & \Psi_N(\mathbf{r}_2) \\ \vdots & \vdots & \ddots & \vdots \\ \Psi_1(\mathbf{r}_N) & \Psi_2(\mathbf{r}_N) & \cdots & \Psi_N(\mathbf{r}_N) \end{vmatrix} \tag{2.6}$$

While the method accounts for the exchange interactions due to the Pauli exclusion principle, it does not fully describe the dynamic interactions between electrons. This means that electron-electron correlations are not captured, which play a significant role in many systems (especially in systems with strong correlations). As a result, Hartree-Fock can give inaccurate results for systems like transition metal complexes, strongly correlated materials, or systems with a significant degree of electron correlation. This has been taken care of in Density Functional Theory, discussed in the next section.

2.1.4 The Idea Behind DFT

Density Functional Theory (DFT) is a computational approach that focuses on electron density, $\rho(\mathbf{r})$, as the central variable for describing the physical properties of a system instead of the many-body wavefunction. This shift in perspective represents a significant conceptual difference compared to wavefunction-based methods and leads to a substantial simplification in calculations. The wavefunction of a many-electron system depends on $3N$ variables (where N is the number of electrons), making it computationally very expensive to solve. In contrast, the electron density depends only on three spatial coordinates—x, y, and z—regardless of the number of electrons, dramatically reducing the complexity of the problem.

The basic ideas behind DFT date back to the early twentieth century and were first introduced by Thomas [115] and Fermi [116]. They proposed that the kinetic energy of any given system can be expressed as a functional of the electron density, and electron-electron interactions can be introduced in a mean-field way. Such a notion was vital because it highlighted that one could figure out the ground-state properties of a system from the electron density and not the full wave function. However, the early Thomas-Fermi approximation was a semi- classical method, neglecting important quantum mechanical effects, such as the exchange and correlation between electrons, resulting in significant errors.

In the 1920s, Dirac attempted to refine this approach by including the exchange energy, which accounts for the quantum mechanical effects of the indistinguishability of electrons [117]. While this improvement was a step forward, it still did not fully address the electron-electron correlation effects and did not lead to accurate results for a broad range of systems. It was clear that more work was needed to capture these essential effects.

The breakthrough in DFT came in 1964 when Hohenberg and Kohn published their seminal work [118]. They proved that the ground-state energy of a system is uniquely determined by the electron density, which is the key idea behind modern DFT. They also showed a functional relationship between the electron density and the system's total energy, paving the way for practical calculations. This was further refined by Kohn and Sham in the same year, who introduced the concept of the Kohn-Sham equations [119], a set of self-consistent equations that allow for practical implementation of DFT. These equations treat the interacting electron system as a system of non-interacting particles in an effective potential, making the method computationally feasible.

2.1.4.1 Hohenberg-Kohn Theorem

The Hohenberg-Kohn Theorem was proposed by Pierre Hohenberg and Walter Kohn in 1964. It establishes that the ground-state properties of a many-electron system can be entirely determined by the electron density rather than the many-body wave function. This theorem revolutionized the way we approach the study of quantum systems, significantly simplifying the problem of many-body physics. The theorem consists of two main parts:

(1) According to the first theorem, the external potential, $V_{external}$ or the ground state energy E is a unique functional of the density [120].

(2) According to the second theorem, electron density that minimizes the total energy functional (which includes both the kinetic and potential energies) is the actual ground-state density of the system [120]. Accordingly, the ground state of the interacting electrons in an external potential $V_{external}$ is given by the energy functional:

$$E[\rho(\mathbf{r})] = F[\rho(\mathbf{r})] + \int V_{external}(\mathbf{r})\rho(\mathbf{r})d\mathbf{r} \tag{2.7}$$

where $F[\rho(\mathbf{r})]$ is a universal function of energy density $\rho(r)$ that accounts for the kinetic energy of the electrons and the electron-electron interactions. The second term arises from the interaction of the electron with the external potential. The goal of DFT is to find the electron density $\rho(\mathbf{r})$ that minimizes the energy functional $E[\rho(\mathbf{r})]$, which corresponds to the true ground-state density of the system.

2.1.4.2 The Kohn-Sham Framework in Density Functional Theory

While DFT, through the Hohenberg-Kohn theorem, showed that the electron density $\rho(\mathbf{r})$ could determine all the properties of a system; it did not provide a practical way to calculate the ground-state energy because the functional $F[\rho(\mathbf{r})]$(which includes the kinetic energy of the electrons and the electron-electron interactions) is not known exactly. Thus, the real challenge was in handling the electron-electron interactions and the kinetic energy term in DFT.

The Kohn-Sham (KS) method offers a practical way to apply DFT by using a set of imaginary, non-interacting particles [119]. These imaginary particles have the same electron density as the real, interacting system. The idea is to simplify the complex many-electron system by replacing it with non-interacting particles that move in a special potential. This effective potential is created to ensure that the electron density and the effects of interactions between electrons are accurately represented. This approach converts the multi-electron systems into single-electron problems in an effective potential that obeys a Schrödinger-like equation:

$$(H_{KS} - \epsilon_i)\Phi_i(\mathbf{r}) = 0 \tag{2.8}$$

In this Kohn-Sham equation, H_{KS} is the Kohn-Sham Hamiltonian operator, which includes the kinetic energy of the electrons and the effective potential that accounts for the external potential and electron-electron interactions. ϵ_i is the energy eigenvalue associated with the ith-electron and $\Phi_i(\mathbf{r})$ single-particle wavefunction (also called the Kohn-Sham orbital) for the ith-electron. The mathematical form of Kohn-Sham Hamiltonian is given as:

$$H_{KS} = \frac{-\hbar^2}{2m_e}\Delta^2 + V_{eff} \tag{2.9}$$

The first term is the kinetic energy of the electron, and the second term is the effective potential.

$$V_{eff} = V_{external}(\mathbf{r}) + V_H(\mathbf{r}) + V_{xc}(\mathbf{r}) \tag{2.10}$$

Here, the first term is the external potential, the second one is the Hartree potential, and the third term is the exchange-correlation potential. The Hartree potential is given as:

$$V_H(\mathbf{r}) = \frac{1}{2}\int \frac{\rho(\mathbf{r})\rho(\mathbf{r}')\mathbf{drdr'}}{\mid \mathbf{r\text{-}r'} \mid} \tag{2.11}$$

and the exchange-correlation potential is given as :

$$V_{xc}(\mathbf{r}) = \frac{\delta E_{xc}(\mathbf{r})}{\delta\rho} \tag{2.12}$$

The density is expressed as a summation over the individual Kohn-sham orbitals, i.e.,

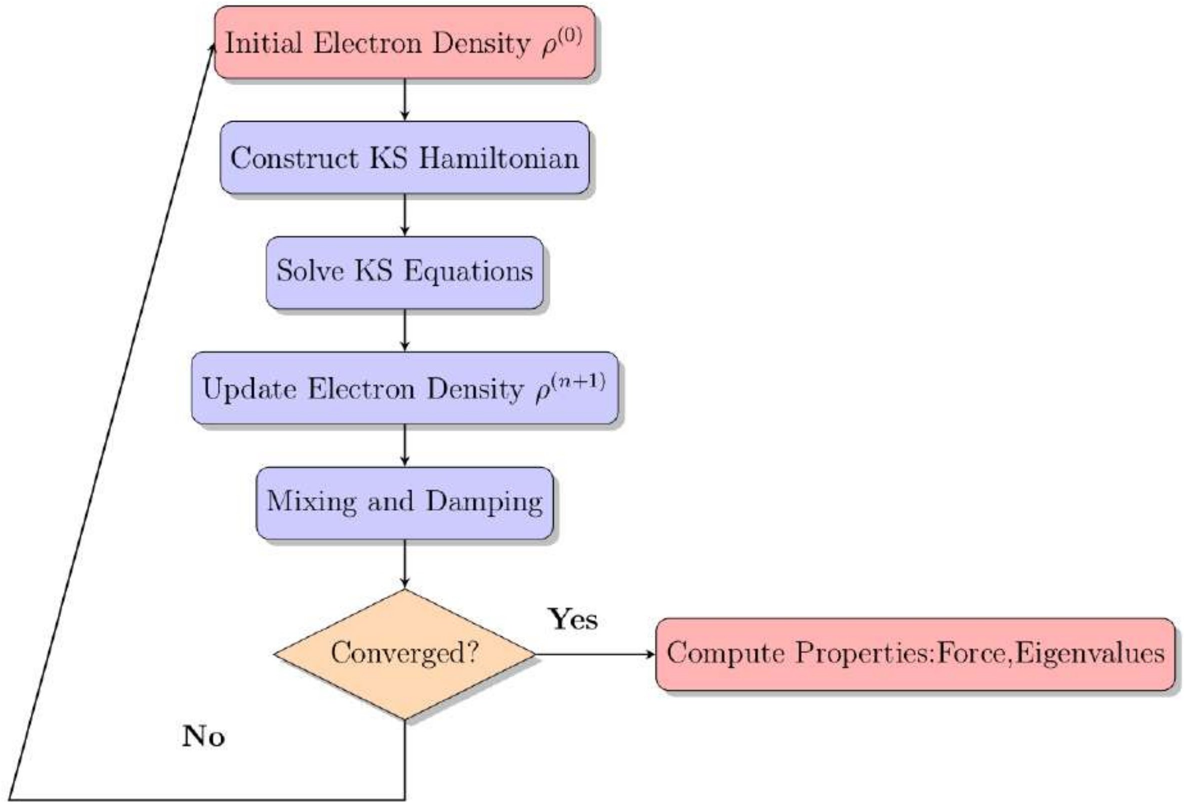

Figure 2.1: Flowchart for solving self-consistent Kohn Sham (KS) equation

$$\rho(\mathbf{r}) = \sum_{i}^{N} \mid \Phi_i(\mathbf{r}) \mid^2 \tag{2.13}$$

By integrating this density, the total number of electrons is obtained, i.e.:

$$N = \int \rho(\mathbf{r}) d\mathbf{r} \tag{2.14}$$

The Kohn-Sham energy functional is given as :

$$E_{KS} = T_s(\rho) + \int V_{external}(\mathbf{r})\rho(\mathbf{r})d\mathbf{r} + E_H(\rho) + E_{xc}(\rho) \tag{2.15}$$

The Kohn-Sham equation is solved iteratively by first providing an initial guess for the electron density, $\rho(\mathbf{r})$, and the exchange-correlation functional, $E_{xc}([\rho(\mathbf{r})])$. Schematic of a DFT calculation is shown in Figure 2.1.

In Density Functional Theory (DFT), incorporating spin effects to model magnetism is a relatively simple extension. The Kohn-Sham equations are solved separately for the spin states, spin-up (↑), and spin-down (↓). To determine the total electron density, the densities of both spin channels are added together ($\rho\uparrow + \rho\downarrow$), giving the overall charge distribution. Meanwhile, the spin density, which characterizes the magnetic moment, is calculated as the difference between the spin-up and spin-down densities ($\rho\uparrow$ - $\rho\downarrow$). This method allows DFT to effectively capture the magnetic behavior of systems by treating the spin polarization explicitly in the calculations.

2.1.4.3 Exchange Correlation Energy Functional

In the above Kohn-Sham energy functional, the exact form of the exchange-correlation energy functional E_{xc} is not known. The exchange part of the functional accounts for the Pauli exclusion principle, which ensures that no two electrons with the same spin can occupy the same quantum state. The correlation part describes the tendency of electrons to avoid each other due to their Coulomb repulsion, taking into account their dynamic correlation. So, to model the form of E_{xc}, various approximations are there. The simplest and the most basic approximation is Local Density Approximation (LDA) [119]. It assumes that the exchange-correlation energy at each point in space depends only on the local electron density at that point as if the system was uniform. This means that for a given spatial point, the system is treated as though it behaves like a homogeneous electron gas with the same density as the local electron density at that point. Mathematically :

$$E_{xc}^{LDA}(\rho(\mathbf{r})) = \int \rho(\mathbf{r}) E_{xc}^{hom}(\rho(\mathbf{r})) d^3\mathbf{r} \tag{2.16}$$

Here E_{xc}^{hom} is the exchange-correlation energy of a homogeneous electron gas of density $\rho(\mathbf{r})$. The Local Density Approximation (LDA) performs quite well in systems where the electron density changes gradually, such as in covalent materials and simple metals. One of the reasons behind its surprising success is that the errors introduced by LDA in the exchange energy and correlation energy tend to cancel each other out. Specifically, LDA tends to overestimate the exchange energy while underestimating the correlation energy. However, the combination of these errors often results in a good approximation of the total exchange-correlation energy.LDA struggles when the electron density varies sharply across space, such as at surfaces, interfaces, or small molecules.LDA also tends to underestimate certain many-body effects, particularly in systems where electron-electron correlations are strong. An improvement over this is Generalized Gradient Approximation(GGA) [121, 122].GGA improves the accuracy of the calculations by considering electron density at each point and how that density changes around it (gradient of electron density), leading to better predictions for things. The energy functional is given as:

$$E_{xc}^{GGA}(\rho(\mathbf{r})) = \int \rho(\mathbf{r}) E_{xc}^{hom}(\rho(\mathbf{r}), \bigtriangledown\rho(\mathbf{r})) d^3\mathbf{r} \tag{2.17}$$

Some of the well known Generalized Gradient Approximation (GGA) functionals are : PBE (Perdew-Burke-Ernzerhof) [123] , PW91 (Perdew-Wang 1991) [124] , BLYP (Becke-Lee-Yang-Parr) and PBEsol (PBE for solids) [125] . In this thesis, PBE functionals is used throughout.

2.1.5 DFT based electronic structure methods

DFT-based electronic structure approaches can be broadly categorized based on how the Kohn-Sham orbitals are represented. The accuracy and computational efficiency of a simulation are significantly influenced by the representation that is used. Finding the ideal balance between numerical accuracy and efficiency while solving the Kohn-Sham equations is one of the main issues in computational materials research. In the core or atomic regions, where wavefunctions exhibit rapid oscillations, a dense numerical grid or carefully selected small basis set is sufficient, as the wavefunctions are relatively unaffected by the surrounding chemical environment. Conversely, in the interatomic regions, the wavefunctions are generally smoother but highly responsive to changes in the local environment. This necessitates the use of more flexible and extensive basis sets to accurately capture the physics. This subsection introduces two distinct DFT implementations, each employing a different basis set strategy, both of which have been applied for calculation purpose in this thesis.

2.1.5.1 Projector Augmented Wave (PAW) method

In DFT calculations, the wavefunctions of the electrons are typically expanded in terms of a basis set. The plane wave basis is one of the most common choices for representing these wavefunctions. Their basic advantage is that plane waves are computationally simple and easy to handle because they form a complete set of functions in a periodic system. However, plane wave basis sets are not well-suited for describing electron wavefunctions in all regions, particularly when it comes to the core electrons that are tightly bound to the nucleus. These core orbitals have rapidly oscillating wavefunctions, and representing them accurately with plane waves would require an impractically large number of plane waves, making the calculation computationally expensive and inefficient. Moreover, the valence electrons, which are more relevant for bonding and chemical reactions, also experience rapid oscillations near the core, making their representation with a plane wave basis cumbersome.

To address this issue, the concept of pseudopotentials (PPs) was introduced. Pseudopotentials are effective potentials that replace the strong Coulomb potential of the nucleus and core electrons with a smoother potential that only acts on the valence electrons, removing the rapid oscillations of wavefunctions in the core region. This results in a much smoother wavefunction for the valence electrons, which can be efficiently represented using a more manageable number of plane waves. This reduction in the number of plane waves significantly reduces the computational cost of simulations, making the method much more computationally feasible. There are mainly two different types of pseudopotential methods .
(1) Norm-Conserving Pseudopotentials (NCPPs): Norm-conserving pseudopotentials are constructed to ensure that the total number of electrons is conserved and that the wavefunction outside the core region remains the same as the true all-electron wavefunction.
(2) Ultrasoft Pseudopotentials (USPPs) [126]: They allow for a reduced plane-wave basis set by softening the interaction between the valence electrons and the nucleus. This makes them more computationally efficient than norm-conserving pseudopotentials because they require fewer plane waves for the same level of accuracy.

While the pseudopotential method offers several advantages, such as reducing memory usage and computational demands, it does come with some significant drawbacks. One notable issue is that this method compromises the authentic all-electron wavefunction in the vicinity of atomic nuclei, as the wavefunctions in the pseudopotential area are artificially smoothed. This smoothing can lead to inaccuracies in computed properties that rely heavily on the electronic structure close to the nucleus, affecting phenomena like hyperfine interactions, electric field gradients, and core-level spectroscopy. Additionally, another limitation of the pseudopotential technique is its reliance on various adjustable parameters during the generation process. This means a pseudopotential tailored for one specific system may not yield trustworthy results in a different scenario, raising valid concerns regarding its transferability and consistency across diverse contexts.

In 1994, Peter Blöchl introduced the Projector Augmented Wave (PAW) technique to overcome these obstacles [127]. This novel method successfully combines pseudopotential and all-electron approaches. The PAW formalism uses a linear transformation to recreate the entire all-electron wavefunction from a more manageable pseudo-wavefunction. It does this by dividing the wavefunction into two distinct regions: a partial wave expansion within atom-centered augmentation spheres—where both core and valence states are represented with precision;and smooth envelope functions in the interstitial area. A linear transformation links these components at the boundary of the spheres.

Thus, the PAW method combines the computational efficiency of pseudopotentials with the accuracy of all-electron calculations, making it especially suitable for calculating desired material properties. In this section, we provide a brief overview of the PAW formalism .

In the PAW method, the all-electron wavefunction $|\psi_n\rangle$ is represented by a smooth wavefunction after a linear transformation with operator T:

$$|\psi_n\rangle = T\left|\tilde{\psi}_n\right\rangle \tag{2.18}$$

An augmentation sphere is constructed around each atom such that $|\mathbf{r} - \mathbf{R}^a| < r_c^a$, where r_c^a denotes the cut-off radius, a refers to the atomic index, and $\mathbf{R}^a$ represents the position of atom a. Within this framework, the linear transformation operator T is expressed as:

$$T = 1 + \sum_a T^a \tag{2.19}$$

where T^a only acts in the augmentation sphere. Inside this region, the smooth wavefunction is represented as a linear combination of smooth partial waves denoted by $\left|\tilde{\phi}_i^a\right\rangle$:

$$\left|\tilde{\psi}_n\right\rangle = \sum_{ia} c_{ni}^a \left|\tilde{\phi}_i^a\right\rangle \tag{2.20}$$

The all-electron wavefunction in the same way can be written as:

$$|\psi_n\rangle = \sum_{ia} c_{ni}^a |\phi_i^a\rangle \tag{2.21}$$

The smooth partial wave, upon application of the linear transformation operator, takes the form:

$$|\phi_i^a\rangle = T\left|\tilde{\phi}_i^a\right\rangle = (1 + T^a)\left|\tilde{\phi}_i^a\right\rangle \tag{2.22}$$

As T^a only acts inside the augmented sphere, so the Eq. 2.22 at $r > r_c^a$ becomes

$$|\phi_i^a\rangle = \left|\tilde{\phi}_i^a\right\rangle \tag{2.23}$$

Now the true wavefunction is expressed as :

$$|\psi_n\rangle = \left|\tilde{\psi}_n\right\rangle - \sum_{ia} c_{ni}^a \left|\tilde{\phi}_i^a\right\rangle + \sum_{ia} c_{ni}^a |\phi_i^a\rangle \tag{2.24}$$

As the transformation operator T is linear, the coefficient of the smooth partial wave must be a scalar product, and

$$c_{ni}^a = \left\langle \tilde{p}_i^a \middle| \tilde{\psi}_n \right\rangle \equiv \mathcal{P}_{ni}^a \tag{2.25}$$

where $\tilde{p}_i^a$ are some smooth projector operators. So the transformation operator T becomes

$$T = \sum_a \sum_i \left(|\phi_i^a\rangle - \left|\tilde{\phi}_i^a\right\rangle \right) \langle \tilde{p}_i^a| \tag{2.26}$$

After the transformation in Eq. 2.26, the Kohn-Sham wavefunction is

$$\begin{aligned} |\psi_n\rangle &= \left|\tilde{\psi}_n\right\rangle + \sum_a \sum_i \left(|\phi_i^a\rangle - \left|\tilde{\phi}_i^a\right\rangle \right) \left\langle \tilde{p}_i^a \middle| \tilde{\psi}_n \right\rangle \\ &= \left|\tilde{\psi}_n\right\rangle + \sum_a \left(\sum_i \left(|\phi_i^a\rangle \left\langle \tilde{p}_i^a \middle| \tilde{\psi}_n \right\rangle - \left|\tilde{\phi}_i^a\right\rangle \left\langle \tilde{p}_i^a \middle| \tilde{\psi}_n \right\rangle \right) \right) \end{aligned} \tag{2.27}$$

From Eq. 2.27, the wavefunction can be decomposed as the sum of the smooth wavefunctions (smooth everywhere) and sum over the subtraction of one-centered all electron contribution and one-centered pseudo part. By substituting Equation 2.27 into Equation 2.18, one can derive a more concise formulation for several quantities used in the PAW method, as described in previous works [128, 129, 130, 131]. Throughout the thesis, I have used PAW method for calculation of ground state properties and electronic structure as implemented in Vienna Ab Initio Simulation Package (VASP) [132].

2.1.5.2 Full-Potential Linear Muffin-Tin Orbital (FP-LMTO) method

The complementary approach to the Pseudopotential Plane wave based method is the class of methods that use the full electronic potential. FP-LMTO is one of them [133] . It uses Linear Muffin tin orbitals (LMTO) as the basis instead of the plane waves. In LMTO method, potentials at atomic sites are described by the muffin-tin approximation. The muffin-tin approximation divides the space in a crystal into regions around each atom, called muffin-tin regions. Within this muffin tin region, the basis is linear combinations of spherical waves given as :

$$\Psi_M(\mathbf{k}, \mathbf{r}) = \sum_L \mathcal{Y}_L(\mathcal{D}_\tau \hat{\boldsymbol{r}}_\tau) \left(\mathcal{K}_\ell(\kappa_i, s_\tau) \delta(\tau, \tau_i) \delta(L, L_i) + \mathcal{J}_L(\kappa, s_\tau) B_{L,L_i}(\kappa_i, \boldsymbol{r} - \boldsymbol{r}' - \boldsymbol{k}) \right) \tag{2.28}$$

where

$$\mathcal{Y}_{\ell m}(\hat{\boldsymbol{r}}) \equiv i^\ell Y_{\ell m}(\hat{\boldsymbol{r}}) \tag{2.29}$$

$$\mathcal{K}_\ell(\kappa, r) \equiv -\kappa^{\ell+1} \begin{cases} n_\ell(\kappa r) - i j_\ell(\kappa r), & \kappa^2 < 0 \\ n_\ell(\kappa r), & \kappa^2 > 0 \end{cases} \tag{2.30}$$

also

$$\mathcal{K}_L(\kappa, \boldsymbol{r}) \equiv \mathcal{K}_\ell(\kappa, r)\, \mathcal{Y}_L(\hat{\boldsymbol{r}}) \tag{2.31}$$

and,

$$\mathcal{J}_\ell(\kappa, r) \equiv \frac{j_\ell(\kappa r)}{\kappa^\ell} \tag{2.32}$$

and,

$$\mathcal{J}_L(\kappa, \boldsymbol{r}) \equiv \mathcal{J}_\ell(\kappa, r)\, \mathcal{Y}_L(\hat{\boldsymbol{r}}) \tag{2.33}$$

Here, Y is spherical harmonic.n_l and j_l are spherical Neumann and Bessel functions, respectively. D_τ is a transformation local to the site τ . l and m are angular momentum parameters of the spherical wave concerning its parent cell. In the interstitial region between the muffin-tin spheres, bases are Bloch sums of spherical Hankel or Neumann functions. So for the site, τ, in the unit cell basis function is given as :

$$\psi_i(\boldsymbol{k},\boldsymbol{r})\Big|_{r\in\mathcal{I}} = \sum_{\boldsymbol{R}} e^{i\boldsymbol{k}\cdot\boldsymbol{R}}\,\mathcal{K}_{\ell_i}(\kappa_i, |\boldsymbol{r}-\boldsymbol{\tau}_i-\boldsymbol{R}|)\,\mathcal{Y}_{\ell_i m_i}(\mathcal{D}_{\tau_i}(\boldsymbol{r}-\boldsymbol{\tau}_i-\boldsymbol{R})) \tag{2.34}$$

Unlike the standard LMTO method, which assumes spherical symmetry within muffin-tin regions (i.e., a simplified approximation of the atomic potential), the FP-LMTO method considers the material's full potential. This means it allows for more accurate descriptions of the electronic structure, especially for materials with highly non-spherical potentials or complex atomic arrangements. The FP-LMTO or any other full potential method is very useful in cases where total energy accuracy is non-negotiable. In this thesis, we have used FP-LMTO method as implimented in Relativistic Spin polarised Toolkit (RSPT) [134] . This method has been used for accurate calculations of small energy differences as is required for calculation of magnetic exchange interactions (see section 2.2.1).

2.2 Computation of physical quantities

2.2.1 Magnetic Exchange Interactions

The magnetic pair exchange parameters are computed to understand the nature of the magnetic interactions of the systems studied in this thesis. These parameters provide valuable insights into the strength and orientation of the interactions between neighboring spins, which are crucial for determining the overall magnetic properties of the material. By analyzing the exchange parameters, we can gain a deeper understanding of phenomena such as magnetic ordering, spin dynamics, and phase transitions.The Heisenberg model Hamiltonian is written as

$$H = -\sum_{i,j} J_{ij}\mathbf{e}_i.\mathbf{e}_j \tag{2.35}$$

Here, J_{ij} is the isotropic exchange parameter between the ith and jth atom. $\mathbf{e}_i$ is the unit vector along the magnetization direction of the ith atom. The values of J_{ij} can be extracted from first principle electronic structure calculations.

There are various approaches to derive exchange parameters from electronic structure calculations. One of them involves computing the total energies for different magnetic configurations and mapping them to a classical Heisenberg model. However, this method presents quite a few challenges. First, a large number of magnetic configurations must be considered to obtain accurate results, which can be computationally expensive. Second, the output is typically a single value for the exchange interaction, making it challenging to extract further insights. For instance, it does not provide clear information about the specific orbitals or electronic states contributions to the exchange interaction. Additionally, distinguishing between different mechanisms of exchange coupling, such as direct exchange, superexchange, or double exchange, becomes challenging.

The alternative approach given by Lichtenstein in 1987, is based on the Magnetic Force Theorem [135] . In this approach, the magnetic exchange parameters are evaluated by calculating the small change in the total energy due to small deviations of some magnetic moments from the ground-state magnetic configuration. The expression for the exchange parameter is given as :

$$J_{ij} = \frac{1}{4\pi} \int_{-\infty}^{E_F} ImTr(\Delta_i \widehat{T_\sigma^{ij}} \Delta_j \widehat{T_\sigma^{ji}}' d\epsilon) \tag{2.36}$$

Here, $\widehat{T}$ is the scattering path operator, and σ is the spin indices. Also $\Delta_i = \widehat{t}_{i\sigma}^{-1} - \widehat{t'}_{i\sigma}^{-1}$, where t is the single site scattering matrix . The sign of the exchange parameter J_{ij}determines whether the exchange interaction is ferromagnetic or antiferromagnetic. If J_{ij} is positive, the interaction is ferromagnetic, leading to parallel alignment of the magnetic moments on sites i and j. Conversely, if J_{ij} is negative, the interaction is antiferromagnetic, favoring antiparallel alignment of the magnetic moments. Since this is based on multiple-scattering formalism, FP-LMTO is the appropiate method .Throughout this thesis , we have calculated J_{ij} by the FP-LMTO method as implemented in RSPt code .

2.2.2 Monte Carlo Simulation and Transition Temperature Calculation

The magnetic transition temperature is the temperature at which a material experiences a change in its magnetic properties. For example, in ferromagnetic materials, it is known as the Curie temperature, and it marks the point at which the material loses its permanent magnetism; below this temperature, the magnetic moments of atoms are aligned, but above it, they become disordered, and the material behaves like a paramagnet. In antiferromagnetic materials, the transition occurs at the Néel temperature, where the material changes from an ordered state, where adjacent magnetic moments point in opposite directions, to a disordered state, where the moments lose their alignment. Monte Carlo simulations [136] are often applied to study statistical properties of magnetic systems, such as the transition temperature, by modelling the system's behavior at different temperatures based on an underlying energy model (Ising or Heisenberg model). For the calculations in this work, a Monte Carlo simulation using the Metropolis algorithm [137], as implemented in the uppASD code [138], was employed. A two-dimensional lattice of size S×S is constructed, with periodic boundary conditions along both the x- and y-directions. The value of S depends on the specific system being studied. The general workflow can be summarized as follows:
(1) An initial spin configuration of the system is chosen, and a magnetic atom is selected randomly.
(2)The spin of the selected magnetic atom is flipped while the spins of the other atoms are kept constant.
(3) The energy differrence is evaluated as $\Delta E = E_c - E_n$ .Where E_c is the energy of the current configuration and E_n is the energy of the new configuration after flipping. The probability of accepting the new magnetic configuration is given by:

$$\begin{aligned} W(x \longrightarrow x') &= exp(-\Delta E/K_BT) \quad if \Delta E > 0 \\ &= 1, \quad Otherwise \end{aligned} \tag{2.37}$$

(4) The decision to accept or reject the new spin configuration is as follows: (a) If the energy of the new configuration is lower, it is accepted as the new configuration. (b) If the energy is higher, a random number between 0 and 1 is generated. The new configuration

is accepted if this random number is greater than or equal to W. (c) Otherwise, the old configuration is retained.

The procedures mentioned above are followed for all sites. The first few steps are discarded for thermalization until equilibrium is reached. Once equilibrium is reached, the statistical quantities can be evaluated. The magnetic moment and susceptibility can be obtained as :

$$M = \frac{1}{N}\langle\sum_i m_i\rangle_T \tag{2.38}$$

and

$$\chi = \frac{1}{N}\frac{\langle M^2\rangle - \langle M\rangle^2}{K_B T} \tag{2.39}$$

Magnetic transition temperature can be obtained by plotting this susceptibility as a function of temperature.

2.2.3 Magnetic Anisotropy Energy(MAE)

Magnetic anisotropy energy is the energy that depends on the direction in which a material's magnetic moments are pointing. In simple terms, it tells us how much the energy changes when the magnetization of a material is aligned in different directions. This effect happens because of factors like the material's crystal structure or how the spins interact with each other. Some directions are easier for the magnetization to align with (called the "easy axis"), while others are harder (the "hard axis"). The difference in energy between these directions is what we call magnetic anisotropy, and it is important for things like making strong magnets and storing information in magnetic devices.

Greater accuracy and a finer sampling of the Brillouin zone are required to evaluate magnetic anisotropy energy in DFT. The magnetic anisotropy energy is often much smaller than other energy contributions. As a result, the calculation needs to be precise to accurately capture this small energy difference between different magnetic configurations, such as aligning the magnetic moments along different crystallographic axes. A finer Brillouin zone sampling ensures the accuracy while handling energy differences of the order of μeV .

The expression for MAE is :

$$E_{MAE} = E_{||} - E_{\perp} \tag{2.40}$$

Here $E_{||}$ and $E_{\perp}$ are the total energy of a system when the magnetic moments are aligned parallel and perpendicular to the plane respectively. In evaluating the above values of energy, spin-orbit coupling (SOC) is also taken into account. A positive (negative) value of MAE indicates the existence of an easy axis perpendicular to the MXene surface(easy plane).

For transition-metal-based systems like MXenes, MAE primarily originates from spin–orbit coupling (SOC) interactions between occupied and unoccupied d-states. Within the framework of second-order perturbation theory, SOC can be treated as a weak perturbation to the spin-polarized ground state, allowing a quantitative estimation of MAE. This perturbative approach expresses MAE as a function of the SOC matrix elements and the energy differences between these states. The MAE is given as [139, 140]:

$$E_{MAE} = \xi^2 \sum_{o,u,\alpha,\beta} (-1)^{1-\delta_{\alpha\beta}} \frac{|\langle o^\alpha \mid L_z \mid u^\beta\rangle|^2 - |\langle o^\alpha \mid L_x \mid u^\beta\rangle|^2}{\epsilon_u^\beta - \epsilon_o^\alpha}. \tag{2.41}$$

Here L_z/L_x are the angular momentum operators capturing the anisotropy in SOC strength between the out-of-plane and in-plane directions.The prefactor ξ is strength of SOC . α and β are the spin indices where as o/u represents the occupied or unoccupied orbitals. This expression highlights that the MAE is dominated by transitions between states near the Fermi level. Since the contribution to MAE is inversely proportional to the energy difference between occupied and unoccupied states, transitions involving states close in energy—especially those straddling the Fermi level—contribute most significantly. As a result, the densities of states , particularly the distribution of d-orbitals within 1–2 eV of the Fermi level, plays a critical role in determining the magnitude and sign of MAE in MXenes.

Chapter 3

Surface passivation and tunable magnetic properties of Cr-based MXenes

In this chapter we explore magnetic and electronic properties of a few Cr-based double transition metal MXenes where there is inplane ordering of transition metal constituent i.e. i-MXenes . The tunability with regard to the transition metal atoms in these compounds offers a lot of scope to obtain various magnetic structures exhibiting multiple functional properties associated with magnetism. This is particularly important in the backdrop of two-dimensional (2D) magnetic materials garnering immense interest in recent years [19, 141, 20, 142]. Though no i-MXene with magnetic transition metal atom as constituents is yet synthesized, first-principles Density Functional Theory [143] based calculations on more than 300 i-MXenes [105] proposed several magnetic i-MXenes exhibiting superior functional properties. A multiferroic i-MXene $(Ta_{2/3}Fe_{1/3})_2C$ [144] was also proposed from the results of DFT calculations. In these two works, there are two aspects that are not addressed: first, in both works, the magnetic constituent was M′, proportionally half of the non-magnetic transition metal constituent M, and second, the effects of different functional groups passivating the surfaces of i-MXenes were not considered. The first point bears relevance in the sense that the relative proportions of magnetic and non-magnetic component in a system can be very crucial in the resulting magnetic properties through re-normalisation of magnetic exchange interactions. Regarding the second point,reference [105], the most comprehensive work on the i-MXenes, did not consider the role of the functional groups in spite of the well-known facts that their presence is inevitable, given the status of experimental techniques to exfoliate i-MXenes from the corresponding i-MAX phases and that they can influence the electronic properties significantly. Apart from these, it is also worth exploring magnetism in i-MXenes by changing M′. A recent work [145] took care of the two aspects mentioned above for $(V_{2/3}Zr_{1/3})_2CT_2$ i-MXenes. However, their work was limited for M′=Zr only.

To address these issues, in this work, we have employed DFT-based techniques to investigate the structural, electronic and magnetic properties of Cr-based i-MXenes, specifically pristine and surface passivated $(Cr_{2/3}Y_{1/3})_2C$, $(Cr_{2/3}Zr_{1/3})_2C$, and $(Cr_{2/3}Sc_{1/3})_2C$. Functional groups -O and -F have been considered as T for surface passivated i-MXenes $(Cr_{2/3}M'_{1/3})_2CT_2$. The reason behind choice of these three compounds is (1) the cor-

---

The contents of this chapter are published in 2024, The Journal of Physical Chemistry C, 128(38), 16133-16142, DOI: 10.1021/acs.jpcc.4c04094.

responding i-MAX compounds $(Cr_{2/3}Zr_{1/3})_2AlC$, $(Cr_{2/3}Sc_{1/3})_2AlC$ and $(Cr_{2/3}Y_{1/3})_2AlC$ have been synthesized [51, 46] suggesting the possibility of exfoliation to i-MXene phases, (2) the magnetic element Cr has a larger proportion than the transition metal element M′ (3) DFT calculations of the i-MAX phases of these compounds reveal that the magnetic ground states change across the compounds in spite of the strong magnetic element Cr being present in same proportion and (4) the choice of -O and -F as functional groups is consistent with the fact that the usual procedure of obtaining MXene monolayers through acid rinsing mostly lead to surface passivation by these groups only. In our work, we investigate, apart from the electronic and magnetic ground states, the finite temperature properties and the magnetic anisotropy energies for pristine, O- and F- functionalized i-MXenes. Our results provide important insights into understanding the magnetism in this new class of compounds and their operational usefulness.

3.1 Methods

For computations of ground state properties and the electronic structures, projector augmented wave (PAW) [146] pseudopotentials and a plane wave basis set up to 600 eV are used. The exchange-correlation part of the Hamiltonian is approximated using the generalized gradient approximation (GGA) parameterized by Perdew-Burke-Ernzerhof (PBE)[123]. Van-Der Waals interactions are included using the DFT-D3 method [147] to account for long-range dispersion interactions. The energy and force convergence criteria are set as 10^{-6} eV and 0.01 eV/Å, respectively. A 11 × 11 × 1 Monkhorst-Pack [148] k-point mesh is used for geometry optimization. A larger k-mesh of 37 × 37 × 1 is used for electronic structure calculations. Spin-orbit coupling (SOC) is included in the calculation of the magnetic anisotropy energy (MAE). A 20 Åvacuum is considered to prevent interactions between adjacent layers.

Two important quantities associated with the formation of the i-MXenes, the exfoliation energy E_{exf} [149] and the formation energy E_{form} are calculated the following way

$$\begin{aligned} E_{exf} &= \frac{-[E_{total}(i-MAX) - 2E_{total}(i-MXene) - 2E_{total}(Al)]}{4S} \qquad (3.1) \\ E_{form} &= \frac{(E[(Cr_{2/3}M'_{1/3})_2CT_2] - E[(Cr_{2/3}M'_{1/3})C] - 6E(X_g)}{6}. \qquad (3.2) \end{aligned}$$

$E[(Cr_{2/3}M'_{1/3})_2CT_2], E[(Cr_{2/3}M'_{1/3})C], E(X_g)$ are the total energies of i-MXenes functionalized by T, pristine i-MXene and that of functional group T in gas phase, respectively. The factor 2 in front of $E_{total}(i-MXene)$ and $E_{total}(Al)$ in the expression for E_{exf} arises because i-MAX monolayer consists of two i-MXene slabs and an Al layer. The factor of 6 is due to the presence of 6 X atoms in the unit cell. $E_{total}(i-MAX), E_{total}(i-MXene), E_{total}(Al)$ are the total energies of the precursor i-MAX, the exfoliated pristine i-MXene and Aluminium in its bulk phase, respectively. S is the surface area of the exfoliated i-MXene. The dynamical stability of the i-MXenes are obtained by computing their phonon band structures. The supercell method, as implemented in PhonoPy package [150] is used for this purpose. Supercells of size 3 × 3 × 1 have been used.Higher energy convergence of 10^{-8} eV is set to ensure convergence of phonon frequencies.

In order to compute the pairwise magnetic exchange interactions $\mathrm{J_{ij}}$, a full-potential spin-polarized scaler relativistic Hamiltonian with angular momentum cut off $l_{max} =$

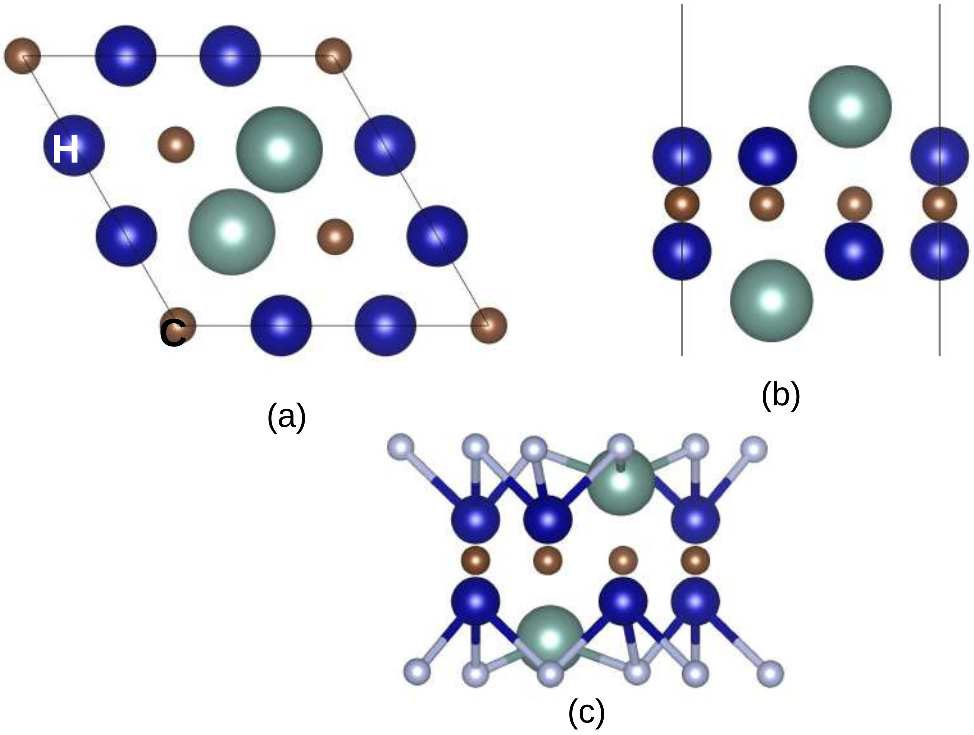

Figure 3.1: Conventional cell of $(Cr_{2/3}M'_{1/3})_2C$ i-MXene. Figures (a) and (b) show top and side views, respectively. Figure(c) is side view of a functionalised i-MXene. Blue, brown,green and white balls stand for Cr,C, M′ and functional group (O/F) atoms, respectively.

8 is used along with a converged k mesh for Brillouin zone integrations. The energy convergence criterion is set to 10^{-8} eV for the self-consistency cycles. The Matsubara frequency is set to 1500 after carefully checking its convergence. Using these exchange parameters, the magnetic transition temperatures are estimated by the Classical Monte Carlo simulation (MCS) . Here, calculations are performed for three ensembles in supercell size of 45 × 45 × 1. The periodic boundary condition is invoked in each case. 10^5 Monte Carlo steps are performed at each temperature to achieve convergence in energies.

3.2 Results and discussion

3.2.1 Structural models, and energetics

In Figure 3.1, the structure of pristine i-MXene $(Cr_{2/3}M'_{1/3})_2C$ (M′=Sc/Zr/Y) is shown. Pristine $(Cr_{2/3}M'_{1/3})_2C$ is essentially a trilayer structure, with a single layer of C atoms sandwiched between two layers of Cr/M′ atoms. The M′ atoms are slightly misaligned with respect to the Cr atoms (Figure 3.1(b)). The structure of the conventional cell of i-MXene considered in this work is taken from Reference [105]. The pristine i-MXene unit cell consists of four Cr atoms, two M′ atoms and three C atoms . In functionalised i-MXenes , in addition to the above, six functional group atoms (F/O) are also present (Figure 3.1(c)). In order to assess the possibility of exfoliation of the i-MXenes from their corresponding i-MAX phases, we first calculate their exfoliation energies(E_{exf}).

The calculated exfoliation energies are shown in Figure 3.2. The exfoliation energies

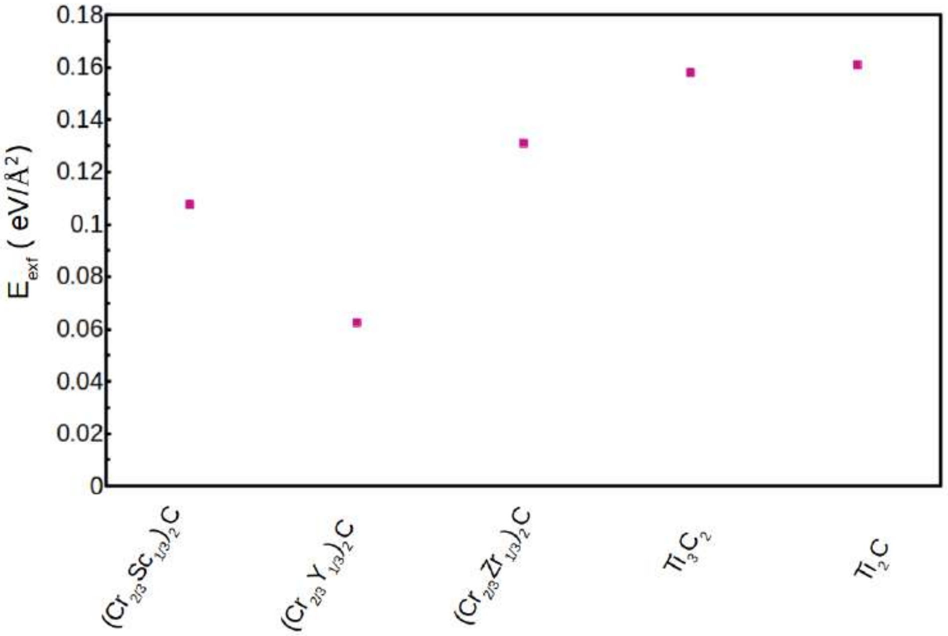

Figure 3.2: Exfoliation energies of the i-MXenes considered in this work.

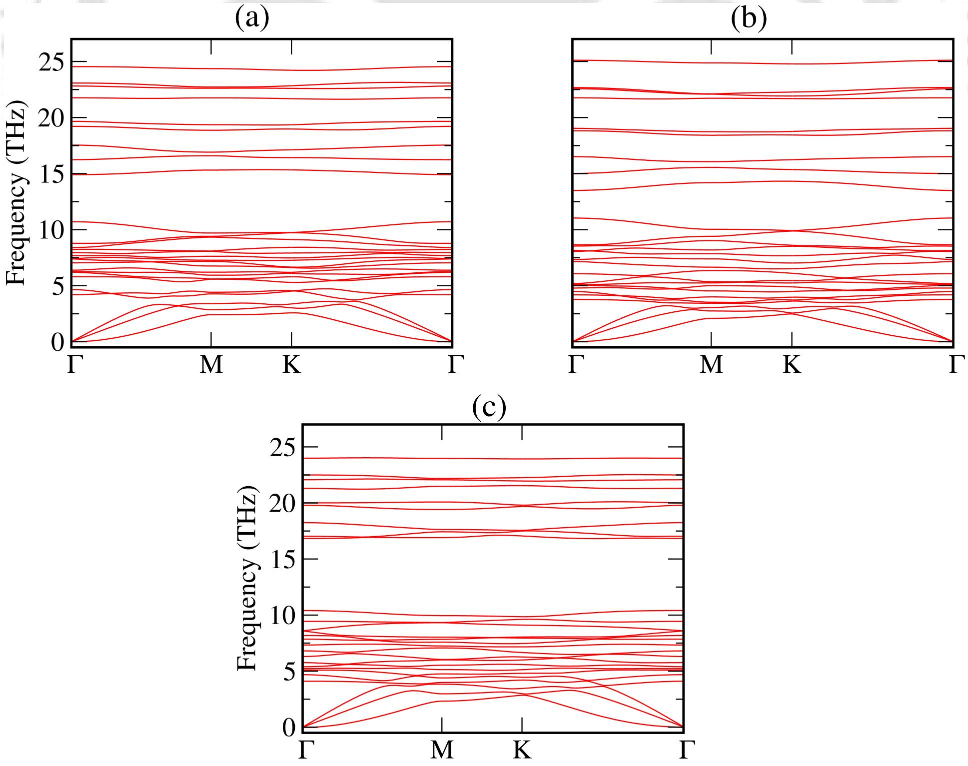

Figure 3.3: Phonon spectra of (a) $(Cr_{2/3}Sc_{1/3})_2C$,(b)$(Cr_{2/3}Y_{1/3})_2C$ and (c) $(Cr_{2/3}Zr_{1/3})_2C$

Table 3.1: DFT total energies of F and O functionalised i-MXenes computed for four different structural models. The energies are in meV per unit cell.

Structure	models	Energy	Structure	models	Energy
$(Cr_{2/3}Sc_{1/3})_2CF_2$	CC	deformed	$(Cr_{2/3}Sc_{1/3})_2CO_2$	CC	1628.66
	HH	0		HH	0
	HC	125.18		HC	726.78
	TT	deformed		TT	deformed
$(Cr_{2/3}Y_{1/3})_2CF_2$	CC	142.72	$(Cr_{2/3}Y_{1/3})_2CO_2$	CC	674.08
	HH	0		HH	73.78
	HC	798.55		HC	0(deformed)
	TT	deformed		TT	deformed
$(Cr_{2/3}Zr_{1/3})_2CF_2$	CC	80.56	$(Cr_{2/3}Zr_{1/3})_2CO_2$	CC	2743.69
	HH	0		HH	0
	HC	399.39		HC	1140.18
	TT	deformed		TT	deformed

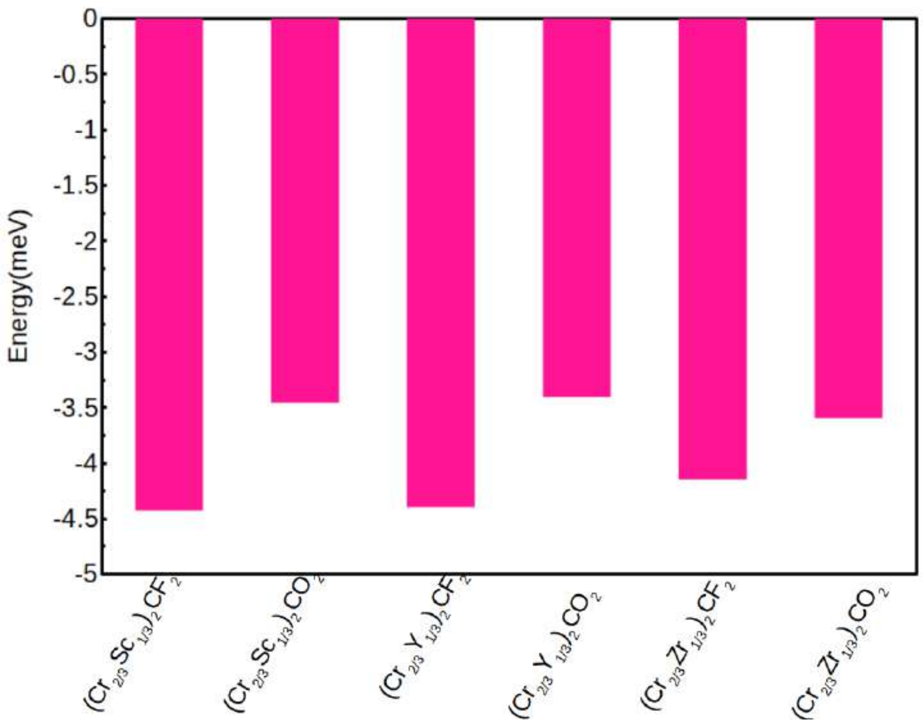

Figure 3.4: Formation energies of i-MXenes considered in this work.

are significantly less than that of the well-known and commercially synthesized MXene Ti_3C_2; the value being 0.158 eV/Å^2 [151] for exfoliating from Ti_3AlC_2. This suggests that the i-MXenes considered in this work can be easily exfoliated from the corresponding i-MAX phases. To check whether the i-MXenes are dynamically stable, we have calculated phonon dispersion relations for the three pristine compounds. The results are shown in Figure 3.3. We find that all three systems in their pristine forms are dynamically stable. Since pristine compounds are dynamically stable, we expect their stability will also be maintained upon functionalisation as well. The structures of functionalised i-MXenes can be obtained by considering the total energies of various structural models of functionalisations. The functional groups passivating their surfaces have three different positions to occupy. Two of them denoted as C and H, are shown in Figure 3.1(a); C(H) represents the hollow site above the C(Cr/M′) atom. The third position, T (not shown in the figure), is the one right above the transition metal atom site. Thus, there can be four different structural models of surface functionalization: HH (CC) model, where functional groups occupy hollow site H(C) of both surfaces; HC model, where functional groups attached to hollow site H of one surface and hollow site C of the other surface, or vice versa; and TT model, where the functional groups occupy the T sites associated with both surfaces. The total energies of these models for each i-MXene considered are provided in Table 3.1. The results suggest that for all three compounds, irrespective of the functional groups, the lowest energy configuration is obtained in the HH model. The energy of HH model is lower than the stable model that is energetically immediately higher than it, by 125.18 meV/cell(726.78 meV/cell), 142.72 meV/cell(73.78 meV/cell) and 80.56 meV/cell(1140.18 meV/cell) for $(Cr_{2/3}Sc_{1/3})_2CF_2((Cr_{2/3}Sc_{1/3})_2CO_2)$, $Cr_{2/3}Y_{1/3})_2CF_2((Cr_{2/3}Y_{1/3})_2CO_2)$ and $Cr_{2/3}Zr_{1/3})_2CF_2$ $(Cr_{2/3}Zr_{1/3})_2CO_2)$, respectively. After obtaining the optimized structures of the functionalized i-MXenes, the formation energy of each one of them is calculated to confirm their stability. The results are shown in Figure 3.4. The large and negative formation energies indicate the formation of strong chemical bonds in these systems.

3.2.2 Magnetic ground states

In order to find the magnetic ground state structure, spin-polarized calculations with various ordered magnetic configurations are done on the stable crystal structures of functionalized MXenes. Four different magnetic configurations, illustrated in Figure 3.5, are considered. Apart from the ferromagnetic (FM) configuration where all Cr spins are aligned along c-direction, three antiferromagnetic(AFM) configurations are considered : (a)AFM$_1$ where antiferromagnetic (ferromagnetic) alignment is considered along $b(c)$-direction (b) AFM$_2$ where antiferromagnetic (ferromagnetic) alignment is considered along $c(b)$-direction and (c) AFM$_3$ where the alignment is antiferromagnetic along both b and c directions. The magnetic properties of the i-MXenes considered in this work are provided in Table 3.2.

The results clearly show that surface passivation influences the magnetic ground states of these i-MXenes. The pristine i-MXenes, $(Cr_{2/3}Sc_{1/3})_2C$, $(Cr_{2/3}Y_{1/3})_2C$, and $(Cr_{2/3}Zr_{1/3})_2C$, stabilize in antiferromagnetic (AFM) ground states although the AFM configurations vary across systems. While $(Cr_{2/3}Y_{1/3})_2C$ and $(Cr_{2/3}Sc_{1/3})_2C$ stabilise in AFM$_3$ configuration, $(Cr_{2/3}Zr_{1/3})_2C$ stabilises in AFM$_1$ state. The former two compounds have near identical Cr moments while that in $(Cr_{2/3}Zr_{1/3})_2C$ is slightly less. This suggests an identical mechanism driving the magnetic ground states in $(Cr_{2/3}Y_{1/3})_2C$

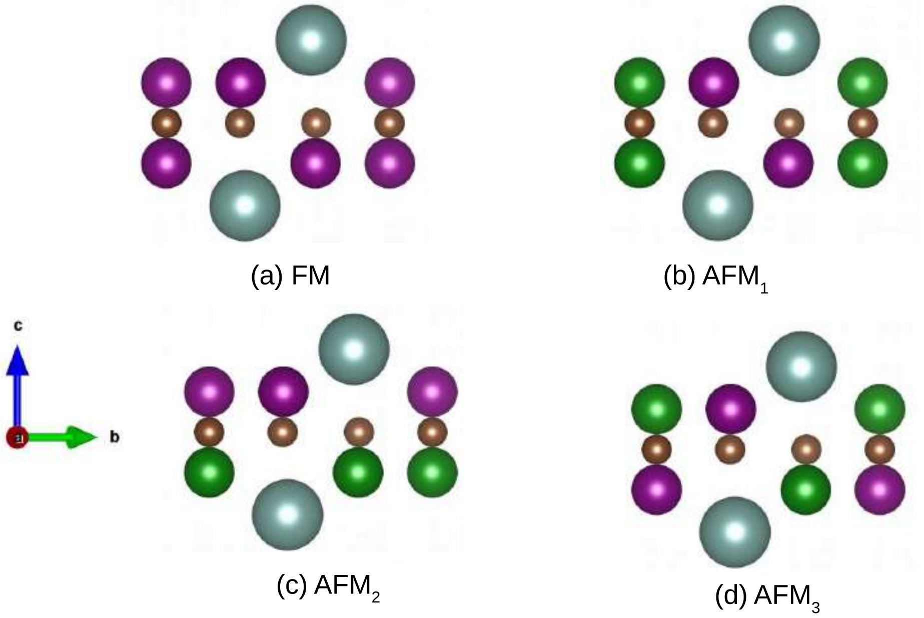

(a) FM

(b) AFM$_1$

(c) AFM$_2$

(d) AFM$_3$

Figure 3.5: Four magnetic configurations considered in this work.The purple(green) ball indicates spin of the Cr atom pointing along (against) the c-axis. Brown and grey balls depict C and M$'$ atoms, respectively.

.

Table 3.2: The energy differences ΔE (in meV per unit cell) of the three AFM configurations relative to the FM configuration, magnetic moment per Cr atom $\mathrm{M_{Cr}}$ (in μ_B), magnetic ordering temperature $\mathrm{T_C/T_N}$ (in K), and magnetic anisotropy energy E_{MAE} (in meV per unit cell) for pristine and functionalized i-MXenes.

System	$\Delta E_{\mathrm{AFM_1-FM}}$	$\Delta E_{\mathrm{AFM_2-FM}}$	$\Delta E_{\mathrm{AFM_3-FM}}$	$\mathrm{M_{Cr}}$ (μ_B)	$\mathrm{T_C/T_N}$ (K)	E_{MAE} (meV)
$(Cr_{2/3}Y_{1/3})_2C$	-39.59	-6.88	-109.80	1.10	55	0.38
$(Cr_{2/3}Sc_{1/3})_2C$	-11.50	-9.40	-21.63	1.15	30	0.34
$(Cr_{2/3}Zr_{1/3})_2C$	-53.00	-46.81	-46.81	0.96	30	0.30
$(Cr_{2/3}Y_{1/3})_2CF_2$	220.00	-355.30	82.78	1.92	85	0.16
$(Cr_{2/3}Sc_{1/3})_2CF_2$	195.80	-555.30	56.20	2.06	140	-0.01
$(Cr_{2/3}Zr_{1/3})_2CF_2$	190.20	-189.46	190.20	1.85	155	0.36
$(Cr_{2/3}Y_{1/3})_2CO_2$	369.70	366.00	313.41	1.54	115	0.03
$(Cr_{2/3}Sc_{1/3})_2CO_2$	178.28	278.02	208.40	1.48	70	0.16
$(Cr_{2/3}Zr_{1/3})_2CO_2$	-10.36	11.50	143.32	1.73, 0.72	50	0.08

and $(Cr_{2/3}Sc_{1/3})_2C$. Identical magnetic ground states are obtained in -F functionalized i-MXenes. -F functionalisation stabilises the AFM$_2$ order in all three systems considered. The Cr magnetic moment increases by about 1 μ_B as compared to that in the pristine compounds. With -O functionalization, the ground state magnetic structures change again. $(Cr_{2/3}Y_{1/3})_2CO_2$ and $(Cr_{2/3}Sc_{1/3})_2CO_2$ now stabilise in FM states. $(Cr_{2/3}Zr_{1/3})_2CO_2$, on the other hand, stabilises in AFM$_1$ state. However, in this magnetic structure, the magnetic moments of the two Cr atoms are not identical: moment of the Cr atom with spin aligned(anti-aligned) along c-direction is 1.73(0.72) μ_B. Thus, the ground state of $(Cr_{2/3}Zr_{1/3})_2CO_2$ is Ferrimagnetic (FiM). The Cr moments of -O functionalized i-MXenes are found to be lying in between those of pristine and the -F functionalized ones. That the

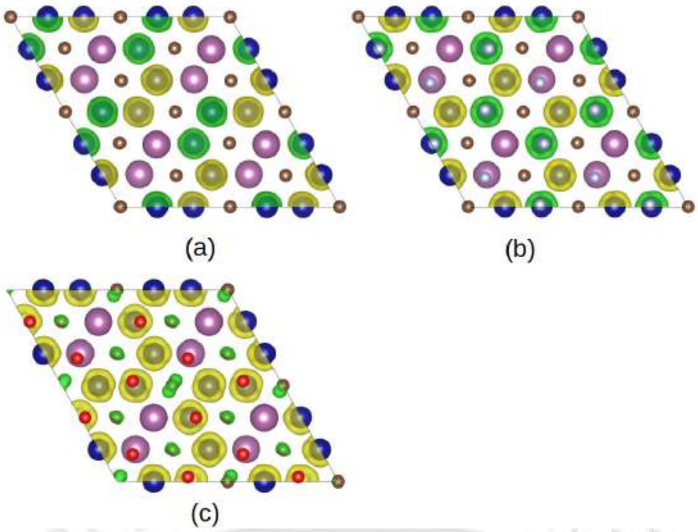
(a)

(b)

(c)

Figure 3.6: Spin density profiles for (a) $(Cr_{2/3}Sc_{1/3})_2C$, (b) $(Cr_{2/3}Sc_{1/3})_2CF_2$, and (c) $(Cr_{2/3}Sc_{1/3})_2CO_2$.Yellow (Green) colour refers to spin densities of spin-up(spin-down)electrons.

functional group passivating the surfaces along with the alloying at the transition metal site affects the magnetic order in MXenes is evident from these results. A comparison with existing results for conventional MXenes Cr_2CF_2 [152] and Cr_2CO_2 [86] corroborates this. While Cr_2CF_2 stabilises in an AFM structure, Cr_2CO_2 has a non-magnetic ground state. The emergence of significant Cr moment in -O functionalized i-MXenes, therefore, is due to alloying with a non-magnetic transitional metal atom. The difference between conventional and i-MXene in the case of -F functionalized systems considered here is reflected in the considerable reduction of the Cr moments. The DFT calculated Cr moments in Reference [152] are 3 μ_B, 50% more than the results obtained for the i-MXenes in the present work. Even in the case of pristine compounds, the ground states and the magnetic moments of $(Cr_{2/3}M'_{1/3})_2C$ are different from conventional MXene Cr_2C that is found to be stabilized in FM configuration with a magnetic moment of 4 μ_B per Cr atom. The effects of the functionalization of surfaces in i-MXenes can also be observed by looking at the spin density profiles. To this end, we have plotted the spin density profiles of pristine and functionalized $(Cr_{2/3}Sc_{1/3})_2C$ in Figure 3.6. The spin density profiles indicate that while in pristine and -F functionalized i-MXenes, the spin density is localized on the Cr atoms, delocalization has happened for the -O functionalized system. In this system, spin density is induced on the C atoms due to delocalised nature of Cr *d*-orbitals. These features of spin density profiles are correlated with the electronic structures and can be used to understand the origin of the magnetic ground states in these systems. In the next sub-section, this is discussed in detail.

3.2.3 Electronic Structure

The total, atom, and orbital-projected spin polarised densities of states of the systems considered are shown in Figure 3.7, and Figure 3.8. Comparison of the three pristine i-MXenes (Figure 3.7(a),(d) and (g), indicates that while $(Cr_{2/3}Sc_{1/3})_2C$ and $(Cr_{2/3}Zr_{1/3})_2C$ are metallic, $(Cr_{2/3}Y_{1/3})_2C$ is a semiconductor with a small band gap of 20 meV.The

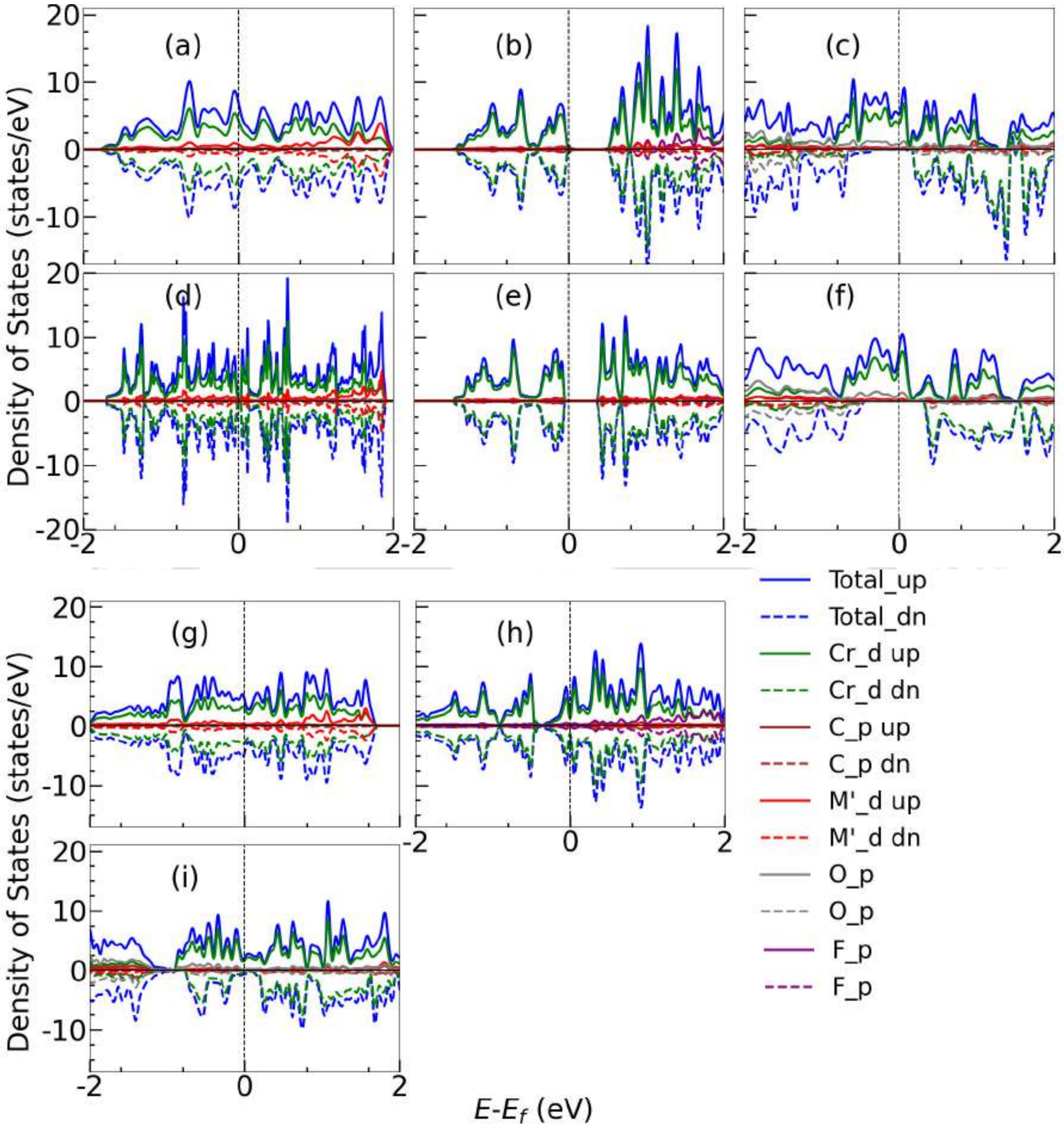

Figure 3.7: Total,atom-projected and orbital-projected densities of states of (a) $(Cr_{2/3}Sc_{1/3})_2C$,(b) $(Cr_{2/3}Sc_{1/3})_2CF_2$, (c) $(Cr_{2/3}Sc_{1/3})_2CO_2$, (d)$(Cr_{2/3}Y_{1/3})_2C$, (e) $(Cr_{2/3}Y_{1/3})_2CF_2$,(f) $(Cr_{2/3}Y_{1/3})_2CO_2$,(g) $(Cr_{2/3}Zr_{1/3})_2C$,(h)$(Cr_{2/3}Zr_{1/3})_2CF_2$ and (i) $(Cr_{2/3}Zr_{1/3})_2CO_2$. "up" and "down" indicate the orientations of the spins with respect to c-direction. Contributions from d orbitals of transition metals Cr,M′ and p orbitals of C and the functional groups are plotted along with the total densities of states.

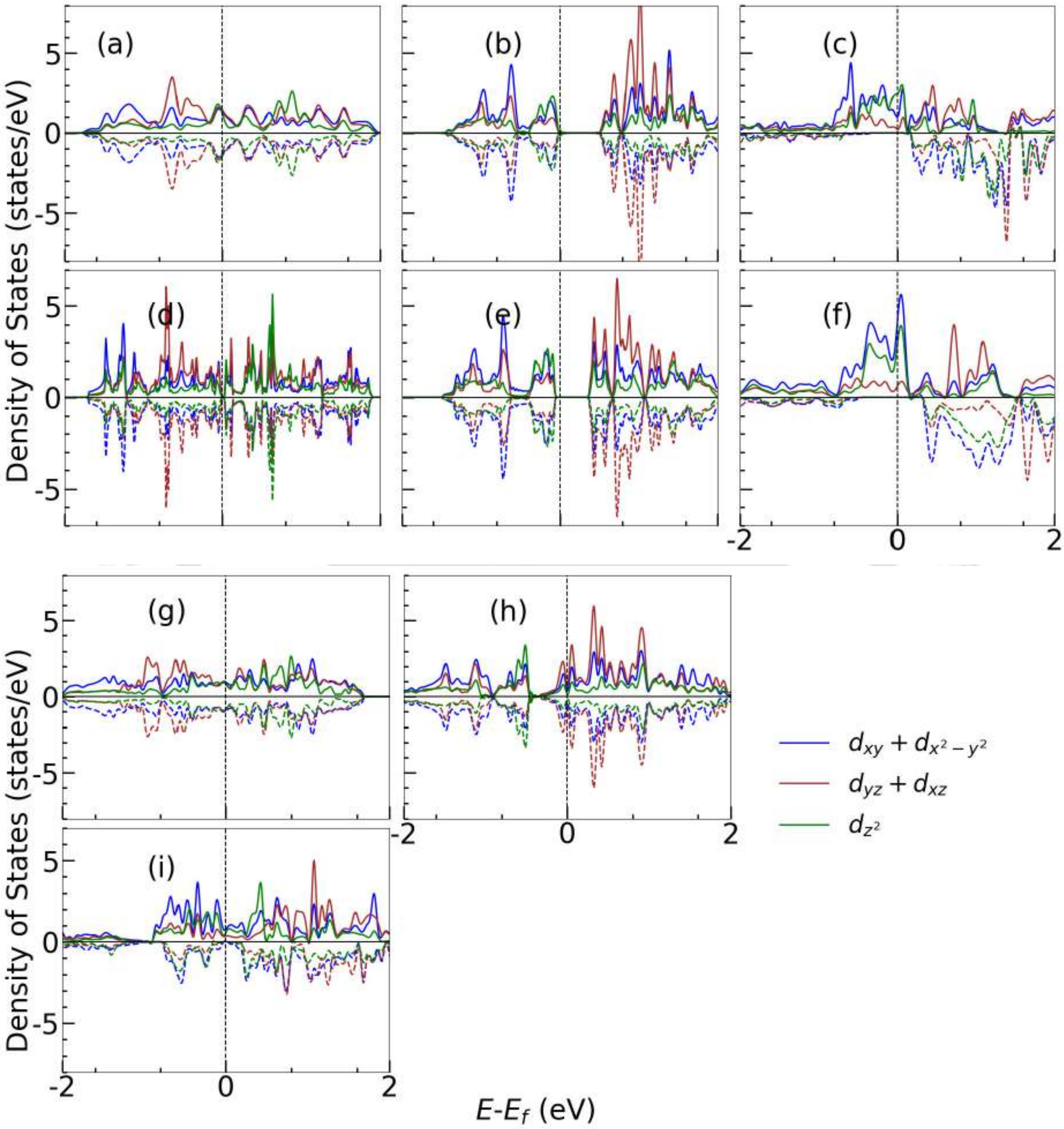

Figure 3.8: *d*-orbital resolved spin polarised densities of states of (a) $(Cr_{2/3}Sc_{1/3})_2C$, (b) $(Cr_{2/3}Sc_{1/3})_2CF_2$, (c)$(Cr_{2/3}Sc_{1/3})_2CO_2$,(d)$(Cr_{2/3}Y_{1/3})_2C$, (e)$(Cr_{2/3}Y_{1/3})_2CF_2$,(f)$(Cr_{2/3}Y_{1/3})_2CO_2$,(g) $(Cr_{2/3}Zr_{1/3})_2C$, (h)$(Cr_{2/3}Zr_{1/3})_2CF_2$ and (i)$(Cr_{2/3}Zr_{1/3})_2CO_2$.

atom-projected densities of states indicate strong hybridization between d-orbitals of the transition metal constituents and p-orbitals of C. The differences in the electronic ground states of the three compounds can be understood from the orbital-decomposed densities of states shown in Figure 3.8. In the pristine i-MXenes, each transition metal atom sits in a C_{3v} crystal field of three C-atoms. Under the C_{3v} symmetry, the d-orbitals of transition metal atoms split into $a_1(d_{z^2})$, doubly degenerate $e_2(d_{xz}, d_{yz})$ and $e_1(d_{x^2-y^2}, d_{xy})$ orbitals, in ascending order of energy [153].We find that $(Cr_{2/3}Sc_{1/3})_2C$ and $(Cr_{2/3}Zr_{1/3})_2C$ have almost similar orbital contributions to the densities of states near fermi level. Unlike the other two pristine compounds, the localized orbitals in $(Cr_{2/3}Y_{1/3})_2C$ are responsible for the semiconducting ground state.

Upon functionalization with F or O, the transition metal atom is now coordinated to six metal atoms and is in the D_{3d} crystal field. Due to this the d-orbitals split into doubly degenerate $e_1(d_{xz}, d_{yz})$, single $a_1(d_{z^2})$ and doubly degenerate $e_2(d_{x^2-y^2}, d_{xy})$ in ascending order of energy. Changes in the local crystal field upon functionalisation causes such changes in the hierarchy of energy levels. This affects changes in the orbital occupancies leading to changes in electronic structures. F-functionalization localizes the d-states of transition metals resulting in semiconducting ground states in $(Cr_{2/3}\ Y_{1/3})_2CF_2$ and $(Cr_{2/3}Sc_{1/3})_2CF_2$, the band gaps being 0.565 eV and 0.679 eV, respectively. The deep-lying -F states push the d-states in the occupied part of the spectrum towards lower energies, opening the gaps in both spin channels. The high magnetic moments of Cr atoms in -F functionalized i-MXenes is an artifact of this. Although localization is also observed in $(Cr_{2/3}Zr_{1/3})_2CF_2$, the states in the unoccupied parts too are pushed substantially to the lower energies resulting in a metallic ground state. This is primarily due to the delocalized a_1 states at the bottom of the conduction bands.

All three -O functionalized i-MXenes turn out to be half-metallic. The densities of states of $(Cr_{2/3}Y_{1/3})_2CO_2$, $(Cr_{2/3}Sc_{1/3})_2CO_2$ and $(Cr_{2/3}Zr_{1/3})_2CO_2$ have an empty Cr spin down band. The spin-up channels of the three compounds are metallic. Due to strong local magnetic moments, these compounds create strong local magnetic exchange fields, which, tend to align the spins of neighbouring electrons . The exchange field pushes the minority spin-states above the Fermi energy. This shift creates an energy gap between the occupied and unoccupied minority spin states, resulting in different electronic properties for majority and minority spin channels.The spin-down bands of M' are also pushed towards lower energies, opening up a semiconducting gap. This arises due to hybridizations with the deep-lying O p states. In case of $(Cr_{2/3}Zr_{1/3})_2CO_2$, the half-metallic gap is much smaller. This is due to different exchange splittings of two Cr atoms, which leads to more states closer to the Fermi level. The O states in all three cases are delocalized, corroborating the results from the spin density profiles. The trait of -O functionalised i-MXenes considered in this work is important from a utility point of view as these materials are promising candidates for spin filters. The features in the electronic structures help us understand the origin of the magnetic ground states of the three i-MXenes obtained in our calculations. The origin of the magnetic ground states of the pristine and functionalised i-MXenes can be understood in terms of magnetic exchange interactions between the Cr-atoms. There are two exchange mechanisms: (a) Direct exchange interactions between the two Cr atoms and (b) 90-degree superexchange between the Cr atoms through non-magnetic atoms C/O/F. The direct exchange is predominantly antiferromagnetic, whereas 90-degree superexchange is ferromagnetic. The interplay of these two interactions determines the magnetic ground state. In pristine i-MXenes direct exchange along b-direction is dominating. This is due to small Cr-Cr distances(less than 2.9 Åfor all

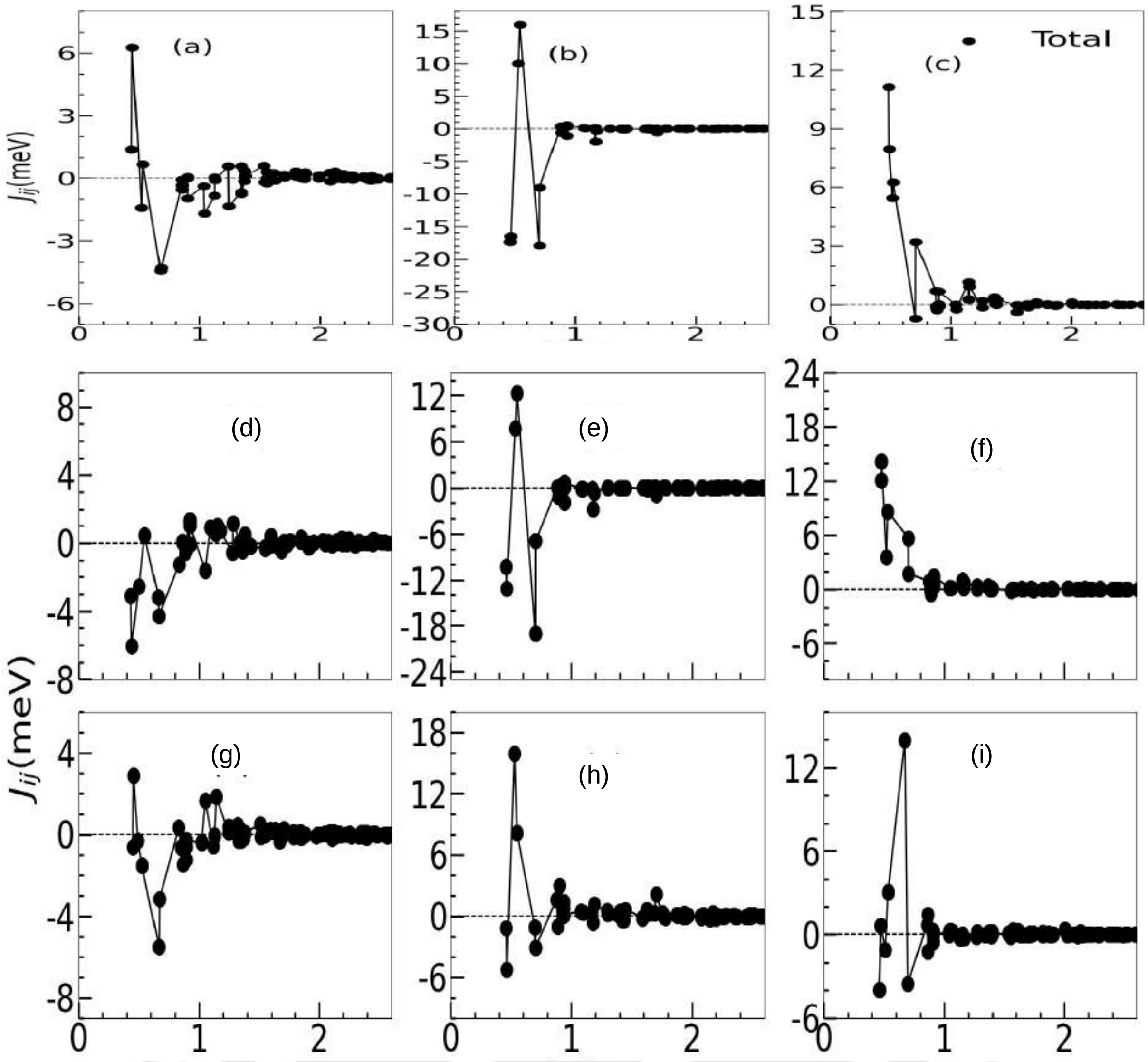

Figure 3.9: Inter-atomic exchange parameters as a function of inter-atomic distances for (a) $(Cr_{2/3}Sc_{1/3})_2C$, (b) $(Cr_{2/3}Sc_{1/3})_2CF_2$ and (c) $(Cr_{2/3}Sc_{1/3})_2CO_2$(d) $(Cr_{2/3}Y_{1/3})_2C$, (e) $(Cr_{2/3}Y_{1/3})_2CF_2$, (f)$(Cr_{2/3}Y_{1/3})_2CO_2$,(g)$(Cr_{2/3}Zr_{1/3})_2C$, (h)$(Cr_{2/3}Zr_{1/3})_2CF_2$, (i)$(Cr_{2/3}Zr_{1/3})_2CO_2$.

cases) along b. This leads to AFM_1 or AFM_3 as the ground state. Functionalisation with F or O gives rise to an additional superexchange path through the passivators. Further, the functionalisation leads to an increase in the Cr-Cr distance along b . As a result direct exchange (superexchange) along b weakens (strengthens) leading to dominant ferromagnetic superexchange along b. Along c, direct exchange dominates over superexchange in F-functionalized i-MXenes. This happens due to the localised Cr d states as can be seen from the densities of states. This is the origin of AFM_2 ground states in F-functionalised i-MXenes considered. In O-functionalised system, the Cr d states are rather delocalised (Figure 3.7(c),(f),(i)). This makes the superexchange interaction via O atoms the dominant exchange mechanism giving rise to ferromagnetic (or ferrimagnetic) ground states.

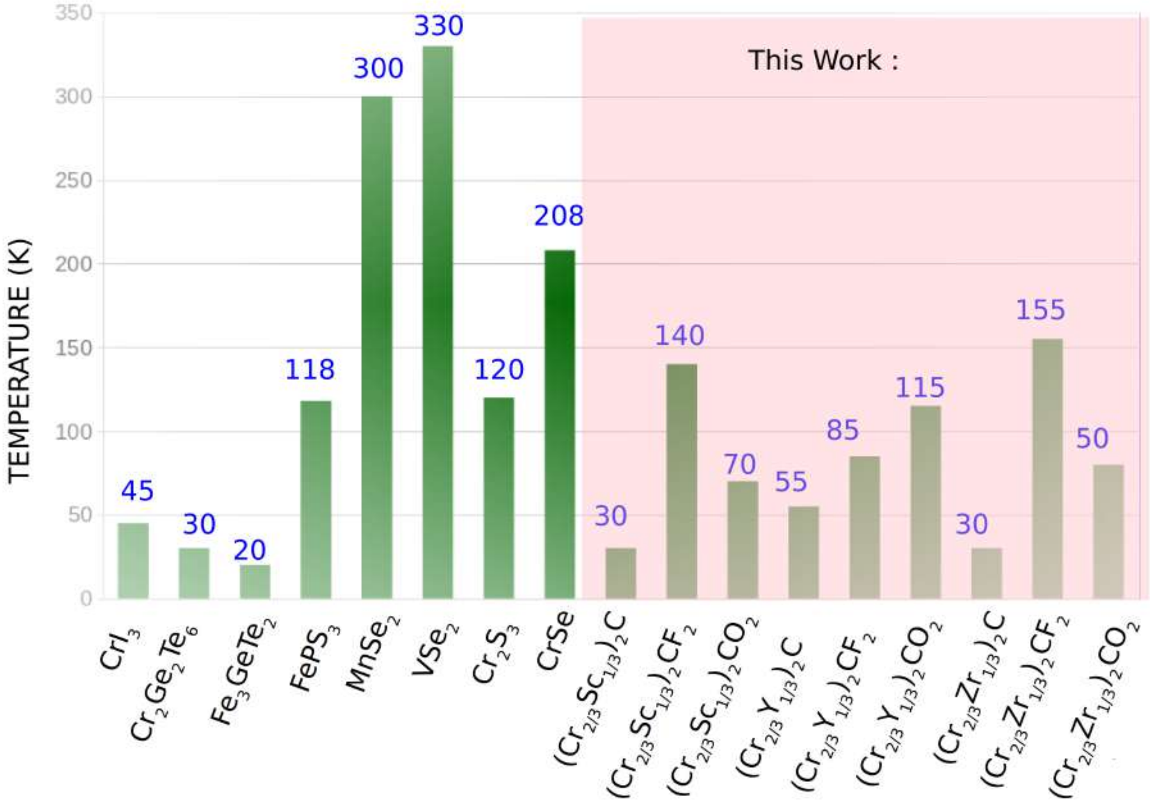

Figure 3.10: Magnetic transition temperatures of the i-MXenes considered in this work along with those of some well known 2D materials [154, 155, 156, 22]

3.2.4 Interatomic exchange parameters and Transition temperatures

In Figures 3.9 , we show the Cr-Cr magnetic exchange parameters as a function of interatomic distances. Results reveal that only the first few nearest neighbors make significant contributions to the total interactions, while long-range interactions ($R_{ij}/a > 2.5$) are negligibly small. Figure 3.9(a) shows the exchange parameters for $(Cr_{2/3}Sc_{1/3})_2C$. The figure suggests that there are significant AFM interactions from the third, fifth, and sixth nearest neighbors that counter the FM interactions in the first two nearest neighbor shells leading to an AFM ground state in this compound. In the -F functionalized compound $(Cr_{2/3}Sc_{1/3})_2CF_2$ (Figure 3.9(b)), the magnetic interactions among first and second nearest neighbor Cr atoms are strongly AFM as is the case with the fifth nearest neighbors. These collectively overcome strong FM interactions between the third and fourth nearest neighbor Cr atoms and stabilize an AFM ground state. Strong FM interactions are found among the first four neighbors of a Cr atom in $(Cr_{2/3}Sc_{1/3})_2CO_2$ (Figure 3.9(c)), explaining the origin of an FM ground state in this compound. The same trends are found in the case of the other two i-MXenes with the exception of $(Cr_{2/3}Zr_{1/3})_2CO_2$ (Figure 3.9)(i)) where a few interactions are AFM. However, this is consistent with the FiM ground state of this compound.

These exchange interactions are used to calculate the magnetic transition temperatures employing Monte Carlo simulation. The estimated values are given in Table 3.2.

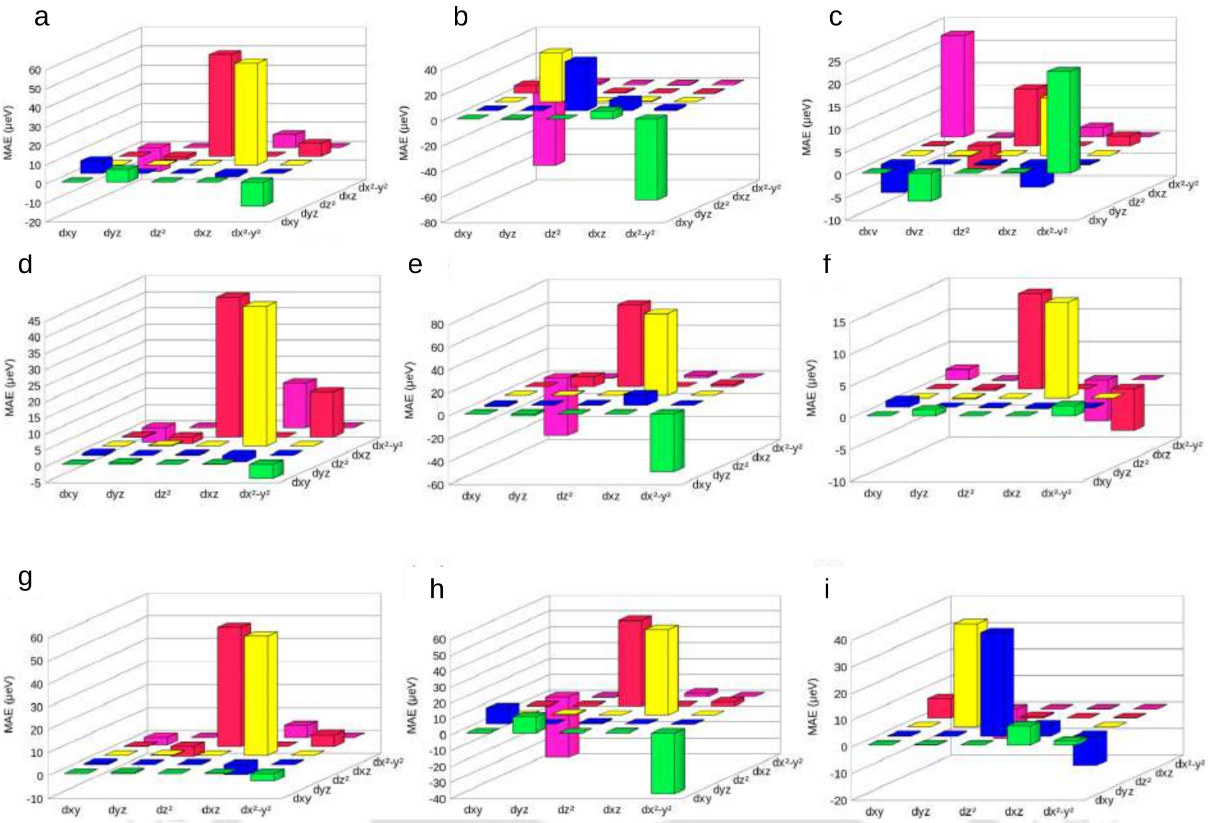

Figure 3.11: Orbital resolved MAE for (a) $(Cr_{2/3}Sc_{1/3})_2C$, (b) $(Cr_{2/3}Sc_{1/3})_2CF_2$ (c) $(Cr_{2/3}Sc_{1/3})_2CO_2$,(d)$(Cr_{2/3}Y_{1/3})_2C$, (e)$(Cr_{2/3}Y_{1/3})_2CF_2$, (f)$(Cr_{2/3}Y_{1/3})_2CO_2$, (g)$(Cr_{2/3}Zr_{1/3})_2C$, (h)$(Cr_{2/3}Zr_{1/3})_2CF_2$,and (i)$(Cr_{2/3}Zr_{1/3})_2CO_2$.

We find that the transition temperatures are higher for functionalized i-MXenes in comparison with the pristine compounds; the highest transition temperatures are achieved in the case of -F functionalized i-MXenes. This is due to the strongest exchange between the Cr atoms in these compounds. The transition temperatures of these i-MXenes are comparable to few of the established 2D magnetic materials like CrI_3, $FePS_3$ and $Cr_2Ge_2Te_6$ (Figure3.10).

3.2.5 Magnetic anisotropy energy

Magnetic anisotropy energy (MAE) of a material is important from the point of view of device application as it is instrumental in the stabilization of the magnetic long-range order in the system. For the estimation of MAE from DFT, the in-plane energies are calculated along the (100) and (010) directions, while the out-of-plane energies are calculated along the (001) direction. Results for the i-MXenes considered in this work are presented in Table 3.2. A positive MAE value signifies the presence of an easy axis perpendicular to the MXene surface, while a negative sign indicates that the easy direction aligns parallel to the MXene surface. Our results imply that for pristine MXenes, the MAE values are nearly identical, and the magnetization easy axis for all of them is along (001). Among the F-functionalised i-MXenes, the magnitudes of MAE differ significantly. While $(Cr_{2/3}Zr_{1/3})_2CF_2$ has MAE comparable to the pristine compounds, the other two have noticeable lower values. Moreover, result for $(Cr_{2/3}Sc_{1/3})_2CF_2$ implies an in-plane magnetisation. O-functionalization reduces MAE values further. However, all

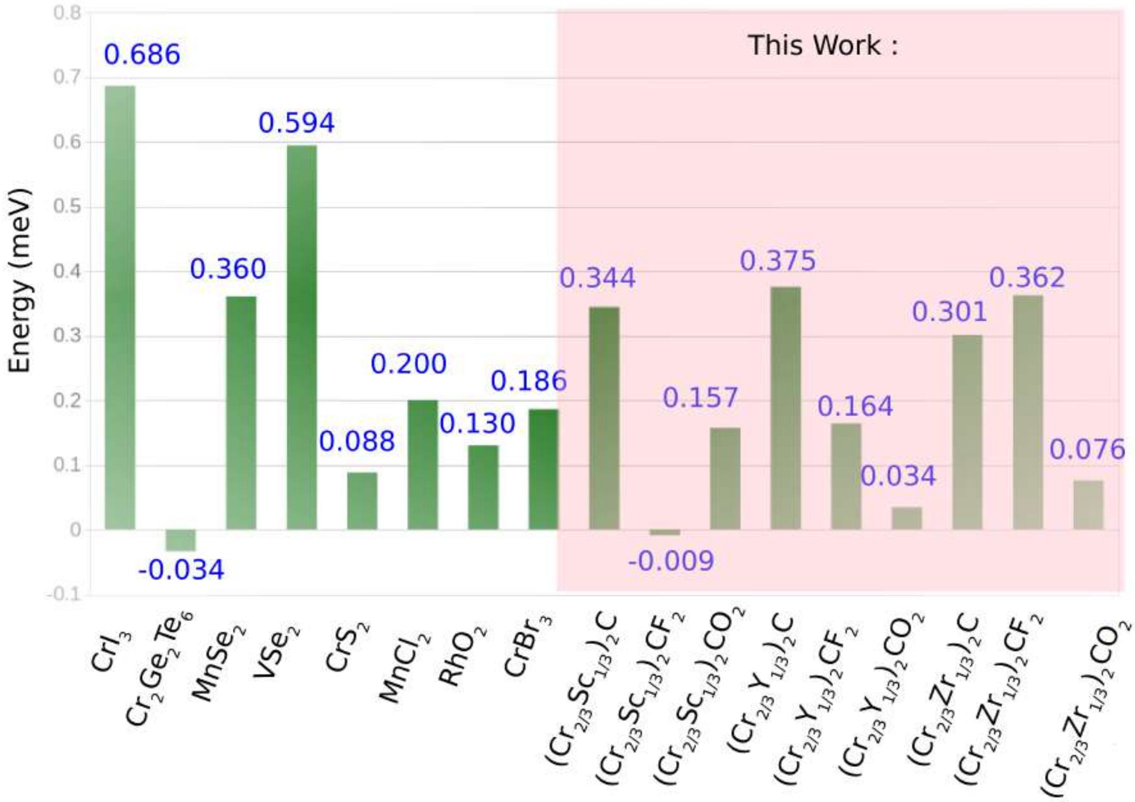

Figure 3.12: Results of MAE of the i-MXenes considered here along with those of some well known 2D magnets [21, 139, 157, 158, 159, 156]

three O-functionalised compounds have (001) as the magnetization easy axis. In Figure 3.12, we compare our calculated MAE values for the three i-MXenes with those of a few established 2D magnetic materials. We find that though the calculated MAE values of these i-MXenes are not as large as those obtained for CrI_3 or VSe_2, they are comparable with or larger than the MAE of other investigated 2D magnets like $CrBr_3$ and $Cr_2Te_2Ge_6$.

The MAE of the i-MXenes is considered to come predominantly from the Cr atoms. The contributions from other atoms are negligible. This is due to the fact that the states near the Fermi level majorly contribute to the MAE. This is also the reason for MAE getting substantially modified upon functionalization of the pristine i-MXenes. Thus, to get an insight into the origin of MAE in these i-MXenes, investigations into the contributions of various Cr d orbitals towards their MAE can be useful. As discussed in chapter 2 , the MAE associated with a transition metal can be understood based on spin-orbit coupling (SOC) interactions between the occupied and unoccupied d-states as seen from equation 2.41. Denoting the SOC interactions between the Cr 3d orbitals as $d_i \otimes d_j$ [139], contributions of various orbitals i towards MAE are illustrated in Figure 3.11 .

For the pristine compounds, a large positive contribution comes from $d_{z^2} \otimes d_{xz}$ interactions. For $(Cr_{2/3}Y_{1/3})_2C$, additional positive contribution comes from $d_{xz} \otimes d_{x^2-y^2}$ interactions (Figure 3.11(d). This additional interaction produces the highest MAE in this compound. Interactions between the other orbitals do not have any significant contribution. Since the contributions of the dominant $d_{z^2} \otimes d_{xz}$ interaction are nearly the same, these three compounds have near identical MAE values. Very low and negative MAE value in $(Cr_{2/3}Sc_{1/3})_2CF_2$ (Figure 3.11(b)) is due to a competition between two sets of orbital interactions: a negative contribution coming from $d_{xy} \otimes d_{x^2-y^2}$ and a near equal positive contribution coming from the $d_{z^2} \otimes d_{yz}$ interactions. Similarly, relatively smaller but positive MAE found in $(Cr_{2/3}Sc_{1/3})_2CO_2$ is due to relatively smaller positive contributions from $d_{xy} \otimes d_{x^2-y^2}$ and $d_{z^2} \otimes d_{xz}$ interactions and non-negligible negative contributions from $d_{xy} \otimes d_{yz}$ and $d_{yz} \otimes d_{xz}$ interactions (Figure 3.11(c)). The decrease in MAE values for -O functionalised $(Cr_{2/3}Y_{1/3})_2C$ and $(Cr_{2/3}Zr_{1/3})_2C$ by one order of magnitude as compared to $(Cr_{2/3}Sc_{1/3})_2CO_2$ is due to smaller(larger) positive(negative) contributions from $d_{xy} \otimes d_{x^2-y^2}(d_{z^2} \otimes d_{xz})$ interactions. MAE values of the remaining two -F functionalized i-MXenes can be understood in a similar way.

It is worth mentioning that the MAE is indicative of whether the ground state can be a non-collinear one [160]. The calculated MAE for all systems considered here except $(Cr_{2/3}Sc_{1/3})_2CF_2$is positive. Thus, they are intrinsic Ising ferromagnets with easy axes that are out of plane i.e along (001) direction. The negative MAE of $(Cr_{2/3}Sc_{1/3})_2CF_2$ suggests an easy magnetization plane. This system can be described as a XY magnet [160]. In such a system, the ground state magnetic configuration can be a non-collinear one due to anisotropic spin-orbit interactions. This is worth investigating in future.

3.3 Summary

The structural and composition flexibility of 2D MXenes is exploited in this work to explore the possibility of obtaining tunable magnetism in Cr-based MXenes. Using Density functional theory-based calculations, we have investigated the electronic and magnetic properties of three Cr-based MXenes, known as i-MXenes, which order in-plane with the transition metal site having an alloy of Cr and another early transition metal non-magnetic constituent with a fixed composition ratio. Our calculations demonstrate that the electronic and magnetic properties of these compounds are significantly influenced by the surface functionalization, the chemical nature of the functional group, and the non-magnetic constituent. Thus, the electronic and magnetic properties can be tuned by changing the non-magnetic transition metal component and the functional group. For the three compounds considered in this work, the -O functionalistion stabilizes ferromagnetic half-metallic states. This makes these compounds suitable as spin-filters which are essential in spintronics for controlling and manipulating spin currents [161]. By analyzing the electronic structures and the magnetic exchange parameters, we explain the reasons behind the occurrence of different magnetic ordering upon changes in the compositions. Our results on magnetic transition temperatures and magnetic anisotropy energies show that the quantities in these systems are comparable to quite a few established 2D magnets. This implies that these i-MXenes can be useful as magnetic devices. Since these materials possess perpendicular magnetic anisotropy (PMA), they are suitable for constructing Spin Transfer Torque Magnetic Random Access Memory (STT-MRAM) [162]. The advantage of PMA systems over those with in-plane magnetic anisotropy lies in the lower critical switching current density and higher thermal stability in the former [163]. Moreover, PMA-based systems are more scalable and cost-effective. Another possible application of these i-MXenes with PMA is in the construction of sensors [164]. The perpendicular anisotropy in the studied i-MXenes will ensure consistent and reliable sensor responses over time, crucial for applications requiring precise magnetic field detection. Specifically, $(Cr_{2/3}Zr_{1/3})_2CF_2$ with magnetic anisotropy energy comparable to $MnSe_2$ and magnetic transition temperature comparable to Cr_2S_3 and CrSe can have multiple utilities as device, as these two compounds have already found applications in construction of magnetic tunnel junction [165], for low power magnetoresistance operations [166] and for antiferromagnetic spintronic applications [167, 168]. With the increasing exploration of MXenes for magnetic applications, this work, the first one to investigate the structure-property relationships in functionalized i-MXenes, can serve as useful input to the experimentalists.

Chapter 4

Tunable magnetism in Nitride MXenes:consequences of atomic layer stacking

4.1 Introduction

$M_{n+1}X_n$ (where n=1-3) MXenes, obtained through chemical exfoliation of their corresponding MAX phases , have (n+1) layers of hcp M atoms intercalated by n layers of hcp X atoms with fcc stacking. This stacking of layers is known as ABC stacking. Though almost all MXenes synthesized so far have the layers stacked in ABC way, a very recent experiment on synthesizing V_2N and Mo_2N from their respective parent carbides by ammonia treatment observed that Mo_2N crystallized in a structure with hcp D_{3h} symmetry instead of the usual trigonal D_{3d} symmetry, seen in MXenes with ABC stacking sequence [58]. This stacking sequence can be described as ABA. Subsequently, a comprehensive study of 54 different MXenes [169]using robust first-principles Density Functional Theory (DFT) [143] based calculations was performed to assess the possibility of alternative ABA stacking in MXenes. The study found that the ABA stacking is realized more in the thinnest ($n = 1$) nitride MXenes where their surfaces are passivated by -O. The possibility of obtaining the ABA stacking pattern is also dependent on the number of *d*-electrons in the transition metal constituents of the MXenes. This investigation provided enough hints towards the alteration of surface phenomena due to changes in the stacking pattern. That this can have serious consequences on the functional properties of these compounds is proved in -O terminated carbide MXenes where ABA stacking is predicted to infuse greater electrocatalytic activity on their surfaces, boosting the hydrogen evolution reaction [170].

Magnetism is one area where structural aspects have significant influences. Plethora of studies on magnetic MXenes have demonstrated that the composition [171, 172, 173, 174, 175, 176], surface functional groups [177, 104, 178] and number of layers [179, 180] affect magnetic properties substantially. Changes in atomic arrangements can alter the bonding and magnetic exchange interactions, resulting in changes in the electronic and magnetic ground states and even finite temperature properties like magnetic transition temperatures. All these have serious consequences on the feasibility of using these compounds

---

The contents of this chapter are published in 2024, Nanoscale, 16(37) DOI: https://doi.org/10.1039/D4NR02246G in practical applications. Thus, motivated by the results of reference [143] and [170], we perform a comprehensive study of several thinnest Nitride MXene M_2NT_2 (M=Sc, Ti, Cr, V, Mn; T=O, F) with a focus on a comparative analysis of their electronic and magnetic properties when stacking pattern changes between ABC and ABA. Finite temperature magnetic properties and magneto-crystalline anisotropy energy (MAE), both essential with regard to using the materials as devices, have also been investigated and analyzed from a microscopic point of view. We find that the stacking pattern can be used as another agency to tune the magnetic properties of these MXenes to a great extent.

4.2 Computational Details

The ground state properties and the electronic structures are calculated by the projector Augmented Wave (PAW) method [146]. The exchange-correlation part of the Hamiltonian is approximated using Generalized Gradient Approximation (GGA), parameterized by Perdew-Burke-Ernzerhof (PBE)[123]. DFT+U method [181] has been used to include strong correlations among electrons of the transition metal constituents. The U parameters for Sc, Ti, V, Cr, and Mn are taken as 3.0 eV, 4.0 eV,3.0 eV, 4.0 eV and 4.0 eV, respectively, after carefully checking the literature [182, 173, 183]. To include the Van-der- Waals interactions, the DFT-D3 method was employed [147]. Plane waves up to 600 eV and a Γ-centred $8 \times 8 \times 1 (18 \times 18 \times 1)$ k-mesh for geometry optimization (electronic structure calculations) have been used. The convergence criterion for energies (forces) is set to 10^{-6} eV(0.01 eV/Å). For magnetic anisotropy energy (MAE) calculation, spin-orbit coupling (SOC) and a denser k-mesh are used along with an increased convergence criteria of 10^{-8} eV for energy. The MXene mono-layers are simulated for all calculations by considering a large vacuum of 20 Å in the perpendicular direction.

The dynamical stability of the systems considered is verified by computing their phonon dispersion relations by the supercell method as implemented in the PhonoPy package [150]. $4 \times 4 \times 1$ supercells are used to compute the phonons. The convergence criteria for energy is kept at a high value of 10^{-8} eV to achieve good convergence. For calculation of the magnetic exchange interactions , the angular momentum cutoff is taken as $l_{\mathrm{max}} = 8$, Brillouin zone integration is done by the tetrahedron method, and the convergence criterion is set to 10^{-8} for self-consistence cycles. The Matsubara frequency is set at 1500 after carefully checking the convergences. The exchange parameters obtained are then used to estimate the magnetic ordering temperature through the Classical Monte Carlo simulation (MCS) method. Calculations are performed for three ensembles in supercell of size $30 \times 30 \times 1$.Periodic boundary conditions are taken into account. At each temperature, 80,000 Monte Carlo steps are considered to achieve energy convergence.

4.3 Results and Discussions

4.3.1 Structural models and stability of functionalised MXenes

In Figure 4.1, we present the structure of monolayer MXene. Figures 4.1(a) and (c) ((b) and (d)) are the structures with ABC (ABA) stacking pattern. The difference between the two stacking types is in the alignments of the M layers with respect to each other. In the ABC stacking, the layers are not aligned. A sliding motion of one of the M layers would bring it to the ABA structure. Based upon the sites of functionalization, the

Table 4.1: Structural Models of functionalisation for ABA stacked MXenes considered in this work.

Compounds	Structural Model
Cr_2NF_2,Sc_2NO_2,Mn_2NF_2 ,Sc_2NF_2	HH
Cr_2NO_2,V_2NO_2,Ti_2NF_2,V_2NF_2,	CC

structures of M_2NT_2 can be different. In the case of usual ABC stacking, it is well known that there are three possible sites of functionalization, H, C, and T (Figure 4.1(c)). Site H is the hollow site associated with the M atom, while site C is the hollow site associated with the X atom. The site T is the one right on top of M. In ABA stacking, C and T sites are identical to those in ABC stacking. The hollow site H now is the one at the center of the hexagon consisting of M and X atoms (Figure 4.1 (b)). Consequently, for either stacking, there are four possible structural models of surface functionalization: HH, CC, HC(CH), and TT. In the HH(CC) model, functional groups on both surfaces occupy hollow site H(C), while the site occupancy pattern is mixed for the HC model. Existing results on the MXenes considered here are with ABC stacking where all of them were considered to stabilize in the HH model [173, 184, 176, 179, 185]. Therefore, we consider the 10 MXenes mentioned in Section 4.1 in ABA stacking only and calculate the total energy of each one of them in four structural models. In each case, the structural model that produces the lowest total energy is considered the structural model for that particular compound. We calculate its phonon dispersion relations to check whether a given compound is dynamically stable with the optimized structural model. In Figure 4.2, we show the phonon spectra of all 10 MXenes considered here. We find that except Mn_2NO_2 and Ti_2NO_2, all are dynamically stable in ABA stacking.The structural models of functionalization for these eight are listed in Table 4.1. We find that the compounds are evenly distributed among HH and CC models of functionalization. Since Mn_2NO_2 and Ti_2NO_2 are dynamically stable in ABC stacking only [186, 187], they are not considered for further investigation.

4.3.2 Stacking dependent magnetic and electronic ground states

In order to investigate the impact of stacking on the magnetic and electronic ground state properties of the 8 MXenes that are dynamically stable in both stacking patterns, we perform spin-polarised calculations first to determine the magnetic ground states. Four different magnetic configurations, shown in Figure 4.3, are considered for this purpose: (a) ferromagnet(FM) where all spins are aligned along the c-axis, (b) AFM1(AFM2) where antiferromagnetic alignment of spins is along c(b) axis only and (c) AFM3 where antiferromagnetic alignment of spins are along both a and b axes. Supercells of dimensions 2×2×1 have been constructed to obtain these four magnetic configurations. The magnetic ground state of a system with a particular stacking is then determined by identifying the magnetic configuration with the lowest total energy. The ground state magnetic configurations and the atomic magnetic moments are presented in Table 4.2.

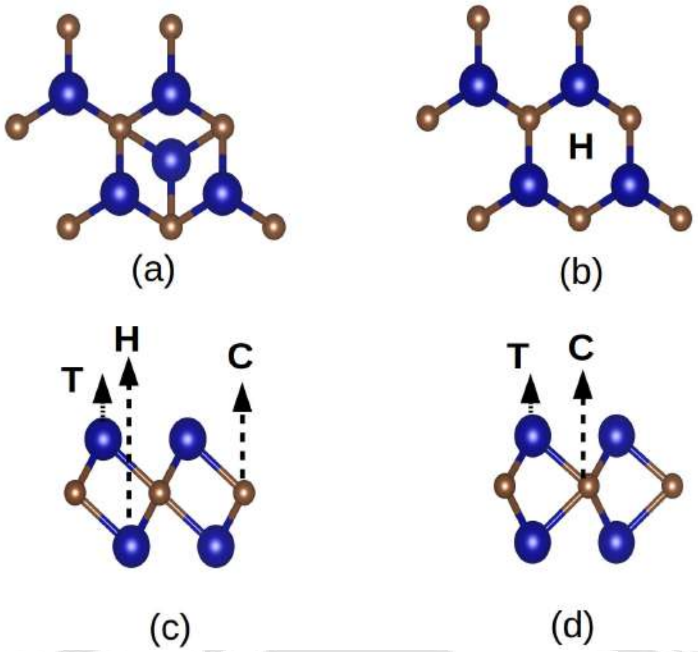

Figure 4.1: Top (a) ((b)) and side (c)((d)) view of ABC (ABA) stacked MXene, M_2X. Blue(brown) spheres are M(X) atoms.

4.3.2.1 Ground states of MXenes in ABC stacking: comparison with existing results

We first discuss our results with ABC stacking since comparison is possible with other calculations. Comparison with DFT+U calculations from Reference [173] shows that for Ti_2NF_2, V_2NF_2 and Cr_2NO_2 , magnetic ground states from our calculations exactly match with their results. The magnetic ground state of V_2NO_2 from our calculations, on the other hand, matches with that from Reference [176]. In case of Cr_2NF_2 and Mn_2NF_2, the results differ from one another. In both cases, our calculations predict AFM3 to be the ground state. The reason for the difference between our results and that of Reference [173] is due to the fact that they did not consider AFM3 as one of the possible configurations while determining the ground state. In both cases, we find that the ground state claimed in Reference [173] is the first one above ground state in our calculations. This implies that had the AFM3 configuration not been considered in our calculations, our results would have agreed with that of Reference [173] for these two compounds as well. In the case of V_2NO_2, the origin of different ground states obtained from our calculations and that of Reference [173] is their inability to obtain an AFM1 state with unequal atomic moments. On the other hand, the differences between our calculated ground state and that obtained in Reference [176] can be due to the use of different U values in the DFT+U calculations for Cr_2NF_2. Moreover, the origin of AFM1 configuration as the ground state of V_2NF_2 as reported in Reference [176] is the small energy difference ($\sim$ 4 meV/atom)between their AFM1 and AFM2 configurations. The only available DFT calculation for Sc_2NF_2 using the exact exchange HSE06 exchange-correlation functional [185] is done on a non-magnetic (NM) state. We, too, get the NM as the ground state in our total energy calculations. For Sc_2NO_2, a DFT+HSE06 calculation [184] obtains an FM ground state while we find the system to be NM. This discrepancy can be an artifact of using an exchange-correlation functional that addresses

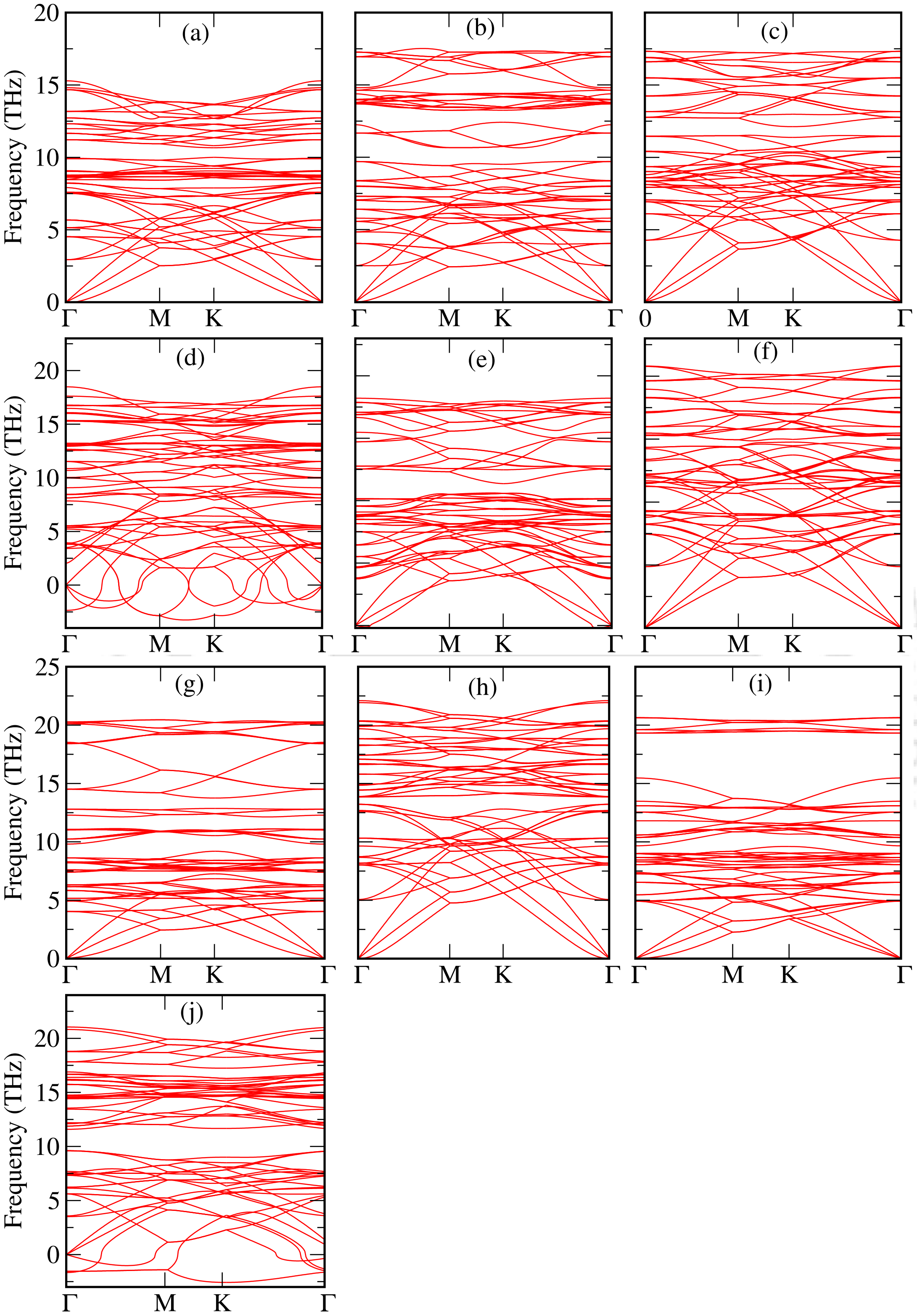

Figure 4.2: Phonon dispersion curve of (a)Sc_2NF_2 (b) Sc_2NO_2 (c) Ti_2NF_2 (d) Ti_2NO_2 (e) V_2NF_2 (f) V_2NO_2 (g) Cr_2NF_2 (h) Cr_2NO_2 (i) Mn_2NF_2 (j) Mn_2NO_2

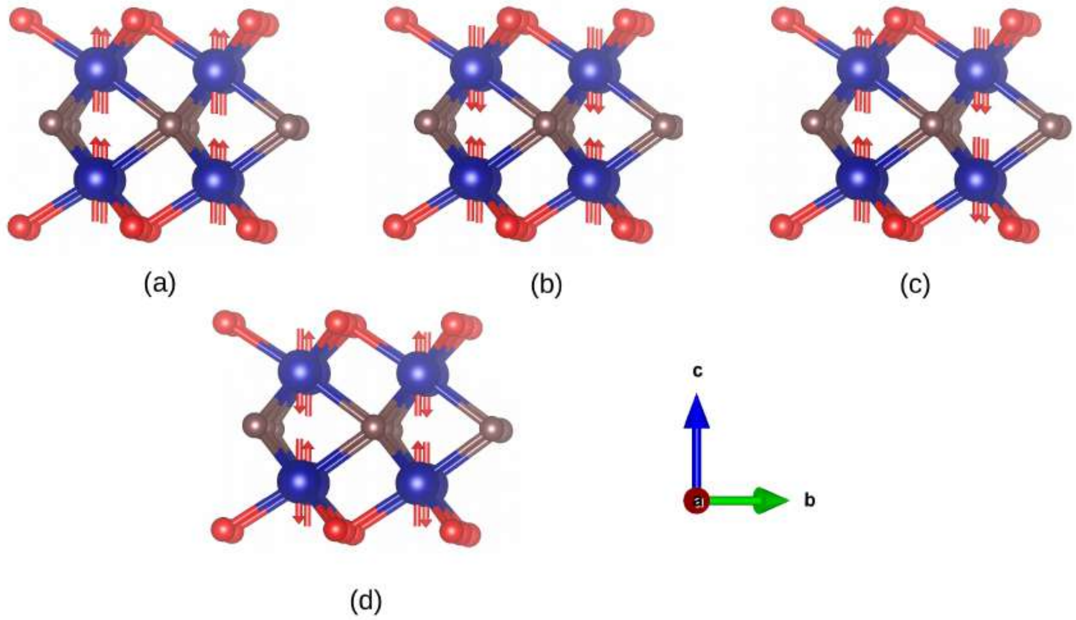

Figure 4.3: Various magnetic configurations considered in this work to find the magnetic ground state of a given MXene. (a)-(d) stand for FM, AFM1, AFM2 and AFM3 configurations, respectively. Blue, brown and red spheres are M, N and T in M_2XT_2 MXene.

the localized states of transition metals better than DFT+U. This can be inferred from the values of atomic magnetic moments in Table 4.2. In Reference [184], Sc atoms have no moment, as is the case for our calculations. The FM state obtained in their calculation is due to induced spin polarisation in the N atom. According to their calculations, a total moment of about $\sim 1\mu_B$ is due to N moment only. For the six other materials with different magnetic ground states, atomic magnetic moments obtained in our calculations have an excellent agreement with the existing DFT+U calculations [173, 176]. With regard to electronic ground states, our calculations have substantial agreement with the existing results. The electronic ground states in our calculations can be understood from the average densities of states (Figure 4.4 (b),(d),(f),(h),(j),(l),(n),(p)). We find that Ti_2NF_2,V_2NF_2, V_2NO_2 and Cr_2NF_2 are semiconductors, in agreement with Reference [176]. Among the remaining four, Sc_2NF_2, Sc_2NO_2 and Mn_2NF_2 are metals while Cr_2NO_2 is a half-metal. The electronic ground states of Sc_2NF_2 and Cr_2NO_2 agree with those obtained in Reference [185] and [173], respectively. Differences is observed in cases of Sc_2NO_2 which is a spin gapless semiconductor and Mn_2NF_2, a half metal. The reason for this difference for the former is the usage of HSE06 exchange-correlation functional induced localization in Reference [184] and consideration of FM magnetic configuration for the latter. Thus, overall, our results have substantial agreement with existing DFT-based calculations as far as magnetic ground states, magnetic moments, and electronic ground states with ABC stacking are concerned.

4.3.2.2 Comparison of properties in ABC and ABA stacking

Having established the quality of our calculations, we now investigate the effects due to changes in stacking patterns. We make a comparative analysis of properties obtained when stacking changes from ABC to ABA by first separating the eight compounds into

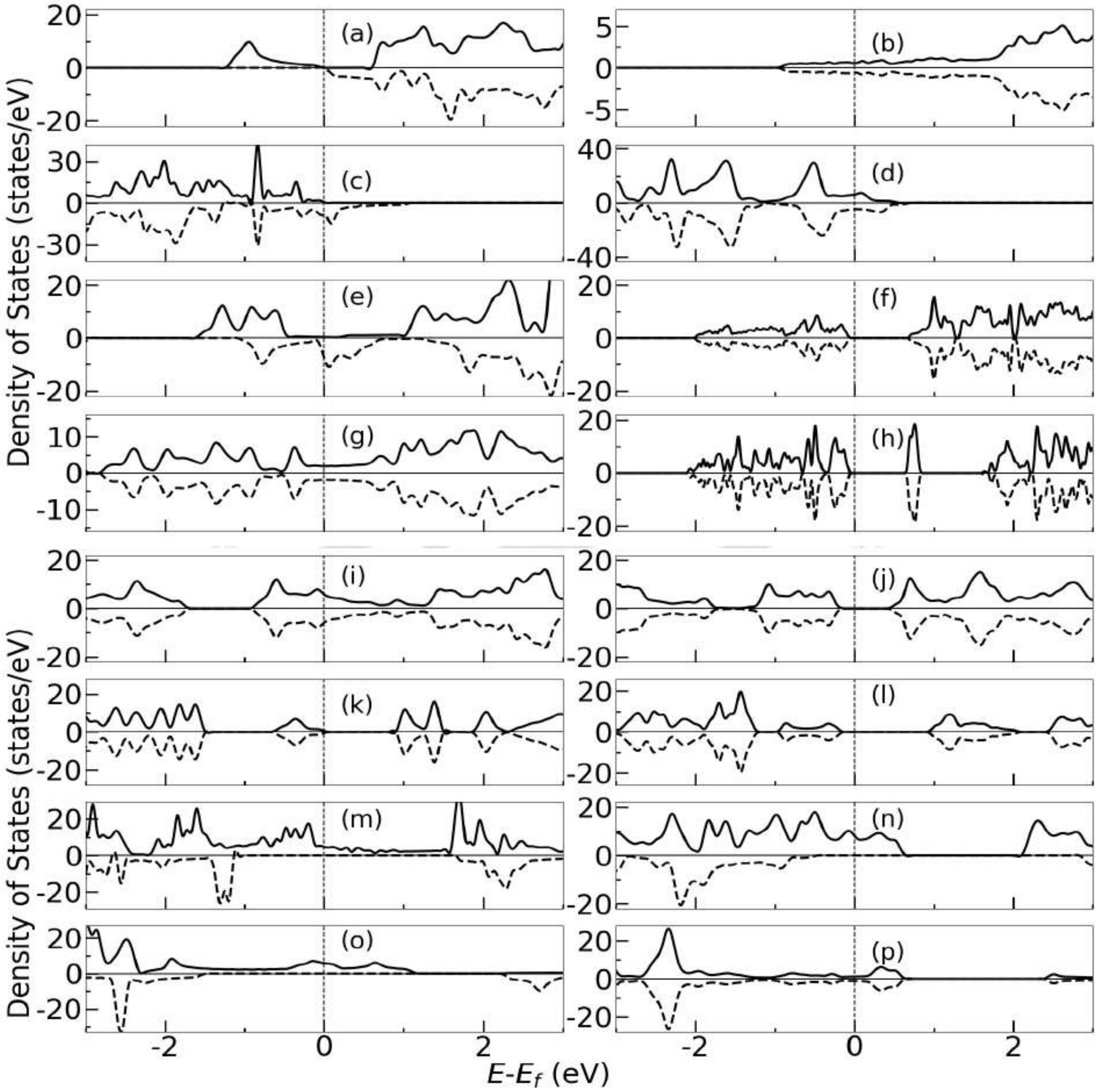

Figure 4.4: Total densities of states of ABA (left panel) and ABC (right panel) stacked MXenes Sc_2NF_2((a),(b)),Sc_2NO_2((c),(d)), Ti_2NF_2((e),(f)),V_2NF_2((g),(h)), V_2NO_2((i),(j)),Cr_2NF_2((k),(l)),Cr_2NO_2((m),(n)),Mn_2NF_2((o),(p))

two groups according to their structural models of functionalization (Table 4.1). Sc_2NF_2, Sc_2NO_2, Cr_2NF_2 and Mn_2NF_2 are the four MXenes that stabilize in the same structural model HH when the stacking pattern changes. Inspecting Table 4.2, we find that in all four cases, the magnetic ground state changes upon changing the stacking from ABC to ABA. The NM ground states in ABC stacking change to FM ones for both Sc_2NT_2 MXenes. In case of the other two, AFM3 ground states in ABC change to FM(for Mn_2NF_2) and AFM1(for Cr_2NF_2). In these two compounds, the magnetic moments of the transition metal constituents undergo insignificant changes. Significant changes in the electronic ground states are observed as stacking changes. In the ABA stacking, Sc_2NF_2 is a spin gapless semiconductor (Figure 4.4(a)) with total magnetic moment $1\mu_B$ while Mn_2NF_2 is a half-metal (Figure 4.4(o))with a total moment of $9\mu_B$. On the other hand, upon stacking

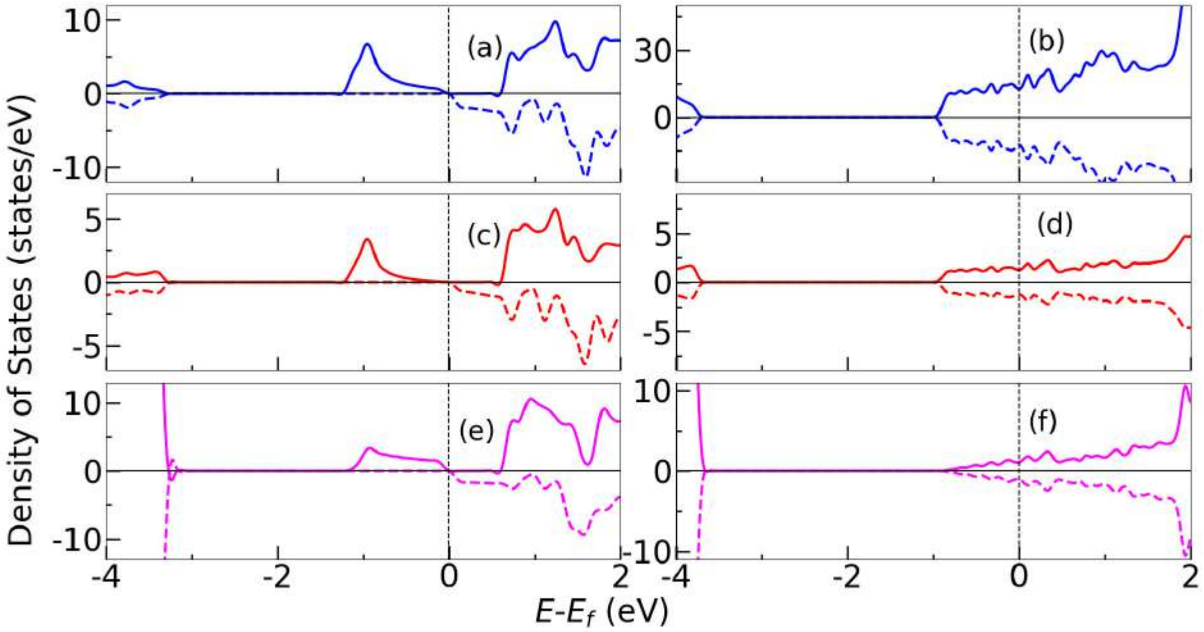

Figure 4.5: Atom resolved spin polarised densities of states of ABA stacked (left panel) and ABC stacked (right panel) Sc_2NF_2 .(a,b), (c,d) and (e,f) are the densities of states of Sc, F and N, respectively.

change, Sc_2NO_2 becomes a near half-metal (Figure 4.4(c))with near integer total moment of $0.9\mu_B$. The electronic ground state of Cr_2NF_2 remains semiconducting upon change in stacking. More robustness of magnetic and electronic ground states are observed in some of the four remaining MXenes, Ti_2NF_2,V_2NF_2, V_2NO_2 and Cr_2NO_2 that stabilize in CC configurations when the stacking pattern is ABA. V_2NF_2 and Cr_2NO_2 have the same magnetic ground states as those found in ABC stacking; the total and transition metal atomic magnetic moments in the later case remain completely unchanged. The electronic ground state of Cr_2NO_2 remains a half-metal too (Figure 4.4(m,n)). The electronic ground states of V_2NT_2 and Ti_2NF_2 change from semiconductor to metallic and near half-metal, respectively (Figure 4.4(e),(g),(i)). The atomic magnetic moments in these compounds change substantially when the stacking changes from ABC to ABA.

4.3.2.3 Understanding changes in magnetic moments and electronic ground states, with stacking

The magnetic and electronic properties of the MXenes can be analyzed from the splitting of d-orbitals due to the crystal fields of the anions, their subsequent arrangements, and filling based upon associated local symmetry. In the case of compounds conforming to the HH structural model, the local D_{3d} crystal field splits d-levels of M atoms of M_2NT_2 into doubly degenerate $e_1(d_{xz}, d_{yz})$, single $a_1(d_{z^2})$ and doubly degenerate $e_2(d_{x^2-y^2}, d_{xy})$ in ascending order of energy. The stacking is not supposed to matter as long as the compounds adhere to the same structural model leading to the same local symmetry around M. We find this is indeed true for Cr_2NF_2 and Mn_2NF_2. The unequal magnetic moment on two inequivalent Cr atoms can be explained in the following way: each Cr donates 1 electron to N and 1 to the F attached to its surface. Since N requires another electron, one of the Cr has to donate from its share. In this case, it is Cr^{II}. As a result,

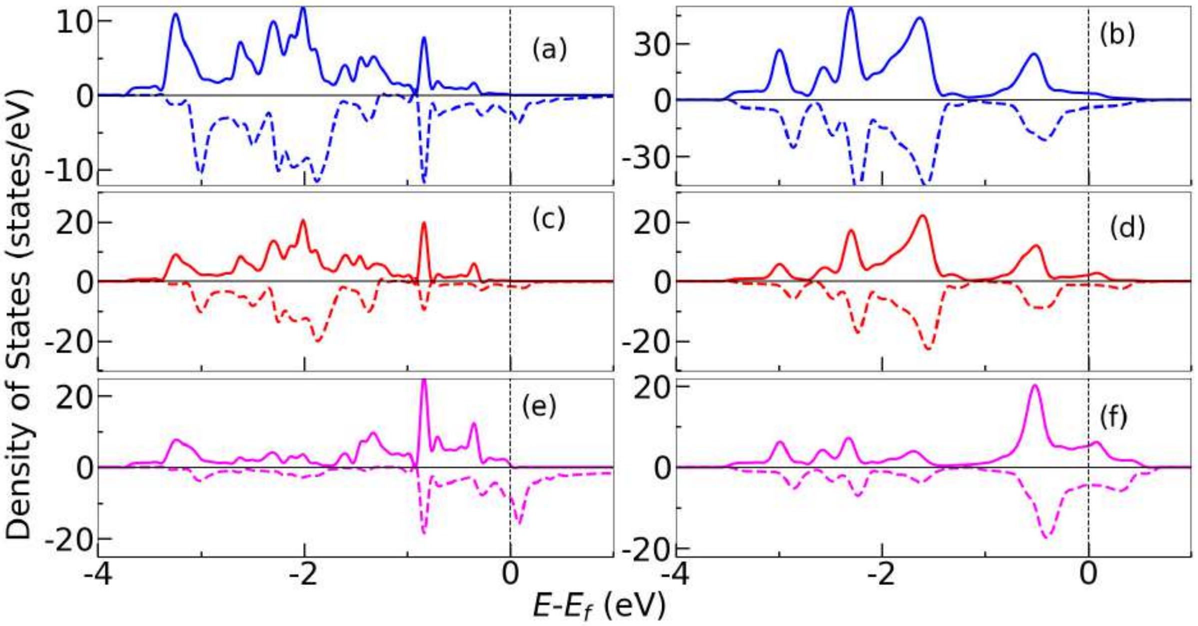

Figure 4.6: Atom resolved spin polarised densities of states of ABA stacked (left panel) and ABC stacked (right panel) Sc_2NO_2.(a,b), (c,d) and (e,f) are the densities of states of Sc, O and N, respectively.

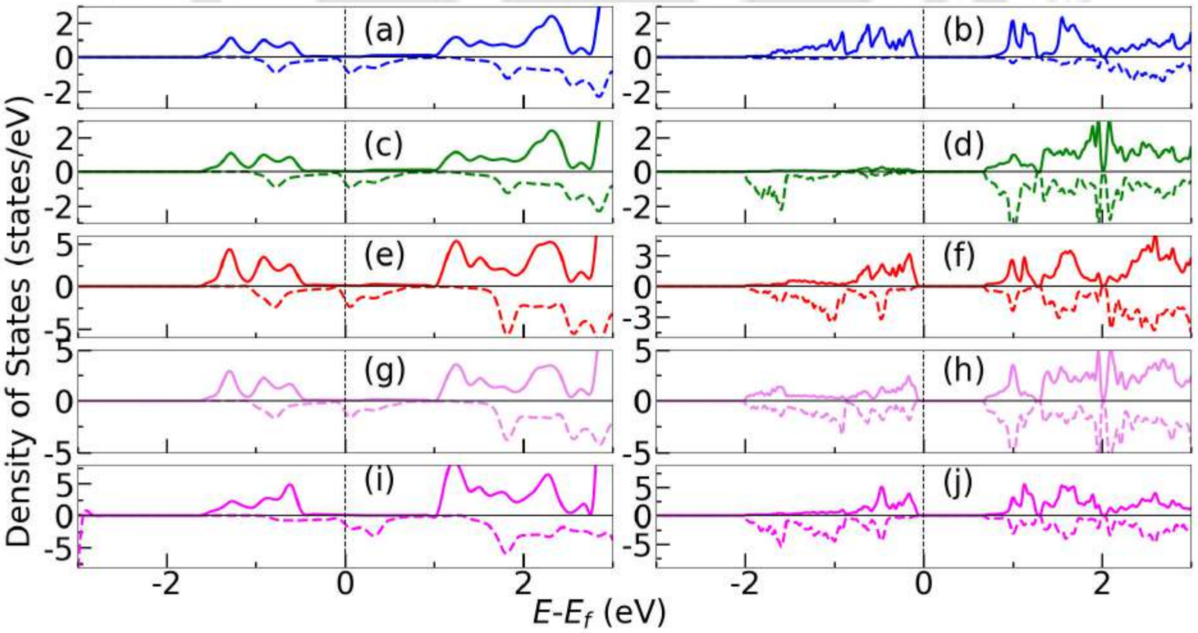

Figure 4.7: Atom resolved densities of states of ABA stacked (left panel) and ABC stacked (right panel) Ti_2NF_2. (a and b), (c and d), (e and f), (g and h) and (i and j) are the densities of states of Ti^I, Ti^{II},F^I,F^{II} and N, respectively. F^I and F^{II} are fluorene atoms associated with Ti^I and Ti^{II}

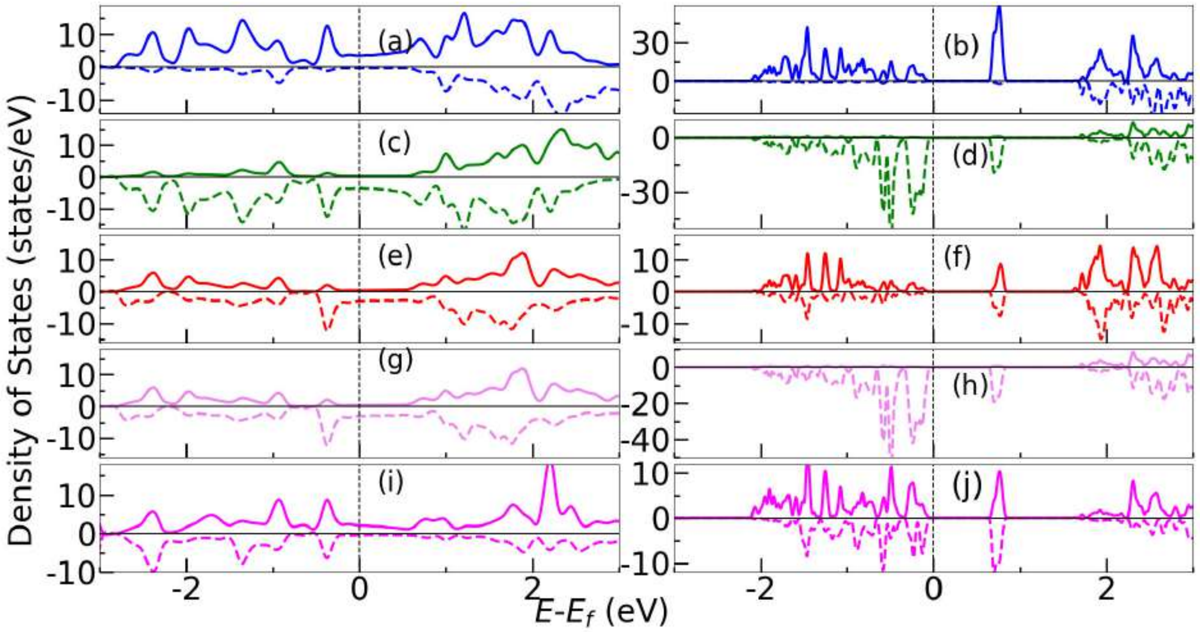

Figure 4.8: Atom resolved densities of states of ABA stacked (left panel) and ABC stacked (right panel) V_2NF_2.(a and b), (c and d), (e and f), (g and h) and (i and j) are the densities of states of V^I, V^{II},F^I,F^{II} and N, respectively. F^I and F^{II} are fluorene atoms associated with V^I and V^{II}

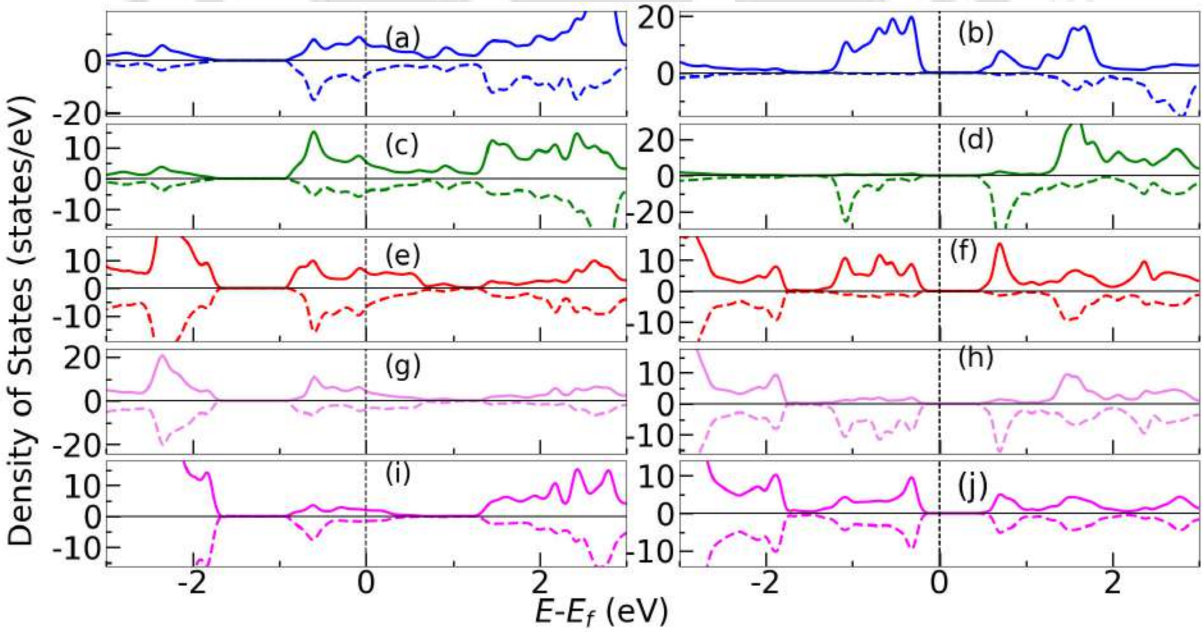

Figure 4.9: Atom resolved densities of states of ABA stacked (left panel) and ABC stacked (right panel) V_2NO_2.(a and b), (c and d), (e and f), (g and h) and (i and j) are the densities of states of V^I, V^{II},O^I,O^{II} and N, respectively. $O^I$and O^{II} are fluorene atoms associated with V^I and V^{II}

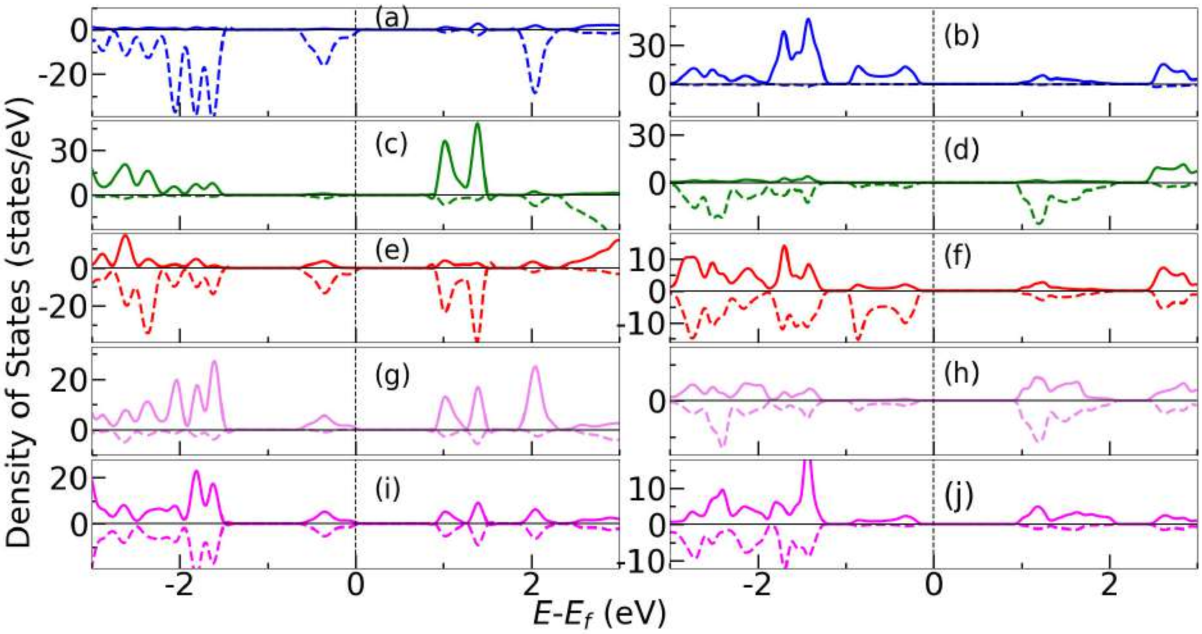

Figure 4.10: Atom resolved densities of states of ABA stacked (left panel) and ABC stacked (right panel) Cr_2NF_2.(a and b), (c and d), (e and f), (g and h) and (i and j) are the densities of states of Cr^I, Cr^{II},F^I,F^{II} and N, respectively. F^I and F^{II} are fluorene atoms associated with Cr^I and Cr^{II}

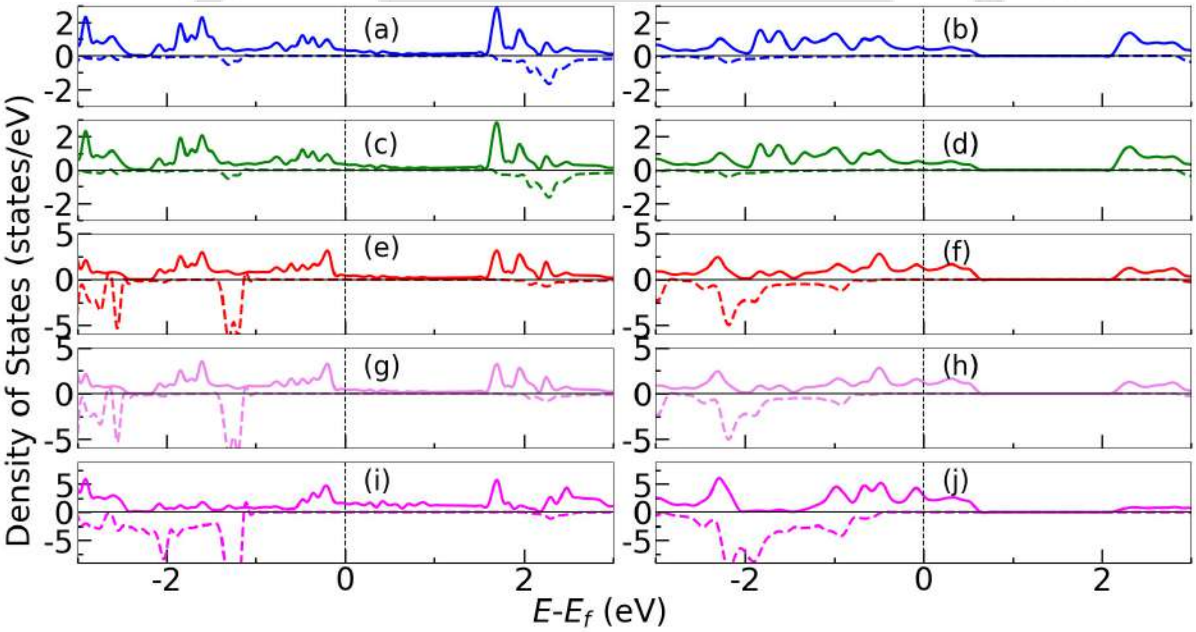

Figure 4.11: Atom resolved densities of states of ABA stacked (left panel) and ABC stacked (right panel) Cr_2NO_2.(a and b), (c and d), (e and f), (g and h) and (i and j) are the densities of states of Cr^I, Cr^{II},O^I,O^{II} and N, respectively. O^I and O^{II} are fluorene atoms associated with Cr^I and Cr^{II}

ideally $Cr^I(Cr^{II})$ should have a magnetic moment of $4(3)\mu_B$ per atom. From Table 4.2, we find that the calculated values (in either stacking) are close to these. For a given spin band, the arrangement of electrons among d bands of Cr^I (Cr^{II})should be $e_1^2a_1^1e_2^1(e_1^2a_1^1e_2^0)$.

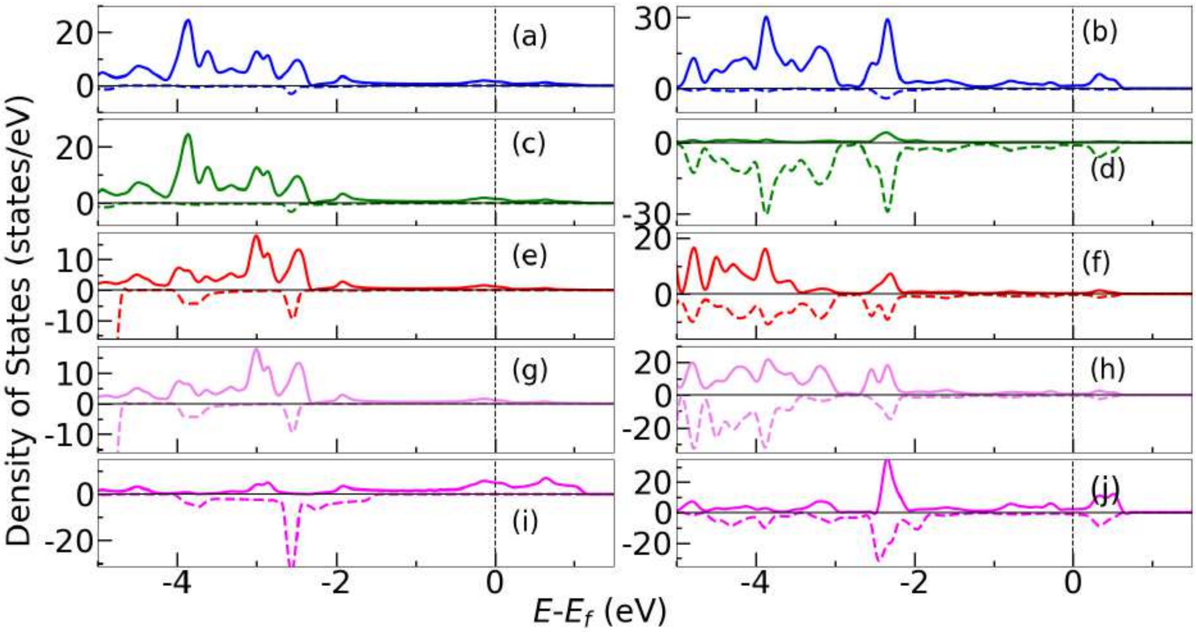

Figure 4.12: Atom resolved densities of states of ABA stacked (left panel) and ABC stacked (right panel) Mn_2NF_2.(a and b), (c and d), (e and f), (g and h) and (i and j) are the densities of states of Mn^I, Mn^{II},F^I,F^{II} and N, respectively. F^I and F^{II} are fluorene atoms associated with Mn^I and Mn^{II}

Table 4.2: Magnetic properties of the 8 MXenes in both stacking patterns. M^I and M^{II} are the magnetic moments (in μ_B/atom) of two non-equivalent transition metal atoms. M^N is the magnetic moment of the Nitrogen atom. T_C/T_N is the magnetic transition temperature in K. MAE is the magnetic anisotropy energy per unit cell in μeV.

Compound	Stacking Type	Magnetic Ground State	M^I	M^{II}	M^N	T_C/T_N	MAE
Sc_2NF_2	ABA ABC	FM NM	0.44 0	0.44 0	0.05 0	16 -	-2.28 -
Sc_2NO_2	ABA ABC	FM NM (FM[184])	0 0	0 0	0.56 0.03 (1.0[184])	30 -	23.80 -
Ti_2NF_2	ABA ABC	FM AFM2 (AFM2[173])	0.40 1.3 (1.3[173])	0.40 1.0 (1.0[173])	0.04 0.02	35 50	19.38 -4.76
V_2NF_2	ABA ABC	AFM2 AFM2 (AFM2[173], AFM1[176])	1.78 2.4 (2.5[173], 2.7[176])	1.78 2.0 (2.0[173], 2.1[176])	0.07 0.01	350 90	-148.40 1.5
V_2NO_2	ABA ABC	AFM2 AFM1 (AFM2[173], AFM1[176])	0.50 1.75 (1.8[173], 1.9[176])	0.50 1.11 (1.0[173], 1.2[176])	0.03 0.00	45 60	6.4 -55.5
Cr_2NF_2	ABA ABC	AFM1 AFM3 (AFM2[173], AFM1[176])	3.70 3.65 (3.7[173], 3.9[176])	3.10 3.11 (3.0[173], 3.1[176])	0.07 0.0	50 60	148.50 -48.51
Cr_2NO_2	ABA ABC	FM FM (FM[173])	2.91 2.87 (2.8[173])	2.91 2.87 (2.8[173])	0.45 0.23	90 200	-166.40 36.95
Mn_2NF_2	ABA ABC	FM AFM3 (AFM1[173])	4.50 4.5 (4.5[173])	4.50 4.5 (4.5[173])	0.37 0.05	50 60	-13.50 19.87

That the two Cr atoms are inequivalent with regard to their oxidation states can be understood from their atom projected densities of states in Figure 4.10 for both stacking types. By comparing the densities of states of Cr^I (Figure 4.10 (b)) and Cr^{II} (Figure 4.10 (d)), we find that while one spin band in Cr^I is completely empty, the other is nearly full. It is not so for Cr^{II}. The same features are observed in ABA stacking (Figure 4.10 (a),(c)). In Figures 4.21 and 4.22 we show the densities of states associated with different *d*-orbitals of Cr^I and Cr^{II} respectively. As mentioned above, we find the a_1 orbitals for one-spin is completely full while other two orbitals are nearly full for Cr^I. Significant

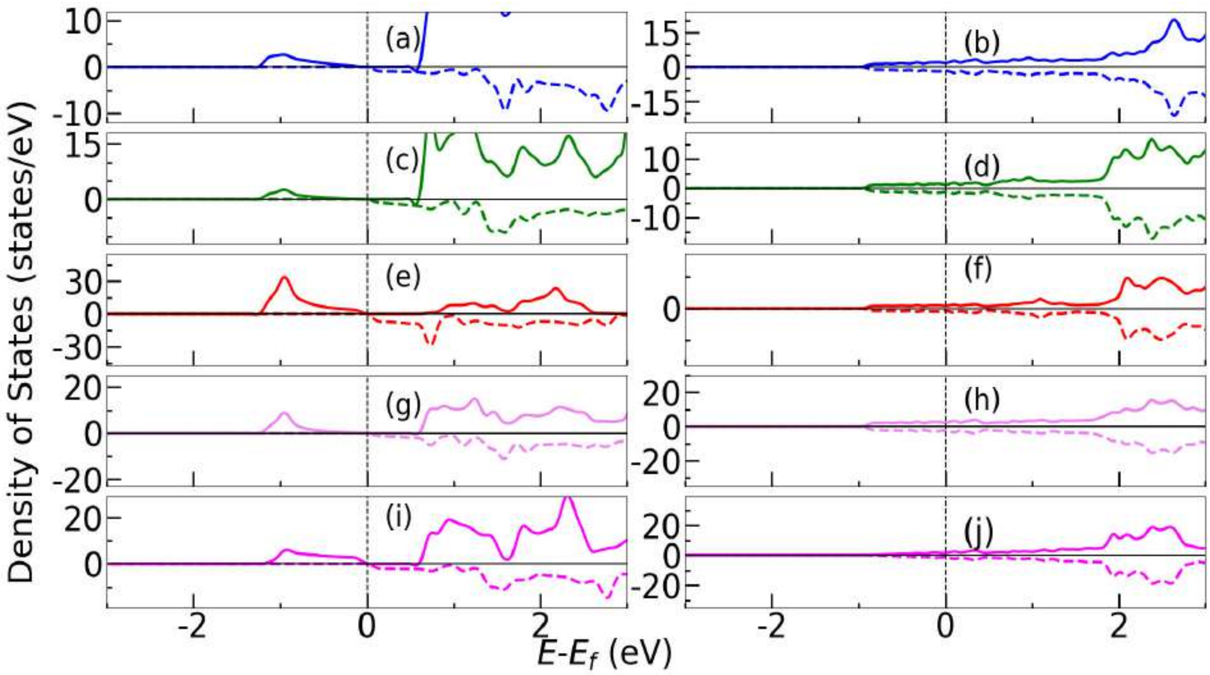

Figure 4.13: Densities of states of e_2 (a and b), e_1(c and d), a_1 (e and f) orbitals of Sc along with F (g and h) and N (i and j) of Sc_2NF_2.The left panel is for ABA and right panel is for ABC.

electronic re-distribution happens between e_1 and e_2 due to hybridizations with N and F states. In the case of Cr^{II}, e states lie deeper in energy, signifying the deficit of an electron as compared to Cr^{I}. In case of Mn_2NF_2, two Mn atoms have identical magnetic moment of 4.5 μ_B, irrespective of the stacking pattern. In this compound, one of the Mn should have 5 electrons while the other should have 4 electrons after donating to the F and N atoms. This should lead to unequal moments of 5 μ_B and 4 μ_B. However, upon inspecting the atom-projected densities of states (Figure 4.12) and Mn d-orbital-projected densities of states (Figure 4.24), we find that contributions of both Mn are identical, with one of the spin bands near full. Like Cr_2NF_2, the a_1 states are full while the e orbitals are near full. Compared to the ABC stacking, in ABA stacking, the states are pushed towards lower energies. The departure of Mn moments from integer values is due to the re-distribution of electrons among the d-orbitals as a consequence of strong hybridizations with anions. The delocalized states of F and N, particularly in ABC stacking, suggest significant hybridization.

The picture is very different in case of Sc_2NF_2 and Sc_2NO_2. Figures 4.5, 4.6, 4.13, and 4.14 show that the exchange splitting in these compounds in ABC stacking is weak, leading to an NM ground state. Sc has a valence electron configuration of $4s^2 3d^1$. In Sc_2NF_2, after donating 5 electrons to N and two F atoms, there is one extra electron in the system. In ABA stacking, this is shared by the two Sc atoms, leading to an equal amount of magnetic moment on them. Change in stacking from ABC to ABA enhances the exchange splitting. The Sc-N bond lengths increase by 2% , localizing the unpaired electron. This splits the majority band with a gap right at the Fermi level. The minority band states near the Fermi level in ABC now move to the unoccupied part of the energy spectra. The orbital-projected densities of states show that the peak in the majority band around -1 eV in ABA has contributions from all three d-orbitals(Figure

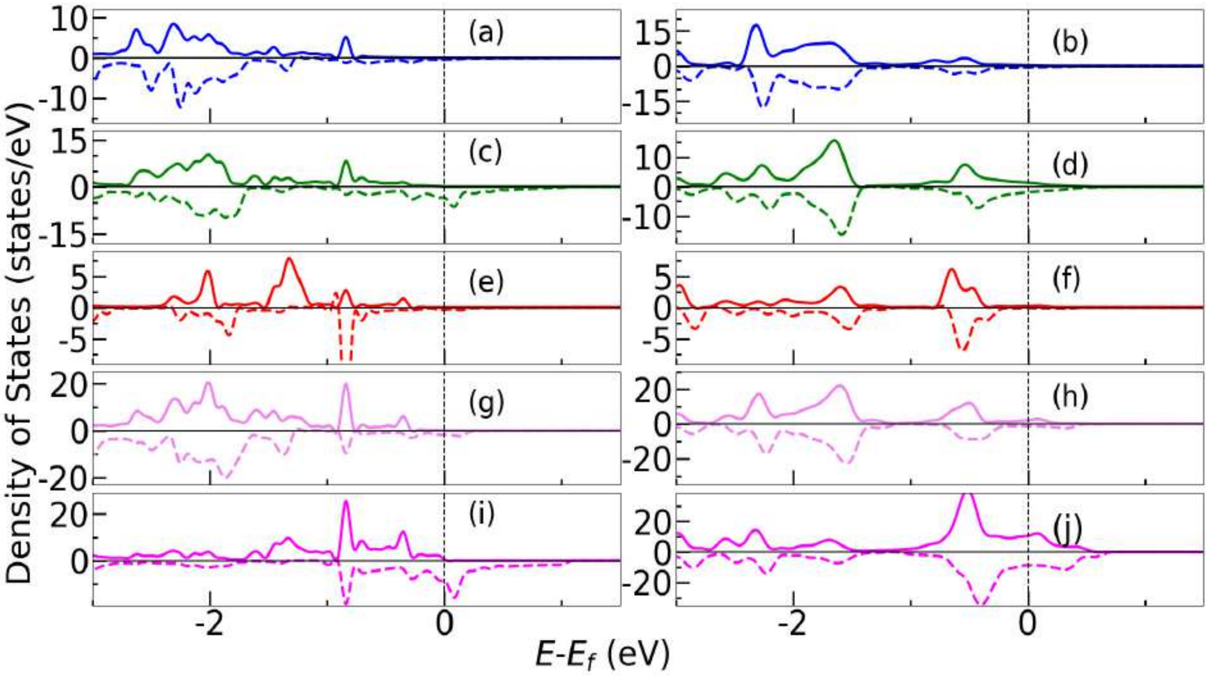

Figure 4.14: Densities of states of e_2 (a and b), e_1(c and d), a_1 (e and f) orbitals of Sc along with O (g and h) and N (i and j) of Sc_2NO_2.The left panel is for ABA and right panel is for ABC.

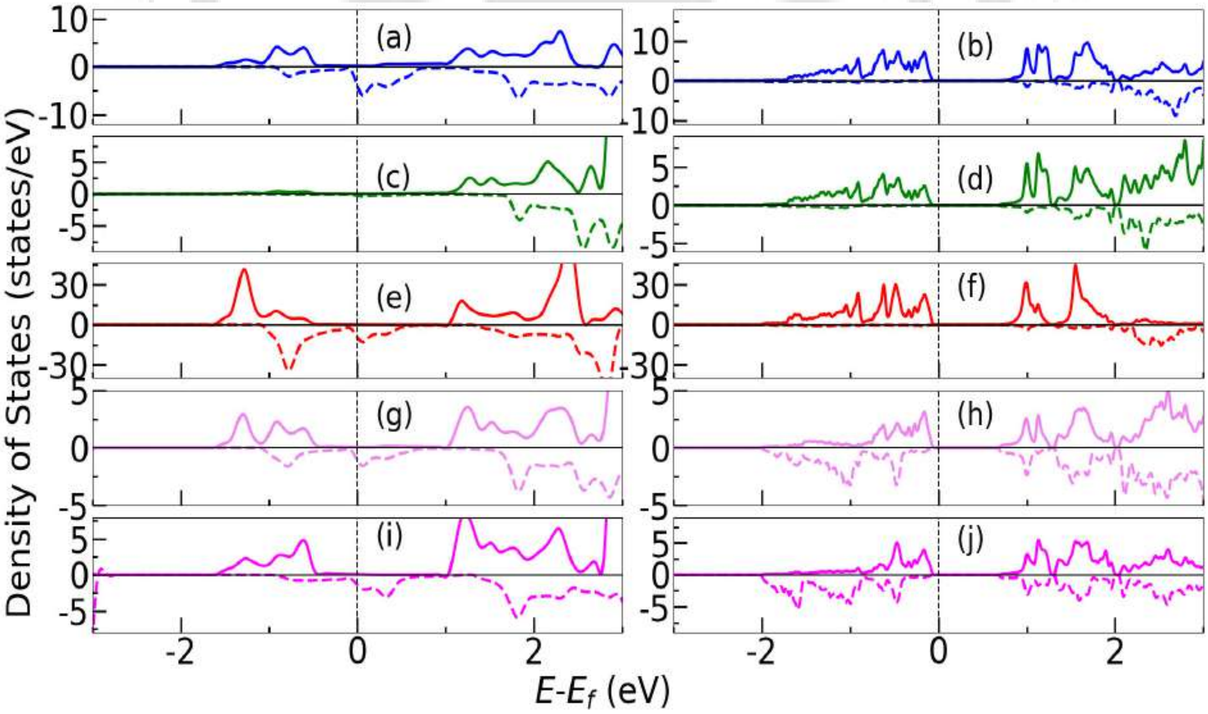

Figure 4.15: Densities of states of e_2 (a and b), e_1(c and d), a_1 (e and f) orbitals of Ti^I along with F (g and h) and N (i and j) of Ti_2NF_2.The left panel is for ABA and right panel is for ABC.

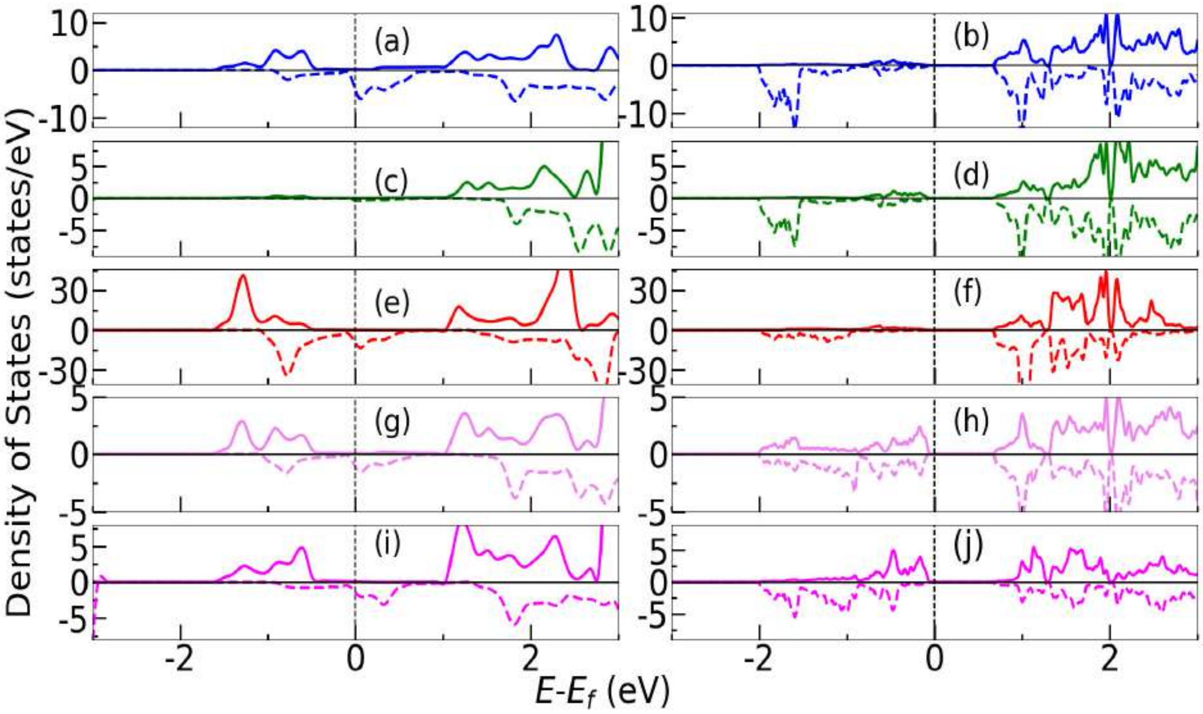

Figure 4.16: Densities of states of e_2 (a and b), e_1(c and d), a_1 (e and f) orbitals of Ti^{II} along with F (g and h) and N (i and j) of Ti$_2$NF$_2$.The left panel is for ABA and right panel is for ABC.

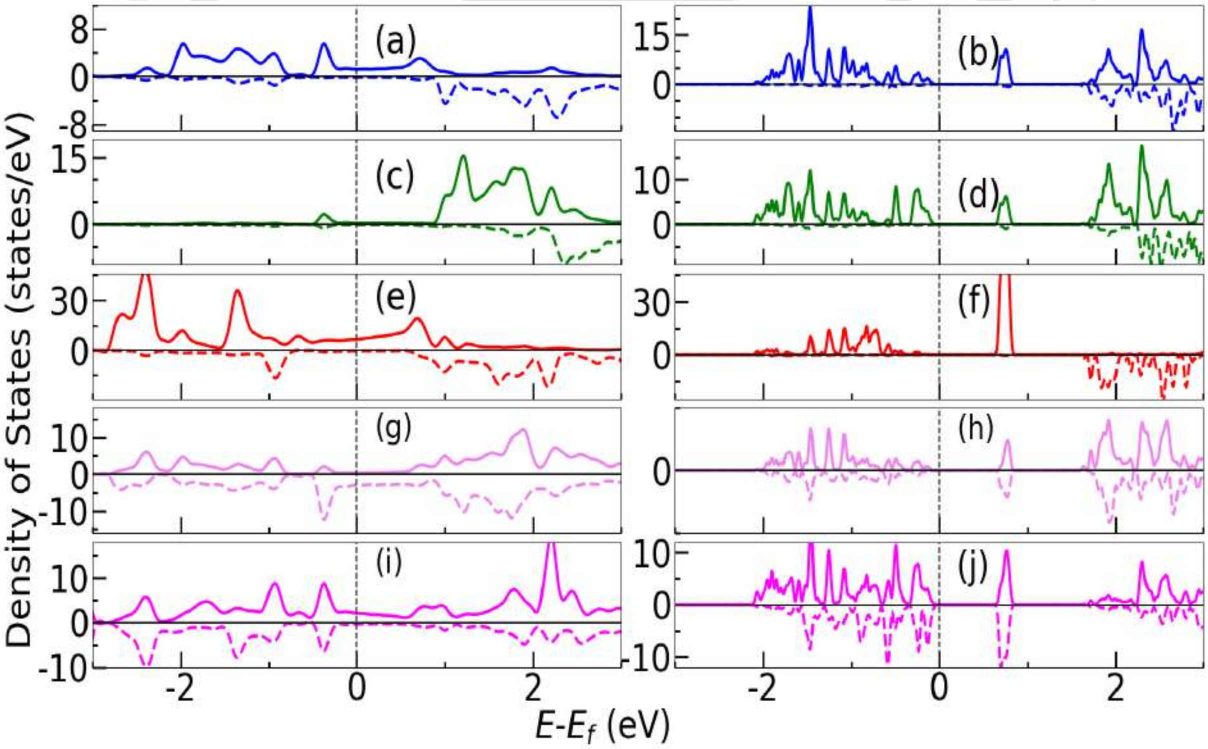

Figure 4.17: Densities of states of e_2 (a and b), e_1(c and d), a_1 (e and f) orbitals of V^I along with F (g and h) and N (i and j) of V$_2$NF$_2$.The left panel is for ABA and right panel is for ABC.

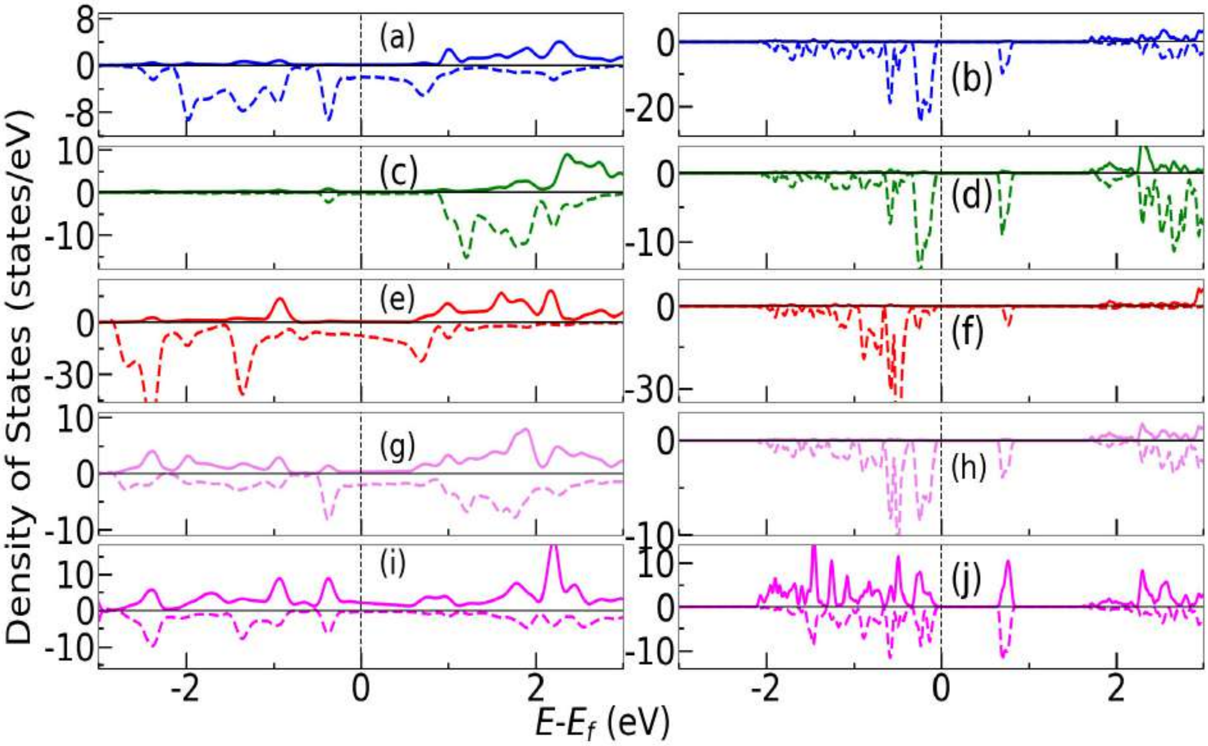

Figure 4.18: Densities of states of e_2 (a and b), e_1(c and d), a_1 (e and f) orbitals of V^{II} along with F (g and h) and N (i and j) of V_2NF_2.The left panel is for ABA and right panel is for ABC.

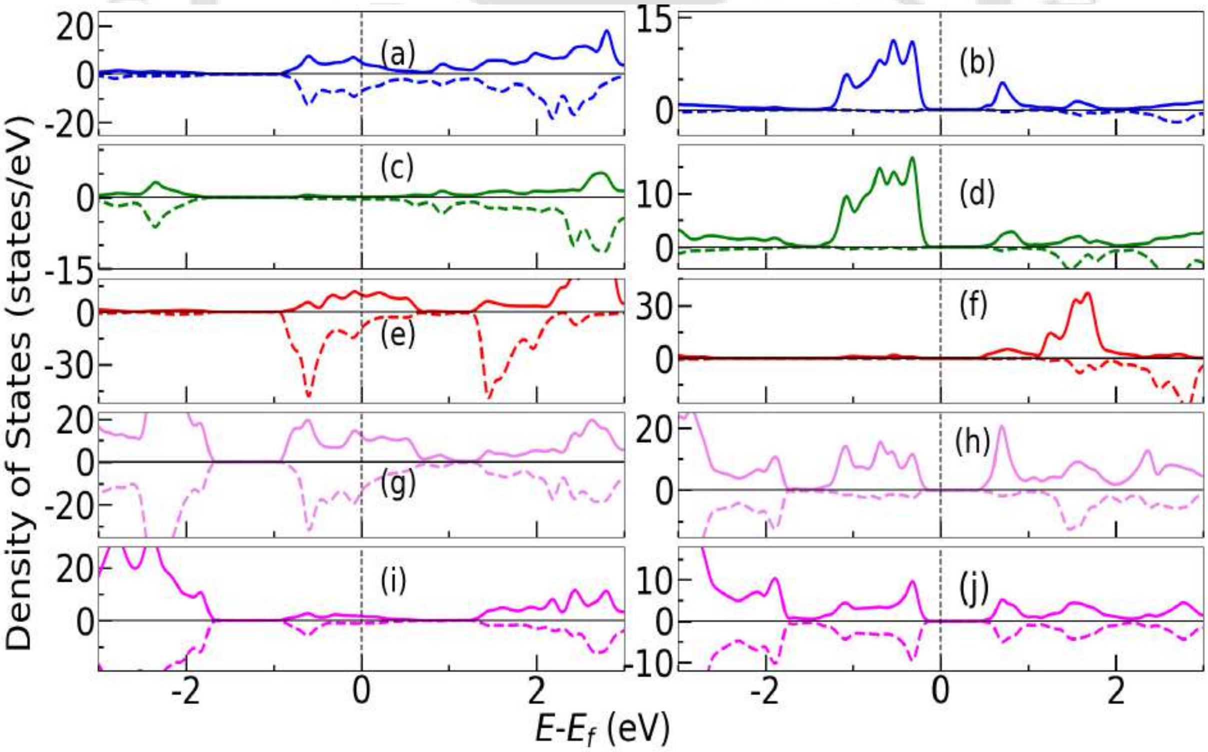

Figure 4.19: Densities of states of e_2 (a and b), e_1(c and d), a_1 (e and f) orbitals of V^{I} along with O (g and h) and N (i and j) of V_2NO_2.The left panel is for ABA and right panel is for ABC.

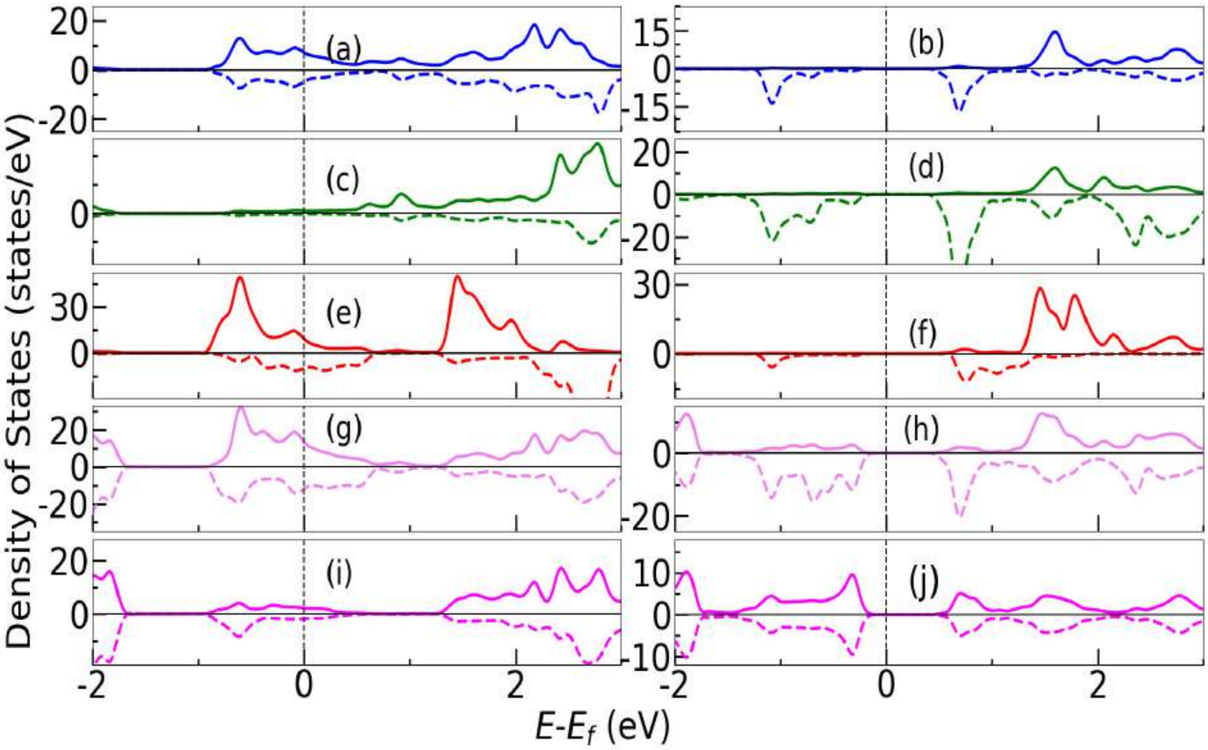

Figure 4.20: Densities of states of e_2 (a and b), e_1(c and d), a_1 (e and f) orbitals of V^{II} along with O (g and h) and N (i and j) of V_2NO_2.The left panel is for ABA and right panel is for ABC.

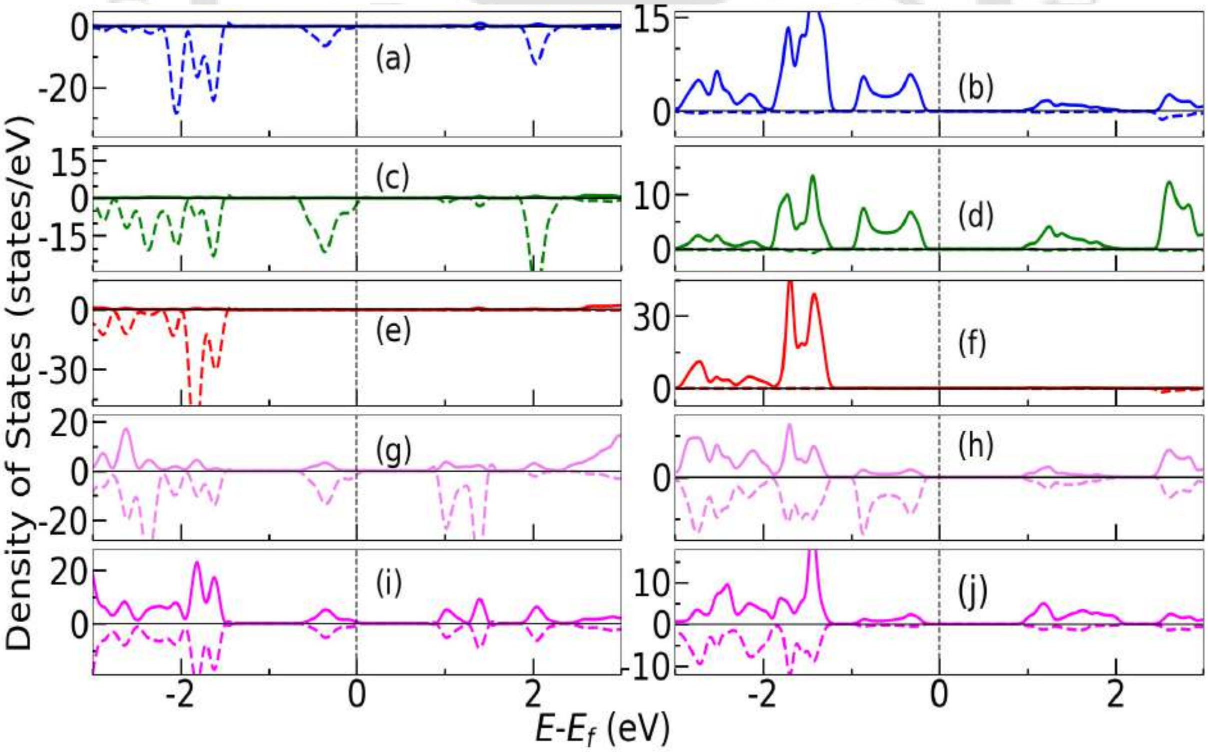

Figure 4.21: Densities of states of e_2 (a and b), e_1(c and d), a_1 (e and f) orbitals of Cr^{I} along with F (g and h) and N (i and j) of Cr_2NF_2.The left panel is for ABA and right panel is for ABC.

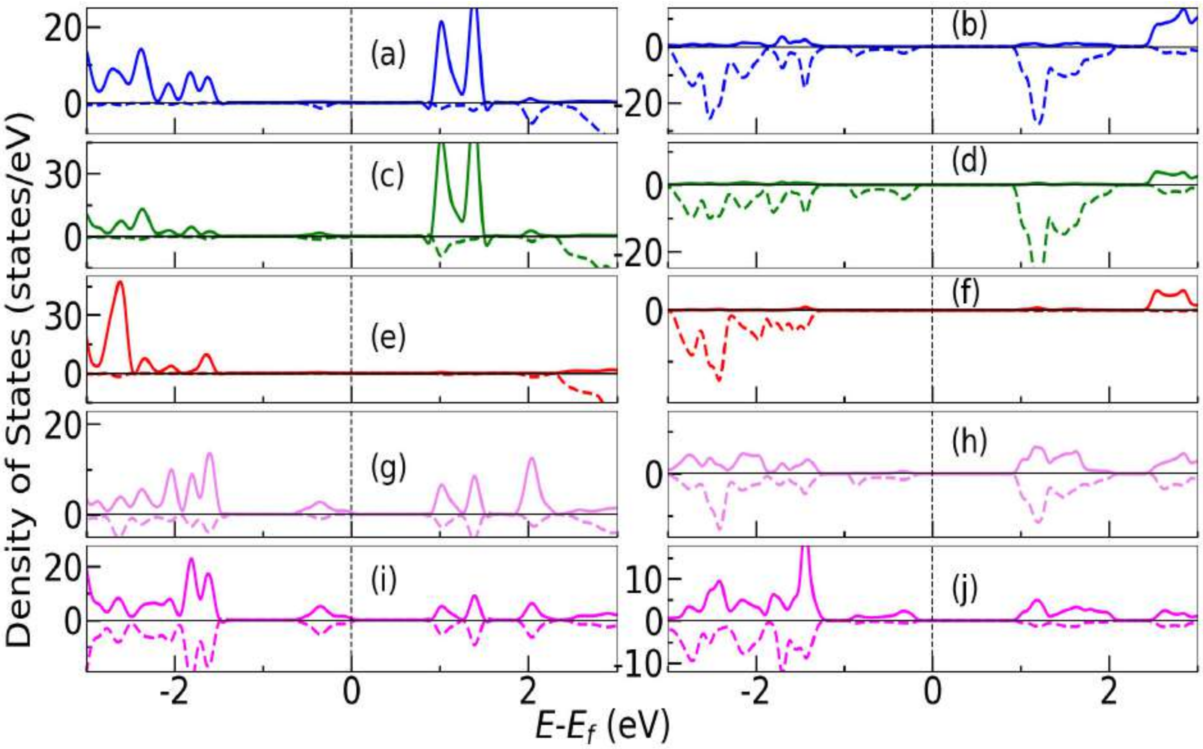

Figure 4.22: Densities of states ofee_2 (a and b), e_1(c and d), a_1 (e and f) orbitals of Cr^{II} along with F (g and h) and N (i and j) of Cr_2NF_2.The left panel is for ABA and right panel is for ABC.

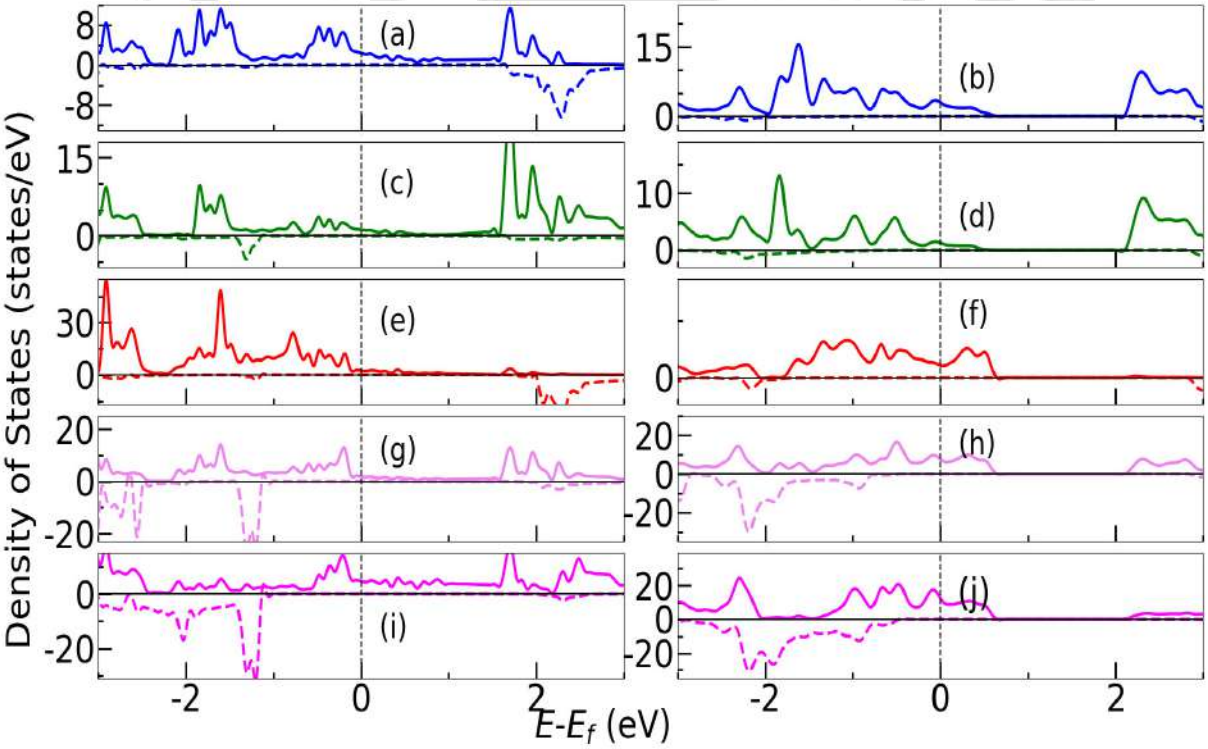

Figure 4.23: Densities of states of e_2 (a and b), e_1(c and d), a_1 (e and f) orbitals of Cr along with O (g and h) and N (i and j) of Cr_2NO_2.The left panel is for ABA and right panel is for ABC.

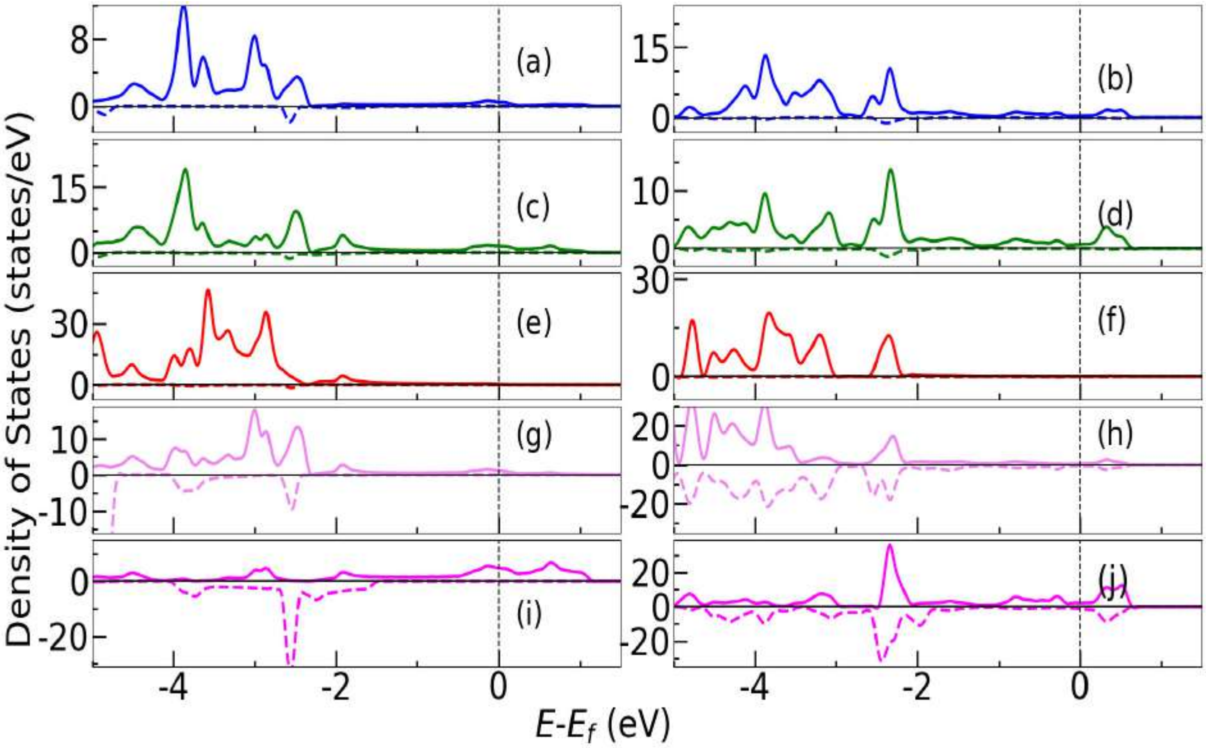

Figure 4.24: Densities of states of e_2 (a and b), e_1(c and d), a_1 (e and f) orbitals of Mn along with F (g and h) and N (i and j) of Mn_2NF_2.The left panel is for ABA and right panel is for ABC.

4.13 (a),(c),(e)). Sc_2NO_2, on the other hand does not have any unpaired d electron left in the system. It rather has an unpaired N electron. In ABC stacking, the Sc bands of both spins are thus fully occupied, leading to an NM state. In ABA stacking, Sc atoms do not contribute to the magnetic moment. The unpaired N leads to a spin polarisation in N with a net magnetic moment. Subsequently, the ground state magnetic structure in these two compounds in ABA stacking is FM. The remaining four MXenes stabilize in the CC structural model in ABA stacking. Except Cr_2NO_2, the atomic magnetic moments in the other three compounds, Ti_2NF_2, V_2NF_2 and V_2NO_2, change considerably with change in stacking. In the CC structural model, the local crystal field symmetry surrounding the transition metal atoms is trigonal C_{3v}. In this case, the d orbitals split into a_1, e_1 and e_2 in the ascending order of energy. The changes in the atomic magnetic moments can be understood accordingly. To do this, we first consider Cr_2NO_2 where the two Cr atoms are equivalent. Each Cr donates 2 electrons to the corresponding O atom and 1 to the N atom out of its six valence electrons. Thus, each Cr atom is left with three unpaired electrons. However, N requires one more electron, which is contributed by both Cr, resulting in a magnetic moment of 5 μ_B for the system. The electron sharing between the cations and anions is strong, resulting in polarisations in N and O atoms in either stacking. This is evident from the atom-projected densities of states (Figure 4.11). In ABC stacking, the exchange splitting in the anions is nearly equal, while in ABA stacking, exchange splitting in N is greater than O, as is seen in Figure 4.11, (i). In the ABA stacking, the N majority states deplete in the energy range -1.0 to -3.0 eV when compared with O densities of states. The arrangement of electrons in various d orbitals can be understood from the orbital-projected densities of states (Figure 4.23). In ABC stacking, we can see that the minority spin band of Cr is nearly empty. The electrons are distributed among the three orbitals, and none of them are fully occupied. There is significant hybridization between the majority states of Cr a_1 and p orbitals of the O and N. In the ABA stacking, the lowest-lying a_1 majority band is full, and the minority band is empty. This is not so with the higher-lying e orbitals. As such, there is little difference in the overall filling of electrons in energy levels when the stacking changes. Large differences in the atomic magnetic moments of the transition metal atoms as the stacking changes are observed for Ti_2NF_2 and V_2NO_2. In the case of Ti_2NF_2, each Ti donates 1 electron to F and 1 to N from its four valence electrons. From the remaining total of 4 electrons among them, 1 electron is to be donated to N. Ideally, one of the Ti should have a magnetic moment of $2\mu_B$ while the other should have a moment of $1\mu_B$. In the ABC stacking, we find the inequivalent Ti atoms; Ti^I is having a moment of 1.3 μ_B and Ti^{II} of $1\mu_B$. Once again, the atom projected densities of states (Figure 4.7 (b),(d),(f),(h),(j)) suggests that only one of the spin bands of each Ti atom is partially full while the other one is either completely (in case of Ti^I) or near completely (in case of Ti^{II}) empty. The variations in the exchange splitting due to this are responsible for unequal magnetic moments of Ti. Upon inspecting the orbital-projected densities of states (Figure 4.15-4.16, (b),(d),(f)), we find that the major difference among Ti^I and Ti^{II} is that in the latter case the a_1 orbitals of both spin bands are almost empty. The e states for Ti^I are spread out up to nearly -2 eV, while those of Ti^{II} are more localized near -2 eV. There is significant hybridization leading to electron sharing among Ti^I and the anions, as the contributions from all of them happening in the same energy window. Different sequences of d-orbital levels and subsequent filling are responsible for the substantial reduction of Ti moments in ABA stacking (Figure 4.7 (a),(c),(e),(f),(g) and 4.15-4.16 (a),(c),and(e)). Here, the lowest lying a orbitals of both spins are partially filled, the e_1 is completely empty, and e_2 has partial filing in both spin bands. The smaller exchange splittings, thus, reduce the Ti moments in ABA stacking. V_2NO_2 has identical situation. Atomic magnetic moments and their changes with stacking change, too, can be understood in a similar way (Figures 4.9, 4.19-4.20). In the case of V_2NF_2, though the changes in magnetic moments with stacking are not as large as observed in these two compounds, they are substantial. The five unpaired V electrons are distributed asymmetrically among two V atoms, making them non-equivalent with respect to magnetic moments in ABC stacking. Strong cation-anion hybridization and localized states are the prominent features of the electronic structure of this compound in ABC stacking (Figure 4.8, 4.17-4.18 (b),(d),(f),(h),(j)). The split d-levels have one spin band empty, and each one of the other spin is partially filled. In ABA stacking, the states are less localized. The minority spin bands associated with the split d levels are not completely empty. This explains the reduction in moments with respect to the moments obtained in ABC stacking. The electrons totally occupy the a_1 and e_2 levels only as e_1 is completely empty.

The changes in the electronic ground states with changes in the stacking are intricately related to the above-discussed patterns of orbital occupation and anion-cation hybridizations. For example, V_2NF_2 has an identical magnetic ground state but is a semiconductor(metal) in the ABC(ABA) stacking. The localized anion-cation orbital overlap is responsible for a semiconducting ground state. Compared to this, there is much more itinerancy in the d states when the stacking is ABA. The anion d-cation p interaction is weak, too (Figure 4.8), leading to a metallic ground state. The changes in the electronic ground states with stacking for other compounds can be understood this way. A noteworthy point here is that except in Cr_2NF_2, ABA stacking renders all transition metal

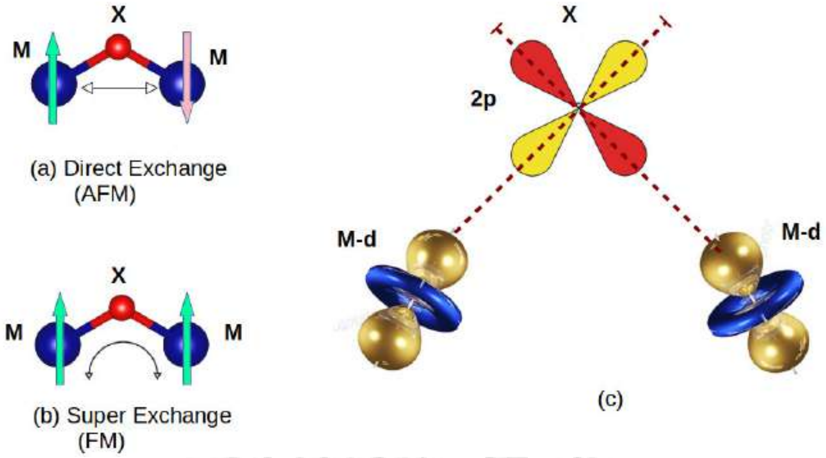

Figure 4.25: Various exchange mechanisms in the MXenes considered are shown. (a) and (b) show the direct exchange and superexchange, respectively. (c) shows the schematics of cation-anion-cation orbital overlaps in superexchange where same cation *d*-orbitals interact with different *p* orbitals of the same anion.

constituents equivalent. It is not so in the case of ABC stacking. Apart from Cr_2NF_2, Ti_2NF_2, V_2NF_2 and V_2NO_2 have two inequivalent M as can be made out from unequal magnetic moments on them. This is due to the inhomogeneous environment around the M atoms in these systems. Although the chemical species around them are identical, the variations in the anion-cation bond distances introduce inhomogeneity in the environment, leading to different exchange splittings of inequivalent atoms. For example, in V_2NO_2, V-O(V-N) bond distances are 2.0 Å(1.92 Å) and 2.19 Å(2.13 Å) in ABC stacking. A difference of 9.5 % and 11 % in the V-O and V-N bond distances associated with two V, respectively, can be correlated with large differences in their magnetic moments. V^{II}-N/O bonds are much larger than the V^{I}-N/O bonds. As a result, V^{II} states are more localized with less hybridization with anions and a smaller exchange splitting (Figure 4.9). In ABA stacking, there is uniformity in both bond distances; the V-O(V-N) bond distance is 1.96 Å(2.11 Å). In Cr_2NF_2, Cr-F (Cr-N) bonds vary by 1.4%(6.4%) in ABC stacking. The numbers are 1.9% (Cr-F) and 4.7% (Cr-N) in ABA stacking. Larger variations in Cr-N bond lengths affect cation-anion hybridizations and, subsequently, the magnetic moments on inequivalent atoms.

4.3.2.4 Understanding the origin of magnetic ground states and their stacking dependence

For all MXenes considered in this work, the M-X-M bond angle is close to 90°. This allows the *d*-orbitals of transition metal atoms to overlap with different *p*-orbitals of the anions. According to Goodenough Kanamori rule [188], this superexchange results in an FM arrangement of the M atoms (Figure 4.25(b),(c)). On the other hand, direct exchange between M atoms (Figure 4.25(a)) leads to an AFM arrangement. The competition between these two exchange mechanisms often determines the magnetic ground state configuration. It depends on the degree of occupancy of the *d* orbitals and/or the inter-atomic distances. For the MXenes considered here, the origin of a particular magnetic ground state in a given stacking can, by and large, be explained this way. In Ti_2NF_2, the origin of an FM ground state in ABA stacking is the nearly filled a_1 states that weaken the AFM exchange interaction, making the superexchange dominating. In ABC stacking, half-filled e_1 states promote direct exchange as hopping through spin flipping is allowed. This results in the AFM2 ground state. Since e_1 orbitals of opposite spin bands coming from inequivalent Ti atoms lying on the same surface are half-filled, the dominating direct exchange is between the inequivalent atoms leading to the AFM2 configuration. The origin of an AFM ground state in V_2NF_2 with ABC stacking can be explained similarly. Moreover, the inter-atomic distance between inequivalent V atoms in the ABC stacking is 2.92 Å. With ABA stacking, the inter-atomic distance between V atoms reduces further to 2.8 Å. Typically, inter-atomic distances beyond 3.0 Å make the direct exchange weaker. Thus, in this compound, direct exchange is promoted over superexchange. The inter-atomic distance is crucial in deciding the ground state magnetic structure of V_2NO_2 as well. In ABA stacked V_2NO_2, the distance between nearest neighbor V atoms lying in the same plane is only 2.78 Å. This results in a dominant direct exchange and an AFM2 ground state. With the change of stacking to ABC, the distance between inequivalent atoms lying in the same plane increases to 2.97 Å. This weakens the direct exchange. The dominant superexchange results in an in-plane FM arrangement. However, the inter-planar distance being smaller than this (2.93 Å), the direct exchange prevails along c-direction leading to an AFM1 ground state magnetic configuration. In Cr_2NF_2, ABA(ABC) stacking leads to an AFM1(AFM3) ground state. Here, the origin of this difference can be traced back to the intra-planar and inter-planar distances between Cr atoms. The intra-planar Cr-Cr distance is greater in ABA stacking (3.18 Å in ABA and 3.08 Å in ABC). Consequently, the direct exchange (superexchange) in ABA is less (more) than that in ABC. This leads to an in-plane FM(AFM) configuration in ABA(ABC). On the other hand, the inter-planar Cr-Cr distance in ABA is much smaller than that in ABC (2.49 Å in ABA and 3.09 Å in ABC). As a result, in ABA(ABC), the dominant inter-planar exchange is a direct exchange (superexchange) giving rise to AFM1 (AFM3) ground state. In Mn_2NF_2, there is an AFM to FM transition of the ground state magnetic configuration as stacking changes from ABC to ABA. Here, the ground state is determined by the competition between intra- and inter-planar interactions. In ABA, the inter-planar Mn atoms are the first and third nearest neighbors. The nearest neighbor distance being larger than 3.0 Å, superexchange is promoted. The second, fourth, and sixth neighbors lie in the same plane. However, the inter-planar distances being close to 3.0 Å and higher, superexchange dominates. Strong anion-cation overlap is also observed in ABA (Figure 4.12). In the ABC stacking, the overlap of Mn d and F p orbitals is relatively weak, as can be seen from the atom-projected densities of states in the region of -2 to -4 eV (Figure 4.12). Naturally, it leads to an AFM ground state. The occurrence of FM ground state in Cr_2NO_2, irrespective of stacking pattern, can be similarly explained from the atom projected densities of states (Figure 4.11) which show strong anion p-cation d overlap suggesting dominant superexchange mechanism.

4.3.3 Interatomic exchange parameters, magnetic transition temperatures and their dependencies on stacking pattern

Figure 4.26(4.27) show the interatomic exchange interactions of the systems in ABA(ABC) type stacking. The calculated exchange interaction parameters corroborate the explanations for the obtained magnetic ground states given in the previous subsection. For ABA stacked Ti_2NF_2 (4.26(c)), the dominant interactions from the first three neighbors are ferromagnetic, with the nearest neighbor interaction having a strength of 2.21 meV. The

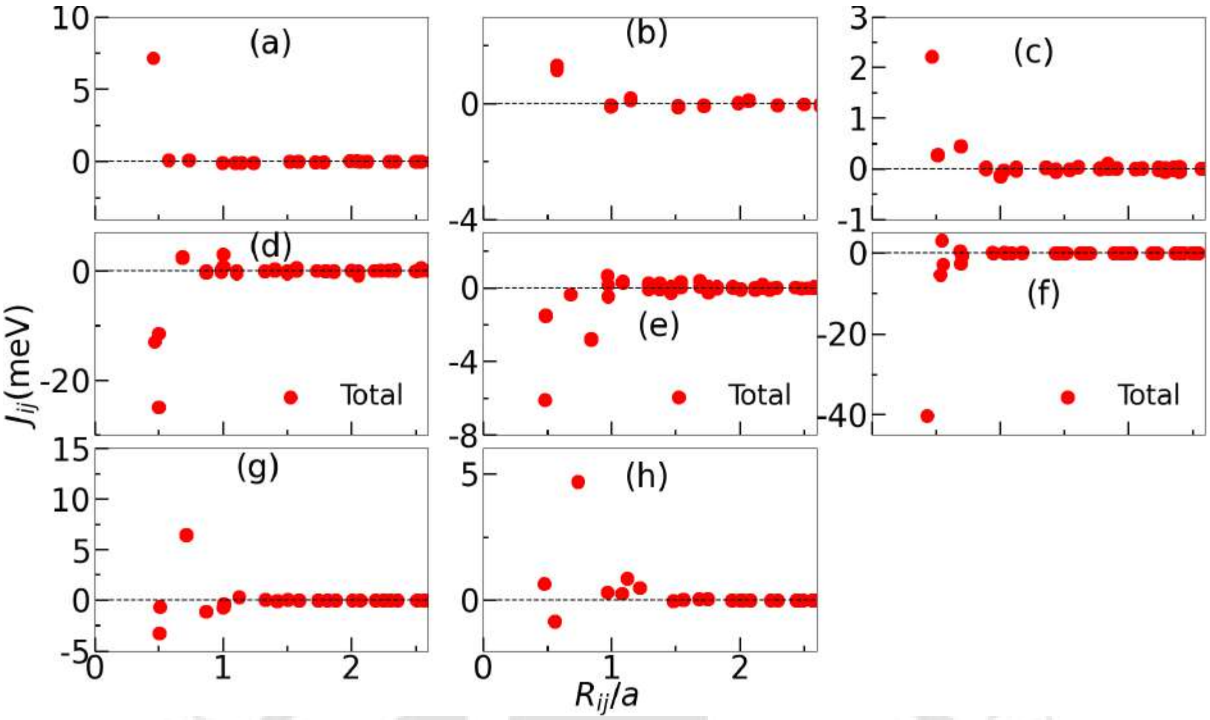

Figure 4.26: Inter-atomic exchange parameters as a function of inter-atomic distance for (a) Sc_2NF_2 and (b) Sc_2NO_2 and (c) Ti_2NF_2 (d)V_2NF_2 (e)V_2NO_2 (f) Cr_2NF_2 (g) Cr_2NO_2 and (h) Mn_2NF_2 in ABA stacking.

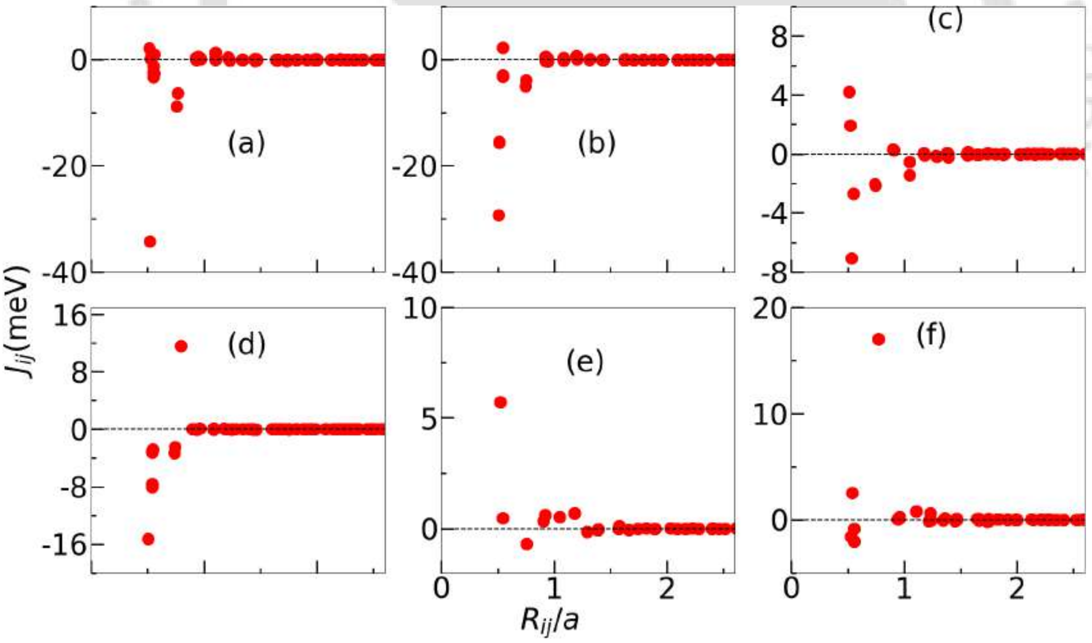

Figure 4.27: Inter-atomic exchange parameters as a function of inter-atomic distance for ((a) Ti_2NF_2 (b)V_2NF_2 (c)V_2NO_2 (d) Cr_2NF_2 (e) Cr_2NO_2 and (f) Mn_2NF_2 in ABC stacking

interactions beyond the first three neighbors are negligibly small. This makes the magnetic ground state of this compound FM. The first few interactions in V_2NO_2 are AFM (4.26(e)), with the strongest one of magnitude 6.05 meV coming from the nearest neighbor pairs. Here, the nearest neighbors lie in the same plane across a distance of 2.78

Å. As discussed earlier, such a distance makes the dominant in-plane interaction AFM and favors an AFM2 ground state. In ABA stacked Cr_2NF_2 (Figure 4.26(f)), we find the nearest neighbor interaction strong AFM with a magnitude of -40 meV. Here, the nearest neighbor pairs are situated out-of-plane. The strong out-of-plane AFM interaction drives the ground state AFM1.

In ABC stacking, the inequivalent Ti atoms of Ti_2NF_2 lie in the same plane. Strong AFM interaction from first neighbor pairs ($\sim$ 35 meV) (Figure 4.27(a))followed by AFM interactions from a few higher neighbors is the reason behind the AFM ground state. Since the nearest neighbors are the inequivalent atoms, the resulting AFM configuration is AFM2. In ABC stacked V_2NO_2, we find competing FM and AFM interactions in the first few neighbors. The nearest neighbor distance in the ABC stacked compound is now 2.93 Å, connecting out-of-plane V atoms. This is substantially larger(2.78 Å) than that in the ABA stacked compound. The in-plane distance of V atoms is 2.97 Å. From Figure 4.27(c), we find the competing FM and AFM interactions. The out-of-plane nearest neighbors connect via strong AFM exchange, while the third and fourth neighbor interactions are FM with competitive magnitudes. The in-plane FM ordering and out-of-plane AFM ordering happen as an outcome. In Cr_2NF_2, ABC stacking puts the in-plane inequivalent atoms at the nearest neighboring distance. The strong AFM interactions among the nearest neighbor and a few subsequent higher-order pairs keep the in-plane interaction AFM, resulting in an AFM3 ground state (4.27(d)). The changes in the exchange interactions and subsequent stabilization of the ground state magnetic configuration with changes in stacking for the other five MXenes can be interpreted similarly.

The exchange interactions reported above are used to compute the magnetic transition temperatures. The results are given in Table 4.2. Substantial changes in magnetic transition temperature upon a change in stacking pattern are observed in V_2NF_2 and Cr_2NO_2. For the former, ABA stacking led to a transition temperature of 350K, which is close to room temperature. For the latter, a transition temperature of 200K is obtained in ABC stacking. Such differences can be attributed to the changes in magnetic exchange parameters. Notably, most of the systems considered in this work have magnetic ordering temperatures substantially higher than CrI_3 [19], the prototype 2D magnet.

4.3.4 Magnetic Anisotropy energy and its microscopic origin

Magnetic anisotropy enables magnetism to survive in the 2D limit. It is also important from the perspective of device application as it stabilizes the magnetic long-range order in a given system. The DFT estimated values of MAE for our systems are given in Table 4.2.

The calculated values of MAE show that the nature of anisotropy, in-plane(MAE< 0) or out-of-plane (MAE> 0), in these MXenes, depends on the type of stacking. Quite a few MAE values are comparable to those obtained in well-known 2D magnets like $CrBr_3$, RhO_2, $Cr_2Ge_2Te_6$ and CrS_2 [21, 139, 158, 159]. Significant differences of MAE when the stacking changes , are observed in three cases: Cr_2NO_2 and V_2NF_2 where ABA stacking leads to very large in-plane anisotropy while ABC stacked compounds show out-of-pane anisotropy with MAE either very small(for V_2NF_2) or moderate (for Cr_2NO_2) and Cr_2NF_2 where ABA(ABC) stacked compound exhibits very large(moderate) out-of-plane(in-plane) anisotropy. In all the other MXenes where both stackings led to a magnetic order, the qualitative nature of anisotropy is observed to have changed with

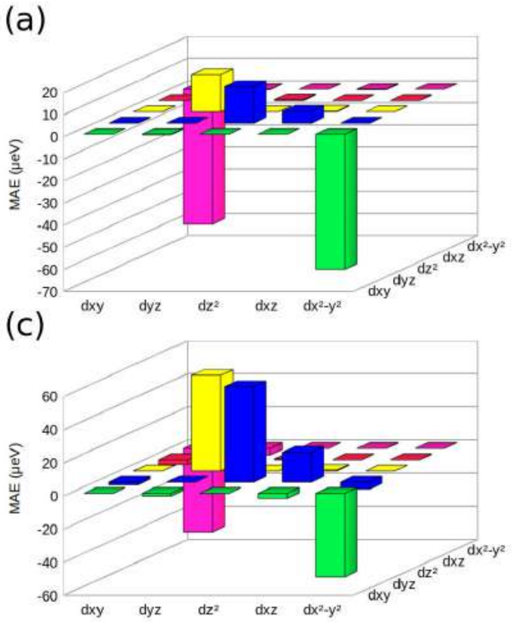

Figure 4.28: Contributions of various orbitals towards magnetic anisotropy energy of (a) Cr_2NO_2,(b) Cr^I of Cr_2NF_2 and (c)Cr^{II} of Cr_2NF_2. Results are for ABA stacking.

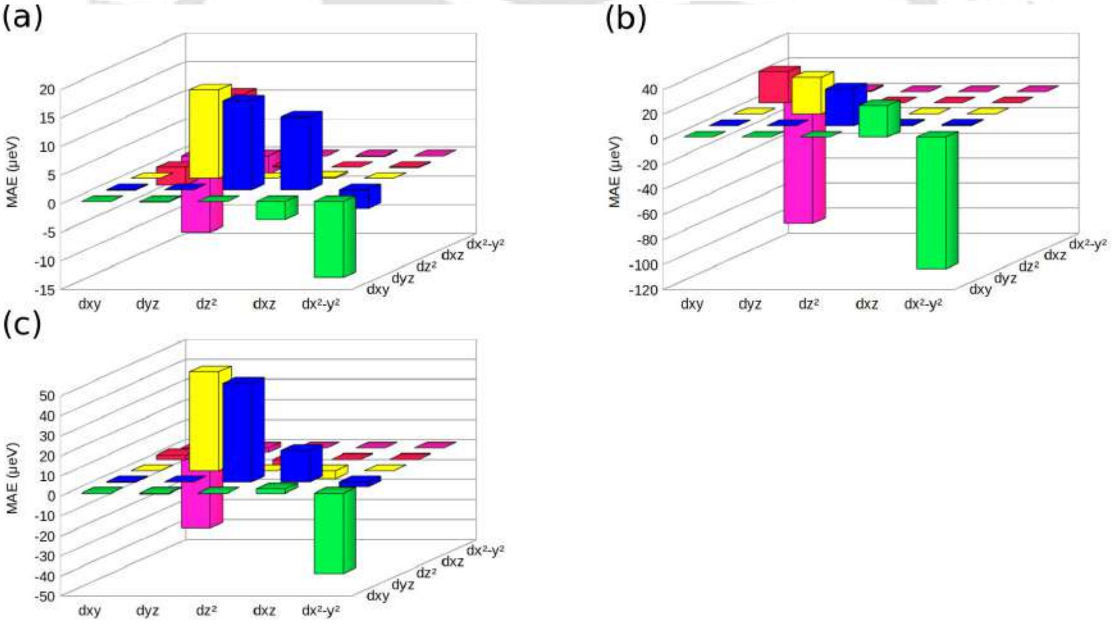

Figure 4.29: Contributions of various orbitals towards magnetic anisotropy energy of (a) Cr_2NO_2,(b) Cr^I of Cr_2NF_2 (c)Cr^{II} of Cr_2NF_2.The results are for ABC stacking.

stacking. The changes in the qualitative and, in some cases, quantitative nature of the magnetic anisotropy can be understood from the calculation of MAE using second-order perturbation theory as discussed in chapter 2 (Equation 2.41).

To understand the qualitative and quantitative nature of MAE and its changes with stacking, we consider Cr_2NO_2 and Cr_2NF_2 since these are the compounds where significant qualitative and quantitative changes occur when stacking changes. Contributions from the interactions of various pairs of *d*-orbitals in ABA (ABC) stacked compounds

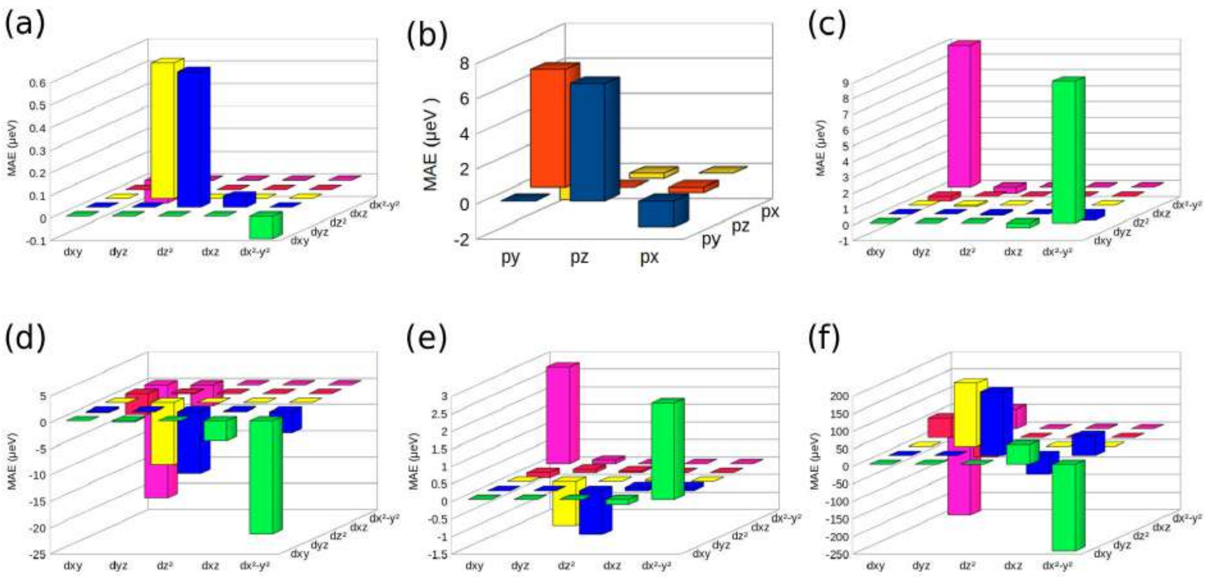

Figure 4.30: Orbital decomposition of Magnetic anisotropy energy (a)Sc_2NF_2 (b) Sc_2NO_2 (c) Ti_2NF_2(d) V_2NF_2 (e) V_2NO_2 (f) Mn_2NF_2 in ABA stacking

are presented in Figure 4.28(Figure 4.29). Only the contributions from the d-orbitals of Cr atoms are considered, as the other contributions are negligible. The interactions of d-orbitals contributing to the MAE are represented as $d_i \otimes d_j$ interactions [139]. We first consider the case of Cr_2NO_2. Results for Cr_2NO_2 in ABA stacking (Figure 4.28(a)) suggest that the main contributions to MAE come from $d_{xy} \otimes d_{x^2-y^2}$ and $d_{yz} \otimes d_{z^2}$ pairs. The contribution from $d_{xy} \otimes d_{x^2-y^2}$ is large and negative whereas the contribution from $d_{yz} \otimes d_{z^2}$ is small and positive . Therefore, it is primarily due to $d_{xy} \otimes d_{x^2-y^2}$ contributions, Cr_2NO_2 has a large and negative value of MAE in ABA stacking.

In the case of ABC stacked Cr_2NO_2, the main contributions to MAE come from three pairs of interactions represented as $d_{xy} \otimes d_{x^2-y^2}$, $d_{yz} \otimes d_{z^2}$, and $d_{yz} \otimes d_{xz}$ (Figure 4.29(a)). $d_{yz} \otimes d_{z^2}$, and $d_{yz} \otimes d_{xz}$ have positive contributions whereas the contribution from $d_{xy} \otimes d_{x^2-y^2}$ is negative . The positive contributions of $d_{yz} \otimes d_{xz}$ is almost equal to the negative contribution from $d_{xy} \otimes d_{x^2-y^2}$. Thus, it is the positive contribution from $d_{yz} \otimes d_{z^2}$ that is responsible for a modest and positive MAE in Cr_2NO_2. Since $d_{xy} \otimes d_{x^2-y^2}$ coupling is the major contributor, irrespective of stacking pattern, further analysis of this contribution and its changes with stacking is required. The $d_{xy} \otimes d_{x^2-y^2}$ interaction has four components: (a) $(o^{\uparrow}|u^{\uparrow})$ indicating SOC interaction between occupied and unoccupied spin-up orbitals, (b) $(o^{\uparrow}|u^{\downarrow})$ implying SOC interaction between occupied spin-up and unoccupied spin-down orbitals (c) $(o^{\downarrow}|u^{\uparrow})$ signifying SOC interaction between occupied spin-down and unoccupied spin-up states and (d) $(o^{\downarrow}|u^{\downarrow})$ coming from SOC interaction between occupied and unoccupied spin-down states. Contributions from $(o^{\uparrow}|u^{\uparrow})$ and $(o^{\downarrow}|u^{\downarrow})$ are > 0 whereas that from $(o^{\uparrow}|u^{\downarrow})$ and $(o^{\downarrow}|u^{\uparrow})$ are < 0. The origin of overwhelmingly larger contributions from $(o^{\uparrow}|u^{\downarrow})$ in ABC lies in their electronic structures. From the d-orbital resolved densities of states of both ABA and ABC stacked Cr_2NO_2(Figure 4.23), we observe that in ABA stacking, states in the unoccupied spin-down channel of $d_{xy}/d_{x^2-y^2}$ are nearer to Fermi level than in the ABC stacking. Consequently, the contributions of $o^{\uparrow}$ and $u^{\downarrow}$ are less in ABC stacking. Also, contributions from $o^{\downarrow}$ and $u^{\uparrow}$ are

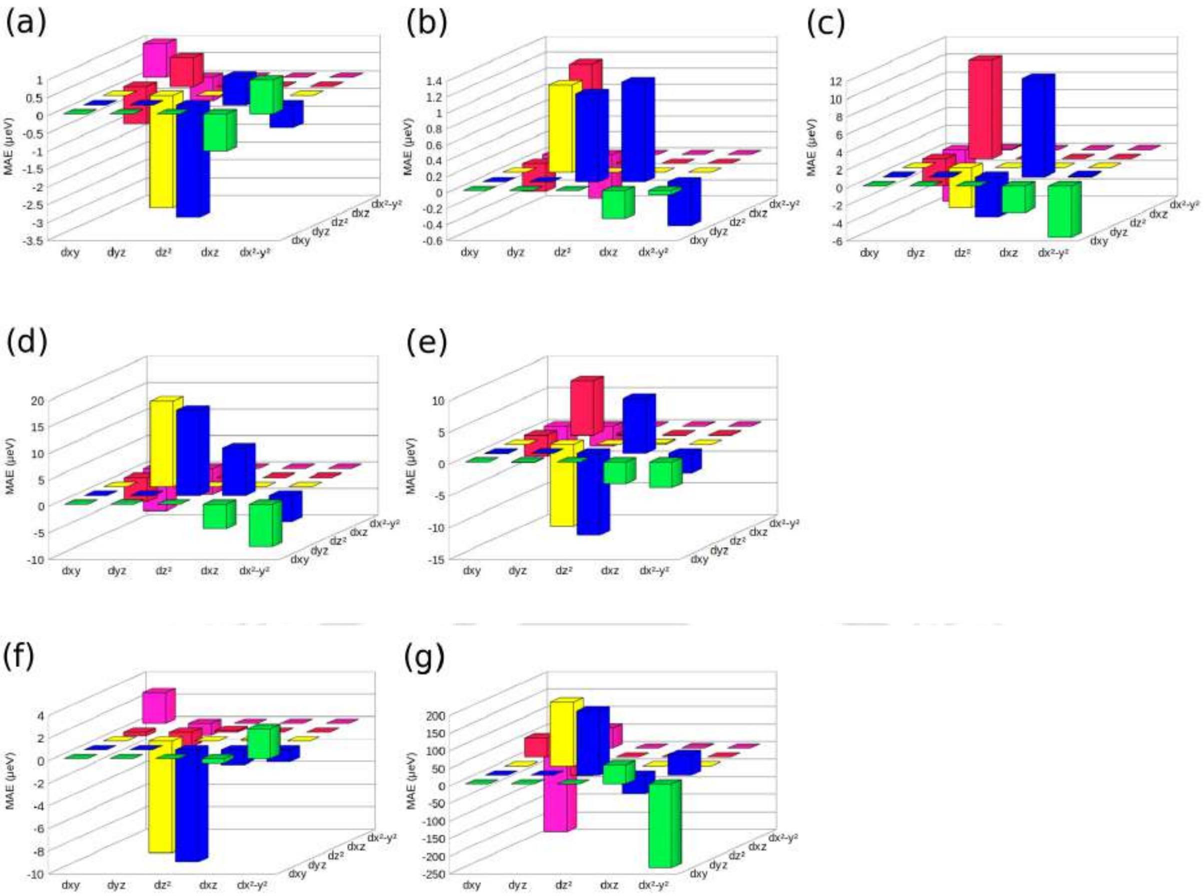

Figure 4.31: Orbital decomposition of Magnetic anisotropy energy (a)Ti^I of Ti_2NF_2 (b) Ti^{II} of Ti_2NF_2 (c) V^I of V_2NF_2(d) V^{II} of V_2NF_2 (e) V^I of V_2NO_2(f) V^{II} of V_2 NO_2 (g) Mn_2NF_2 (h)Mo^I of Mo_2NF_2 (i) Mo^{II} of Mo_2NF_2 in ABC stacking

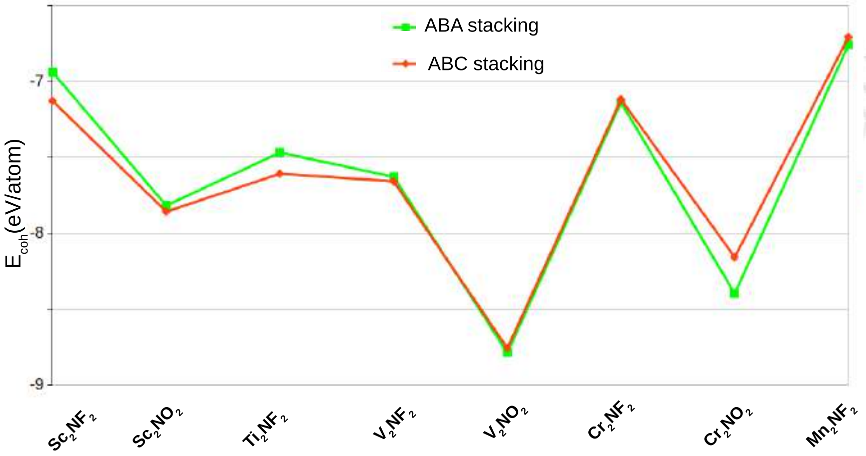

Figure 4.32: Cohesive energies of ABA and ABC stacked nitride MXenes

negligible because the corresponding states are far from the Fermi level. This explains the reason behind large(moderate) and negative(positive) contribution from $d_{xy} \otimes d_{x^2-y^2}$ interactions towards the total MAE in ABA(ABC) stacked Cr_2NO_2.

In Figure 4.28 and 4.29 (b)-(c), the contributions of various $d_i \otimes d_j$ interactions are shown for Cr_2NF_2.Since, irrespective of stacking, the Cr atoms in this compound are inequivalent, their contributions to the magnetic anisotropy energy (MAE) also differ. In the ABA stacked case, the contributions from Cr^I and Cr^{II} are 0.11 meV and 0.041 meV, respectively. in the ABC stacked case, contributions from Cr^I and Cr^{II} are -0.11 meV and 0.049 meV, respectively. Thus, we observe that the contribution from Cr^{II} towards total MAE is nearly the same in either stacking. More importantly, it is positive in both cases. This implies that the differences in the total MAE when stacking changes are solely due to Cr^I. Although the magnitude-wise contribution from Cr^I is the same in both stacking, one is positive, and the other is negative. To understand this in further detail, we look at the orbital resolved contributions (Figures 4.28(b,c) and 4.29(b,c)). In ABA stacking,$d_{yz} \otimes d_{z^2}$ interaction is the dominant contributor to Cr^I. This is large and positive. Some negative contribution from $d_{xy} \otimes d_{x^2-y^2}$ interaction and a small positive contribution from $d_{yz} \otimes d_{x^2-y^2}$ interaction add to the total making it positive and large.In ABC stacking, the positive contribution from the $d_{yz} \otimes d_{z^2}$ interactions reduces significanty. The main contribution to MAE now is from $d_{xy} \otimes d_{x^2-y^2}$. This contribution is negative and slightly larger in magnitude than that in ABA stacked compound . This is primarily responsible for the negative MAE in the ABC stacked compound. The contributions from interactions between other *d*-orbitals cannot change the overall qualitative nature. The origin of such a difference lies in the differences in the electronic structure. Comparing *d*-orbital resolved densities of states of Cr^I in ABA and ABC stacked compound (Figure 4.21), we observe that in ABC stacked case, d_{yz}/d_{z^2} states in the unoccupied part of the spectrum are closer to Fermi level. Consequently, the coupling between the occupied and unoccupied states of the same spin is enhanced. This enhances the negative contributions and provides more negative contributions to $d_{yz} \otimes d_{z^2}$ in comparison to that in the ABA stacked compound. This also leads to contributions from $d_{xy} \otimes d_{x^2-y^2}$ interaction that is more negative (than in ABA stacked compound). A similar analysis for all other MXenes considered in this work using the orbital-resolved MAE (Figures 4.30-4.31) can explain the qualitative changes in their magnetic anisotropy as stacking changes.

4.3.5 Relative stabilities of ABA and ABC stacked MXenes

The cohesive energies of the ABA and ABC stacked MXenes are evaluated using the expression :

$$E_{coh} = E_{MXene} - 2E_M - E_N - 2E_T$$

Here E_{MXene} represents the total energy of the MXenes under consideration, while E_M, E_N , and E_T denote the energies per atom of the free transition metal atoms (Ti, Sc, V, Cr, Mn), nitrogen, and functional group (O/F), respectively. The values obtained for these energies per atom are presented in Figure 4.32 .For MXenes containing heavy transition metal atoms such as V, Cr, and Mn, the cohesive energy of the ABA stacking is either lower or the same as that of the ABC stacking. So for these systems ABA stacking can be easily obtained . Conversely, for Sc and Ti-based MXenes, the ABC stacking exhibits slightly lower cohesive energy. This observation aligns with findings reported in the reference [169, 189] for O- and F-functionalized nitride MXenes. However, due to the minimal energy difference between the two stacking configurations, we expect that following bottomup approaches these MXenes can also be synthesised experimentally in ABA stacked configurations .

4.4 Summary

MXenes have drawn attention recently due to immense tunability in them, originating from their compositional and structural flexibility. However, so far, the option of flexibility in stacking the transition metal layers hasn't been investigated, primarily because of the fact that any stacking other than the conventional ABC one wasn't discovered experimentally. Taking a cue from the experimental discovery [58] and subsequent theoretical calculations of several MXenes [169], we have investigated in detail the effects of stacking patterns on the electronic and magnetic properties of various nitride MXenes functionalized with two different functional groups. We find that stacking adds to the degree of flexibility, leading to a number of different magnetic and electronic ground states in the same composition. We find that transitions between various AFM orders, AFM to FM, and even non-magnetic to FM, are possible due to this.Moreover, the electronic ground states can also be tuned by changing the stacking, leading to transformations like non-magnetic metal to spin gapless semiconductors and metal to half-metal. Such tunability makes these systems suitable for several magnetism-driven applications. Even large magnetic anisotropy energy, comparable to a few well-known 2D magnets and magnetic transition temperatures close to room temperature, are obtained upon changing the stacking pattern from conventional ABC to ABA. These certainly should provoke more investigations in this direction for other systems in the MXene family. We have analyzed the obtained results in great detail and made connections to the structural parameters and the electronic structures of the systems, resulting in a lucid picture of the microscopic physics responsible for the fascinating properties obtained. Although all but one MXene with unconventional stacking has been discovered, the calculations in Reference [169] have clearly shown that in MXenes, the transformation from conventional ABC to unconventional ABA would not cost a large amount of energy. Therefore, even though energetically, ABA stacking may not be preferable in some of the cases, the transformation to it can be easily achieved. This is an essential aspect that can be exploited to utilize the tunability of magnetic MXenes established in this work to further advantage.

Chapter 5

Consequences of magneto-electrical coupling in multiferroic VSe_2/Sc_2CO_2 heterostructures.

5.1 Introduction

The non-volatile electrical control of magnetic devices can be realized in multiferroic materials where the magnetism is controlled by the ferroelectric polarization. Since ferroelectric materials are endowed with bi-stable polarized states, their electrical switching is completely non-volatile. Thus, if the magnetic properties can be coupled with the states of electric polarization, the resulting magneto-electric coupling will lead to non-volatile electrical control of magnetic states [190, 191, 192]. However, single-phase multiferroics are not very attractive for this applications as none of the existing materials combine large and robust electric and magnetic polarizations at room temperature [193]. This has been circumvented by forming two-phase composites with a Ferroelectric and a ferromagnetic component. The magneto-electric effect is significant if the coupling at the interface of the two is large. This is more effective if the area at the interface is large.

Making 2D Van der Waals (vdW) heterostructures with a 2D ferroelectric and a 2D ferromagnet, thus, can be a useful way to achieve this. With the synthesis of several 2D ferroelectrics [194, 195, 196, 197, 198, 199], construction of such heterostructures no longer remains a distant reality. Very recently, this idea has been demonstrated to be working as a proof of concept through Density Functional Theory [143] based calculations [200, 201, 202, 203, 204, 205]. In those calculations, MXene Sc_2CO_2, recently predicted to be possessing large out-of-plane ferroelectric polarization [206] from DFT calculations, is considered to be the ferroelectric component in the 2D heterostructure. Different 2D ferromagnets having minimal lattice mismatch with Sc_2CO_2 have been used as the magnetic component. The calculations showed that the electronic ground states of the heterostructure can be altered between semiconducting and half-metallic upon changes in the ferroelectric polarization. Taking a cue from these recent developments, in this work, we have explored the consequences of magneto-electrical coupling in bi-layer and tri-layer VSe_2/Sc_2CO_2 heterostructures. The transition-metal dichalcogenide(TMDC)-MXene heterostructures have been chosen as both have flexibilities in their compositions

---

The contents of this chapter are published in 2025,The Journal of Physical Chemistry C ,129,6466-6476 DOI: https://doi.org/10.1021/acs.jpcc.4c08598

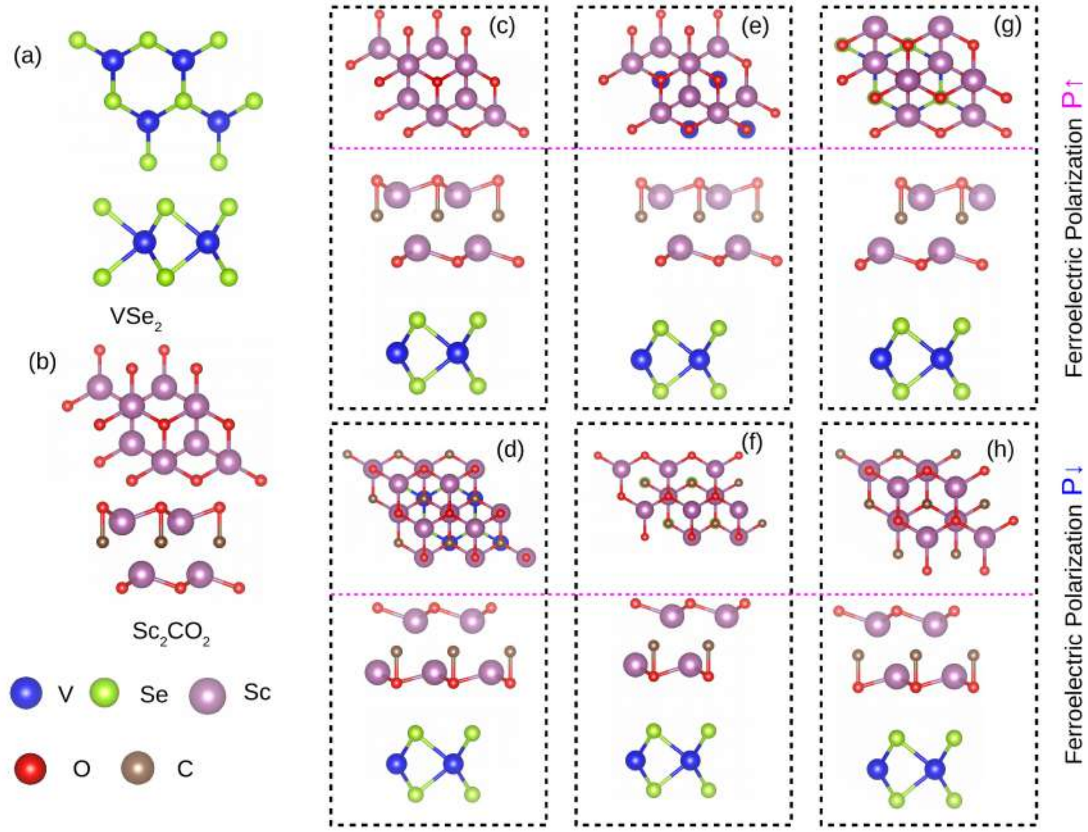

Figure 5.1: Top and side views of (a)VSe$_2$ (b) Sc$_2$CO$_2$ monolayer crystal structures. (c),(e),(g) show the stacking patterns of AA-P↑, BB-P↑ and CC-P↑ heterostructures, respectively. (d),(f) and (h) are for the same three stackings when the ferroelectric polarisation is P↓. Both top and side views are shown in each case.

and structures that can be exploited to realize tunable functional properties. As the magnetic component of the heterostructures, we have considered the 2H phase of VSe$_2$ as its monolayer has been synthesized recently [207]. Our results show that the electronic ground states of these heterostructures can be reversibly switched between semiconducting and half-metallic states upon switching electrical polarization of Sc$_2$CO$_2$. Based on these findings, we propose these heterostructures for multiple applications like bi-polar magnetic semiconductors, tunneling field effect transistors, and low-cost, power-efficient non-volatile memory devices. Unlike in the two works presented in the previous chapters, here the MXene is non-magnetic but its physical state controls the electronic properties of the magnetic component in the heterostructure. This control, in turn influences spin transport. Thus, this work demonstrates how MXene, inspite of being non-magnetic , can propel magnetism related functionalities in a 2D system.

5.2 Computational methods

Ground state properties and electronic structures are calculated by DFT framework where the electron-ion interactions are described using projector augmented wave (PAW) basis set [146]. The exchange-correlation part of the Hamiltonian is approximated by generalized gradient approximation (GGA) as parameterized by Perdew-Burke-Ernzerhof (PBE)

[123]. The kinetic energy cutoff of the plane wave is set to be 600 eV. The energy and force cutoff for structural optimization are 10^{-6} eV and 0.01 eV/Å, respectively. To include the van-der-Waals interactions, the DFT-D3 method is employed [147]. The Brillouin zone is sampled using Monkhorst-Pack [208]$14 \times 14 \times 1$ k-point mesh. Dipole corrections are also taken into account in all the calculations. A 20 Åvacuum is considered along z-direction to avoid any interactions between the adjacent layers.

5.3 RESULTS AND DISCUSSIONS

5.3.1 Ferroelectric polarisation driven modifications in the electronic properties of VSe_2/Sc_2CO_2

Figure 5.1(a) presents the top and side views of monolayer 2H-VSe_2, the magnetic component of the heterostructure. It crystallizes in a honeycomb-like structure where each V(Se)-atom is surrounded by six(three) neighboring Se(V) atoms. The V atoms are in a trigonal prismatic crystal field formed by the surrounding ligands. This VSe_2 phase exhibits ferromagnetism with a very high Curie temperature of 425 K [141]. Due to its high transition temperature, it can be directly used for applications above room temperature. The lattice constant of VSe_2 from our calculation is 3.33 Å , which agrees very well with the reported result [209]. The magnetic moment of each V atom is 1 μB.

The ground state structure of MXene monolayer Sc_2CO_2, the ferroelectric component of the heterostructure, is shown in Figure 5.1(b). Monolayer Sc_2CO_2 possesses out-of-plane ferroelectricity with significantly large electric polarisation [206]. The structure lacks inversion symmetry. The O-atom on one of the surfaces occupies the hollow site associated with the Sc atom. The O-atom, on the other surface, occupies the hollow site associated with the C-atom. Consequently, the Sc atom on the lower surface (00-1 surface) is in an octahedral crystal field, while the Sc atom on the top surface (001 surface) is in a trigonal prismatic crystal field. The lattice parameter for Sc_2CO_2 from our calculations is 3.41 Å , in excellent agreement with the reported results [203, 210].

Our result demonstrates that the lattice mismatch between VSe_2 and Sc_2CO_2 is nearly 2.4 % only. Hence, these two monolayers can be vertically stacked to form a 2D van der Waals (vdW) heterostructure. The two ferroelectric polarization states of Sc_2CO_2 are differentiated by the position of the C atom in the unit cell. When the C atom is close to the upper(lower) surface, the polarisation state is depicted as P↑(P↓). These two polarisation states can be reversibly switched by applying an electric field and occur through an intermediate antiferroelectric structure [206]. The heterostructure with VSe_2 can be formed with either state of ferroelectric polarisation. Accordingly, we construct six different heterostructures, three each for a given ferroelectric polarisation: (i) AA: The O-atom closest to VSe_2 is directly above the V-atom (Figure 5.1(c),(d)) (ii) BB: The O-atom closest to VSe_2 is directly above the Se atom (Figure 5.1(e),(f)) and (iii) CC: The O-atom closest to VSe_2 is above a V-Se bond in VSe_2 (Figure 5.1(g),h)).

The stability of the six heterostructures is assessed by calculating their binding energies given by

$$E_b = (E_{hetero} - E_{VSe_2} - E_{Sc_2CO_2})/A$$

E_{hetero} is the total energy of the heterostructure. E_{VSe_2} and $E_{Sc_2CO_2}$ are the energies of pristine monolayers of VSe_2 and Sc_2CO_2, respectively .A is the surface area of the

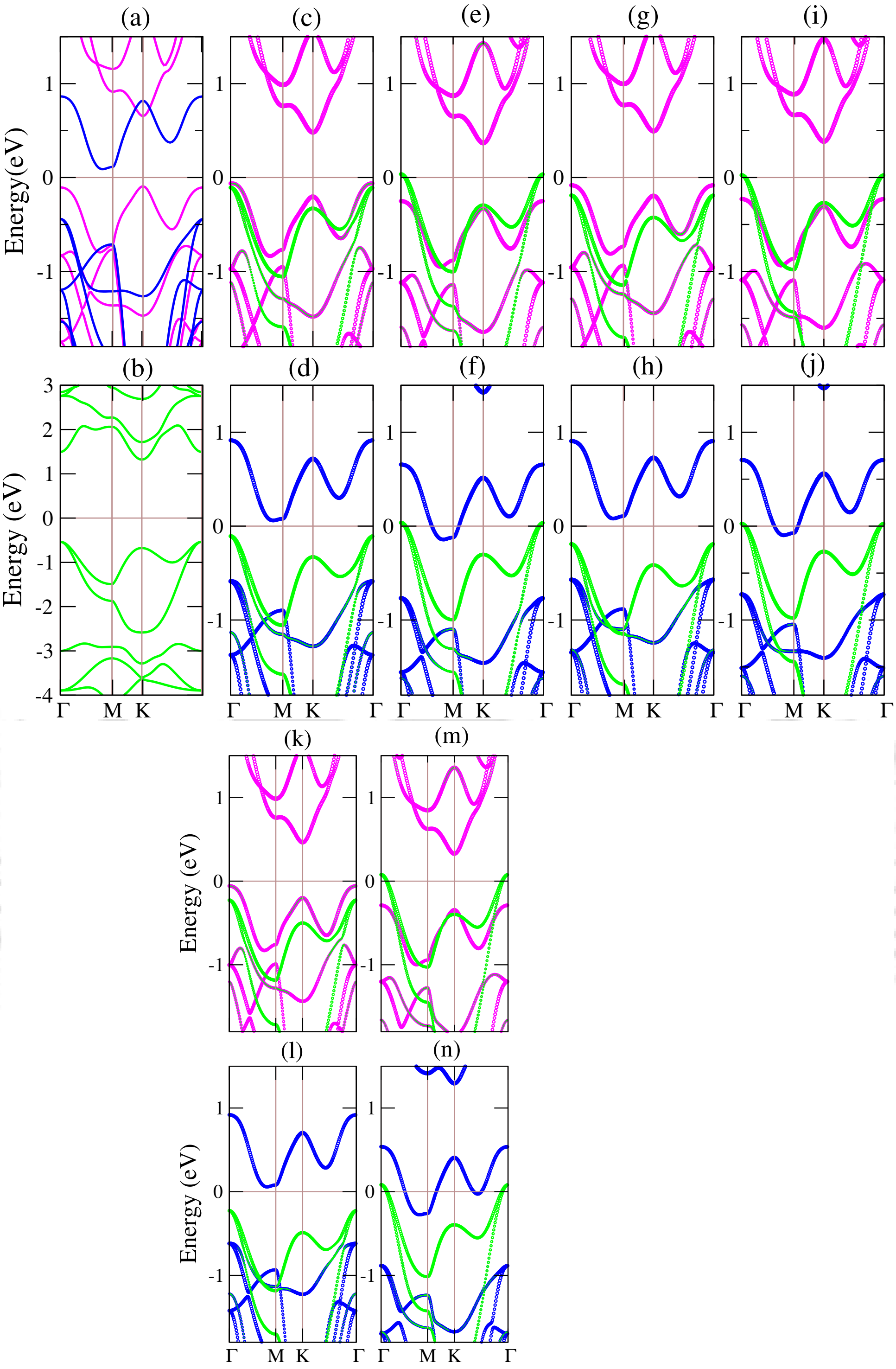

Figure 5.2: Electronic band structure for (a) Monolayer VSe_2 and (b) Monolayer Sc_2CO_2. (c),(d) are the spin-up and spin-down bands of AA-P↑ heterostructure, respectively. (e),(f) are the spin-up and spin-down bands of AA-P↓ heterostructure, respectively.(g),(h) are the spin-up and spin-down bands of BB-P↑ heterostructure, respectively. (i),(j) are the spin-up and spin-down bands of BB-P↓ heterostructure,respectively.(k),(l) are the spin-up and spin-down bands of CC-P↑ heterostructure, respectively. (m),(n) are the spin-up and spin-down bands of CC-P↓ heterostructure,respectively.Green, magenta and blue lines represent contributions from Sc_2CO_2,spin-up and spin-down states of VSe_2, respectively.

Table 5.1: Calculated parameters of VSe_2/Sc_2CO_2 vdw heterostructure . d is interlayer distance, E_b is interface binding energy.

Stacking	d (Å)	E_b (meV/Å^2)	Band Gap(eV)
AA-P↑	2.90	-19.84	0.12
AA-P↓	2.81	-31.50	0.00
BB-P↑	3.4	-13.27	0.16
BB-P↓	3.35	-17.5	0.00
CC-P↑	3.02	-17.8	0.12
CC-P↓	2.93	-31.4	0.00

heterostructure. The results are presented in Table 5.1. The results imply that the heterostructures can be grown experimentally. The interlayer distance d in each case is also given in Table 5.1. We find that the interlayer distances decrease when the ferroelectric polarisation of Sc_2CO_2 changes from P↑ to P↓. For a given structural configuration, the maximum changes in the interlayer distances are about 3% only upon a change in the state of ferroelectric polarisation.

We next investigate the magneto-electric coupling in the bi-layer VSe_2-Sc_2CO_2 by computations of band structures of the heterostructures considered in this work. In Figure 5.2(a) and 5.2(b), we show the band structures of monolayer VSe_2 and Sc_2CO_2, respectively. VSe_2 turns out to be a ferromagnetic semiconductor with a band gap of 0.75 eV(0.53 eV) in the spin-up(spin-down) channel, in agreement with existing results [209]. Our calculations show Sc_2CO_2 a semiconductor with an indirect band gap of 1.84 eV, in excellent agreement with other calculations [200]. The spin-projected band structures of bi-layer VSe_2/Sc_2CO_2 for different heterostructures and different ferroelectric polarisations are shown in Figure 5.2(c)-(n). A common feature seen in all cases is that the band structure of the heterostructures is essentially a superposition of bands contributed by the constituents. This is the characteristic of 2D vdW heterostructures with weak coupling between the layers. The other common feature connected to the magneto-electrical coupling in this system is the dependence of spin projected band structure on the ferroelectric polarisation of MXene Sc_2CO_2. In Figure 5.2 (c) and (d), we show the spin up and spin down bands of the AA heterostructure, respectively, when the ferroelectric polarisation is P↑. We find that the system behaves as a magnetic semiconductor with a band gap of 0.12 eV (Table 5.1). Here, both the valence band minima (VBM) and conduction band maxima (CBM) are due to contributions from VSe_2, demonstrating a type-I band alignment. Such heterostructures with type-I band alignment are useful for confining electrons and holes, facilitating carrier recombination, and thus sought after for applications in optical devices. Significantly, the VBM and the CBM are composed of oppositely polarised spin bands. As such, the heterostructure behaves like a Bipolar Magnetic Semiconductor (BMS). In this system, a completely spin polarisation current with reversible spin polarisation can be created and controlled simply by applying a gate voltage [211]. When the polarisation state of Sc_2CO_2 ferroelectric is switched to P↓, the heterostructure behaves as a half-metal (Figure 5.2 (e),(f)). In the spin-up channel, the system remains semiconducting with little changes in the band structure (Figure 5.2(e)). Major changes are observed in the spin-down bands (Figure 5.2(f)). The spin-down band corresponding to VSe_2, right above Fermi level in case of both monolayer VSe_2 and the heterostructure with P↑ ferroelectric state, is pushed towards lower energy, closing the

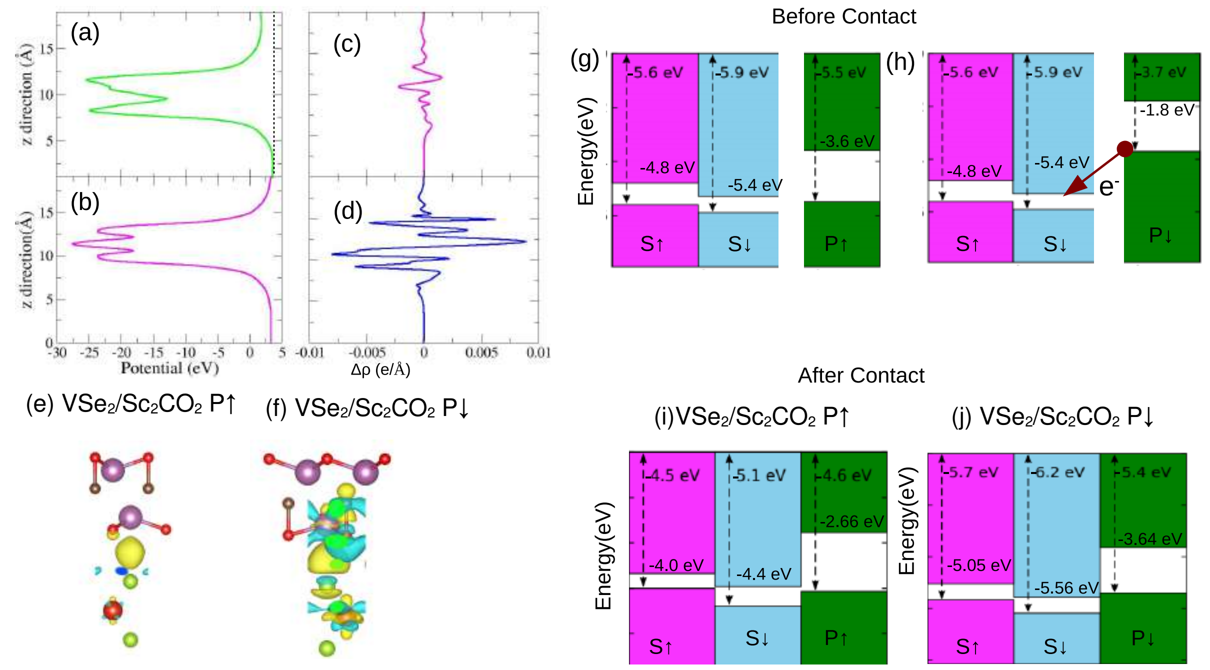

Figure 5.3: Plane-averaged electrostatic potential of (a) Sc_2CO_2 and (b)VSe_2 along z. (c) and (d) are variations in the plane-averaged differential charge density of VSe_2/Sc_2CO_2 (P↑)and VSe_2/Sc_2CO_2 (P↓)heterostructures along z, respectively; (e) and (f) are the corresponding charge density differences. (g) and (h) are the band-alignments of the individual monolayers before contact, while(i) and (j) are the band alignments of VSe_2/Sc_2CO_2(P↑)and VSe_2/Sc_2CO_2(P↓) heterostructures, respectively.

semiconducting gap, leading to a half-metallic ground state of the heterostructure.

In experiments, switching between the two states, P↑ and P↓, can be done by applying an electric field. Sc_2CO_2, being ferroelectric, is bistable. As a result, the application of an electric field can change its polarization state. It remains in a given state of polarisation even after removing the electric field, making the switching completely reversible and non-volatile. Figure 5.2, therefore, shows that the ground state of Sc_2CO_2/VSe_2 heterostructure can be switched between a magnetic semiconductor and a half-metal by reversible switching of the ferroelectric polarisation.

5.3.2 Coupling mechanism and interfacial interaction in VSe_2/Sc_2CO_2 heterostructure

The observed changes in the electronic structures of VSe_2/Sc_2CO_2 upon changing the ferroelectric polarisation state can be understood by analyzing the changes in the charge distribution or coupling across the monolayer interfaces. Due to broken spatial symmetry, the work function associated with two surfaces of Sc_2CO_2 is different by about 1.8 eV as seen from the plane-averaged potential versus distance in the z-direction plot (Figure 5.3(a)). No such asymmetry across the surfaces is observed in the case of VSe_2 (Figure 5.3(b)). The calculated Work functions of VSe_2 monolayer, the C_{top} side and C_{bottom} side of Sc_2CO_2 monolayer are -5.46 eV, -4.96 eV and -3.13 eV, respectively; C_{top}(C_{bottom}) refers to the position of C-atom layer in Sc_2CO_2 when the ferroelectric polarisation is P↑(P↓). Thus, when VSe_2 is stacked with Sc_2CO_2, depending on which surface of Sc_2CO_2 is used

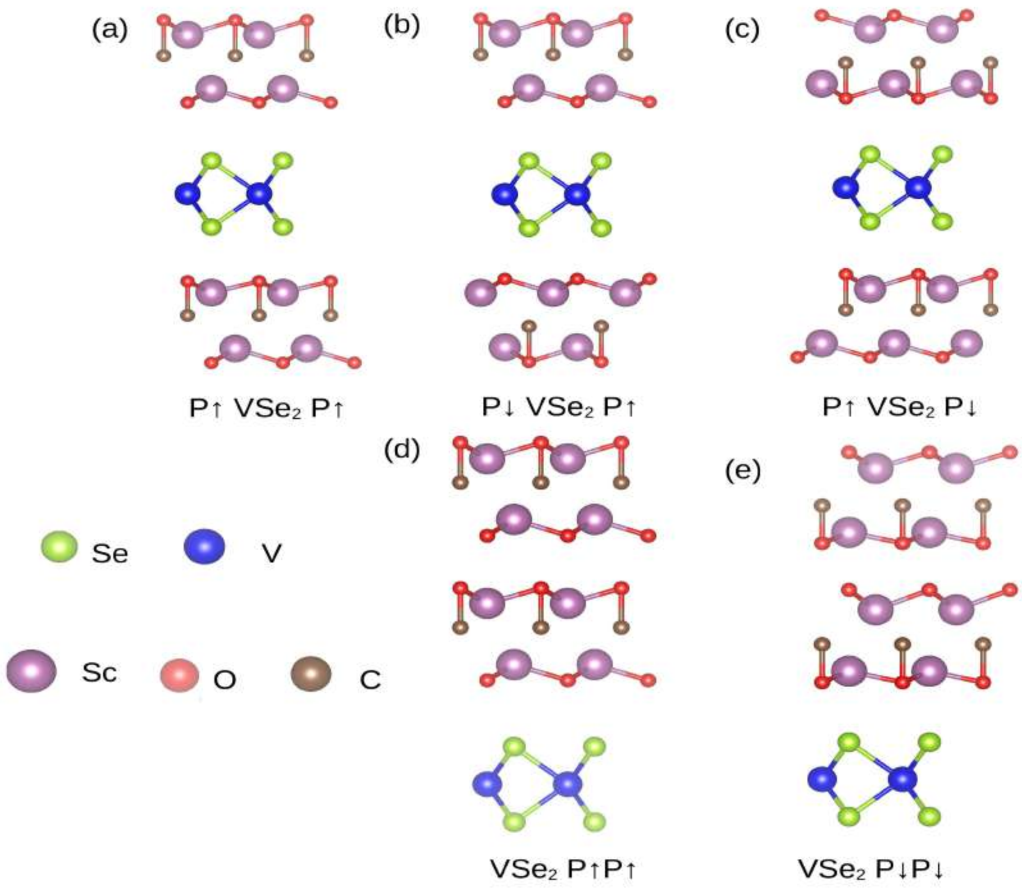

Figure 5.4: Optimized geometries of Sc_2CO_2/VSe_2/Sc_2CO_2 and VSe_2/Sc_2CO_2/Sc_2CO_2 trilayer heterostructures with differrent polarisations .

for stacking, charge transfer across the interface differs significantly. When Sc_2CO_2 is in the P↑ polarisation state, the spin-up(S↑) and spin-down(S↓) valence band maxima (VBM) (conduction band minima(CBM)) of VSe_2 are lower(higher) than the conduction band minima (CBM)(valence band maxima (VBM)) of Sc_2CO_2 (Figure5.3(g)). Thus, in VSe_2/Sc_2CO_2(P↑) heterostructure, there is no electron transfer between Sc_2CO_2 and VSe_2. Nevertheless, due to differences in the work functions of Sc_2CO_2 and VSe_2 the interfacial interaction causes a spontaneous flow of electrons from Sc_2CO_2 to VSe_2. Accordingly, the Fermi level of Sc_2CO_2 shifts slightly towards lower energy, and that of VSe_2 shifts slightly towards higher energy, reaching a common level. As a result, a small amount of electron accumulates in VSe_2, giving rise to an internal electric field. The charge transfer, however, is not sufficient to close the energy gap, resulting in a type I band alignment (Figure 5.3(i)). The variations in the plane-averaged differential charge density with distance along z (Figure 5.3(c)) and charge density difference (Figure 5.3(e)) results corroborate this.

When the polarization of Sc_2CO_2 changes to P↓ (Figure 5.3(h)),the VBM of $Sc_2CO_2$is at a higher position than CBM of VSe_2 associated with either spin band. Therefore, electron transfer can occur from the valence band of Sc_2CO_2 to the conduction band of the spin-down channel of VSe_2. Due to this, the spin-down conduction band of VSe_2 is shifted towards lower energy considerably, closing the semiconducting gap in this spin channel and giving rise to metallic behavior (Figure 5.3(j)). The band alignment shown

Table 5.2: Calculated interface binding energies (E_b)of trilayer vdw heterostructures (in meV/Å^2).

System	E_b
Sc_2CO_2(P↑)/VSe_2/Sc_2CO_2(P↑)	-30.00
Sc_2CO_2(P↓)/VSe_2/Sc_2CO_2(P↑)	-21.75
Sc_2CO_2(P↑)/VSe_2/Sc_2CO_2(P↓)	-31.24
VSe_2/Sc_2CO_2(P↑)Sc_2CO_2(P↑)	-29.60
VSe_2/Sc_2CO_2(P↓)Sc_2CO_2(P↓)	-51.95

in Figure 5.3(j) indicates that this heterostructure exhibits an almost broken-gap type-III alignment. Heterostructures with such band alignment can facilitate tunneling of electrons directly from the VBM of Sc_2CO_2 to the CBM of VSe_2. Therefore, band-to-band tunneling (BTBT) is possible, making these heterostructures highly desirable for tunnel field-effect transistors. The plane-averaged differential charge density (Figure 5.3(d)) and charge density difference(Figure 5.3(f)) plots show a significant amount of charge transfer across the interface justifying the band alignment described above. Such large charge transfer across the interface can be explained in terms of the significant difference in the Work functions of VSe_2 and C_{bottom} side of the Sc_2CO_2 monolayer.

5.3.3 Ferroelectric polarisation driven modifications in the electronic properties of Sc_2CO_2/VSe_2/Sc_2CO_2

Next, we investigate the interrelations between a number of layers in the VSe_2-Sc_2CO_2 heterostructure, the ferroelectric polarisation, and the ground state electronic structure. For this purpose, we construct a tri-layer Sc_2CO_2/VSe_2/Sc_2CO_2 heterostructure. Since the AA stacking configuration has the lowest binding energy in the bi-layer heterostructure, and since a different stacking configuration did not produce any qualitatively different result, we have considered only the AA stacking configuration for this trilayer heterostructure. Three different arrangements, (a) Sc_2CO_2(P↑)/ VSe_2/ Sc_2CO_2(P↑) (b)Sc_2CO_2(P↓)/ VSe_2/ Sc_2CO_2(P↑) (c) Sc_2CO_2(P↑)/ VSe_2/ Sc_2CO_2(P↓), are considered. Additionally,two more arrangements, Sc_2CO_2(P↑)/Sc_2CO_2(P↑)/VSe_2 and Sc_2CO_2(P↓)/Sc_2CO_2(P↓)/VSe_2 are considered for the purpose of comparison. The arrangements are shown in Figure 5.4. Binding energies corresponding to them are given in Table 5.2. The negative values of binding energies indicate that the heterostructures can form with these arrangements.

Figure 5.5 shows the spin-projected band structures of these trilayer arrangements of VSe_2-Sc_2CO_2 heterostructure.Among the three arrangements with VSe_2 as the intermediate layer, half-metallic ground state is observed for Sc_2CO_2(P↑)/VSe_2/Sc_2CO_2(P↑) (Figure 5.5(a),(f)) and Sc_2CO_2(P↑)/VSe_2/Sc_2CO_2(P↓)(Figure 5.5(c),(h)). In both cases, the spin-down(spin-up) band is metallic (semiconducting). In contrast, Sc_2CO_2(P↓)/ VSe_2/ Sc_2CO_2(P↑) heterostructure is semi-conducting in both spin channels (Figure 5.5(b),(g)). Thus, semiconductor to half-metallic ground state can be realized in these tri-layer heterostructures by changing polarisations of the MXene layers through the application of an external electric field. This implies that the tri-layer heterostructures of Sc_2CO_2-VSe_2 with the latter sandwiched between two MXene layers can act as a multiferroic. This is not so with the other two tri-layers, which basically are heterostructures of a bi-layer

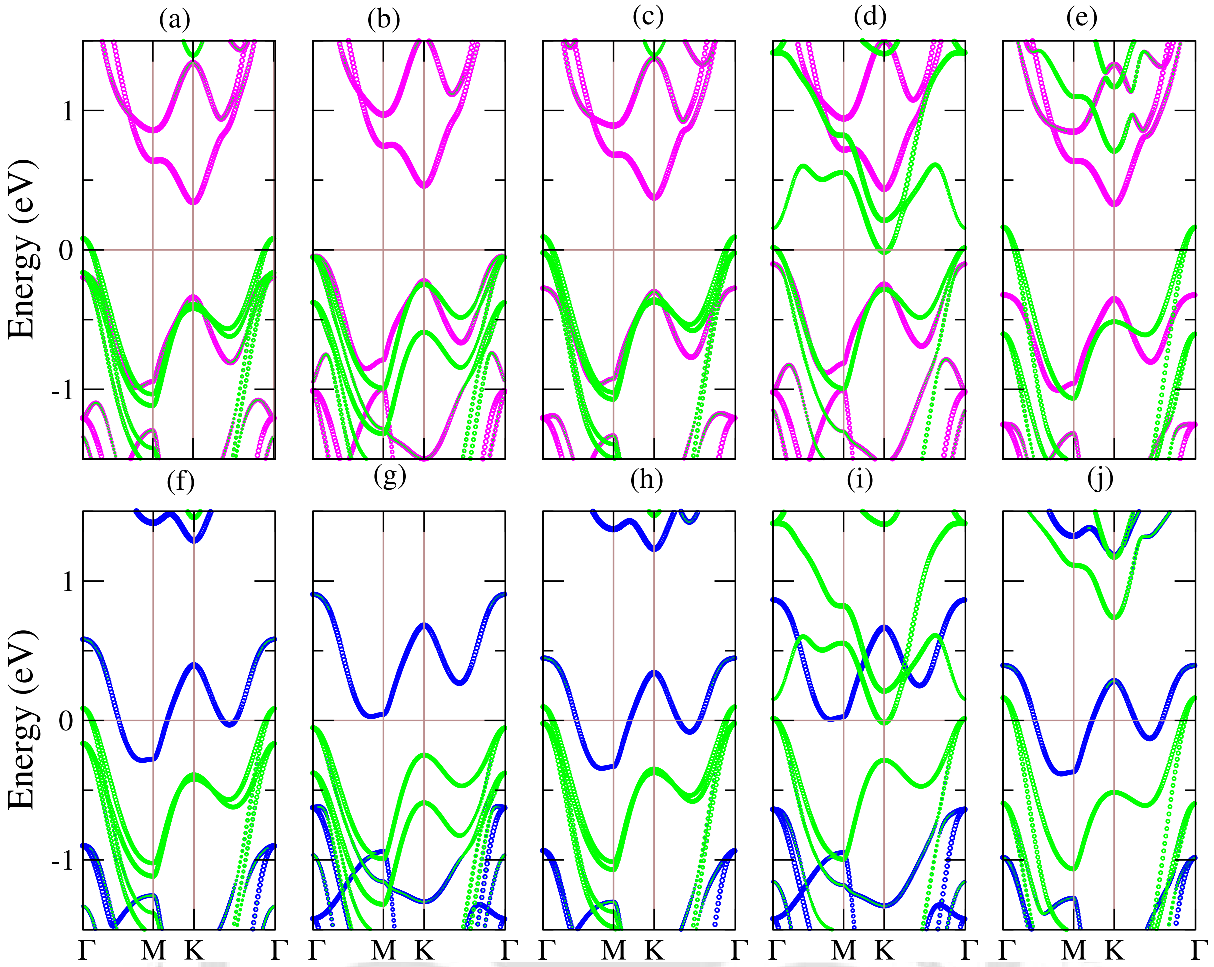

Figure 5.5: (a)-(e) show spin-up band structures for Sc_2CO_2(P↑)/ VSe_2/ Sc_2CO_2(P↑), Sc_2CO_2(P↓)/ VSe_2/ Sc_2CO_2(P↑) , Sc_2CO_2(P↑)/ VSe_2/ Sc_2CO_2(P↓), Sc_2CO_2(P↑)/Sc_2CO_2(P↑)/VSe_2 and Sc_2CO_2 (P↓)/Sc_2CO_2(P↓)/VSe_2, respectively. Corresponding spin-down band structures are shown in (f)-(j), respectively.

Sc_2CO_2 and a mono-layer of VSe_2.Upon reversal of polarisation in the bi-layer Sc_2CO_2 from P↑ to P↓, the heterostructure ground state changes from a semi-metallic to a metallic one only(Figures 5.5(d),(i) and (e),(j)).

5.3.4 Coupling Mechanism and interfacial interaction in $Sc_2CO_2/VSe_2/Sc_2CO_2$ heterostructure

As observed in the case of the bilayer heterostructures, the changes in the electronic structures with stacking and/or electric polarization can be understood through an analysis of charge transfers across the interfaces. The stacking of layers in Sc_2CO_2(P↑)/VSe_2/Sc_2CO_2(P↑) (Figure 5.4(a)) resembles a combination of two bi-layers VSe_2-Sc_2CO_2(P↑) (Figure 5.1(g)) and VSe_2-Sc_2CO_2(P↓) (Figure 5.1(h)). The top (bottom) surface of the tri-layer has the C_{bottom}(C_{top}) side of MXene Sc_2CO_2 interfacing with VSe_2. Since the differences in the Work functions of C_{top}(C_{bottom}) side of Sc_2CO_2 and VSe_2 is small(large), the charge transfer across the top (bottom)interface of the tri-layer heterostructure should be negligible (significant) as was the cases for the bi-layer heterostructures. The variations in the plane averaged differential charge density with z (Figure 5.6(a)) and the charge density

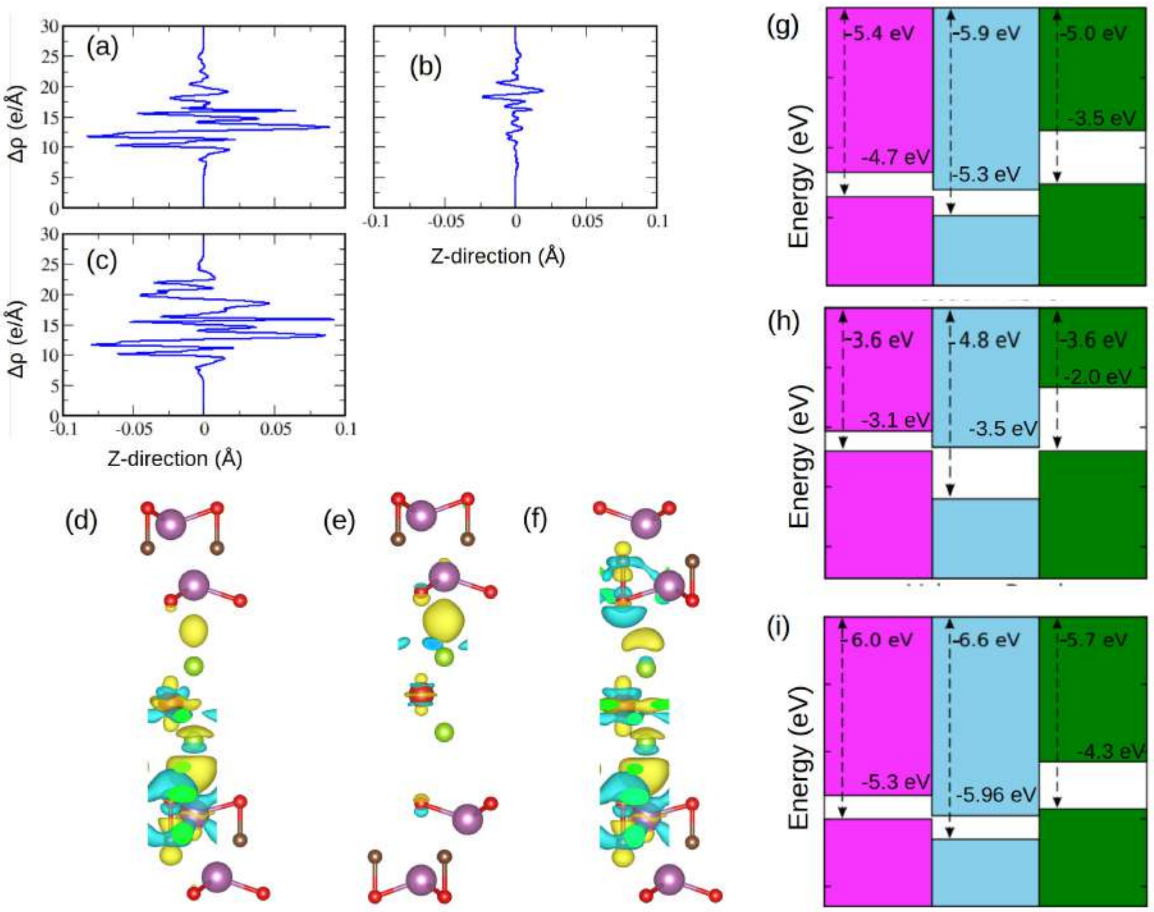

Figure 5.6: Plane averaged differential charge density (a-c), Charge density differences (d-f) and band alignments (g-i) of Sc_2CO_2(P↑)/ VSe_2/ Sc_2CO_2(P↑), Sc_2CO_2(P↓)/ VSe_2/ Sc_2CO_2(P↑) and Sc_2CO_2(P↑)/ VSe_2/ Sc_2CO_2(P↓) heterostructures, respectively

differences (Figure 5.6(d)) demonstrate this. Due to such charge transfer, the spin-down conduction band of VSe_2 shifts downwards in the energy, closing the semiconducting gap and resulting in a metallic behavior in this spin channel. This makes the ground state of this tri-layer heterostructure half-metallic. The alignment of bands in this heterostructure, shown in Figure 5.6(g), indicates a broken gap type-III band alignment.

In contrast,in Sc_2CO_2(P↓)/VSe_2/Sc_2CO_2(P↑) both interfaces consist of C_{bottom} part of Sc_2CO_2(Figure 5.4(b)). The expectation, therefore, is that apart from the small charge transfer due to the internal electric field, there will be no significant charge transfer across the interfaces. Consequently, the Sc_2CO_2(P↓)/VSe_2/Sc_2CO_2(P↑) heterostructure will have a gap opening in both spin channels making the system semiconducting. This explains the band structure corresponding to this heterostructure (Figure 5.6(b)). The variations in the planar averaged differential charge density (Figure 5.6(b)) and the charge density differences (Figure 5.6(e)) support this argument. The band alignment diagram of this heterostructure, shown in Figure 5.6(h), indicates a band alignment of Type-I.

In the Sc_2CO_2(P↑)/VSe_2/Sc_2CO_2(P↓) configuration shown in Figure 5.4(c), both interfaces consist of C_{top} side of Sc_2CO_2.As a result, significant charge transfer occurs across both interfaces(Figures 5.6(c),(f)), leading to the closing of the semiconducting gap in the spin-down channel, making the ground state half-metallic. Consequently, the band alignment (Figure 5.6(i)) is a broken type-III one. The results imply that by applying an

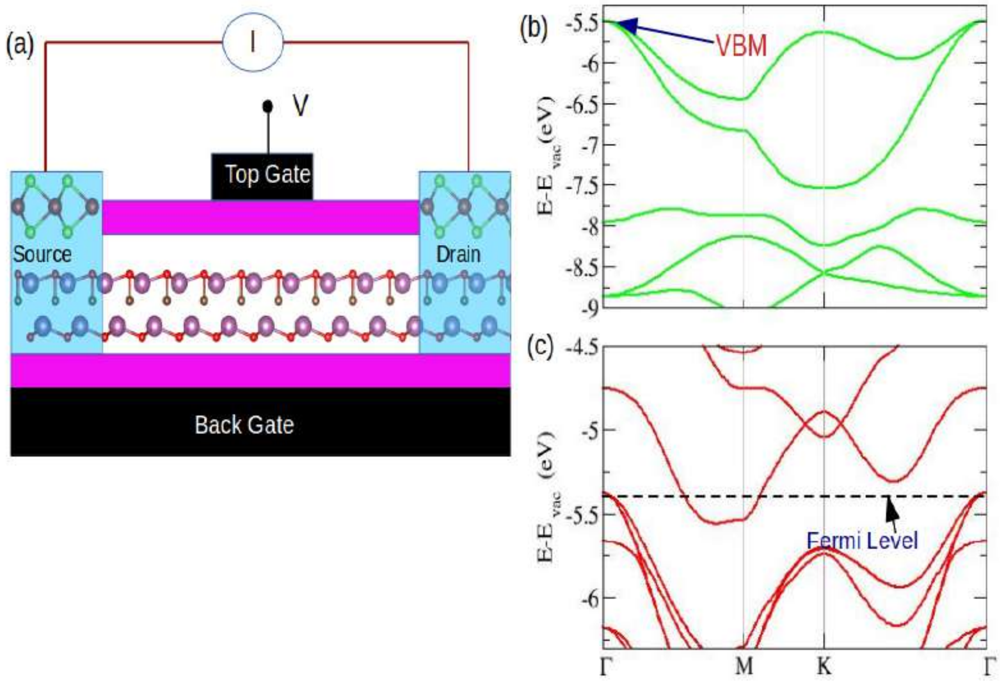

Figure 5.7: (a) Schematic diagram of VSe_2-contact Sc_2CO_2 FET (b) VBM of semiconducting Sc_2CO_2 (c) Fermi level of metal electrode $Sc_2CO_2(P\downarrow)/VSe_2$

electric field, one can switch between a type-I and a broken-gap type-III system.

5.4 Applications

5.4.1 Field-effect transistor(FET)

Since VSe_2 becomes half-metallic when interfaced with $Sc_2CO_2(P\downarrow)$, it can form a van der Waals-contacted metal-semiconductor junction (MSJ) with Sc_2CO_2. Such MSJ can play a significant role in FET as the performance of the FET depends strongly on the height of the Schottky barrier(SB) across the junction [200] since this barrier provides resistance to charge carrier injection across the junction. Smaller the barrier, lower is the resistance, resulting in better FET performance. The SB height for hole injection can be estimated as $\phi_h = E_F - E_{VBM}$. For electron injection, it is $\phi_e = E_{CBM} - E_F$; E_F is the Fermi energy of the heterostructure while E_{CBM} and E_{VBM} are the conduction band minimum and the valence band maximum of semiconducting Sc_2CO_2. The schematic diagram for a field-effect transistor (FET) using this heterostructure is shown in Figure 5.7(a) while the position of the VBM of Sc_2CO_2 and Fermi level of the heterostructure is shown in Figure 5.7(b) and (c), respectively. The fermi level is slightly higher than VBM for the system under consideration. Consequently, ϕ_h is only 0.09 eV. This implies that the MSJ constructed out of this system will have a very small SB for hole injection. Further, for better performance of the FET, the semiconductor used in the heterostructure should also have a moderate bandgap and high carrier mobility. Sc_2CO_2, with a bandgap of 1.83 eV, is a moderate bandgap semiconductor. It is found to possess high hole mobility as well [190]. Thus, half-metallic VSe_2-contacted Sc_2CO_2 FET will have a very small SB

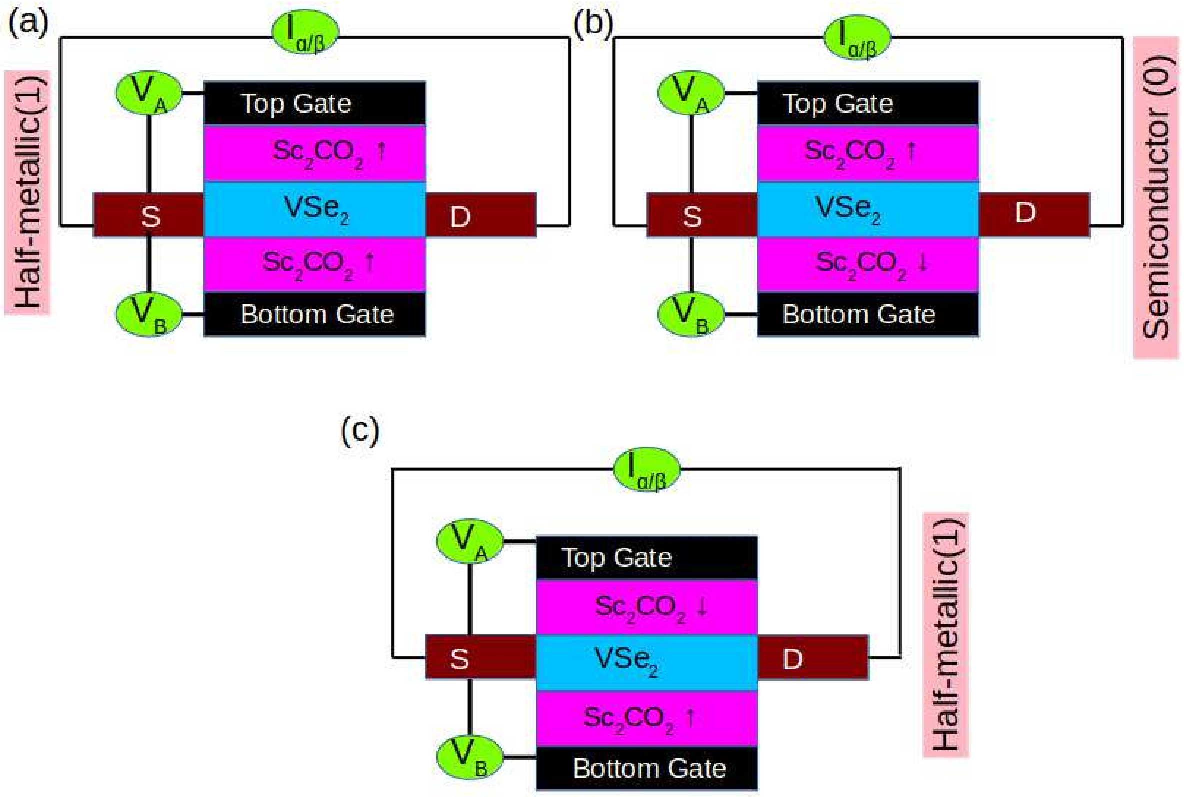

Figure 5.8: Schematic diagram of atom-thick multiferroic memory device using $Sc_2CO_2/VSe_2/Sc_2CO_2$ heterostructure.

and a high on/off ratio.

5.4.2 Prototype of a multiferroic memory

Two-dimensional (2D) ferroelectrics and 2D ferromagnets are promising nanodevices for information storage. While 2D ferromagnets suffer from non-volatility, 2D ferroelectrics are highly suitable for writing data but are less efficient for reading, the latter operation often being destructive. Memory devices constructed from Sc_2CO_2/VSe_2 or $Sc_2CO_2/VSe_2/Sc_2CO_2$ can overcome this difficulty. Non-volatile nanodevices for data storage can be constructed out of these heterostructures by utilizing the magnetoelectric coupling. In this nanodevice, the mechanism of data writing is the same as that of isolated monolayer Sc_2CO_2, achieved by switching the polarization state through the application of an electric field. Thus, isolated ferroelectrics' efficient data writing properties are retained in these multiferroics. The data reading part is done the following way: the multiferroic heterostructure (both bilayer or trilayer structure) is a half-metal or semiconductor, depending on the polarization state of Sc_2CO_2. As a result, the electric signal of the heterostructure will differ from state to state. The destructive effect observed in monolayer ferroelectrics can be genuinely avoided by reading the magnetoelectric coupling-induced signal differences with a damage-free current [203]. A prototype of this device using trilayer $Sc_2CO_2/VSe_2/Sc_2CO_2$ is shown in Figure 5.8. Here, the polarisation states of the two Sc_2CO_2 layers can be controlled by the application of two different voltages. Voltage V_A, applied between the top gate and VSe_2, helps to control the polarisation state of the top Sc_2CO_2 layer. Similarly, V_B, applied between the bottom gate and VSe_2, helps to control the polarisation state of the bottom Sc_2CO_2 layer.

5.5 Summary

Using first-principles-based DFT calculations, we have demonstrated that the electronic properties of bi-layer VSe_2/Sc_2CO_2 and tri-layer $Sc_2CO_2/VSe_2/Sc_2CO_2$ heterostructures can be reversibly tuned through the application of an electric field. Depending on the polarization states of Sc_2CO_2, these heterostructures exhibit semiconducting or half-metallic behavior. The switching mechanism can be understood based on the charge redistribution across the heterostructure interface. The heterostructures exhibit broken-gap type-III band alignment in their half-metallic state, making them ideal for tunnel field-effect transistors (TFETs). Further, the magneto-electric coupling in these heterostructures leading to the electric-field controlled switching of the electronic state provides an ideal platform for a non-volatile atom-thick high-density data storage. Since a number of MXene ferroelectrics with substantial polarization have been predicted from DFT-based high throughput calculations very recently [212], this work paves the ground for further exploration of MXene-TMDC heterostructures of different thicknesses towards the realization of more memory devices at the nanoscale.

Chapter 6

Rashba and Zeeman splitting in non-magnetic MXene Ta_2CS_2: consequences of non-centrosymmetry and strong spin-orbit coupling

6.1 Introduction

In this chapter, we demonstrate a MXene in single phase which inspite of being non-magnetic, exhibits potential for spin transport, coupled with other degrees of freedom. The effect arises out of structural features of the MXene and thus is a wonderful example of novel structure-property relations MXene family can manifest.

Strong interaction between the spin and orbital degrees of freedom creates an effective magnetic field which for noncentrosymmetric systems can lift the Kramer's degeneracy and give rise to novel effects like the Rashba that arises from structural inversion asymmetry [213, 214], or the Dresselhaus resulting due to the absence of bulk inversion asymmetry [215]. On top of these, a combination of non time-reversal invariant k-point and lack of inversion symmetry also leads to spin splitting of bands in the momentum space similar to the Zeeman effect [216]. Further, possibility of spin splitting of bands in a non-magnetic, non-centrosymmetric crystal, in the presence of spin-orbit coupling (SOC), has recently been shown where split bands do not show any net spin polarisation along certain high symmetry points of the Brillouin zone. Such systems with band splitting but having zero spin polarisation offer tunability with respect to the spin polarisation [217]. Such non-trivial spin splittings leads to diverse spin textures in presence of SOC, making the materials ideal candidates for spin valleytronics where spin textures can be manipulated by accessing different valleys around high symmetry k points [218, 219] enabling the design of spin transistors [220] and other devices. In recent times, two-dimensional materials have gained significant attention as good candidate materials for spin-related applications [221, 222, 223, 224]. Due to a variety of electronic properties that are strikingly different from their bulk counterparts there is large scope of tunability in 2D systems due to the flexibility in their structures and compositions. In this respect, two-dimensional transition metal dichalcogenides (TMDCs) have been extensively studied as potential candidates for spintronics materials [225, 226, 227, 228]. Strong SOC, generated from the d-orbitals of the transition metals in these compounds, have been understood to be responsible for the various spin-orbit-related behaviour, such as the large Rasbha effect

[229].

Recently, MXenes have emerged as promising materials for spintronics and valleytronics applications [230, 231, 232].Like TMDCs, the MXenes with heavier transition metals having *d* and/or *f* electrons are expected to display strong SOC and thus can make ideal candidates from device perspective. However, obtaining MXenes with heavier transition metals and non-centrosymmetric structures is particularly challenging. There are two ways to realize a noncentrosymmetric structure in MXenes: (1) creation of Janus structures by tuning compositions of the two surfaces and (2) the surfaces are chemically identical but the inversion symmetry is intrinsically broken due to the natural positioning of the termination groups. Among these two possibilities, the first one is more challenging. This is evident from the fact that no Janus MXene, till date, has been synthesised. Despite such limitations, DFT based investigations have been carried out to explore effects of SOC in Janus compounds from the MXene family [233, 234]. Mo-based Janus compounds were investigated [233] where large SOC due to the presence of $4d$ orbitals of Mo and asymmetric passivation of surfaces leading to broken inversion symmetry are exploited to show large Rashba effect and nonlinear anomolous Hall conductivity. Significant non-linear Rashba effect is also obtained in W-based Janus MXenes with asymmetric surface termination [234]. Though the results obtained in these two compounds from the MXene family are insightful, the limitations in their synthesis as mentioned above, makes experimental verification and subsequent realization in devices difficult. A more realistic approach, therefore, would be to explore SOC related effects in MXenes that are conventional from compositional aspect and are either experimentally synthesised or can be easily exfoliated from the corresponding MAX compounds that are available experimentally. Accordingly, in this work we have investigated SOC related phenomena in non-centrosymmetric MXene Ta_2CS_2, a compound having $5d$ electrons. Moreover, it is synthesised experimentally by sintering method [235, 236, 237]. Employing a combination of DFT and model Hamiltonian based approach, we find both Rashba and non-trivial Zeeman splitting in this compound. Spin textures obtained from our calculations suggest that this compound may be an ideal candidate for spin valleytronics.

6.2 Structural and Computational Details

6.2.1 Structural Details

Experimentally Ta_2CS_2 can be obtained by exfoliation of its commercially available parent MAX compound Ta_2AlC. As passivation of MXene surfaces by various functional groups during exfoliation from the parent MAX phase is observed to be an inevitability, -S functionalised Ta_2CS_2 MXene can be obtained upon removal of the Al layers during exfoliation. Experimentally Ta_2CS_2 was found to crystallise in a trigonal structure with space group P3m1 (space group 156) [235]. This was corroborated by DFT calculations [236] which showed a non-centrosymmetric structure of the compound where the S atoms on one surface prefers to occupy the hollow sites above the C atoms, while on the other surface they prefer the hollow sites below the Ta atoms (Figure 6.1 (a), (b) and (c)). The Ta atoms in the top layer (Ta_1) are coordinated to six ligands (C/S) in a trigonal prismatic crystal environment, whereas the Ta atoms in the bottom layer (Ta_2) are in an octahedral environment. Our calculations obtain the same structure with a lattice parameter of 3.25 Å which agrees quite well with the reported results [238]. It is worth mentioning that the dynamical and thermal stability of Ta_2CS_2 has already been established [236].

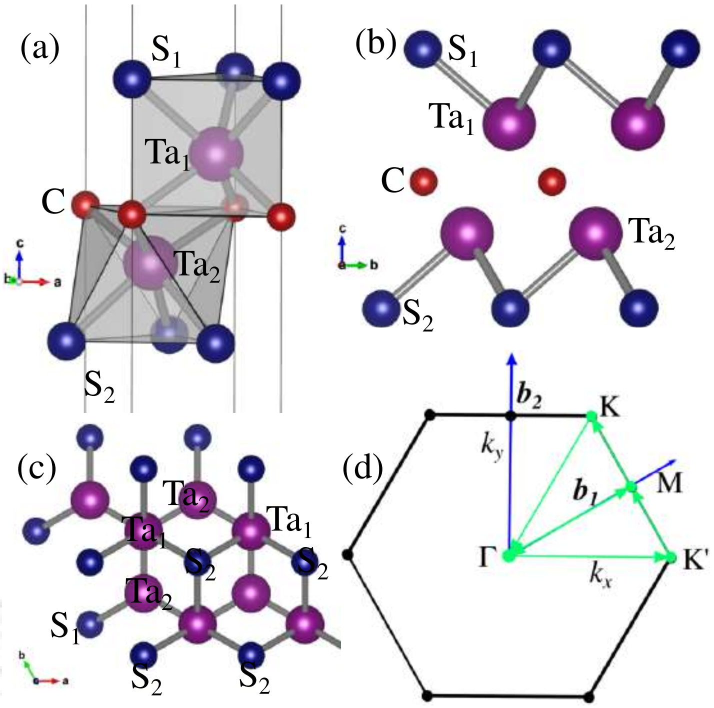

Figure 6.1: (a) Crystal structure of Ta_2CS_2 MXene. The red, blue, and violet atoms correspond to C, S, and Ta, respectively. In the unit cell, the two Ta atoms have different local environments. (b)-(c) Side and top views of the Ta_2CS_2 monolayer. (d) Brillouin zone corresponding to the MXene with a triangular unit cell.

Figure 6.1 (d) shows the Brillouin zone corresponding to the Ta_2CS_2. The Brillouin zone (BZ) has a hexagonal shape, with various high-symmetry points marked. The various high-symmetry points of the BZ in the reciprocal lattice co-ordinate system, include $\Gamma(0,0,0)$ at the center of the BZ, $K(\frac{1}{3},\frac{1}{3},0)$ and $K'(\frac{2}{6},-\frac{1}{3},0)$ at the corner of the hexagonal Brillouin zone, and $M(\frac{1}{2},0,0)$ at the center of line joining the corners. Among these points, Γ and M are TRIM (Time reversal invariant momentum) points, while K and K' are non-TRIM points.

6.2.2 Computational method

The DFT calculations to obtain the electronic structures are done using using projector augmented wave (PAW) method [146]. The exchange-correlation part of the Hamiltonian is approximated by generalized gradient approximation (GGA) as parameterized by Perdew-Burke-Ernzerhof (PBE) [123]. The kinetic energy cutoff of the plane wave is set to be 550 eV. The energy and force cutoff for structural optimization are 10^{-6} eV and 0.01 eV/Å, respectively. To include the van-der-Waals interactions, the DFT-D3 method is employed [147]. The Brillouin zone is sampled using Monkhorst-Pack $14 \times 14 \times 1$ k-point mesh. Dipole corrections are also taken into account in all the calculations. A 20 Å vacuum is considered along z-direction to avoid any interactions between the adjacent layers.

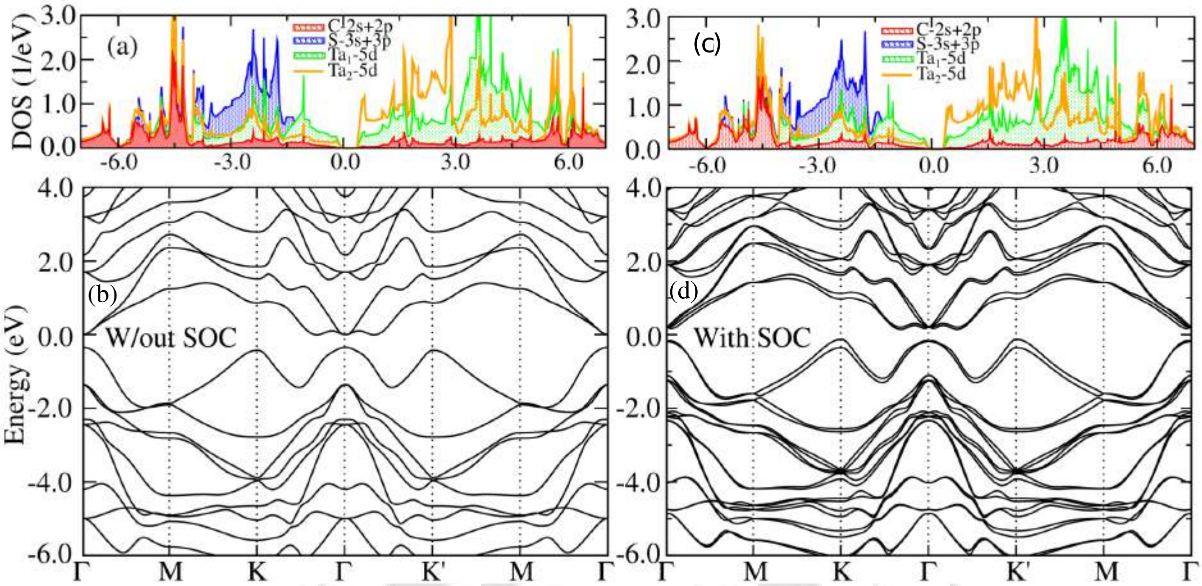

Figure 6.2: The densities of states and electronic band structure of Ta_2CS_2 without and with SOC are shown. In (a) and (b), the total and projected DOS for Ta_1-$5d$, C-$2s + 2p$, and S-$3s + 3p$ states and band structure are presented without SOC, respectively. (c) and (d) show the total and projected DOS and band structure along various high-symmetry points in the Brillouin zone with SOC, respectively. The band structures are plotted along the high-symmetry path: Γ (0,0,0) → M (1/2,0,0) → K (1/3,1/3,0) → Γ (0,0,0) → K' (2/6,-1/3,0) → M (1/2,0,0) → Γ (0,0,0). All positions are given in the reciprocal lattice co-ordinate system. All energies are with respect to the Fermi level.

6.3 Electronic structure

To begin with, we have analysed the densities of states (DOS), both total and atom-projected, along with the band structure of Ta_2CS_2, without SOC (Figure 6.2 (a) and (b), respectively). The compound exhibits semiconducting behaviour. The origin of its semiconducting gap can be understood based on electron filling.

The valence electron count for each atom in Ta_2CS_2 is as follows: each Ta has 5 valence electrons while each C and S have 4 and 6 valence electrons, respectively. Consequently, Ta_2CS_2 has a total of 26 valence electrons. These electrons occupy the available 24 states contributed by C-s, C-p, S-s, and S-p orbitals, as illustrated in Figure 6.2(a). The remaining two electrons fill the low lying isolated 5d state of Ta_1 residing in the prismatic environment. The orbital projected band structure reveal that the topmost valence band is predominantly of Ta_1 $3z^2$-1 character around the Γ point, consistent with the prismatic environment of Ta_1 . The band structure without SOC (Figure 6.2(b)) reveals that Ta_2CS_2 is a direct bandgap semiconductor with a calculated bandgap of 0.34 eV in good agreement with the existing results [236]. Both the valence band maximum (VBM) and conduction band minimum (CBM) are located at the zone center Γ, as shown in Figure 6.2(b).

Figures 6.2(c) and (d) display respectively, the total and orbital projected DOS and band structure of the compound, calculated including SOC. While SOC has a negligible effect on the DOS, its impact is prominent in the band structure, leading to band splitting.

SOC removes the spin degeneracy of bands along various high-symmetry directions in the Brillouin zone. The most significant splitting is observed along the $M-K-\Gamma$ and along $\Gamma-K'-M$ directions. The bandgap in the SOC-included band structure slightly reduces to 0.27 eV. Among the high-symmetry points, the splitting of the bands is large at K and K'. The detailed nature and characteristics of these band splittings are discussed in the following section.

6.4 Nature of Band splitting and spin texture

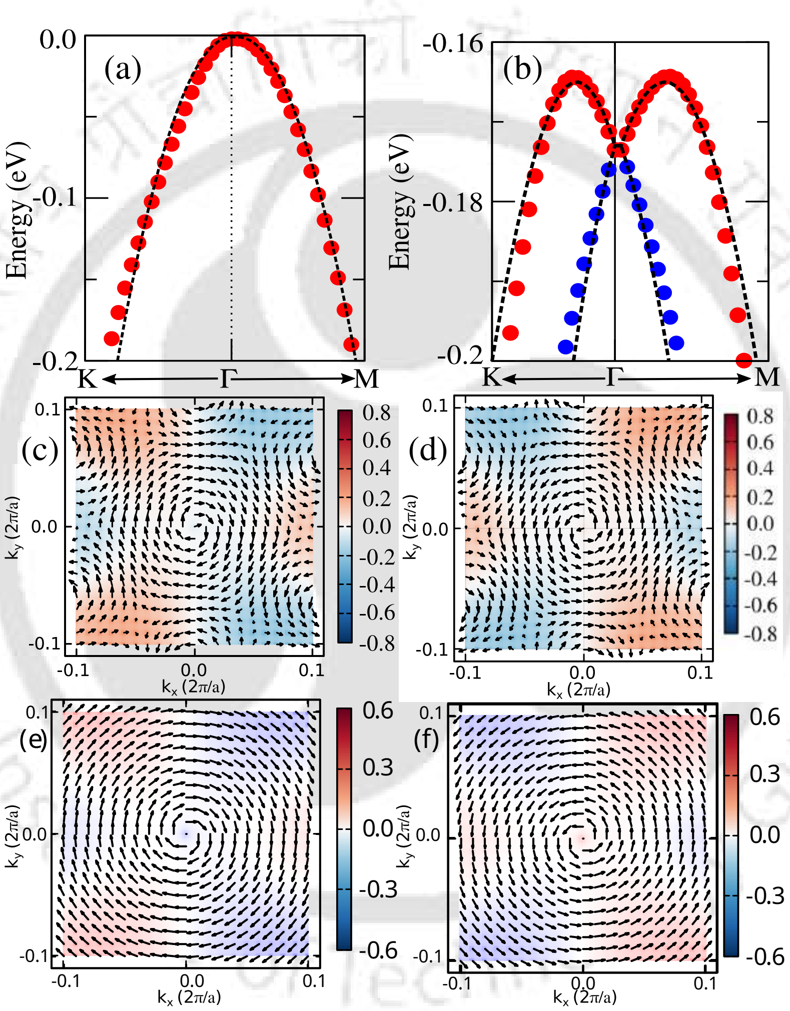

Figure 6.3: (a)-(b) Valence band maximum band structure along $K:\frac{2\pi}{a}(0.07,0,0)$-$\Gamma$: $(0,0,0)$-M: $\frac{2\pi}{a}(0.0,0.07,0)$ obtained without and with SOC . The band structure obtained from DFT is plotted with circles, while the band structure obtained from the **k.p** model Hamiltonian is plotted with dotted lines. (c)-(d) Spin texture (ST) of the inner and outer branches around the Γ point for the valence band maximum obtained from DFT calculations. The in-plane components of the spin expectation values are represented by vectors, while the out-of-plane component is depicted using color bars. (e)-(f) Spin texture (ST) of the inner and outer branches around the Γ point for the valence band maximum obtained from k.p model Hamiltonian.

Table 6.1: Symmetry operations of C_{3v} point group.

Γ point		
Symmetry operation	$\{k_x, k_y, k_z\}$	$\{\sigma_x, \sigma_y, \sigma_z\}$
$C_3^+([001]) = e^{-i\frac{\pi}{3}\sigma_z}$	$\left\{\begin{array}{c} -\frac{1}{2}k_x + \frac{\sqrt{3}}{2}k_y, \\ -\frac{\sqrt{3}}{2}k_x - \frac{1}{2}k_y, \\ k_z \end{array}\right\}$	$\left\{\begin{array}{c} -\frac{1}{2}\sigma_x + \frac{\sqrt{3}}{2}\sigma_y, \\ -\frac{\sqrt{3}}{2}\sigma_x - \frac{1}{2}\sigma_y, \\ \sigma_z \end{array}\right\}$
$C_3^-([001]) = e^{i\frac{\pi}{3}\sigma_z}$	$\left\{\begin{array}{c} -\frac{1}{2}k_x - \frac{\sqrt{3}}{2}k_y, \\ \frac{\sqrt{3}}{2}k_x - \frac{1}{2}k_y, \\ k_z \end{array}\right\}$	$\left\{\begin{array}{c} -\frac{1}{2}\sigma_x - \frac{\sqrt{3}}{2}\sigma_y, \\ \frac{\sqrt{3}}{2}\sigma_x - \frac{1}{2}\sigma_y, \\ \sigma_z \end{array}\right\}$
$\sigma = -i\left(-\frac{1}{2}\sigma_x + \frac{\sqrt{3}}{2}\sigma_y\right)$	$\left\{\begin{array}{c} \frac{1}{2}k_x + \frac{\sqrt{3}}{2}k_y, \\ \frac{\sqrt{3}}{2}k_x - \frac{1}{2}k_y, \\ k_z \end{array}\right\}$	$\left\{\begin{array}{c} -\frac{1}{2}\sigma_x - \frac{\sqrt{3}}{2}\sigma_y, \\ -\frac{\sqrt{3}}{2}\sigma_x + \frac{1}{2}\sigma_y, \\ -\sigma_z \end{array}\right\}$
$\sigma' = -i\left(-\frac{1}{2}\sigma_x - \frac{\sqrt{3}}{2}\sigma_y\right)$	$\left\{\begin{array}{c} \frac{1}{2}k_x - \frac{\sqrt{3}}{2}k_y, \\ -\frac{\sqrt{3}}{2}k_x - \frac{1}{2}k_y, \\ k_z \end{array}\right\}$	$\left\{\begin{array}{c} -\frac{1}{2}\sigma_x + \frac{\sqrt{3}}{2}\sigma_y, \\ \frac{\sqrt{3}}{2}\sigma_x + \frac{1}{2}\sigma_y, \\ -\sigma_z \end{array}\right\}$
$\sigma'' = -i\sigma_x$	$\{-k_x, k_y, k_z\}$	$\{\sigma_x, -\sigma_y, -\sigma_z\}$

6.4.1 Rashba Effect

To begin with, we analyze the valence band maximum of Ta_2CS in the vicinity of the high-symmetry Γ point along the K-Γ-M path. Figures 6.3(a) and 6.3(b) display the DFT band structure (solid circles) in a narrow energy range along the path K-Γ-M without and with SOC, respectively. From Figure 6.3(b), it is evident that the inclusion of SOC results in band splitting into two distinct branches. Moreover, the local band maximum shifts away from the Γ point, exhibiting features similar to the Dresselhaus and Rashba effect.

To identify the dominant effect, we have calculated the DFT spin textures for both branches. The results are presented in Figures 6.3(c) and 6.3(d). Both branches exhibit a chiral spin texture, with the outer branch displaying a spin texture pattern opposite to that of the inner branch. This confirms the presence of the Rashba effect around the high-symmetry Γ point. Furthermore, from Figures 6.3(c) and 6.3(d), we observe that in addition to the spin expectation values $\langle\sigma_x\rangle$ and $\langle\sigma_y\rangle$, a finite $\langle\sigma_z\rangle$ spin expectation value is also present. This indicates the presence of higher-order k dependent terms [219].

To gain deeper insight into these DFT results, we derive next a low-energy $\mathbf{k}\cdot\mathbf{p}$ model Hamiltonian. The little group symmetry around the Γ point is C_{3v}. Under C_{3v} symmetry, a C_3 rotation is present with respect to the trigonal axis k_z in both clockwise and anticlockwise directions. The little group also includes three mirror planes. One mirror plane lies in the k_y-k_z plane and is defined as σ''. The other two mirror planes can be obtained by applying C_3 and C_3^2 operations to the initial mirror plane. These are defined as σ and σ', respectively. Under these symmetry operations, momentum and spin operators transform as listed in Table 6.1. Thus, the symmetry-adapted $\mathbf{k}\cdot\mathbf{p}$ model

Hamiltonian for the valence band at the Γ point is:

$$\begin{aligned} H_{\Gamma}^{V}(k) &= H_0(k) + H_{SOC}(k) \\ &= -\frac{\hbar^2}{2m^*}\left(k_x^2 + k_y^2\right) + \alpha_R\left(\sigma_y k_x - \sigma_x k_y\right) \\ &\quad +\gamma\left(k_x^3 - 3k_x k_y^2\right)\sigma_z \end{aligned} \tag{6.1}$$

A symmetry-adapted cubic term in the model Hamiltonian is included to explain the out-of-plane spin component. The band structures, obtained from the $\mathbf{k}\cdot\mathbf{p}$ model Hamiltonian with and without SOC, are plotted as dotted lines in Figures 6.3(a) and 6.3(b), respectively. A comparison with DFT band structures (solid circles) reveal a good agreement between the DFT results and the $\mathbf{k}\cdot\mathbf{p}$ model Hamiltonian calculations.

The fitted Rashba parameter is found to be $\alpha_R = 0.4$ eV Å, and the cubic parameter is $\gamma = 10.8$ eV Å^3. The spin textures obtained from the $\mathbf{k}\cdot\mathbf{p}$ model Hamiltonian calculations, shown in Figures 6.3(e) and 6.3(f), exhibit a good agreement with those obtained from DFT calculations. This consistency confirms the robustness of the low-energy $\mathbf{k}\cdot\mathbf{p}$ model Hamiltonian [Eq. 6.1].

6.4.2 Zeeman Effect

We now examine the spin splitting and consequent spin textures around the non-TRIM points (K) and (K'). The band structure of the top most valence band is shown around the high-symmetry points K and K' along the path $M \to K \to \Gamma \to K' \to M$, both without and with SOC, in Fig. 6.4(a)-(b), respectively. We observe that the spin degeneracy of the bands are lifted upon the inclusion of SOC. Contrary to the Rashba and Dresselhaus effect, the spin splitting around the non-TRIM points K and K' does not have band crossing, rather the splitting is similar to that observed for magnetic systems with broken time reversal symmetry referred to as Zeeman effect. The intrinsic magnetic field due to broken inversion symmetry induces Zeeman like spin splitting, leading to an energy splitting 232 meV at the K and K' points for the top most valence band.

Next we analyse the orbital composition of the topmost valence band around the high-symmetry points (K) and (K') shown in Figure 6.4(c). The results reveal that the topmost valence band of Ta_2CS_2 around K and K' is predominantly composed of ($d_{x^2-y^2}$) and (d_{xy}) orbital character, while the Γ point has $d_{3z^2-r^2}$ character. This is consistent with the prismatic crystal field where the d-states split into three configurations: ($\{d_{x^2-y^2}, d_{xy}\}$), ($\{d_{3z^2-r^2}\}$), and ($\{d_{xz}, d_{yz}\}$). Interestingly, at the K and K' points, the states combine as ($d_{x^2-y^2} - id_{xy}$) and ($d_{x^2-y^2} + id_{xy}$), respectively, belonging to the eigenstate of the (L_z) operator,

$$L_z\left(|d_{x^2-y^2}\rangle \pm |id_{xy}\rangle\right) = \pm 2\hbar\left(|d_{x^2-y^2}\rangle \pm i\,|d_{xy}\rangle\right) \tag{6.2}$$

In Fig. 6.4(d) we have shown the projected $|(d_{x^2-y^2} \pm id_{xy})\rangle$ character and find that $L_z = -2$ corresponds to the K point while at K' point it is $L_z = +2$.

The three components of the spin expectation values $\langle\sigma_x\rangle$, $\langle\sigma_y\rangle$, $\langle\sigma_z\rangle$ along the path $M \to K \to \Gamma \to K' \to M$ are shown in Fig. 6.5(a), 6.5(b) and 6.5(c) respectively. We find around the high symmetry point K and K' the predominant contribution is provided by the $\langle\sigma_z\rangle$ component of the spin expectation value. Further at the K and K' valley, the sign of the spin polarization is opposite.

To understand the Zeeman-type band splitting , as well as the spin-momentum flipping at these points, we conducted a symmetry analysis. At the non-TRIM high-symmetry

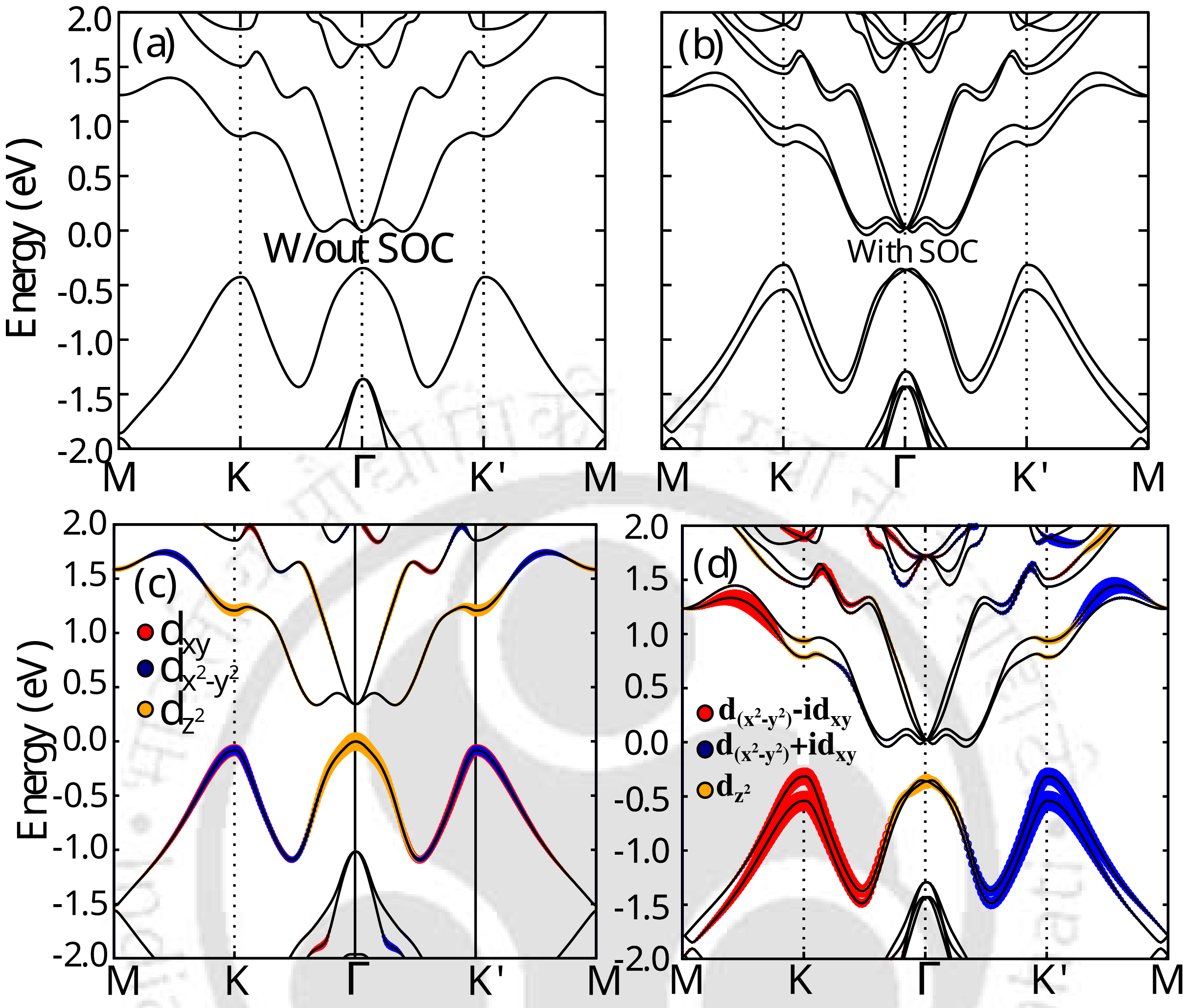

Figure 6.4: (a)-(b) Band structure without and with SOC along the path M-K-Γ-K'-M. (c)-(d) Band structure (black lines) with projected orbital characters, without and with SOC, respectively. The Fermi level of the system is set to zero on the energy axis. The orbital characters of the bands correspond to Ta-$d_{x^2-y^2} - id_{xy}$ (red), Ta-$d_{x^2-y^2} + id_{xy}$ (blue), and Ta-d_{z^2} (orange) for with SOC.

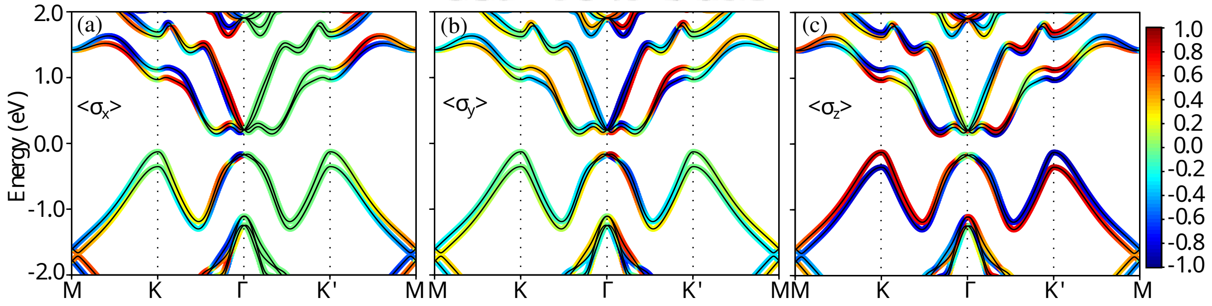

Figure 6.5: (a)-(c) Band structure and spin texture in the presence of SOC along the path M-K-Γ-K'-M. The color code represents the orientation of the spin components.

points K and K', the little group symmetry is (C_3). Under the (C_3) little group, a (C_3) rotation is present with respect to the trigonal axis (k_z), operating in both clockwise and counter clockwise directions. The (C_3) operation transforms (r_+, r_-, z) as follows:

$$(r_+, r_-, z) \rightarrow \left(e^{2\pi i/3} r_+, e^{-2\pi i/3} r_-, z\right) \tag{6.3}$$

where $(r_\pm = x \pm iy)$ and z remain invariant. The allowed $(\mathbf{k} \cdot \mathbf{p})$ model Hamiltonian at the non-TRIM K, K' points preserving SOC-induced effects and (C_3) symmetry, is given by [228]:

$$H_{K/K'} = H_0(k) - \lambda \hat{L}_z \hat{\sigma_z} \tag{6.4}$$

where $H_0(k)$ represents the usual free electron dispersion. This Hamiltonian explains the Zeeman type splitting at the (K) and (K') points. The flipping of the spin expectation values is attributed to $L_z = -2(+2)$ at the $K\,(K')$ respectively. This spin splitting is intrinsically linked to the valley index, establishing a spin-valley coupling mechanism. As a result, when charge carriers transit between valleys, they must simultaneously reverse their spin direction while undergoing a significant momentum change. This transition is expected to be relatively slow, enabling long valley lifetimes-potentially reaching microseconds-which is a crucial property for valleytronic applications.

6.5 Summary

In this work, we have investigated in detail the effect of spin-orbit coupling on the electronic structure of a representative non-centrosymmetric, non-magnetic MXene Ta_2CS_2. Our calculations reveal that the valence bands near the Fermi level are predominantly contributed by Ta_1-d states in a prismatic environment. The inclusion of spin-orbit interaction leads to band splitting around various high-symmetry points with characteristic spin textures.

At the polar time-reversal invariant momentum (TRIM) point Γ, where the system possesses C_{3v} little-group symmetry, upon inclusion of SOC, we observe that both linear and higher-order Rashba effect are responsible for the band splitting. The presence of σ_z component in the spin texture is attributed to higher order Rashba terms. Notably, the higher-order Rashba term exhibit a greater strength than the linear term.

Around the two valleys, K and K', the top most valence band display Zeeman-type spin splitting with a strength of 232 meV. This giant splitting originates from the strong SOC of the Ta_1-d orbitals. The observed splitting is analogous to that in transition metal dichalcogenides (TMDs), where the transition metal also resides in a prismatic environment. Additionally, we observe an opposite spin splitting of bands at the K and K' points, which arises due to the different orbital compositions at these high-symmetry points.

Similar to TMDs, Ta_2CS_2 exhibits valley-dependent complex orbital characters and spin splitting in the valence bands. The former gives rise to orbital momentum with opposite signs at the K and K' valleys, that potentially may lead to a large orbital Hall effect. Meanwhile, the spin splitting can result in a nonzero spin Hall effect, as observed in TMDs [239]. These findings highlight the potential of Ta_2CS_2 for spintronic and valleytronic applications. In recent times, several chalcogen-terminated MXenes with transition metals from $4d$ and $5d$ series with non-centrosymmetric crystal environment have been synthesised [240, 241, 242, 243]. DFT based calculations have also identified several of them [236]. The potential of Ta_2CS_2 for spintronics and valleytronics applications identified in this work will pave the way for further investigations and subsequent useful insight into this family of compounds. Building upon the findings of this work, similar spin–orbit coupling (SOC) effects can be anticipated in other members of the MXene family. As previously discussed, the key requirements for observing such effects are that the MXene must be non-centrosymmetric, semiconducting, and contain a heavy element. From this standpoint, materials such as Y_2CO_2 and Y_2CS_2 are promising candidates, as they fulfill all these criteria [236]. Another intriguing direction involves Janus MXenes, which allow for a wide range of permutations and combinations of constituent transition metals. This compositional flexibility offers a tunable platform for engineering SOC-related phenomena in them.

Chapter 7

Summary and future direction

7.1 Summary

In this dissertation, I have explored the potential of MXenes for various magnetism-related applications — an area that remains relatively new and underexplored. We have explored both MXenes that are magnetic themselves and the ones that are non-magnetic, but magnetism-related phenomena occur in systems where they are constituents. The first two chapters focus on a detailed investigation of the magnetic behavior of single and double transition metal (i-MXene) MXenes. Our results demonstrate that these materials exhibit significant tunability, making them strong candidates for use in various magnetic devices. The following two chapters shift attention to emerging fields such as spintronics and valleytronics, where the unique properties of MXenes can be effectively utilized. As the MXene family continues to grow, the insights from this work are expected to assist experimentalists in better prediction and design of new materials. A brief summary of each chapter is provided below.

In **Chapter 3**, how the structural and chemical flexibility of Cr-based i-MXenes can be used to modify their magnetic characteristics is explored. We analyze three i-MXenes of Cr coupled with a non-magnetic transition metal using density functional theory (DFT). We find that changes in surface functional groups and the presence of non-magnetic elements can significantly affect the electrical and magnetic behavior. In particular, ferromagnetic half-metallic states are often stabilized by –O functionalization, making these materials perfect for spintronic applications such as spin filters. Additionally, some compounds have perpendicular magnetic anisotropy (PMA), which improves performance and stability and is helpful for applications such as magnetic sensors and memory technologies like STT-MRAM. Notably, $(Cr_{2/3}Zr_{1/3})_2CF_2$ shows strong magnetic properties similar to known 2D magnets used in real devices, highlighting the potential of i-MXenes for practical applications in magnetic technologies.

MXenes are known for their flexible composition and structure, which is the source of their tunability. However, the possibility of changing how the metal layers are stacked (beyond the usual ABC stacking) hasn't been explored much until recently. Inspired by new experimental and theoretical studies, we investigated in **Chapter 4** how different stacking patterns affect the electronic and magnetic behavior of nitride MXenes with two types of surface functionalization. Our results show that stacking changes can lead to changes in magnetic ground states—like switching between antiferromagnetic (AFM), ferromagnetic (FM), and even non-magnetic phases. We also observed that the electronic properties can shift dramatically, such as turning a metal into a half-metal or a spin-gapless semiconductor. Some stacking patterns even give rise to strong magnetic anisotropy and magnetic ordering temperatures close to room temperature. These findings open new possibilities for magnetic MXene applications and suggest that changing the stacking is a viable way to tune their properties.

In **Chapter 5** , we focus on a magnetic heterostructure comprising of a magnetic TMDC VSe_2 and a non-magnetic but ferroelectric MXene Sc_2CO_2. We show that the electronic behavior of bi-layer VSe_2/Sc_2CO_2 and tri-layer $Sc_2CO_2/VSe_2/Sc_2CO_2$ structures can be easily switched by applying an electric field so that these heterostructures behave like multiferroics. Depending on how the Sc_2CO_2 layers are electrically polarized, these heterostructures can act as semiconductors or half-metals. This switching happens because of charge transfer across interfaces. In their half-metallic states, these structures have a special band alignment (broken-gap type-III), making them great candidates for tunnel field-effect transistors (TFETs). Additionally, the magneto-electric coupling allows electric control over their ground states, making them perfect for non-volatile, ultra-thin, high-density data storage devices. With many MXene ferroelectrics recently predicted to have strong polarization, this study opens up new possibilities to explore MXene-TMDC layered materials for future nanoscale memory technologies.

In **Chapter 6**, we have explored critically the role of spin-orbit coupling (SOC) on the electronic properties of another non-magnetic MXene Ta_2CS_2. Our results show that the valence bands near the Fermi level mainly come from Ta_1-d orbitals in a prismatic structure. When SOC is included, these bands split near certain points in the Brillouin zone, showing unique spin patterns. At the center point (Γ), the splitting is due to both regular and higher-order Rashba effects, with the higher-order term being stronger and causing an out-of-plane spin polarisation. At the K and K' points (valleys), a large Zeeman-type spin splitting of 232 meV is seen, that is caused by the strong SOC of Ta. This is similar to what is found in TMD materials. These valleys also show opposite spin splitting and orbital characters, suggesting that Ta_2CS_2 might exhibit both spin Hall and orbital Hall effects. Overall, this work shows that Ta_2CS_2 has promising properties for use in spintronics and valleytronics. Since many similar MXenes with strong SOC have recently been made or predicted, our study opens the door for more research in this area with MXenes.

7.2 Future Direction

The studies presented in this thesis open up significant opportunities for future research. Some potential directions for extending this work are outlined below:

- Solid-solution MXenes represent a largely unexplored category regarding their magnetic behavior. These materials hold the potential to exhibit intriguing and tunable magnetic properties.

- Janus MXenes can be explored from a multiferroic perspective. Due to their inherent asymmetry, they lack inversion symmetry, which leads to a built-in electric field. Furthermore, by carefully selecting and tuning the transition metal constituents, it may be possible to achieve multiferroic behavior in these materials.

- MXene-based heterostructures offer a promising platform for exploring twistronics-related phenomena. By introducing a twist angle between MXene layers or between MXene and other 2D materials, novel electronic and magnetic behaviors may emerge. Such studies could open new directions in tunable quantum devices and moiré engineering.

- The study of MXene/TMDC heterostructures can be further extended toward the design of field-effect transistor (FET) devices. Investigating their transport properties within such architectures could unveil promising functionalities for nanoelectronic applications.

- MXenes can be utilized in the construction of magnetic tunnel junctions. A promising direction would be to design a heterostructure where one magnetic electrode is an alter magnet such as RuO_2, and the non-magnetic spacer layer is an MXene. The second magnetic electrode is either an MXene or a transition metal dichalcogenide (TMDC).

References

[1] LD Landau. Landau and lifshitz course of theoretical physics 5: Statistical physics part 1, 1980.

[2] Pere Miró, Martha Audiffred, and Thomas Heine. An atlas of two-dimensional materials. *Chemical Society Reviews*, 43(18):6537–6554, 2014.

[3] Kostya S Novoselov, Andre K Geim, Sergei V Morozov, De-eng Jiang, Yanshui Zhang, Sergey V Dubonos, Irina V Grigorieva, and Alexandr A Firsov. Electric field effect in atomically thin carbon films. *science*, 306(5696):666–669, 2004.

[4] Vestince B Mbayachi, Euphrem Ndayiragije, Thirasara Sammani, Sunaina Taj, Elice R Mbuta, et al. Graphene synthesis, characterization and its applications: A review. *Results in Chemistry*, 3:100163, 2021.

[5] Chaoliang Tan, Xiehong Cao, Xue-Jun Wu, Qiyuan He, Jian Yang, Xiao Zhang, Junze Chen, Wei Zhao, Shikui Han, Gwang-Hyeon Nam, et al. Recent advances in ultrathin two-dimensional nanomaterials. *Chemical reviews*, 117(9):6225–6331, 2017.

[6] Valeria Nicolosi, Manish Chhowalla, Mercouri G Kanatzidis, Michael S Strano, and Jonathan N Coleman. Liquid exfoliation of layered materials. *Science*, 340(6139):1226419, 2013.

[7] Jonathan N Coleman, Mustafa Lotya, Arlene O'Neill, Shane D Bergin, Paul J King, Umar Khan, Karen Young, Alexandre Gaucher, Sukanta De, Ronan J Smith, et al. Two-dimensional nanosheets produced by liquid exfoliation of layered materials. *Science*, 331(6017):568–571, 2011.

[8] Aleksander A Tedstone, David J Lewis, and Paul O'Brien. Synthesis, properties, and applications of transition metal-doped layered transition metal dichalcogenides. *Chemistry of Materials*, 28(7):1965–1974, 2016.

[9] Saju Joseph, Jainy Mohan, Seetha Lakshmy, Simil Thomas, Brahmananda Chakraborty, Sabu Thomas, and Nandakumar Kalarikkal. A review of the synthesis, properties, and applications of 2d transition metal dichalcogenides and their heterostructures. *Materials Chemistry and Physics*, 297:127332, 2023.

[10] Amir Pakdel, Yoshio Bando, and Dmitri Golberg. Nano boron nitride flatland. *Chemical Society Reviews*, 43(3):934–959, 2014.

[11] Nasrin Sultana, Annabelle Degg, Samiran Upadhyaya, Tom Nilges, and Neelotpal Sen Sarma. Synthesis, modification, and application of black phosphorus, few-layer black phosphorus (flbp), and phosphorene: a detailed review. *Materials Advances*, 3(14):5557–5574, 2022.

[12] Hideyuki Nakano, Takuya Mitsuoka, Masashi Harada, Kayo Horibuchi, Hiroshi Nozaki, Naoko Takahashi, Takamasa Nonaka, Yoshiki Seno, and Hiroshi Nakamura. Soft synthesis of single-crystal silicon monolayer sheets. *Angewandte Chemie International Edition*, 45(38):6303–6306, 2006.

[13] Michael Naguib, Murat Kurtoglu, Volker Presser, Jun Lu, Junjie Niu, Min Heon, Lars Hultman, Yury Gogotsi, and Michel W Barsoum. Two-dimensional nanocrystals produced by exfoliation of ti3alc2. In *MXenes*, pages 15–29. Jenny Stanford Publishing, 2023.

[14] Laixiang Qin and Li Wang. Two-dimensional materials, the ultimate solution for future electronics and very-large-scale integrated circuits. *Nano-Micro Letters*, 17(1):1–53, 2025.

[15] Tanmoy Das and Jong-Hyun Ahn. Development of electronic devices based on two-dimensional materials. *FlatChem*, 3:43–63, 2017.

[16] N David Mermin. Crystalline order in two dimensions. *Physical review*, 176(1):250, 1968.

[17] Oleg V Yazyev and Lothar Helm. Defect-induced magnetism in graphene. *Physical Review B—Condensed Matter and Materials Physics*, 75(12):125408, 2007.

[18] Qinghua Miao, Lidong Wang, Zhaoyuan Liu, Bing Wei, Fubiao Xu, and Weidong Fei. Magnetic properties of n-doped graphene with high curie temperature. *Scientific reports*, 6(1):21832, 2016.

[19] Bevin Huang, Genevieve Clark, Efrén Navarro-Moratalla, Dahlia R Klein, Ran Cheng, Kyle L Seyler, Ding Zhong, Emma Schmidgall, Michael A McGuire, David H Cobden, et al. Layer-dependent ferromagnetism in a van der waals crystal down to the monolayer limit. *Nature*, 546(7657):270–273, 2017.

[20] Cheng Gong, Lin Li, Zhenglu Li, Huiwen Ji, Alex Stern, Yang Xia, Ting Cao, Wei Bao, Chenzhe Wang, Yuan Wang, et al. Discovery of intrinsic ferromagnetism in two-dimensional van der waals crystals. *Nature*, 546(7657):265–269, 2017.

[21] Xue Jiang, Qinxi Liu, Jianpei Xing, Nanshu Liu, Yu Guo, Zhifeng Liu, and Jijun Zhao. Recent progress on 2d magnets: Fundamental mechanism, structural design and modification. *Applied Physics Reviews*, 8(3), 2021.

[22] Manuel Bonilla, Sadhu Kolekar, Yujing Ma, Horacio Coy Diaz, Vijaysankar Kalappattil, Raja Das, Tatiana Eggers, Humberto R Gutierrez, Manh-Huong Phan, and Matthias Batzill. Strong room-temperature ferromagnetism in vse2 monolayers on van der waals substrates. *Nature nanotechnology*, 13(4):289–293, 2018.

[23] Xingzhi Wang, Kezhao Du, Yu Yang Fredrik Liu, Peng Hu, Jun Zhang, Qing Zhang, Man Hon Samuel Owen, Xin Lu, Chee Kwan Gan, Pinaki Sengupta, et al. Raman spectroscopy of atomically thin two-dimensional magnetic iron phosphorus trisulfide (feps3) crystals. *2D Materials*, 3(3):031009, 2016.

[24] Kangwon Kim, Soo Yeon Lim, Jungcheol Kim, Jae-Ung Lee, Sungmin Lee, Pilkwang Kim, Kisoo Park, Suhan Son, Cheol-Hwan Park, Je-Geun Park, et al. Antiferromagnetic ordering in van der waals 2d magnetic material mnps3 probed by raman spectroscopy. *2D Materials*, 6(4):041001, 2019.

[25] Jia Li, Bei Zhao, Peng Chen, Ruixia Wu, Bo Li, Qinglin Xia, Guanghua Guo, Jun Luo, Ketao Zang, Zhengwei Zhang, et al. Synthesis of ultrathin metallic mte2 (m= v, nb, ta) single-crystalline nanoplates. *Advanced Materials*, 30(36):1801043, 2018.

[26] Boyi Zhou, Yiping Wang, Gavin B Osterhoudt, Paula Lampen-Kelley, David Mandrus, Rui He, Kenneth S Burch, and Erik A Henriksen. Possible structural transformation and enhanced magnetic fluctuations in exfoliated α-rucl3. *Journal of Physics and Chemistry of Solids*, 128:291–295, 2019.

[27] Mykola Abramchuk, Samantha Jaszewski, Kenneth R Metz, Gavin B Osterhoudt, Yiping Wang, Kenneth S Burch, and Fazel Tafti. Controlling magnetic and optical properties of the van der waals crystal crcl3- xbrx via mixed halide chemistry. *Advanced materials*, 30(25):1801325, 2018.

[28] Ruilin Han, Zhou Jiang, and Yu Yan. Prediction of novel 2d intrinsic ferromagnetic materials with high curie temperature and large perpendicular magnetic anisotropy. *The Journal of Physical Chemistry C*, 124(14):7956–7964, 2020.

[29] Yalong Jiao, Weikang Wu, Fengxian Ma, Zhi-Ming Yu, Yunhao Lu, Xian-Lei Sheng, Yunwei Zhang, and Shengyuan A Yang. Room temperature ferromagnetism and antiferromagnetism in two-dimensional iron arsenides. *Nanoscale*, 11(35):16508–16514, 2019.

[30] Xiao Tang, Weiguo Sun, Yuantong Gu, Cheng Lu, Liangzhi Kou, and Changfeng Chen. Cob 6 monolayer: A robust two-dimensional ferromagnet. *Physical Review B*, 99(4):045445, 2019.

[31] Ehsan Elahi, Ghulam Dastgeer, Ghazanfar Nazir, Sobia Nisar, Mudasar Bashir, Haroon Akhter Qureshi, Deok-kee Kim, Jamal Aziz, Muhammad Aslam, Kashif Hussain, et al. A review on two-dimensional (2d) magnetic materials and their potential applications in spintronics and spin-caloritronic. *Computational Materials Science*, 213:111670, 2022.

[32] Guangchao Shi, Nan Huang, Jingyuan Qiao, Xuewen Zhang, Fulong Hu, Hanwei Hu, Xinyu Zhang, and Jingzhi Shang. Recent progress in two-dimensional magnetic materials. *Nanomaterials*, 14(21):1759, 2024.

[33] Haiyu Wang, Hao Wu, Jie Zhang, Yingjie Liu, Dongdong Chen, Chandan Pandey, Jialiang Yin, Dahai Wei, Na Lei, Shuyuan Shi, et al. Room temperature energy-efficient spin-orbit torque switching in two-dimensional van der waals fe3gete2 induced by topological insulators. *Nature communications*, 14(1):5173, 2023.

[34] Masoumeh Davoudiniya and Biplab Sanyal. Tuning of spin-transfer torque in vse2-based vdw magnetic tunnel junctions by electrode polytypes. *npj 2D Materials and Applications*, 9(1):1–16, 2025.

[35] Sami Ullah, Tayyaba Najam, Aziz ur Rehman, Saleh S Alarfaji, Muhammad Ashfaq Ahmad, Sundas Riaz, Bhargav Akkinepally, Syed Shoaib Ahmad Shah, and Muhammad Altaf Nazir. Mxene nanomaterials: synthesis, properties and applications in energy and environment sector. *Journal of Alloys and Compounds*, page 175172, 2024.

[36] Michel W Barsoum. The mn+ 1axn phases: A new class of solids: Thermodynamically stable nanolaminates. *Progress in solid state chemistry*, 28(1-4):201–281, 2000.

[37] Mohammad Khazaei, Avanish Mishra, Natarajan S Venkataramanan, Abhishek K Singh, and Seiji Yunoki. Recent advances in mxenes: From fundamentals to applications. *Current Opinion in Solid State and Materials Science*, 23(3):164–178, 2019.

[38] Maxim Sokol, Varun Natu, Sankalp Kota, and Michel W Barsoum. On the chemical diversity of the max phases. *Trends in Chemistry*, 1(2):210–223, 2019.

[39] Hassan Bukhari, Asad M Iqbal, Saif Ullah Awan, Danish Hussain, Saqlain A Shah, and Syed Rizwan. Intercalation of c60 into mxene multilayers: A promising approach for enhancing the electrochemical properties of electrode materials for high-performance energy storage applications. *ACS omega*, 9(1):227–238, 2023.

[40] Michael Naguib, Olha Mashtalir, Joshua Carle, Volker Presser, Jun Lu, Lars Hultman, Yury Gogotsi, and Michel W Barsoum. Two-dimensional transition metal carbides. *ACS nano*, 6(2):1322–1331, 2012.

[41] Pooja Srivastava, Avanish Mishra, Hiroshi Mizuseki, Kwang-Ryeol Lee, and Abhishek K Singh. Mechanistic insight into the chemical exfoliation and functionalization of ti3c2 mxene. *ACS applied materials & interfaces*, 8(36):24256–24264, 2016.

[42] Babak Anasori, Martin Dahlqvist, Joseph Halim, Eun Ju Moon, Jun Lu, Brian C Hosler, El'ad N Caspi, Steven J May, Lars Hultman, Per Eklund, et al. Experimental and theoretical characterization of ordered max phases mo2tialc2 and mo2ti2alc3. *Journal of Applied Physics*, 118(9), 2015.

[43] Babak Anasori, Yu Xie, Majid Beidaghi, Jun Lu, Brian C Hosler, Lars Hultman, Paul RC Kent, Yury Gogotsi, and Michel W Barsoum. Two-dimensional, ordered, double transition metals carbides (mxenes). *ACS nano*, 9(10):9507–9516, 2015.

[44] Rahele Meshkian, Quanzheng Tao, Martin Dahlqvist, Jun Lu, Lars Hultman, and Johanna Rosen. Theoretical stability and materials synthesis of a chemically ordered max phase, mo2scalc2, and its two-dimensional derivate mo2scc2 mxene. *Acta Materialia*, 125:476–480, 2017.

[45] Joseph Halim, Ahmed S Etman, Anna Elsukova, Peter Polcik, Justinas Palisaitis, Michel W Barsoum, Per OÅ Persson, and Johanna Rosen. Tailored synthesis approach of (mo 2/3 y 1/3) 2 alc i-max and its two-dimensional derivative mo 1.33 ct z mxene: enhancing the yield, quality, and performance in supercapacitor applications. *Nanoscale*, 13(1):311–319, 2021.

[46] Jun Lu, Andreas Thore, Rahele Meshkian, Quanzheng Tao, Lars Hultman, and Johanna Rosén. Theoretical and experimental exploration of a novel in-plane chemically ordered (cr2/3m1/3) 2alc i-max phase with m= sc and y. *Crystal Growth & Design*, 17(11):5704–5711, 2017.

[47] Martin Dahlqvist, Andrejs Petruhins, Jun Lu, Lars Hultman, and Johanna Rosen. Origin of chemically ordered atomic laminates (i-max): expanding the elemental space by a theoretical/experimental approach. *ACS nano*, 12(8):7761–7770, 2018.

[48] Rahele Meshkian, Martin Dahlqvist, Jun Lu, Björn Wickman, Joseph Halim, Jimmy Thörnberg, Quanzheng Tao, Shixuan Li, Saad Intikhab, Joshua Snyder, et al. W-based atomic laminates and their 2d derivative w1. 33c mxene with vacancy ordering. *Advanced materials*, 30(21):1706409, 2018.

[49] Le Fu and Wei Xia. Max phases as nanolaminate materials: chemical composition, microstructure, synthesis, properties, and applications. *Advanced Engineering Materials*, 23(4):2001191, 2021.

[50] Martin Dahlqvist, Jun Lu, Rahele Meshkian, Quanzheng Tao, Lars Hultman, and Johanna Rosen. Prediction and synthesis of a family of atomic laminate phases with kagomé-like and in-plane chemical ordering. *Science advances*, 3(7):e1700642, 2017.

[51] Liugang Chen, Martin Dahlqvist, Thomas Lapauw, Bensu Tunca, Fei Wang, Jun Lu, Rahele Meshkian, Konstantina Lambrinou, Bart Blanpain, Jozef Vleugels, et al. Theoretical prediction and synthesis of (cr2/3zr1/3) 2alc i-max phase. *Inorganic Chemistry*, 57(11):6237–6244, 2018.

[52] Ingemar Persson, Ahmed El Ghazaly, Quanzheng Tao, Joseph Halim, Sankalp Kota, Vanya Darakchieva, Justinas Palisaitis, Michel W Barsoum, Johanna Rosen, and Per OÅ Persson. Tailoring structure, composition, and energy storage properties of mxenes from selective etching of in-plane, chemically ordered max phases. *Small*, 14(17):1703676, 2018.

[53] Rodrigo Mantovani Ronchi, Jeverson Teodoro Arantes, and Sydney Ferreira Santos. Synthesis, structure, properties and applications of mxenes: Current status and perspectives. *Ceramics International*, 45(15):18167–18188, 2019.

[54] Babak Anasori and Yury Gogotsi. Mxenes: trends, growth, and future directions. *Graphene and 2D Materials*, 7(3):75–79, 2022.

[55] Michael Naguib, Joseph Halim, Jun Lu, Kevin M Cook, Lars Hultman, Yury Gogotsi, and Michel W Barsoum. New two-dimensional niobium and vanadium carbides as promising materials for li-ion batteries. *Journal of the American Chemical Society*, 135(43):15966–15969, 2013.

[56] Chuan Xu, Libin Wang, Zhibo Liu, Long Chen, Jingkun Guo, Ning Kang, Xiu-Liang Ma, Hui-Ming Cheng, and Wencai Ren. Large-area high-quality 2d ultrathin mo2c superconducting crystals. *Nature materials*, 14(11):1135–1141, 2015.

[57] Bhuvaneswari Soundiraraju and Benny Kattikkanal George. Two-dimensional titanium nitride (ti2n) mxene: synthesis, characterization, and potential application as surface-enhanced raman scattering substrate. *ACS nano*, 11(9):8892–8900, 2017.

[58] Patrick Urbankowski, Babak Anasori, Kanit Hantanasirisakul, Long Yang, Lihua Zhang, Bernard Haines, Steven J May, Simon JL Billinge, and Yury Gogotsi. 2d molybdenum and vanadium nitrides synthesized by ammoniation of 2d transition metal carbides (mxenes). *Nanoscale*, 9(45):17722–17730, 2017.

[59] Jie Zhou, Xianhu Zha, Fan Y Chen, Qun Ye, Per Eklund, Shiyu Du, and Qing Huang. A two-dimensional zirconium carbide by selective etching of al3c3 from nanolaminated zr3al3c5. *Angewandte Chemie International Edition*, 55(16):5008–5013, 2016.

[60] Jie Zhou, Xianhu Zha, Xiaobing Zhou, Fanyan Chen, Guoliang Gao, Shuwei Wang, Cai Shen, Tao Chen, Chunyi Zhi, Per Eklund, et al. Synthesis and electrochemical properties of two-dimensional hafnium carbide. *ACS nano*, 11(4):3841–3850, 2017.

[61] Patrick Urbankowski, Babak Anasori, Taron Makaryan, Dequan Er, Sankalp Kota, Patrick L Walsh, Mengqiang Zhao, Vivek B Shenoy, Michel W Barsoum, and Yury Gogotsi. Synthesis of two-dimensional titanium nitride ti 4 n 3 (mxene). *Nanoscale*, 8(22):11385–11391, 2016.

[62] Michael Ghidiu, Michael Naguib, Chenyang Shi, Olha Mashtalir, LM Pan, Bo Zhang, Jian Yang, Yury Gogotsi, Simon JL Billinge, and Michel W Barsoum. Synthesis and characterization of two-dimensional nb 4 c 3 (mxene). *Chemical communications*, 50(67):9517–9520, 2014.

[63] Grayson Deysher, Christopher Eugene Shuck, Kanit Hantanasirisakul, Nathan C Frey, Alexandre C Foucher, Kathleen Maleski, Asia Sarycheva, Vivek B Shenoy, Eric A Stach, Babak Anasori, et al. Synthesis of mo4valc4 max phase and two-dimensional mo4vc4 mxene with five atomic layers of transition metals. *ACS nano*, 14(1):204–217, 2019.

[64] Meikang Han, Kathleen Maleski, Christopher Eugene Shuck, Yizhou Yang, James T Glazar, Alexandre C Foucher, Kanit Hantanasirisakul, Asia Sarycheva, Nathan C Frey, Steven J May, et al. Tailoring electronic and optical properties of mxenes through forming solid solutions. *Journal of the American Chemical Society*, 142(45):19110–19118, 2020.

[65] Wikipedia contributors. MXenes – Wikipedia, The Free Encyclopedia. `https://en.wikipedia.org/wiki/MXenes`, 2025. Accessed: 2025-06-16.

[66] David Pinto, Babak Anasori, Hemesh Avireddy, Christopher E Shuck, Kanit Hantanasirisakul, Grayson Deysher, Joan Ramon Morante, William Porzio, Husam N Alshareef, and Yury Gogotsi. Synthesis and electrochemical properties of 2d molybdenum vanadium carbides–solid solution mxenes. *Journal of Materials Chemistry A*, 8(18):8957–8968, 2020.

[67] Martin Dahlqvist, Michel W Barsoum, and Johanna Rosen. Max phases–past, present, and future. *Materials Today*, 72:1–24, 2024.

[68] Jie Zhou, Quanzheng Tao, Bilal Ahmed, Justinas Palisaitis, Ingemar Persson, Joseph Halim, Michel W Barsoum, Per OÅ Persson, and Johanna Rosen. High-entropy laminate metal carbide (max phase) and its two-dimensional derivative mxene. *Chemistry of Materials*, 34(5):2098–2106, 2022.

[69] Zhiguo Du, Cheng Wu, Yuchuan Chen, Zhenjiang Cao, Riming Hu, Yongzheng Zhang, Jianan Gu, Yanglansen Cui, Hao Chen, Yongzheng Shi, et al. High-entropy atomic layers of transition-metal carbides (mxenes). *Advanced Materials*, 33(39):2101473, 2021.

[70] Zhiguo Du, Cheng Wu, Yuchuan Chen, Qi Zhu, Yanglansen Cui, Haiyang Wang, Yongzheng Zhang, Xiao Chen, Jiaxiang Shang, Bin Li, et al. High-entropy carbonitride max phases and their derivative mxenes. *Advanced Energy Materials*, 12(6):2103228, 2022.

[71] Rabi Khanal and Stephan Irle. Effect of surface functional groups on mxene conductivity. *The Journal of Chemical Physics*, 158(19), 2023.

[72] Barbora Vénosová and František Karlický. Mxene's surface functionalization patterns and their impacts on magnetism. *Physical Chemistry Chemical Physics*, 26(26):18500–18509, 2024.

[73] GR Berdiyorov. Effect of surface functionalization on the electronic transport properties of ti3c2 mxene. *Europhysics Letters*, 111(6):67002, 2015.

[74] Jingjing Ji, Lufang Zhao, Yanfei Shen, Songqin Liu, and Yuanjian Zhang. Covalent stabilization and functionalization of mxene via silylation reactions with improved surface properties. *FlatChem*, 17:100128, 2019.

[75] Zhuoheng Bao, Chengjie Lu, Xin Cao, Peigen Zhang, Li Yang, Heng Zhang, Dawei Sha, Wei He, Wei Zhang, Long Pan, et al. Role of mxene surface terminations in electrochemical energy storage: A review. *Chinese Chemical Letters*, 32(9):2648–2658, 2021.

[76] Minmin Hu, Hui Zhang, Tao Hu, Bingbing Fan, Xiaohui Wang, and Zhenjiang Li. Emerging 2d mxenes for supercapacitors: status, challenges and prospects. *Chemical Society Reviews*, 49(18):6666–6693, 2020.

[77] Aamir Iqbal, Pradeep Sambyal, and Chong Min Koo. 2d mxenes for electromagnetic shielding: a review. *Advanced Functional Materials*, 30(47):2000883, 2020.

[78] Muhammad Zubair, Muhammad Muneeb Ul Hassan, Muhammad Taqi Mehran, Mutawara Mahmood Baig, Sajjad Hussain, and Faisal Shahzad. 2d mxenes and their heterostructures for her, oer and overall water splitting: a review. *International Journal of Hydrogen Energy*, 47(5):2794–2818, 2022.

[79] Yu Zhong, Xinhui Xia, Fan Shi, Jiye Zhan, Jiangping Tu, and Hong Jin Fan. Transition metal carbides and nitrides in energy storage and conversion. *Advanced science*, 3(5):1500286, 2016.

[80] Erdem Balcı, Ünal Özden Akkuş, and Savas Berber. Band gap modification in doped mxene: Sc 2 cf 2. *Journal of Materials Chemistry C*, 5(24):5956–5961, 2017.

[81] Mohammad Khazaei, Masao Arai, Taizo Sasaki, Ahmad Ranjbar, Yunye Liang, and Seiji Yunoki. Oh-terminated two-dimensional transition metal carbides and nitrides as ultralow work function materials. *Physical Review B*, 92(7):075411, 2015.

[82] Mohammad Khazaei, Ahmad Ranjbar, Masao Arai, and Seiji Yunoki. Topological insulators in the ordered double transition metals m 2' m "c 2 mxenes (m'= mo, w; m "= ti, zr, hf). *Physical Review B*, 94(12):125152, 2016.

[83] Tao Hu, Hui Zhang, Jiemin Wang, Zhaojin Li, Minmin Hu, Jun Tan, Pengxiang Hou, Feng Li, and Xiaohui Wang. Anisotropic electronic conduction in stacked two-dimensional titanium carbide. *Scientific reports*, 5(1):16329, 2015.

[84] Hossein Fashandi, Viktor Ivády, Per Eklund, A Lloyd Spetz, Mikhail I Katsnelson, and Igor A Abrikosov. Dirac points with giant spin-orbit splitting in the electronic structure of two-dimensional transition-metal carbides. *Physical Review B*, 92(15):155142, 2015.

[85] Mohammad Khazaei, Ahmad Ranjbar, Masao Arai, Taizo Sasaki, and Seiji Yunoki. Electronic properties and applications of mxenes: a theoretical review. *Journal of Materials Chemistry C*, 5(10):2488–2503, 2017.

[86] Mohammad Khazaei, Masao Arai, Taizo Sasaki, Chan-Yeup Chung, Natarajan S Venkataramanan, Mehdi Estili, Yoshio Sakka, and Yoshiyuki Kawazoe. Novel electronic and magnetic properties of two-dimensional transition metal carbides and nitrides. *Advanced Functional Materials*, 23(17):2185–2192, 2013.

[87] Mohammad Khazaei, Ahmad Ranjbar, Mahdi Ghorbani-Asl, Masao Arai, Taizo Sasaki, Yunye Liang, and Seiji Yunoki. Nearly free electron states in mxenes. *Physical Review B*, 93(20):205125, 2016.

[88] Hongming Weng, Ahmad Ranjbar, Yunye Liang, Zhida Song, Mohammad Khazaei, Seiji Yunoki, Masao Arai, Yoshiyuki Kawazoe, Zhong Fang, and Xi Dai. Large-gap two-dimensional topological insulator in oxygen functionalized mxene. *Physical Review B*, 92(7):075436, 2015.

[89] Yunye Liang, Mohammad Khazaei, Ahmad Ranjbar, Masao Arai, Seiji Yunoki, Yoshiyuki Kawazoe, Hongming Weng, and Zhong Fang. Theoretical prediction of two-dimensional functionalized mxene nitrides as topological insulators. *Physical Review B*, 96(19):195414, 2017.

[90] Chen Si, Kyung-Hwan Jin, Jian Zhou, Zhimei Sun, and Feng Liu. Large-gap quantum spin hall state in mxenes: d-band topological order in a triangular lattice. *Nano letters*, 16(10):6584–6591, 2016.

[91] Konstantina A Papadopoulou, Alexander Chroneos, David Parfitt, and Stavros-Richard G Christopoulos. A perspective on mxenes: Their synthesis, properties, and recent applications. *Journal of Applied Physics*, 128(17), 2020.

[92] Soungmin Bae, Y-G Kang, M Khazaei, Kaoru Ohno, Y-H Kim, Myung Joon Han, Kee Joo Chang, and Hannes Raebiger. Electronic and magnetic properties of carbide mxenes—the role of electron correlations. *Materials Today Advances*, 9:100118, 2021.

[93] Yunliang Yue. Fe2c monolayer: An intrinsic ferromagnetic mxene. *Journal of Magnetism and Magnetic Materials*, 434:164–168, 2017.

[94] Zhuhua Zhang, Xiaofei Liu, Jin Yu, Yang Hang, Yao Li, Yufeng Guo, Ying Xu, Xu Sun, Jianxin Zhou, and Wanlin Guo. Tunable electronic and magnetic properties of two-dimensional materials and their one-dimensional derivatives. *Wiley Interdisciplinary Reviews: Computational Molecular Science*, 6(4):324–350, 2016.

[95] Yong Zhang and Feng Li. Robust half-metallic ferromagnetism in cr3c2 mxene. *Journal of Magnetism and Magnetic Materials*, 433:222–226, 2017.

[96] Yunliang Yue, Buwei Wang, Nanxi Miao, Chao Jiang, Hongwei Lu, Bowen Zhang, Yankai Wu, Jie Ren, and Min Wang. Tuning the magnetic properties of zr2n mxene by biaxial strain. *Ceramics International*, 47(2):2367–2373, 2021.

[97] Guoying Gao, Guangqian Ding, Jie Li, Kailun Yao, Menghao Wu, and Meichun Qian. Monolayer mxenes: promising half-metals and spin gapless semiconductors. *Nanoscale*, 8(16):8986–8994, 2016.

[98] Lin Hu, Xiaojun Wu, and Jinlong Yang. Mn 2 c monolayer: a 2d antiferromagnetic metal with high néel temperature and large spin–orbit coupling. *Nanoscale*, 8(26):12939–12945, 2016.

[99] Junjie He, Pengbo Lyu, and Petr Nachtigall. New two-dimensional mn-based mxenes with room-temperature ferromagnetism and half-metallicity. *Journal of Materials Chemistry C*, 4(47):11143–11149, 2016.

[100] Jianhui Yang, Xuepiao Luo, Xumeng Zhou, Shaozheng Zhang, Jia Liu, Yan Xie, Liang Lv, and Liang Chen. Tuning magnetic properties of cr2m2c3t2 (m= ti and v) using extensile strain. *Computational Materials Science*, 139:313–319, 2017.

[101] Liang Dong, Hemant Kumar, Babak Anasori, Yury Gogotsi, and Vivek B Shenoy. Rational design of two-dimensional metallic and semiconducting spintronic materials based on ordered double-transition-metal mxenes. *The journal of physical chemistry letters*, 8(2):422–428, 2017.

[102] Xiantao Jiang, Artem V Kuklin, Alexander Baev, Yanqi Ge, Hans Ågren, Han Zhang, and Paras N Prasad. Two-dimensional mxenes: From morphological to optical, electric, and magnetic properties and applications. *Physics Reports*, 848:1–58, 2020.

[103] Jun-Jie Zhang, Lingfang Lin, Yang Zhang, Menghao Wu, Boris I Yakobson, and Shuai Dong. Type-ii multiferroic hf2vc2f2 mxene monolayer with high transition temperature. *Journal of the American Chemical Society*, 140(30):9768–9773, 2018.

[104] Nathan C Frey, Arkamita Bandyopadhyay, Hemant Kumar, Angel Babak Anasori, and Yuri Gogotsi. Surface-engineered mxenes: Electric field control of magnetism and enhanced magnetic anisotropy. *ACS Nano*, 13:2831, 2019.

[105] Qiang Gao and Hongbin Zhang. Magnetic i-mxenes: a new class of multifunctional two-dimensional materials. *Nanoscale*, 12(10):5995–6001, 2020.

[106] Erdem Balcı, Unal Ozden Akkus, and Savas Berber. High tmr in mxene-based $mn_2cf_2/ti_2co_2/mn_2cf_2$ magnetic tunneling junction. *ACS Applied Materials & Interfaces*, 11(3):3609–3616, 2018.

[107] Hailin Yu, Mingyan Chen, Zhenguang Shao, Yongmei Tao, Xuefan Jiang, Yaojun Dong, Jie Zhang, Xifeng Yang, and Yushen Liu. Giant tunneling magnetoresistance in in-plane double-barrier magnetic tunnel junctions based on mxene cr 2 c. *Physical Chemistry Chemical Physics*, 25(15):10991–10997, 2023.

[108] Liming Wang, Yonglong Ga, Peng Li, Dongxing Yu, Jiawei Jiang, Jinghua Liang, Shouguo Wang, and Hongxin Yang. Electrical switchable room-temperature magnetic skyrmions in multiferroic mxene. *Physical Review B*, 108(5):054440, 2023.

[109] Kanit Hantanasirisakul, Babak Anasori, Slavomir Nemsak, James L Hart, Jiabin Wu, Yizhou Yang, Rajesh V Chopdekar, Padraic Shafer, Andrew F May, Eun Ju Moon, et al. Evidence of a magnetic transition in atomically thin cr 2 tic 2 t x mxene. *Nanoscale Horizons*, 5(12):1557–1565, 2020.

[110] Kemryn Allen-Perry, Weston Straka, Danielle Keith, Shubo Han, Lewis Reynolds, Bhoj Gautam, and Daniel E Autrey. Tuning the magnetic properties of two-dimensional mxenes by chemical etching. *Materials*, 14(3):694, 2021.

[111] Kaiyu Zhang, Maoyun Di, Lin Fu, Yu Deng, Youwei Du, and Nujiang Tang. Enhancing the magnetism of 2d carbide mxene ti3c2tx by h2 annealing. *Carbon*, 157:90–96, 2020.

[112] M Born and R Oppenheimer. Zur quantentheorie der molekeln annalen der physik, v. 84. 1927.

[113] Douglas R Hartree. The wave mechanics of an atom with a non-coulomb central field. part i. theory and methods. In *Mathematical Proceedings of the Cambridge Philosophical Society*, volume 24, pages 89–110. Cambridge university press, 1928.

[114] Vladimir Fock. Näherungsmethode zur lösung des quantenmechanischen mehrkörperproblems. *Zeitschrift für Physik*, 61:126–148, 1930.

[115] Llewellyn H Thomas. The calculation of atomic fields. In *Mathematical proceedings of the Cambridge philosophical society*, volume 23, pages 542–548. Cambridge University Press, 1927.

[116] Enrico Fermi. Un metodo statistico per la determinazione di alcune priorieta dell'atome. *Rend. Accad. Naz. Lincei*, 6(602-607):32, 1927.

[117] Paul AM Dirac. Note on exchange phenomena in the thomas atom. In *Mathematical proceedings of the Cambridge philosophical society*, volume 26, pages 376–385. Cambridge University Press, 1930.

[118] P Hohenberg and WJPR Kohn. Density functional theory (dft). *Phys. Rev*, 136(1964):B864, 1964.

[119] Walter Kohn and Lu Jeu Sham. Self-consistent equations including exchange and correlation effects. *Physical review*, 140(4A):A1133, 1965.

[120] Matt Probert. Electronic structure: Basic theory and practical methods, by richard m. martin: Scope: graduate level textbook. level: theoretical materials scientists/condensed matter physicists/computational chemists, 2011.

[121] John P Perdew. Unified theory of exchange and correlation beyond the local density approximation. *Electronic structure of solids' 91*, 11, 1991.

[122] John P Perdew and Wang Yue. Accurate and simple density functional for the electronic exchange energy: Generalized gradient approximation. *Physical review B*, 33(12):8800, 1986.

[123] John P Perdew, Kieron Burke, and Matthias Ernzerhof. Generalized gradient approximation made simple. *Phys. Rev. Lett.*, 77(18):3865, 1996.

[124] John P Perdew, P Ziesche, and H Eschrig. Electronic structure of solids' 91, 1991.

[125] John P Perdew, Adrienn Ruzsinszky, Gábor I Csonka, Oleg A Vydrov, Gustavo E Scuseria, Lucian A Constantin, Xiaolan Zhou, and Kieron Burke. Restoring the density-gradient expansion for exchange in solids and surfaces. *Physical review letters*, 100(13):136406, 2008.

[126] PJ Hasnip and CJ Pickard. Electronic energy minimisation with ultrasoft pseudopotentials. *Computer physics communications*, 174(1):24–29, 2006.

[127] Peter E Blöchl. Projector augmented-wave method. *Physical review B*, 50(24):17953, 1994.

[128] Georg Kresse and Jürgen Furthmüller. Efficiency of ab-initio total energy calculations for metals and semiconductors using a plane-wave basis set. *Computational materials science*, 6(1):15–50, 1996.

[129] Georg Kresse and Jürgen Hafner. Ab initio molecular dynamics for liquid metals. *Physical review B*, 47(1):558, 1993.

[130] Georg Kresse and Jürgen Hafner. Ab initio molecular-dynamics simulation of the liquid-metal–amorphous-semiconductor transition in germanium. *Physical Review B*, 49(20):14251, 1994.

[131] Stefaan Cottenier et al. Density functional theory and the family of (l) apw-methods: a step-by-step introduction. *Instituut voor Kern-en Stralingsfysica, KU Leuven, Belgium*, 4(0):41, 2002.

[132] Georg Kresse and J Furthmüller. Vienna ab-initio simulation package (vasp). *Vienna: Vienna University*, 2001.

[133] KH Weyrich. Full-potential linear muffin-tin-orbital method. *Physical Review B*, 37(17):10269, 1988.

[134] John M Wills, Mebarek Alouani, Per Andersson, Anna Delin, Olle Eriksson, and Oleksiy Grechnyev. *Full-Potential Electronic Structure Method: energy and force calculations with density functional and dynamical mean field theory*, volume 167. Springer Science & Business Media, 2010.

[135] A Il Liechtenstein, MI Katsnelson, VP Antropov, and VA Gubanov. Local spin density functional approach to the theory of exchange interactions in ferromagnetic metals and alloys. *Journal of Magnetism and Magnetic Materials*, 67(1):65–74, 1987.

[136] Malvin H Kalos and Paula A Whitlock. *Monte carlo methods*. John Wiley & Sons, 2009.

[137] Nicholas Metropolis, Arianna W Rosenbluth, Marshall N Rosenbluth, Augusta H Teller, and Edward Teller. Equation of state calculations by fast computing machines. *The journal of chemical physics*, 21(6):1087–1092, 1953.

[138] Olle Eriksson, Anders Bergman, Lars Bergqvist, and Johan Hellsvik. *Atomistic spin dynamics: foundations and applications*. Oxford university press, 2017.

[139] Hyungwoo Lee and Minseok Choi. Out-of-plane ferromagnetism in two-dimensional 1T-RhO_2. *Physical Review B*, 106(6):064414, 2022.

[140] Ding-sheng Wang, Ruqian Wu, and AJ Freeman. First-principles theory of surface magnetocrystalline anisotropy and the diatomic-pair model. *Physical Review B*, 47(22):14932, 1993.

[141] Xiong Wang, Dian Li, Zejun Li, Changzheng Wu, Chi-Ming Che, Gang Chen, and Xiaodong Cui. Ferromagnetism in 2d vanadium diselenide. *ACS Nano*, 15(10):16236, 2021.

[142] Jae-Ung Lee, Sungmin Lee, Ji Hoon Ryoo, Soonmin Kang, Tae Yun Kim, Pilkwang Kim, Cheol-Hwan Park, Je-Geun Park, and Hyeonsik Cheong. Ising-type magnetic ordering in atomically thin $FePS_3$. *Nano Letters*, 16(12):7433–7438, 2016.

[143] W Kohn and L J Sham. Self-consistent equations including exchange and correlation effects. *Phys. Rev.*, 140:A1133, 1965.

[144] Mingyu Zhao, Jun Chen, Shan-Shan Wang, Ming An, and Shuai Dong. Multiferroic properties of oxygen-functionalized magnetic i-mxene. *Physical Review Materials*, 5(9):094408, 2021.

[145] Shuo Li, Junjie He, Petr Nachtigall, Lukáš Grajciar, and Federico Brivio. Control of spintronic and electronic properties of bimetallic and vacancy-ordered vanadium carbide mxenes via surface functionalization. *Physical Chemistry Chemical Physics*, 21(46):25802–25808, 2019.

[146] Georg Kresse and Daniel Joubert. From ultrasoft pseudopotentials to the projector augmented-wave method. *Phys. Rev. B*, 59(3):1758, 1999.

[147] Stefan Grimme, Jens Antony, Stephan Ehrlich, and Helge Krieg. A consistent and accurate ab initio parametrization of density functional dispersion correction (dft-d) for the 94 elements h-pu. *J. Chem. Phys.*, 132(15):154104, 2010.

[148] Hendrik J Monkhorst and James D Pack. Special points for brillouin-zone integrations. *Physical Review B*, 13(12):5188, 1976.

[149] Daniel Dolz, Ángel Morales-García, Francesc Viñes, and Francesc Illas. Exfoliation energy as a descriptor of mxenes synthesizability and surface chemical activity. *Nanomaterials*, 11(1):127, 2021.

[150] Atsushi Togo and Isao Tanaka. First principles phonon calculations in materials science. *Scr. Mater.*, 108:1–5, 2015.

[151] Mohammad Khazaei, Ahmad Ranjbar, Keivan Esfarjani, Dimitri Bogdanovski, Richard Dronskowski, and Seiji Yunoki. Insights into exfoliation possibility of max phases to mxenes. *Physical Chemistry, Chemical Physics*, 20(13):8579–8592, 2018.

[152] Chen Si, Jian Zhou, and Zhimei Sun. Half-metallic ferromagnetism and surface functionalization-induced metal–insulator transition in graphene-like two-dimensional Cr_2C crystals. *ACS applied materials & interfaces*, 7(31):17510–17515, 2015.

[153] Jun-Jie Zhang and Shuai Dong. Superconductivity of monolayer mo_2c: The key role of functional groups. *The Journal of chemical physics*, 146(3):034705, 2017.

[154] Xiaoxi Li, Baojuan Dong, Xingdan Sun, Hanwen Wang, Teng Yang, Guoqiang Yu, and Zheng Vitto Han. Perspectives on exfoliated two-dimensional spintronics. *Journal of Semiconductors*, 40(8):081508, 2019.

[155] Xue-Juan Dong, Jing-Yang You, Bo Gu, and Gang Su. Strain-induced room-temperature ferromagnetic semiconductors with large anomalous hall conductivity in two-dimensional Cr_2Ge_2 Se_6. *Physical Review Applied*, 12(1):014020, 2019.

[156] Wen-Qiang Xie, Zhi-Wei Lu, Chang-Chun He, Xiao-Bao Yang, and Yu-Jun Zhao. Theoretical study of tunable magnetism of two-dimensional $MnSe_2$ through strain, charge, and defect. *Journal of Physics: Condensed Matter*, 33(21):215803, 2021.

[157] Shengnan Feng and Wenbo Mi. Strain and interlayer coupling tailored magnetic properties and valley splitting in layered ferrovalley 2H-VSe_2. *Applied Surface Science*, 458:191–197, 2018.

[158] Gang Xiao, Wen-Zhi Xiao, Qiao Chen, and Ling-ling Wang. Novel two-dimensional ferromagnetic materials CrX_2 (x= o, s, se) with high curie temperature. *J. Mater. Chem. C*, 10(46):17665–17674, 2022.

[159] Wen-Rong Liu, Xiao-Jing Dong, Ye-Zhu Lv, Wei-Xiao Ji, Qiang Cao, Pei-Ji Wang, Feng Li, and Chang-Wen Zhang. Magnetic anisotropy and ferroelectric-driven magnetic phase transition in monolayer $Cr_2Ge_2Te_6$. *Nanoscale*, 14(9):3632–3643, 2022.

[160] Nathan C Frey, Hemant Kumar, Babak Anasori, Yuri Gogotsi, and Vivek B Shenoy. Tuning noncollinear spin structure and anisotropy in ferromagnetic nitride mxenes. *ACS Nano*, 12:6319–6325, 2018.

[161] Jianhui Yang, Shaozheng Zhang, Lei Li, Anping Wang, Zhicheng Zhong, and Liang Chen. Rationally designed high-performance spin filter based on two-dimensional half-metal cr2no2. *Matter*, 1(5):1304–1315, 2019.

[162] Rachid Sbiaa, H Meng, and SN Piramanayagam. Materials with perpendicular magnetic anisotropy for magnetic random access memory. *physica status solidi (RRL)–Rapid Research Letters*, 5(12):413–419, 2011.

[163] Bharati Tudu and Ashutosh Tiwari. Recent developments in perpendicular magnetic anisotropy thin films for data storage applications. *Vacuum*, 146:329–341, 2017.

[164] Anmol Mahendra, Peter P Murmu, Susant Kumar Acharya, Atif Islam, Holger Fiedler, Prasanth Gupta, Simon Granville, and John Kennedy. Shaping perpendicular magnetic anisotropy of co2mnga heusler alloy using ion irradiation for magnetic sensor applications. *Sensors*, 23(9):4564, 2023.

[165] Zhao Chen, Xiaofeng Liu, Xingxing Li, Pengfei Gao, ZhongJun Li, Weiduo Zhu, Haidi Wang, and Xiangyang Li. Large tunneling magnetoresistance in spin-filtering 1t-mnse 2/h-bn van der waals magnetic tunnel junction. *Nanoscale*, 15(18):8447–8455, 2023.

[166] Mohamad G Moinuddin, Srikant Srinivasan, and Satinder K Sharma. Probing ferrimagnetic semiconductor with enhanced negative magnetoresistance: 2d chromium sulfide. *Advanced Electronic Materials*, 7(9):2001116, 2021.

[167] Cui Jin and Liangzhi Kou. Two-dimensional non-van der waals magnetic layers: functional materials for potential device applications. *Journal of Physics D: Applied Physics*, 54(41):413001, 2021.

[168] Wenzhou Chen, Yoshiyuki Kawazoe, Xingqiang Shi, and Hui Pan. Two-dimensional pentagonal crx (x= s, se or te) monolayers: antiferromagnetic semiconductors for spintronics and photocatalysts. *Physical Chemistry Chemical Physics*, 20(27):18348–18354, 2018.

[169] José D Gouveia, Francesc Viñes, Francesc Illas, and José RB Gomes. Mxenes atomic layer stacking phase transitions and their chemical activity consequences. *Physical Review Materials*, 4(5):054003, 2020.

[170] Xingshuai Lv, Wei Wei, Pei Zhao, Dequan Er, Bibiao Huang, Ying Dai, and Timo Jacob. Oxygen-terminated bixenes and derived single atom catalysts for the hydrogen evolution reaction. *Journal of Catalysis*, 378:97, 2019.

[171] Mohammad Khazaei, Masaro Arai, Taizo Sasaki, Chan-Yeup Chung, Natarajan S. Venkataramanan, Mehdi Estili, Yoshio Sakka, and Yoshiyuki Kawazoe. Novel electronic and magnetic properties of two-dimensional transition metal carbides and nitrides. *Advanced Functional Materials*, 23:2185, 2013.

[172] Junjin He, Pengbo Lyu, L Z Sun, Angel Morales Garcia, and Petr Nachigall. High temperature spin-polarized semiconductivity with zero magnetization in two-dimensional janus mxenes. *Journal of Materials Chemistry C*, 4:6500, 2016.

[173] Hemant Kumar, Nathan C Frey, Liang Dong, Babak Anasori, Yury Gogotsi, and Vivek B Shenoy. Tunable magnetism and transport properties in nitride mxenes. *ACS nano*, 11(8):7648–7655, 2017.

[174] Shulin Zhong, Bo Xu, Ao Cui, Siyu Li, Susu Liao, Guoqing Wang, Gang Liu, and Baozhen Sun. Robust net magnetic moment in janus v-based nitride mxenes: Insight from first-principles calculations. *ACS Omega*, 5:864, 2020.

[175] Qiang Gao and Hongbin Zhang. Magnetic i-mxenes: a new class of multifunctional two-dimensional materials. *Nanoscale*, 12:5995, 2020.

[176] Sukhito Teh and Horng-Tay Jeng. Magnetoelastic and magnetoelectric coupling in two-dimensional nitride mxenes: a density functional theory study. *Nanomaterials*, 23:2644, 2023.

[177] Chen Si, Jian Zhou, and Zhimei Sun. Half-metallic ferromagnetism and surface functionalization-induced metal-insulator transition in graphene-like two-dimensional cr$_2$c crystals. *Applied Materials & Interfaces*, 7:17510, 2015.

[178] Jiming Zheng, Ruijao He, Yun Wan, Puju Zhao, Ping Guo, and Zhenyi Jiang. Half-metal state of a ti$_2$c monolayer by asymmetric surface decoration. *Physical Chemistry Chemical Physics*, 21:3318, 2019.

[179] Xiao-Ping Wei, Na Yang, Zhen-Yang Mei, Jing Shen, Lan-Lan Du, and Xiaoma Tao. Layer-dependent electronic and magnetic properties for cr$_2$no$_2$ and cr$_2$co$_2$. *Journal of Magnetism and Magnetic Materials*, 563:169952, 2022.

[180] Himangshu Sekhar Sarmah and Subhradip Ghosh. Stacking and layer dependence of magnetic properties in ti$_2$c and fe$_2$c. *Journal of Physics D: Applied Physics*, 56:345002, 2023.

[181] Vladimir I Anisimov, Ferdi Aryasetiawan, and AI Lichtenstein. First-principles calculations of the electronic structure and spectra of strongly correlated systems: the lda+ u method. *Journal of Physics: Condensed Matter*, 9(4):767, 1997.

[182] Bin Liu, Sicong Zhu, Tongtong Wang, and Sheng Liu. Mxene-based sc2cho/sc2nho/sc2cho magnetic tunnel junctions for multi-value logic computing devices: A first principles study. *ACS Applied Nano Materials*, 2023.

[183] Shiladitya Karmakar and Tanusri Saha-Dasgupta. First-principles prediction of enhanced thermoelectric properties of double transition metal mxenes: Ti 3- x mo x c 2 t 2;(x= 0.5, 1, 1.5, 2, 2.5, t=- oh/- o/- f). *Physical Review Materials*, 4(12):124007, 2020.

[184] Jing-He Liu, Xiang Kan, Bin Amin, Li-Yong Gan, and Yong Zhao. Theoretical exploration of the potential applications of sc-based mxenes. *Physical Chemistry Chemical Physics*, 19:32253, 2017.

[185] Bo Xu, Hui Xiang, Lai Wei, Jiang Yin, and Yineng Huang. Band structure engineering of mxenes for low-loss visible epsilon-near-zero properties by first-principles calculation. *Advanced Electronic Materials*, 9:2201119, 2023.

[186] Dashuai Wang, Yu Gao, Yanhui Liu, Di Jin, Yury Gogotsi, Xing Meng, Fei Du, Gang Chen, and Yingjin Wei. First-principles calculations of ti2n and ti2nt2 (t= o, f, oh) monolayers as potential anode materials for lithium-ion batteries and beyond. *The Journal of Physical Chemistry C*, 121(24):13025–13034, 2017.

[187] Ajit Jena, Seung-Cheol Lee, and Satadeep Bhattacharjee. Surface oxygen passivation-driven large anomalous hall conductivity in early transition metal-based nitride mxenes: Can ahc be a tool to determine functional groups in 2d ferro (i) magnets? *The Journal of Physical Chemistry C*, 126(43):18404–18410, 2022.

[188] John B. Goodenough. *Magnetism and the chemical bond.* John Wiley and Sons, 1963.

[189] José D Gouveia and José RB Gomes. Structural and energetic properties of vacancy defects in mxene surfaces. *Physical Review Materials*, 6(2):024004, 2022.

[190] Shuai Dong, Hongjun Xiang, and Elbio Dagotto. Magnetoelectricity in multiferroics: A theoretical perspective. *Natl. Sci. Rev.*, 6(4):629, 2019.

[191] Cheng Gong, Eun Mi Kim, Yuan Wang, Geunsik Lee, and Xiang Zhang. Multiferroicity in atomic van der waals heterostructures. *Nat. Commun.*, 10(1):2657, 2019.

[192] Wei Sun, Wenxuan Wang, Dong Chen, Zhenxiang Cheng, and Yuanxu Wang. Valence mediated tunable magnetism and electronic properties by ferroelectric polarization switching in 2d fei$_2$/in$_2$se$_3$ van der waals heterostructures. *Nanoscale*, 11(20):9931, 2019.

[193] Nicola A Spaldin and Manfred Fiebig. The renaissance of magnetoelectric multiferroics. *Science*, 309:391–392, 2005.

[194] Siyuan Wan, Yue Li, Wei Li, Xiaoyu Mao, Chen Wang, Chen Chen, Jiyu Dong, Anmin Nie, Jianyong Xiang, Zhongyuan Liu, et al. Nonvolatile ferroelectric memory effect in ultrathin α-in$_2$ se$_3$. *Adv. Funct. Mater.*, 29(20):1808606, 2019.

[195] Lin Wang, Xiaojie Wang, Yishu Zhang, Runlai Li, Teng Ma, Kai Leng, Zhi Chen, Ibrahim Abdelwahab, and Kian Ping Loh. Exploring ferroelectric switching in α-in$_2$ se$_3$ for neuromorphic computing. *Adv. Funct. Mater.*, 30(45):2004609, 2020.

[196] Hulei Yu, Dexiang Gao, Xiancheng Wang, Xueyan Du, Xiaohuan Lin, Wenhan Guo, Ruqiang Zou, Changqing Jin, Kuo Li, and Yue Chen. Unraveling a novel ferroelectric gese phase and its transformation into a topological crystalline insulator under high pressure. *NPG Asia Mater.*, 10(9):882, 2018.

[197] Kai Chang, Junwei Liu, Haicheng Lin, Na Wang, Kun Zhao, Anmin Zhang, Feng Jin, Yong Zhong, Xiaopeng Hu, Wenhui Duan, et al. Discovery of robust in-plane ferroelectricity in atomic-thick snte. *Science*, 353(6296):274, 2016.

[198] Fucai Liu, Lu You, Kyle L Seyler, Xiaobao Li, Peng Yu, Junhao Lin, Xuewen Wang, Jiadong Zhou, Hong Wang, Haiyong He, et al. Room temperature ferroelectricity in cuinp$_2s_6$ ultrathin films. *Nat. Commun.*, 7(1):1, 2016.

[199] Mohammad Noor-A-Alam and Michael Nolan. Engineering ferroelectricity and large piezoelectricity in h-bn. *ACS Appl. Mater. Interfaces.*, 15(36):42737, 2023.

[200] Yinghe Zhao, Jun-Jie Zhang, Shijun Yuan, and Zhongfang Chen. Nonvolatile electrical control and heterointerface-induced half-metallicity of 2d ferromagnets. *Adv. Funct. Mater.*, 29(24):1901420, 2019.

[201] Guogang Liu, Tong Chen, Guanghui Zhou, Zhonghui Xu, and Xianbo Xiao. Nonvolatile electrical control and reversible gas capture by ferroelectric polarization switching in 2d fei$_2$/in$_2$se$_3$ van der waals heterostructures. *ACS Sens.*, 8(4):1440–1449, 2023.

[202] Changwei Wu, Shanwei Sun, Weiping Gong, Jiangyu Li, and Xiao Wang. Nonvolatile switchable half-metallicity and magnetism in the mxene $\mathrm{hf_2mnc_2\ o_2\ /sc_2co_2}$ multiferroic heterostructure. *Phys. Chem. Chem. Phys.*, 26(6):5323, 2024.

[203] Liemao Cao, Xiaohui Deng, Guanghui Zhou, Shi-Jun Liang, Chuong V Nguyen, LK Ang, and Yee Sin Ang. Multiferroic van der waals heterostructure $\mathrm{fecl_2/sc_2co_2}$: Nonvolatile electrically switchable electronic and spintronic properties. *Phys. Rev. B*, 105(16):165302, 2022.

[204] Lingling Song, Runlong Ye, Chen Su, Canglong Wei, Dongdong Chen, Xiaofeng Liu, Xiaohong Zheng, and Hua Hao. Strain-tunable half-metallicity in $\mathrm{vse_2/sc_2co_2}$ van der waals heterostructures. *Phys. Rev. B*, 109:094105, 2024.

[205] Guogang Liu and San-Huang Ke. Ferroelectric control of the semiconductor-metal transition in two-dimensional $m\mathrm{si_2p_4/sc_2co_2}$ (m= Mo, W) van der waals heterostructures and application to nonvolatile memory devices. *Phys. Rev. Appl.*, 21:044033, 2024.

[206] Anand Chandrasekaran, Avanish Mishra, and Abhishek Kumar Singh. Ferroelectricity, antiferroelectricity, and ultrathin 2d electron/hole gas in multifunctional monolayer mxene. *Nano Lett.*, 17:3290–3296, 2017.

[207] Jiawen You, Jie Pan, Shun-Li Shang, Xiang Xu, Zhenjing Liu, Jingwei Li, Hongwei Liu, Ting Kang, Mengyang Xu, Shaobo Li, et al. Salt-assisted selective growth of h-phase monolayer $\mathrm{vse_2}$ with apparent hole transport behavior. *Nano Lett.*, 22(24):10167, 2022.

[208] Hendrik J Monkhorst and James D Pack. Special points for brillouin-zone integrations. *Phys. Rev. B*, 13:5188, 1976.

[209] Huei-Ru Fuh, Ching-Ray Chang, Yin-Kuo Wang, Richard FL Evans, Roy W Chantrell, and Horng-Tay Jeng. Newtype single-layer magnetic semiconductor in transition-metal dichalcogenides $\mathrm{vx_2}$ (x= s, se and te). *Sci. Rep.*, 6(1):32625, 2016.

[210] Zhuquan Wang, Nianxiang Qiu, Erxiao Wu, Qing Huang, Peng An, Heming He, and Shiyu Du. First-principles study of electronic and optical properties of $\mathrm{nh_3}$ adsorbed $\mathrm{sc_2co_2}$ monolayer and its application in gas sensors. *J. Mater. Res. Technol.*, 24:173, 2023.

[211] Xingxing Li, Xiaojun Wu, Zhenyu Li, Jinlong Yang, and JG Hou. Bipolar magnetic semiconductors: A new class of spintronics materials. *Nanoscale*, 4(18):5680, 2012.

[212] Lei Zhang, Cheng Tang, Chunmei Zhang, and Aijun Du. First-principles screening of novel ferroelectric mxene phases with a large piezoelectric response and unusual auxeticity. *Nanoscale*, 12:21291–21298, 2020.

[213] Gustav Bihlmayer, O Rader, and Roland Winkler. Focus on the rashba effect. *New journal of physics*, 17(5):050202, 2015.

[214] Aurelien Manchon, Hyun Cheol Koo, Junsaku Nitta, Sergey M Frolov, and Rembert A Duine. New perspectives for rashba spin–orbit coupling. *Nature materials*, 14(9):871–882, 2015.

[215] Shao-Bo Chen, San-Dong Guo, Guang-Zhao Wang, and Yee Sin Ang. The external electric field induces rashba and zeeman spin splitting in non-polar mxene lu2cf2 monolayers for spintronics application. *Vacuum*, 227:113407, 2024.

[216] Yilei Li, Jonathan Ludwig, Tony Low, Alexey Chernikov, Xu Cui, Ghidewon Arefe, Young Duck Kim, Arend M van der Zande, Albert Rigosi, Heather M Hill, Suk Hyun Kim, James Hone, Zhiqiang Li, Dmitry Smirnov, and Tony F Heinz. Valley splitting and polarization by the zeeman effect in monolayer mose$_2$. *Physical Review Letters*, 113:266804, 2014.

[217] Kai Liu, Wei Luo, Junyi Ji, Paolo Barone, Silvia Picozzi, and Hongjun Xiang. Band splitting with vanishing spin polarizations in noncentrosymmetric crystals. *Nature Communications*, 10:5144, 2019.

[218] Jun-Wei Luo, Gabriel Bester, and Alex Zunger. Full-zone spin splitting for electrons and holes in bulk gaas and gasb. *Physical review letters*, 102(5):056405, 2009.

[219] Kunal Dutta, Subhadeep Bandyopadhyay, and Indra Dasgupta. Effect of spin-orbit coupling in noncentrosymmetric half-heusler alloys. *Physical Review B*, 108(24):245146, 2023.

[220] Pojen Chuang, Sheng-Chin Ho, Luke William Smith, Francois Sfigakis, Michael Pepper, Chin-Hung Chen, Ju-Chun Fan, JP Griffiths, Ian Farrer, Harvey Edward Beere, et al. All-electric all-semiconductor spin field-effect transistors. *Nature nanotechnology*, 10(1):35–39, 2015.

[221] Yuan Ping Feng, Lei Shen, Ming Yang, Aizhu Wang, Minggang Zeng, Qingyun Wu, Sandhya Chintalapati, and Ching-Ray Chang. Prospects of spintronics based on 2d materials. *Wiley Interdisciplinary Reviews: Computational Molecular Science*, 7(5):e1313, 2017.

[222] Ethan C Ahn. 2d materials for spintronic devices. *npj 2D Materials and Applications*, 4(1):17, 2020.

[223] John R Schaibley, Hongyi Yu, Genevieve Clark, Pasqual Rivera, Jason S Ross, Kyle L Seyler, Wang Yao, and Xiaodong Xu. Valleytronics in 2d materials. *Nature Reviews Materials*, 1(11):1–15, 2016.

[224] Chaobo Luo, Zongyu Huang, Hui Qiao, Xiang Qi, and Xiangyang Peng. Valleytronics in two-dimensional magnetic materials. *Journal of Physics: Materials*, 7(2):022006, 2024.

[225] Moh Absor, Adhib Ulil, Iman Santoso, Harsojo Harsojo, Kamsul Abraha, Hiroki Kotaka, Fumiyuki Ishii, and Mineo Saito. Polarity tuning of spin-orbit-induced spin splitting in two-dimensional transition metal dichalcogenides. *Journal of Applied Physics*, 122(15), 2017.

[226] Zhiyong Y Zhu, Yingchun C Cheng, and Udo Schwingenschlögl. Giant spin-orbit-induced spin splitting in two-dimensional transition-metal dichalcogenide semiconductors. *Physical Review B—Condensed Matter and Materials Physics*, 84(15):153402, 2011.

[227] Moh Adhib Ulil Absor, Hiroki Kotaka, Fumiyuki Ishii, and Mineo Saito. Strain-controlled spin splitting in the conduction band of monolayer ws 2. *Physical Review B*, 94(11):115131, 2016.

[228] Homayoun Jafari, Evgenii Barts, Przemysław Przybysz, Karma Tenzin, Paweł J. Kowalczyk, Paweł Dabrowski, and Jagoda Sławińska. Robust zeeman-type band splitting in sliding ferroelectrics. *Phys. Rev. Mater.*, 8:024005, Feb 2024.

[229] Qun-Fang Yao, Jia Cai, Wen-Yi Tong, Shi-Jing Gong, Ji-Qing Wang, Xiangang Wan, Chun-Gang Duan, and JH Chu. Manipulation of the large rashba spin splitting in polar two-dimensional transition-metal dichalcogenides. *Physical review B*, 95(16):165401, 2017.

[230] Tahta Amrillah, Angga Hermawan, Yeremia Budi Cristian, Agustina Oktafiani, Diva Meisya Maulina Dewi, Ilma Amalina, Jenh-Yih Juang, et al. Potential of mxenes as a novel material for spintronic devices: a review. *Physical Chemistry Chemical Physics*, 25(28):18584–18608, 2023.

[231] Xiangyu Feng, Zhonglin He, Rui Peng, Ying Dai, Baibiao Huang, and Yandong Ma. Valley-dependent properties in two-dimensional cr 2 cof mxene predicted from first principles. *Physical Review Materials*, 6(4):044001, 2022.

[232] Shuo Li, Junjie He, Lukáš Grajciar, and Petr Nachtigall. Intrinsic valley polarization in 2d magnetic mxenes: surface engineering induced spin-valley coupling. *Journal of Materials Chemistry C*, 9(34):11132–11141, 2021.

[233] Shiladitya Karmakar, Rajdeep Biswas, and Tanusri Saha-Dasgupta. Giant rashba effect and nonlinear anomalous hall conductivity in a two-dimensional molybdenum-based janus structure. *Physical Review B*, 107(7):075403, 2023.

[234] Arjyama Bordoloi and Sobhit Singh. Exploring nonlinear rashba effect and spin hall conductivity in janus mxenes w 2 co x (x= s, se, te). *Physical Review B*, 110(24):245421, 2024.

[235] O Beckmann, H Boller, and H Nowotny. Die kristallstrukturen von ta_2s_2c and $ti_4s_5(ti_{0,81}s)$. *Monatshefte fur Chemie*, 101:945, 1970.

[236] Lei Zhang, Cheng Tang, Chunmei Zhang, and Aijun Du. First-principles screening of novel ferroelectric mxene phases with a large piezoelectric response and unusual auxeticity. *Nanoscale*, 12(41):21291–21298, 2020.

[237] Martin Dahlqvist and Johanna Rosen. Chalcogen and halogen surface termination coverage in mxenes- structure, stability, and properties. *npj:2D materials and applications*, 8:65, 2024.

[238] Shuang Lu, Weijun Ren, Jia He, Cuiqian Yu, Pengfei Jiang, and Jie Chen. Enhancement of the lattice thermal conductivity of two-dimensional functionalized mxenes by inversion symmetry breaking. *Physical Review B*, 105(16):165301, 2022.

[239] Sayantika Bhowal and S. Satpathy. Intrinsic orbital and spin hall effects in monolayer transition metal dichalcogenides. *Phys. Rev. B*, 102:035409, Jul 2020.

[240] S J Hwu, R P Ziebarth, S von Winbush, J E Ford, and J D Corbett. Synthesis and structure of double-metal-layered scandium, yttrium, and zirconium chloride carbides and nitrides, m_2cl_2c and m_2cl_2n. *Inorganic Chemistry*, 25:283, 1986.

[241] H Boller and K Hiebel. Quaternary pseudo-intercalation phases $t_x[nb_2s_2c]$ (t =v,cr, mn, fe,co,ni, cu) andmetastable nb_2s_2c formed by topochemical synthesis. *Journal of Alloys and Compounds*, 183:438, 1992.

[242] K Sakamaki, H Wada, H Nozaki, Y Onuki, and M Kawai. Topochemical formation of van der waals type niobium carbosulfide 1t-nb_2s_2c. *Journal of Alloys and Compounds*, 339:283, 2002.

[243] D Wang, C Zhou, A S Filatov, W Cho, F Lagunas, M Wang, S Vaikunthanathan, C Liu, R F Klie, and D V Talapin. Direct synthesis and chemical vapor deposition of 2d carbide and nitride mxenes. *Science*, 379:1242, 2023.

List of Publications

Published

- **Himangshu Sekhar Sarmah** and Subhradip Ghosh,*Tunable magnetism in nitride MXenes: consequences of atomic layer stacking*, 2024, Nanoscale, 16(37), 17474-17487

- **Himangshu Sekhar Sarmah** and Subhradip Ghosh,*Surface Passivation and Tunable Magnetic Properties of Cr-Based MXenes*, 2024,The Journal of Physical Chemistry C, 128(38), 16133-16142.

- **Himangshu Sekhar Sarmah** and Subhradip Ghosh,*Consequences of Magneto-Electrical Coupling in Multiferroic* VSe_2/Sc_2CO_2 *Heterostructures*,2025,The Journal of Physical Chemistry C ,129,6466-6476.

Under Review

- **Himangshu Sekhar Sarmah**,Kunal Dutta, Subhradip Ghosh and Indra Das Gupta, *Rashba and Zeeman splitting in non-magnetic and non-centrosymmetric MXene* Ta_2CS_2 .

Works that are not part of Thesis

- **Himangshu Sekhar Sarmah** and Subhradip Ghosh,*Stacking and layer dependence of magnetic properties in* Ti_2C *and* Fe_2C, 2023, Journal of Physics D: Applied Physics, 56(34), 345002.

- Mayuri Bora, **Himangshu Sekhar Sarmah** and Subhradip Ghosh,Electrically tunable valleytronics in ferrovalley/ferroelectric heterostructure (Under Review)

Book Chapters

- Mandira Das,**Himangshu Sekhar Sarmah**, Himanshu Murari and Subhradip Ghosh,*Modeling and Simulation of Electrochemical, Thermoelectric, and Magnetic Properties of MXenes*,Age of MXenes, Volume 1. Fundamentals and Artificial Intelligence: Machine Learning Interventions

Conference Attended

- Presented a poster title *Stacking and layer dependence of magnetic properties in* Ti_2C *and* Fe_2C, at **Evolution of Electronic Structure Theory and Experi-**

mental Realization (EESTER-2023)jointly organized by SRM Institute of Science and Technology and Indian Institute of Technology Madras January 4-12 , 2023

- Delivered a talk title *Symmetry lowering and tunable magnetism in Cr-based i-MXenes*, at **International conference on "Emerging phenomena in Quantum materials"**, December11-15,2023 organized jointly by Uppsala University and Savitribai Phule Pune University at Bharatpur.

- Presented a poster title *Tunable magnetism in nitride MXenes: consequences of atomic layer stacking* at **International Conference on 60 Years of DFT: Advancements in Theory and Computation** organised by he Indian Institute of Technology, Mandi, in collaboration with IIT-Ropar and IIT-Guwahati,July 21-26, 2024, IIT Mandi

- Presented a poster title *Role of surface passivation on the magnetic properties of i-MXene* $(Cr_{2/3}M'_{1/3})_2C$ at **E-MRS 2024 FALL MEETING and EXHIBIT** held at held at the University of Technology in Warsaw (Poland) from September 16 to 19, 2024